The Role of Mechanical Loading in Osteoarthritis of the Knee

Jennifer Boyd, Wadham College
DPhil Thesis

Hilary Term 2013

Medial osteoarthritis (OA) and lateral OA have distinct characteristic cartilage lesion locations and knee flexion angles associated with lesion development. These types of OA are suggested to be caused by loading when the knee is in extension and mid-range flexion, respectively.

This project used subject-specific finite element (FE) models to investigate contact conditions within the extended and flexed knee. A method of creating subject-specific FE models by combining geometry (derived from magnetic resonance imaging scans) and load cases (calculated from motion analysis data) collected from the same subject was developed. This model creation method was validated by comparing experimentally-measured pressure data to contact data calculated by FE models.

Models of normal knees in three subjects were created first. Models with larger subject-specific loads had larger displacements and higher stresses and contact pressures. Contact occurred over most of the articulating cartilage surfaces, both in areas of typical cartilage lesions and outside areas of typical cartilage lesions.

Parameters in the normal models were then altered to reflect three mechanical changes hypothesized to lead to OA: increased loading, globally decreased cartilage stiffness, and locally decreased cartilage stiffness. Increased loading led to increased displacements, stresses, and contact pressures. Contact shifted anteriorly in the extended knee models to locations of typical medial OA cartilage lesions; contact remained stationary with elevated stress magnitudes in the flexed knee models. Globally decreasing cartilage stiffness had limited effects on contact results. Locally decreased cartilage stiffness led to locally increased displacement and strain and locally decreased stress and contact pressure. Contact again shifted anteriorly in the extended knee models.

Potential mechanisms of OA initiation were then proposed. Increased weight or locally decreased cartilage stiffness increased strains within the cartilage. High strains can damage the cartilage matrix fibres, further decreasing cartilage stiffness and eventually leading to cartilage lesions and OA.

The Role of Mechanical Loading in Osteoarthritis of the Knee

Jennifer Leigh Boyd
Wadham College



Thesis submitted in partial fulfilment of the requirements for the degree of Doctor of Philosophy at the University of Oxford

Hilary Term 2013

Supervised by Dr Amy B Zavatsky and Prof Harinderjit S Gill

Department of Engineering Science
University of Oxford

Acknowledgements

To my supervisors, Dr Amy Zavatsky and Prof Richie Gill: thank you for your support, guidance, and patience over the years. Amy, thank you for the many discussions about muscle force calculations and modelling approaches. Richie, thank you for providing the project idea and our discussions about validation studies and efficient Matlab coding.

To our postdocs, Dr Stephen Mellon, Dr Cameron Brown, and Dr Elise Pegg: your input and guidance were invaluable. Thank you for taking so much time to discuss the many nuances of FE modelling and of the graduate degree.

To my College advisors, Dr Mark Thompson and Prof Yiannis Ventikos: thank you for welcoming me into Wadham and for being available to discuss questions about College, the DPhil in general, and teaching.

To those who proofread my thesis, Amy, Richie, Barbara, and Hugo - as well as to my examiners, Prof Liz Tanner and Prof Zhanfeng Cui: your useful discussions and input have much improved the clarity and completeness of my thesis!

Thanks also to my lab groups within the Botnar Research Centre. To Barbara (and Laurence) and Jo: you have been a constant source of support, and I truly appreciate the many things you have done for us all over the years. To Richie's lab group (in particular Annie, Monica, Alex, and Aashish) and to Amy's lab group (in particular Lisa, Catriona, Richard, Phil, Alpesh, and Adward): we've had some great times and you've made it a joy to work in the Botnar (on days when it isn't raining and my bike is functioning)!

Many people outside the lab also deserve thanks. First, to my parents and family: thank you for introducing me to engineering but then encouraging me to go into medicine; we will finally have a doctor in the family - though maybe not the kind you expected! To my professors and friends from NC State, in particular Peter, Lianne, and Jennie: thank you for preparing me for this degree and for your unwavering support.

Thanks also to Wadham Boat Club, who heard in detail every success and failure involved in my DPhil. To our coach, Rod: you gave me a reason to get out of bed and provided an example of the unassuming support I hope to provide my own future students and athletes. To the many crews I've rowed with over those years: there are far too many of you to list here - it was a pleasure competing with and for you.

To the MCR: I hope my contributions as a committee member have made it worth the amount of free cake and biscuits I have eaten! Particular thanks to Alice, Mike, Simon, Alex, and Emilie for putting up with my eccentricities while finishing my thesis.

Finally, a special thank you to the National Science Foundation, Whitaker International, Clarendon Scholars, Wadham College, and Phi Kappa Phi for funding my DPhil.

Abstract

Osteoarthritis (OA) is a chronic musculoskeletal disease that affected more than 150 million people worldwide in 2004. With the probable association between OA, obesity, and aging, the number of individuals suffering from OA is projected to continually increase. Despite this prevalence, the cause or causes of OA remain unknown.

The hip, knee, foot, and hand are all common sites of OA; this thesis focused on unicompartmental OA in the knee. Knee OA can begin in either the medial tibiofemoral compartment (medial OA) or in the lateral tibiofemoral compartment (lateral OA). These two types of OA have distinct phenotypes associated with the knee flexion angle at which lesions contact, suggesting a mechanical role in OA initiation.

Medial OA lesions are reported to begin in the central or anterior regions of the cartilage; lateral OA lesions begin in the central or posterior regions of the cartilage. Due to these differences in lesion locations, the femoral cartilage and tibial cartilage lesions in the two types of OA contact at different characteristic knee flexion angles. Medial OA lesions contact at lower knee flexion angles as occur during heel strike of level walking; lateral OA lesions contact at mid-range knee flexion angles as commonly occur during rising from a stool.

This thesis investigated the role of mechanical loading in OA of the knee by calculating contact results from subject-specific finite element (FE) models of the knee in extension and mid-range flexion. Subject-specific models were created by combining model geometry and load cases representative of a single individual (as opposed to combining data from multiple individuals).

The first step in this project was to develop a method of creating subject-specific model geometry from magnetic resonance imaging (MRI) scans. Internal knee structures were segmented from the MRI scan before being processed and assembled to create the knee model geometry. As segmentation required significant user input, intra- and inter-observer studies were conducted to investigate the variation associated with the segmentation process. Knee geometry models were then created from two MRI scans per subject: one scan with the knees fully extended and one scan with the knees flexed to the maximum knee flexion angle achievable within the MRI scanner.

The next step in this project was to develop a method of calculating subject-specific load cases from motion analysis data. Markers placed on the subjects were used to record subject motion during level walking and rising from a stool. The marker locations and ground reaction data were then used in a lower limb model to estimate the muscle forces generated and the joint reaction forces and moments experienced during level walking and rising from a stool. Muscle and joint reaction data were then combined to calculate the FE model load cases. As the applied load case directly affected FE model results, multiple verification studies were conducted. These studies compared the muscle and joint reaction data calculated by the lower limb model to values cited in the literature.

Finally, a method was developed in which the subject-specific geometry and subject-specific load cases were combined to create the subject-specific FE models. This model

creation method was tested in a validation study involving porcine knee specimens. Pressure film was inserted into the porcine specimens, which were then loaded experimentally with known loads. The resulting pressures were then measured by the pressure films. FE models representing the experiment were then created, and the calculated and experimentally-measured data were compared. The validation study results were used to guide the selection of the FE model type and solution method to use for the models of the human knees.

The selected FE model type was then used to create models of the human knee. These models were used in a parameter study and mesh convergence tests to investigate ways to streamline the model and determine the mesh densities necessary for converged contact results.

After developing and testing the various methods, FE models based on data from three normal, healthy subjects were created. The displacements, von Mises stresses, and contact pressures on the articulating surfaces of the tibial cartilage and femoral cartilage were calculated. Contact locations were then compared to locations of typical OA cartilage lesions. Models with larger load cases were found to have larger displacements and higher stresses and contact pressures. Calculated result patterns showed extensive contact over most of the articulating cartilage surfaces, both in areas of typical cartilage lesions and outside areas of typical cartilage lesions.

The normal FE models were then altered to reflect three mechanical changes hypothesized to lead to OA: increased loading, globally decreased cartilage stiffness, and locally decreased cartilage stiffness. Sets of simulated mechanical change models were solved for each of these altered parameters. Increased loading led to increased displacements, stresses, and contact pressures. Contact area also shifted anteriorly in the extended knee models, resulting in contact in the anterior location typical of medial OA cartilage lesions; contact in the flexed knee models remained relatively stationary while the magnitudes of stress increased. Globally decreasing cartilage stiffness by 10% and 20% was shown to have limited effect on the models. It was therefore suggested that larger changes in stiffness are necessary for OA initiation - or more realistically, that local and not global decreases in cartilage stiffness lead to OA. Locally decreasing cartilage stiffness led to local increases in displacement and local decreases in stress and contact pressure. Contact shifted anteriorly in the extended knee models. In addition to displacement, stress, and contact pressure, axial and shear strains were also calculated for the locally decreased cartilage models. Axial strains were larger in extended knee models; shear strains were larger in flexed knee models.

Potential mechanisms of medial OA and lateral OA initiation were proposed using the model results. Displacements increased in each of the simulated mechanical change models; therefore, strain also increased. Increased strain may damage the fibres in the cartilage matrix, potentially leading to cartilage swelling, further decreases in cartilage stiffness, further cartilage damage, and eventually cartilage lesions and OA.

Contents

1 Introduction **1**

1.1 Project motivation 1

1.2 Project aims 2

1.3 Chapter descriptions 3

2 Background **5**

2.1 The normal knee 5

2.1.1 Internal structures 5

2.1.1.1 Bones 5

2.1.1.2 Cartilage 6

2.1.1.3 Menisci 7

2.1.1.4 Ligaments 7

2.1.1.5 Muscles 7

2.1.2 Main functions 8

2.1.2.1 Mobility 8

2.1.2.2 Stability 8

2.1.3 Types of motion 9

2.1.3.1 Passive knee flexion 10

2.1.3.2 Active level walking 11

2.1.3.3 Active rising from a stool 12

2.1.4 Tibiofemoral contact points 13

2.1.4.1 Studies involving quasi-static activities 14

2.1.4.2 Studies involving dynamic activities 16

2.1.5 Estimates of tibiofemoral contact forces from instrumented implants 18

2.1.5.1 Level walking . . . 20
2.1.5.2 Rising from and sitting onto a stool . . . 21
2.1.5.3 Ascending and descending stairs . . . 22
2.1.5.4 Squatting . . . 23
2.1.5.5 Other recreational activities . . . 23
2.1.5.6 Summary . . . 24
2.2 The osteoarthritic knee . . . 24
2.2.1 Definition and types . . . 24
2.2.2 Theorized causes . . . 25
2.2.2.1 Genetic . . . 25
2.2.2.2 Biochemical . . . 27
2.2.2.3 Biomechanical . . . 27
2.2.2.4 Combination of factors . . . 30
2.2.3 Typical cartilage lesion locations . . . 32
2.3 Modelling the knee using FE analysis . . . 34
2.3.1 Background . . . 35
2.3.1.1 Two main solution approaches . . . 36
2.3.1.2 Common difficulties associated with modelling contact . . . 38
2.3.2 Previous FE knee models . . . 41
2.3.2.1 Image modalities used in model geometry acquisition . . . 41
2.3.2.2 Internal knee structures modelled . . . 42
2.3.2.3 Load cases applied . . . 46
2.3.2.4 Current trends in FE knee models . . . 48
2.4 Project overview . . . 52
2.4.1 Introduction . . . 52
2.4.2 Description of steps . . . 53
2.5 Conclusions . . . 55

3 Creating the FE Model Geometry 56

3.1 Methods . . . 56
3.1.1 Collecting the MRI scans . . . 56

3.1.2 Creating 3D objects of the internal structures . . . 58
3.1.3 Defining the surface contours of the 3D objects . . . 59
3.1.4 Creating the knee model assembly . . . 60
3.2 Intra- and inter-observer segmentation and registration marker centre identification study . . . 61
3.2.1 Introduction . . . 61
3.2.2 Methods . . . 62
3.2.3 Intra-observer test results . . . 63
3.2.3.1 Segmentation of structures . . . 63
3.2.3.2 Identification of registration marker centres . . . 63
3.2.4 Inter-observer test results . . . 64
3.2.4.1 Segmentation of structures . . . 64
3.2.4.2 Identification of registration marker centres . . . 64
3.2.5 Comparing the intra- and inter-observer results . . . 64
3.2.5.1 Segmentation of structures . . . 65
3.2.5.2 Identification of registration marker centres . . . 66
3.3 Discussion . . . 66
3.3.1 Limitations . . . 68
3.4 Conclusions . . . 69

4 Calculating the FE Model Load Cases 73

4.1 Methods . . . 73
4.1.1 Collecting the motion analysis data . . . 73
4.1.2 Processing the motion analysis data . . . 76
4.1.3 Applying data to the lower limb model . . . 77
4.1.4 Calculating the muscle and joint reaction load cases . . . 79
4.1.5 Selecting a representative motion cycle . . . 80
4.1.6 Calculating equivalent forces and moments to apply to FE models . 81
4.1.6.1 Calculating equivalent force and moment for muscle data . 83
4.1.6.2 Calculating equivalent force and moment for joint reaction data . . . 85

4.1.6.3 Calculating total equivalent force and moment 86
4.2 Results 87
4.3 Verification studies 89
4.3.1 Comparing calculated muscle forces to forces applied in other FE models 89
4.3.2 Comparing joint contact forces with instrumented implants and other mathematical models 90
4.3.3 Comparing intra-subject muscle forces 92
4.3.4 Comparing inter-subject muscle forces 93
4.3.5 Comparing calculated muscle activation timings to expected EMG activation timings 94
4.3.5.1 Study A: Visual assessment 96
4.3.5.2 Study B: Unweighted differences 96
4.3.5.3 Study C: Weighted differences 98
4.3.5.4 Study D: Percentage activation differences 100
4.4 Discussion 101
4.4.1 Potential sources of differences 103
4.4.2 Limitations 104
4.5 Conclusions 105

5 Creating the FE Knee Models **107**

5.1 Steps in model set-up 107
5.1.1 Importing geometry and defining material properties 107
5.1.2 Generating mesh 108
5.1.3 Assigning boundary conditions 109
5.1.4 Defining interactions between structures 110
5.1.5 Applying load cases 111
5.1.6 Setting model solution parameters 111
5.2 Preliminary FE models 112
5.2.1 Solving Hertzian contact model with generic geometry 112

5.2.2 Progressing towards models with subject-specific bone and cartilage geometry . . . 113
5.2.3 Creating subject- and task-specific models of the extended and flexed knee . . . 115
5.2.4 Incorporating menisci into the models . . . 117
5.3 Conclusions . . . 118

6 Validating the FE Model Creation Method 120
6.1 Preliminary study . . . 121
6.2 Main study . . . 124
6.2.1 Methods . . . 124
6.2.1.1 Collecting the experimental data . . . 124
6.2.1.2 Modelling the experiment using FE models . . . 127
6.2.1.3 Comparing the experimental and calculated results . . . 128
6.2.2 Results . . . 130
6.2.2.1 Axial displacements of femur . . . 131
6.2.2.2 Maximum pressures . . . 131
6.2.2.3 Average pressures . . . 133
6.2.2.4 Pressure patterns . . . 134
6.2.3 Discussion . . . 136
6.2.3.1 Potential reasons that some FE models did not solve . . . 136
6.2.3.2 Selecting representative FE model types . . . 138
6.2.3.3 Limitations . . . 141
6.3 Conclusions . . . 141

7 Last Stages of FE Model Set-Up 143
7.1 Introduction . . . 143
7.2 Parameter study . . . 143
7.2.1 Introduction . . . 143
7.2.2 Methods . . . 144
7.2.3 Results . . . 145

7.2.4 Discussion and conclusions . . . 147
7.3 Mesh convergence tests . . . 148
7.3.1 Introduction . . . 148
7.3.2 Methods . . . 149
7.3.3 Results . . . 150
7.3.4 Discussion and conclusions . . . 152
7.4 Conclusions . . . 153

8 FE Models of the Normal Human Knee 155

8.1 Cartilage lesion locations . . . 156
8.1.1 Medial tibiofemoral compartment . . . 156
8.1.2 Lateral tibiofemoral compartment . . . 158
8.2 Results . . . 159
8.2.1 Extension models . . . 159
8.2.1.1 Medial tibial cartilage results . . . 159
8.2.1.2 Medial femoral cartilage results . . . 160
8.2.2 Mid-range flexion models . . . 161
8.2.2.1 Lateral tibial cartilage results . . . 161
8.2.2.2 Lateral femoral cartilage results . . . 162
8.3 Discussion . . . 163
8.3.1 Limitations . . . 167
8.4 Conclusions . . . 168

9 FE Models with Simulated Mechanical Changes 169

9.1 Increased load case . . . 169
9.1.1 Methods . . . 169
9.1.2 Results . . . 170
9.1.3 Discussion . . . 173
9.1.4 Conclusions . . . 178
9.2 Globally decreased cartilage stiffness . . . 178
9.2.1 Methods . . . 178

9.2.2 Results . . . 179
9.2.3 Discussion . . . 181
9.2.4 Conclusions . . . 182
9.3 Locally decreased cartilage stiffness . . . 182
9.3.1 Methods . . . 182
9.3.2 Results . . . 184
9.3.3 Discussion . . . 186
9.3.4 Conclusions . . . 187
9.4 Discussion . . . 187
9.4.1 Limitations . . . 189
9.5 Conclusions . . . 189

10 Contributions and Future Work **192**
10.1 Contributions . . . 192
10.1.1 Developing a method of creating subject- and task-specific FE models 192
10.1.2 Utilizing subject-specific FE models to investigate potential mechanical causes of OA . . . 193
10.2 Future work . . . 196
10.2.1 Future improvements to work . . . 196
10.2.2 Future extensions to work . . . 198
10.3 Conclusions . . . 199

Appendices **201**

A Instructions for Intra- and Inter-Observer Segmentation Tests **201**
A.1 Introduction . . . 201
A.2 Segmentation protocol steps . . . 202
A.2.1 Screen orientation and segmentation practice . . . 202
A.2.2 Actual segmentation . . . 204
A.3 Registration marker centre determination steps . . . 207

B Testing New Force Plate and Convertor Card **209**

List of Figures

2.1 Internal structures within the knee 6

2.2 Possible translations and rotations of the normal knee 10

2.3 Passive translations and rotations as functions of knee flexion angle 11

2.4 Human gait cycle 12

2.5 Active translations and rotations during stance phase of level walking . . . 13

2.6 Active translations and rotations during rising from a stool 14

2.7 Medial centre of rotation reported for squatting activity 16

2.8 Lateral centre of rotation reported for stance phase of walking 17

2.9 Contact point motion throughout stance phase of walking 18

2.10 Cross-sectional views of strain gauge-based instrumented knees 19

2.11 Cross-sectional views of transducer-based instrumented knees 20

2.12 Illustration of terms frequently-used to describe FE model meshes 36

2.13 Outline of steps within a Standard and Explicit FE model solution increment 37

2.14 Verification of quasi-static conditions in an Explicit FE model 38

2.15 Effect of pinball or tolerance region on Standard FE model results 40

2.16 Chondrocyte shapes and collagen fibre orientations in different cartilage zones 49

2.17 Modelling the zones of cartilage and menisci in FE models 50

2.18 Normal split lines in femoral cartilage and tibial cartilage 51

2.19 Flow map of FE model creation method 53

3.1 Registration marker locations 57

3.2 MRI scans of full extension and mid-range knee flexion 58

3.3 Surface geometry created from segmentation 59

3.4 Hierarchy of grids used to define the surface contours 59
3.5 Steps in defining the surface contours 60
3.6 Example of completed knee assembly for FE model 61

4.1 Marker set used in motion analysis 75
4.2 Dimensions of stool 76
4.3 Example of processed level walking trial 77
4.4 Illustration of a result from the muscle activation calculations 80
4.5 Rationale for muscle and joint reaction data included in equivalent load cases 82
4.6 Example of different locations of muscle attachments 83
4.7 Semimembranosus muscle forces for level walking and rising from a stool (one subject) 92
4.8 Semimembranosus muscle forces for level walking and rising from a stool (three subjects) 94
4.9 Expected muscle activation trends from five EMG studies 95
4.10 Calculated and expected muscle activation timings during level walking . . 97

5.1 Displacements calculated on articulating tibial cartilage surfaces for FE models with different axial/radial meniscal Young's moduli 109
5.2 Hertzian contact FE model 113
5.3 Cartilage-only FE model 114
5.4 Cartilage and femur FE model 115
5.5 Cartilage, femur, and tibia FE model 115
5.6 Medial compartment-only FE model 116
5.7 Von Mises stresses calculated on the articulating medial tibial cartilage surface of Standard and Explicit FE models 117
5.8 Full subject-specific FE model 118

6.1 Posterior view of rig used during validation study 123
6.2 Displacement of femur during 30 preconditioning load cycles 123
6.3 Per cent change in displacement between consecutive load cycles 124
6.4 Posterior view of rig with relative positions of femur and tibia locked . . . 126

6.5 FE model types created for main validation study 129
6.6 Pig 1: Experimental and calculated pressure patterns for 300 N load 135
6.7 Pig 2: Experimental and calculated pressure patterns for 300 N load 136
6.8 Explicit-Rotate-Sep failure mechanism 138

7.1 Parameter study results: Extended knee models 146
7.2 Parameter study results: Flexed knee models 147
7.3 Convergence test results: Extended knee models 151
7.4 Convergence test results: Flexed knee models 152

8.1 Knee orientation and terms used when illustrating and describing FE model results 156
8.2 Expected cartilage lesion locations in the medial compartment 157
8.3 Expected cartilage lesion locations in the lateral compartment 158
8.4 Medial tibial cartilage results 160
8.5 Concentrated von Mises stresses calculated along cartilage-menisci interface border 161
8.6 Medial femoral cartilage results 162
8.7 Lateral tibial cartilage results 164
8.8 Lateral femoral cartilage results 165
8.9 Von Mises stresses calculated on articulating medial tibial cartilage when the same FE model was solved with No Separation and Separation-allowed constraints 166

9.1 Medial tibial cartilage contact pressures reported by Shirazi *et al.* 170
9.2 Increased load case trends 171
9.3 Increased load case results: Medial tibial cartilage 172
9.4 Increased load case results: Medial femoral cartilage 173
9.5 Increased load case results: Lateral tibial cartilage 174
9.6 Increased load case results: Lateral femoral cartilage 175
9.7 Increased load case results: Medial tibial cartilage contact pressure 176

9.8 Effect of changing the Young's modulus of cartilage and menisci on axial femoral displacement as reported by Meakin *et al.* 179
9.9 Globally decreased cartilage stiffness trends 180
9.10 Cartilage lesion locations and Young's modulus values used in locally decreased cartilage stiffness study 184
9.11 Locally decreased cartilage stiffness trends 185
9.12 Locally decreased cartilage stiffness results: Medial tibial cartilage 190
9.13 Locally decreased cartilage stiffness results: Lateral tibial cartilage 191

A.1 Mimics work screen 202
A.2 Multiple slice edit toolbox 203
A.3 Setting thresholding limits 205
A.4 Expected cartilage locations 206

List of Tables

2.1 Maximum reported tibiofemoral forces for activities of daily living 24

2.2 Image modalities used and material properties assigned to previously-published FE models of the knee 45

2.3 Applied load cases: Axial compressive force only 46

2.4 Applied load cases: Combinations of forces and moments 47

3.1 Intra- and inter-observer segmentation results 71

3.2 Intra- and inter-observer registration marker centre results 72

4.1 Maximum muscle forces calculated for level walking and rising from a stool 87

4.2 Maximum joint reaction forces calculated for level walking and rising from a stool 89

4.3 Comparison of maximum muscle forces calculated in the current study for level walking and reported by Delp and Pandy *et al.* 90

4.4 Measured and calculated maximum joint contact forces during level walking 91

4.5 Measured and calculated maximum joint contact forces during rising from a stool 91

4.6 Unweighted per cent differences 98

4.7 Weighted per cent differences 99

4.8 Averages and standard deviations of weighted Type A differences 100

4.9 Percentage activation differences 101

6.1 Pig 1: Experimental and calculated displacements of femur 131

6.2 Pig 2: Experimental and calculated displacements of femur 131

6.3 Pig 1: Experimental and calculated maximum pressures 132

6.4 Pig 2: Experimental and calculated maximum pressures 132
6.5 Pig 1: Experimental and calculated average pressures 133
6.6 Pig 2: Experimental and calculated average pressures 134

7.1 Required times for parameter study FE model solution 148

8.1 Medial tibial and femoral cartilage results 159
8.2 Lateral tibial and femoral cartilage results 163

9.1 Parameters used in locally decreased cartilage stiffness study 183

B.1 Resonant frequencies of force plate 210

Chapter 1

Introduction

1.1 Project motivation

Osteoarthritis (OA) is a chronic degenerative disease that affects articular cartilage as well as other structures within a joint. In 2004, the World Health Organization [109] reported that 151.4 million people worldwide (including 40.2 million Europeans and 22.3 million Americans) were suffering from OA. This number of Europeans and Americans was equal to the combined number of individuals who have survived a stroke or suffer from angina pectoris and symptomatic chronic obstructive pulmonary disease. With the association of OA with old age and obesity, OA is expected to become even more prevalent in the future. The report also ranked OA as the sixth most debilitating condition in the world. Therefore, although OA does not result in the death of those individuals it affects, the disease can significantly reduce quality of life and deserves further research.

Although researchers now generally agree on common characteristics of OA (pain, cartilage lesions, subchondral bone sclerosis, and joint space narrowing), the mechanisms of OA initiation are still debated. Genetics has been proposed as one cause of OA initiation. A definitive gene and chromosome have yet to be identified, and a complex multifactorial inheritance scheme is predicted. Biochemical and biomechanical causes have also been suggested. Research groups investigating biochemical theories propose that OA is caused by biochemical changes within the cartilage matrix. Perhaps a chemical affecting the chondrocytes (cartilage cells) is released, altering the ability of the cartilage to reduce friction or transmit loads. Either change may result in cartilage degradation. On the

other hand, research groups investigating biomechanical theories propose that changes in loading may result in either overloaded or underloaded cartilage. According to this theory, cartilage which cannot adapt to the new loading conditions degenerates. A combination of genetic, biochemical, and biomechanical factors is likely to result in OA, potentially with cyclical effects: biomechanically initiated changes resulting in biochemical signals which cause additional biomechanical changes within the joint.

The project described in this thesis investigated the role of mechanical loading in OA of the knee. Two types of uni-compartmental OA (medial OA and lateral OA) are common in the knee. Medial OA and lateral OA have distinct characteristic cartilage lesion locations and progression patterns as well as flexion angles associated with lesion development, indicating strong involvement of mechanical factors in disease initiation.

This project used subject-specific finite element (FE) models to investigate the contact conditions experienced within the knee during loading in two specific knee flexion angles. The FE models combined subject-specific geometry (derived from magnetic resonance imaging (MRI) scans of the knee) and subject-specific load cases (calculated from motion analysis data) from the same subjects. First, models of healthy subject knees were created and solved to investigate contact in the normal knee. Model parameters were then altered to simulate mechanical changes hypothesized to lead to OA, and these simulated mechanical change FE models were solved. Contact patterns from the normal models and the simulated mechanical change models were then compared to each other as well as to typical OA cartilage lesion locations cited in the literature.

1.2 Project aims

The specific project aims were to:

- Develop a method to create subject-specific knee geometry from MRI scans.
- Develop a method to calculate subject-specific loads (including individual muscle forces and joint reaction forces and moments) from motion analysis data.
- Develop a method to create subject-specific FE models of the knee.
- Calculate tibiofemoral contact patterns in the medial and lateral compartments of the normal FE knee models.
- Develop methods to simulate mechanical changes hypothesized to lead to OA.

- Calculate tibiofemoral contact patterns in the medial and lateral compartments of the simulated mechanical-change FE knee models.
- Compare tibiofemoral contact results for FE models of the normal knee and FE models with simulated mechanical changes.
- Compare tibiofemoral contact result patterns to typical cartilage lesion locations in medial OA and lateral OA.

1.3 Chapter descriptions

This thesis begins by presenting a review of the background material and literature relevant to mechanical loading in the knee and its theorized role in the initiation of OA. This information is provided in Chapter 2 and specifically includes an overview of the internal structures in, and functions of, the normal knee as well as literature reviews on OA and FE modelling of the knee. After presenting background information, the steps included in the project are outlined and the rationale for including each step is provided.

The next two chapters describe data collection and data processing. Chapter 3 focuses on methods for collecting the MRI scans and processing the scans to create the subject-specific FE model geometry. Intra- and inter-observer segmentation and registration marker identification studies were conducted to test the repeatability of segmenting the structures and identifying marker centres. Chapter 4 focuses on data collection in the motion analysis laboratory as well as the steps necessary to calculate the subject-specific loads. Multiple verification studies were then conducted to compare the calculated joint contact and muscle force patterns to forces and patterns published in the literature.

The next three chapters describe preliminary work conducted when developing and testing the FE model creation method. Chapter 5 describes how to combine subject-specific geometry and loads to create subject-specific FE models of the normal knee. This method was then used to create a series of preliminary models. The first models were simple sphere-on-cuboid contact models; models then progressed in complexity and subject-specificity until subject- and task-specific FE models were solved. Chapter 6 details a validation study conducted to compare measured pressure film data to contact results calculated from FE models created using the proposed model creation method.

Chapter 7 then contains the results of a parameter study and mesh convergence tests. The parameter study was conducted to determine whether the models could be streamlined by creating equivalent systems of boundary conditions; the mesh convergence tests determined the mesh densities necessary for converged model results.

The next two chapters include the results of the FE models. Normal model results are presented in Chapter 8. In particular, the calculated tibiofemoral contact locations were compared to typical cartilage lesion locations in OA. The models were then altered to reflect three different mechanical changes hypothesized to lead to OA. Chapter 9 describes these mechanical changes and then provides results and discussion on how each mechanical change affected the contact results. These results were first compared to normal model results before the calculated contact patterns were compared to typical cartilage lesion locations. The simulated mechanical change model results were then used to propose potential mechanisms of medial OA and lateral OA initiation.

The last chapter, Chapter 10, gives a summary of the contributions this work has made to the field. There are some limitations to the work, however, and so recommendations of ways to overcome these limitations in future studies are then suggested. Finally, potential extensions of the current work are proposed.

Chapter 2

Background

This chapter begins with a short description of the internal structures and functions of the normal knee. A review of the literature on knee OA is then provided, followed by a literature review of FE modelling of the knee. While considerable research already exists on these topics, gaps in the knowledge still exist and should be filled. The work undertaken in this thesis aimed to fill some of these knowledge gaps. This chapter therefore ends with an overview of the project, a description of the steps involved in the thesis, and an explanation as to why each step was necessary.

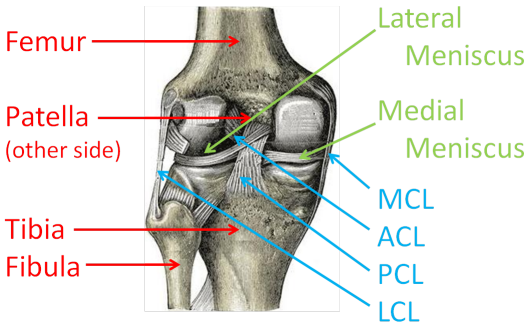
2.1 The normal knee

2.1.1 Internal structures

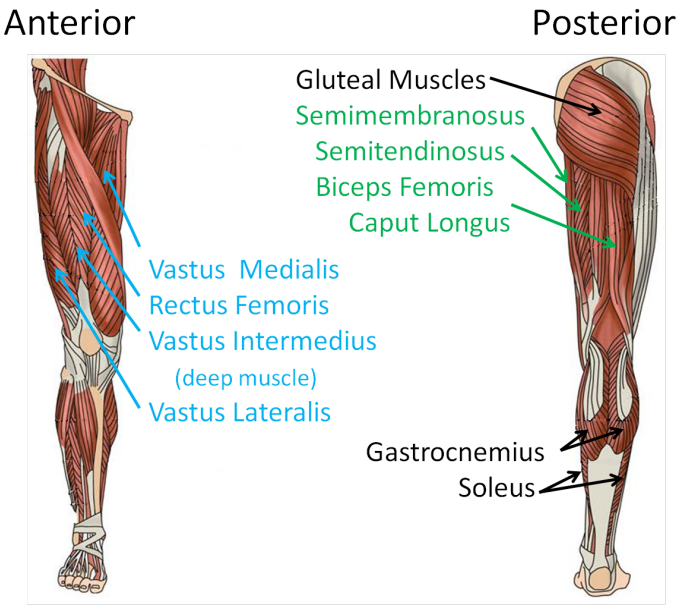
The knee is a complex joint in the lower limb of the human body. It is classified as a diarthrotic synovial joint because it consists of two or more bones (enclosed in a joint capsule) which articulate and allow for motion. Figure 2.1 shows structures within the human knee that are discussed in this thesis.

2.1.1.1 Bones

There are three bones in the knee joint: the femur, tibia, and patella. The articulation within the knee which is most commonly researched is between the femur and tibia; this articulation experiences the majority of the loading during daily events such as walking



(a)



(b)

Figure 2.1: Internal structures within the knee: (a) Posterior view of the (red) bones, (green) menisci, and (blue) ligaments within the knee (figure adapted from Gray's Anatomy, out of copyright.) as well as (b) locations of muscles typically included in knee studies.

or standing. The other articulation in the knee joint is between the femur and patella. This articulation is most heavily loaded at high knee flexion angles.

2.1.1.2 Cartilage

The articulating surfaces of the femur, tibia, and patella are covered with a relatively thin layer of articular cartilage. The two main components of the cartilage matrix are proteoglycans and collagen II fibres. The proteoglycans attract fluid into the matrix, causing the cartilage to swell; the collagen fibres maintain the matrix structure by limiting cartilage expansion. Therefore, fluid can move into or out of the cartilage matrix based

on the loading conditions. The synovial fluid surrounding the cartilage also causes the outer surfaces of cartilage to be nearly frictionless.

2.1.1.3 Menisci

There are two menisci in each knee: a lateral meniscus and a medial meniscus. These highly-fibrous, semilunar-shaped structures help distribute contact forces across the articulating surfaces. The shape of the menisci allows otherwise concentrated contact forces to be spread radially throughout the menisci and distributed to then larger areas of cartilage [47], protecting the cartilage from overloading. Besides distributing contact forces, the menisci also help stabilize the knee. These structures slide slightly to maintain the relative positions of the femur and tibia during flexion of the knee. The amount of permitted sliding, however, depends on the connections between the menisci and the other joint structures (and on the amount of friction). The motion of the medial meniscus, for example, is limited by a peripheral attachment to the deep medial collateral ligament; the lateral meniscus does not have an analogous connection, however, and slides more freely during flexion. On the other hand, the lateral meniscus has an additional attachment to the femur. The ligament of Humphrey and ligament of Wrisberg connect the posterior aspect of the lateral meniscus to the medial femoral condyle [122].

2.1.1.4 Ligaments

Several ligaments are present in the normal knee. Four of the main ligaments include the two cruciate ligaments (anterior (ACL) and posterior (PCL)) and the two collateral ligaments (medial (MCL) and lateral (LCL)). When viewed from the side, the cruciate ligaments form a cross within the middle of the knee and restrain anterior and posterior motion, whereas the collateral ligaments connect the femur and tibia on the medial and lateral sides and prevent axial separation of the two bones. As a group, the main function of the ligaments is to constrain motion within the joint.

2.1.1.5 Muscles

Multiple muscles span the knee joint and can either individually contract to cause motion in the knee or co-contract to control motion in the knee or hold the joint in a static posi-

tion. Two of the major muscle groups acting at the knee are the quadriceps (shown in blue in Figure 2.1) which collectively extend (straighten) the knee and the hamstrings (shown in green in Figure 2.1) which contract to flex (bend) the knee. The quadriceps comprise the rectus femoris, vastus medialis, vastus lateralis, and vastus intermedius muscles; the hamstrings are commonly divided into the semimembranosus, semitendinosus, and biceps femoris longus and brevis muscles. Other muscles generally included in knee studies (shown in black in Figure 2.1) include the gastrocnemius, soleus, and gluteal muscle groups.

2.1.2 Main functions

The inner structures of the knee have two main functions: allowing mobility and maintaining stability. These are competing functions, however. Freely-movable joints are prone to dislocations; therefore, structures that increase stability are necessary. On the other hand, tightly constrained joints have restricted motion. Neither extreme is ideal for a joint like the knee.

2.1.2.1 Mobility

As a diarthrotic joint, one of the main functions of the knee is motion. The body moves forwards, backwards, and sideways during daily activities such as walking, and the knee must be able to move to accommodate these motions. Ideally, these highly repetitive motions will also result in minimal energy expenditure for the body. Various internal structures aid in this task.

The muscles contract to flex and extend the knee, resulting in motion. Meanwhile, the synovial fluid and cartilage allow for nearly frictionless movement of the femur over the tibia and of the patella along the femur.

2.1.2.2 Stability

Free motion within a joint is only desirable to a point, however, and excessive motion may cause the bones to separate and slide into unnatural positions. The ability to control overall body motion may also be impaired, increasing risk of injury due to joint instability.

Fortunately, many of the internal knee structures contribute to knee stability. The ligaments are one of the key stability structures. As a consequence of the specific origin and insertion locations of the ligaments, the ligaments restrain motion between the femur and tibia in each of the anatomical directions. If a large force is exerted in any direction, at least one of the ligaments will act to counteract the force and decrease the likelihood of joint dislocation. In addition to individually restraining motion, the ligaments also act as a unit to lock the knee joint at full extension [15, 96, 97, 122].

The muscles and the menisci also help stabilize the knee. Muscles on opposite sides of the knee can co-contract to lock the knee into place [87, 97, 136]. The wedge-shaped design of the menisci also helps maintain the relative orientations of the femur and tibia [97].

2.1.3 Types of motion

Although sometimes modelled as a hinge joint, the knee can translate and rotate in three directions (Figure 2.2). The three possible translations (shown in blue) are anterior-posterior, medial-lateral, and proximal-distal.

The three possible rotations (shown in red) are flexion-extension, internal-external, and abduction-adduction rotations. Flexion-extension occurs in the sagittal plane and is characterized by the internal angle between the femur and tibia decreasing or increasing, respectively.

Internal-external rotation occurs in the transverse plane and is characterized by the femur and tibia rotating relative to each other. This rotation is coupled with knee flexion angle [42, 156] and is sometimes called the screw-home mechanism because the tibia rotates externally when the knee approaches full extension, locking the knee into place for increased stability [96, 98, 122]. Care should be taken when discussing internal-external rotation as some researchers report tibial rotations while other researchers report femoral rotations. Identifying which bone the rotation is reported with respect to is very important as it will change the direction of rotation; this thesis reports internal and external tibial rotations.

Abduction-adduction occurs in the frontal plane. Abduction of the tibia relative to the femur (clinically known as 'valgus', indicating a knock-kneed alignment) decreases

lateral compartment joint space width. Conversely, adduction of the tibia relative to the femur (clinically known as 'varus', indicating a bowlegged alignment) decreases medial compartment joint space width.

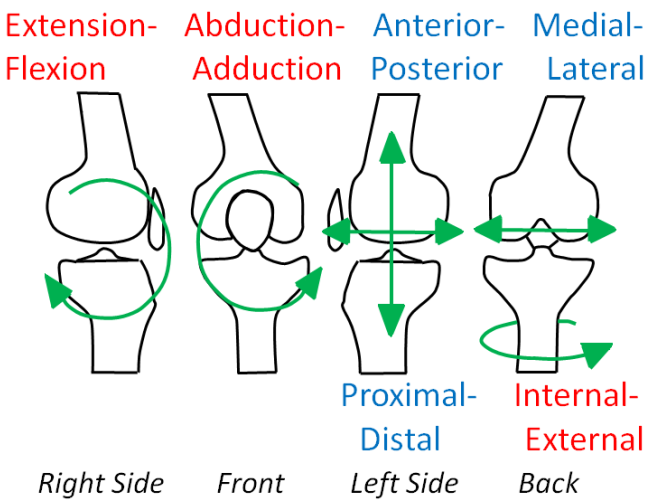


Figure 2.2: Possible (blue) translations and (red) rotations of the normal knee (right knee shown).

Comparing the translations and rotations reported by different studies is difficult because the magnitudes of these motions depend on the specific activity being performed, whether the activity is performed passively or actively, and the locations of the tibial and femoral reference points used when describing motion. Definitions of the rotation axes and the Euler angle sequences will also affect the calculated motions.

2.1.3.1 Passive knee flexion

Ranges of motion recorded during passive knee flexion (Figure 2.3) were reported by Wilson *et al.* [156]. This group passively flexed cadaveric knees from 0° to 100° and calculated translations and rotations of the femoral coordinate system (defined by a transepicondylar axis, functional longitudinal axis, and cross-product of the first two axes) in the fully extended knee relative to a point located at the posterior of the ACL tibial attachment area. The largest translation was in the anterior-posterior direction; the largest rotation (other than the controlled flexion-extension) was in the internal-external direction.

There were approximately 1° and 24° internal rotation at 0° flexion and 100° flexion, respectively. Therefore, the internal-external rotation range was approximately 23° dur-

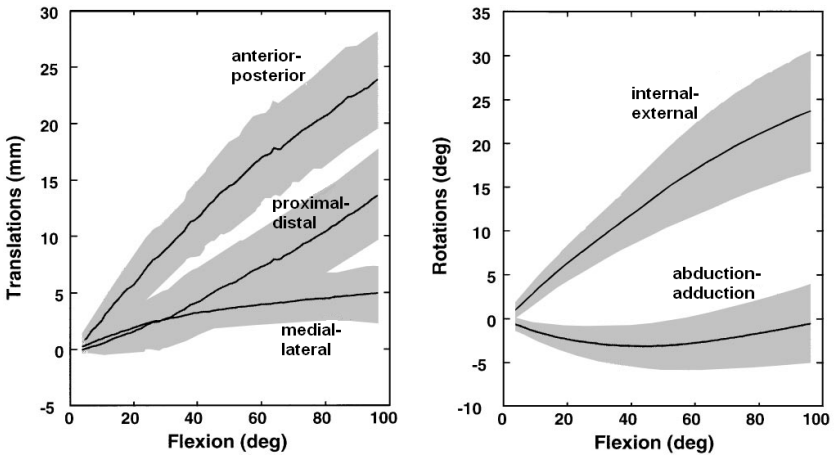


Figure 2.3: Passive translations and rotations as functions of knee flexion angle. ([156], permission to reproduce this (adapted) figure has been granted by Elsevier.)

ing passive knee flexion. Abduction-adduction rotations have been reported to be small enough to be within the measurement error range of some studies. For example, when passively flexed, the knee was adducted approximately 1° at 0° flexion, reached a peak adduction of 4°, and then returned to 1° adduction at 100° flexion [156].

2.1.3.2 Active level walking

Translations and rotations of the knee during level walking have also been investigated. Kozanek *et al.* [85] reported motion of the midpoint of the femoral transepicondylar axis relative to the transverse plane (defined by the tibial long axis and the medial-lateral axis) of the tibia. LaFortune *et al.* [88] used multiple reference frames to describe knee motion during level walking. The tibial reference frame was located at the most proximal point of the medial intercondylar eminence; the femoral reference frame was located at the deepest point of the intercondylar fossa. In both studies, the ranges of translations and rotations from heel strike to toe off (see Figure 2.4 for phases of the gait cycle) were largest in the anterior-posterior direction and flexion-extension direction, respectively.

There are two flexion peaks during level walking (Figure 2.5). The first peak, a local maximum, occurs during stance phase (when the foot is on the ground). This flexion angle is between 8° [85] and 20° [44, 88]. The second and global peak occurs during swing phase (when the foot is not on the ground) and reaches approximately 60° [44, 88]. The maximum flexion angle during stance phase, however, occurs at toe off (just before the

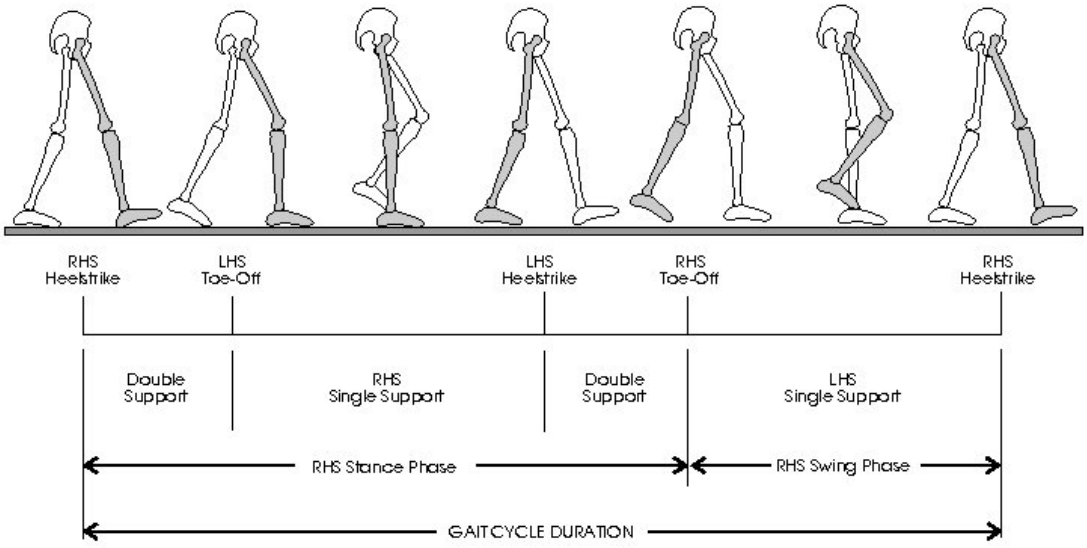


Figure 2.4: Human gait cycle. ([48], permission to reproduce this figure has been granted by Prof Gill.)

foot leaves the ground) and is between 35° [85, 88] and 40° [44].

An internal-external rotation of approximately 10° [88, 104] occurs during level walking. The tibia is externally rotated by approximately 1.6° at heel strike and internally rotated by approximately 7.4° at toe-off [85].

LaFortune *et al.* [88] reported relatively static abduction-adduction rotations, with approximately 1.2° of abduction occurring during level walking. Kozanek *et al.* [85] reported adduction rotations ranging from 1° to 5° during stance phase.

2.1.3.3 Active rising from a stool

Kuo *et al.* [86] reported translations and rotations of the midpoint of the femoral transepicondylar axis relative to a tibial coordinate system associated with a total knee replacement implant (note: subjects had a PCL-retaining knee replacement so motion ranges may differ from those in healthy subjects). As in level walking, the largest translation and rotation were in the anterior-posterior and flexion-extension directions, respectively (Figure 2.6).

The largest flexion angles (approximately 65°) occurred at the beginning of the motion cycle while the subject was sitting on a stool. The tibia rotated by between 4° (based

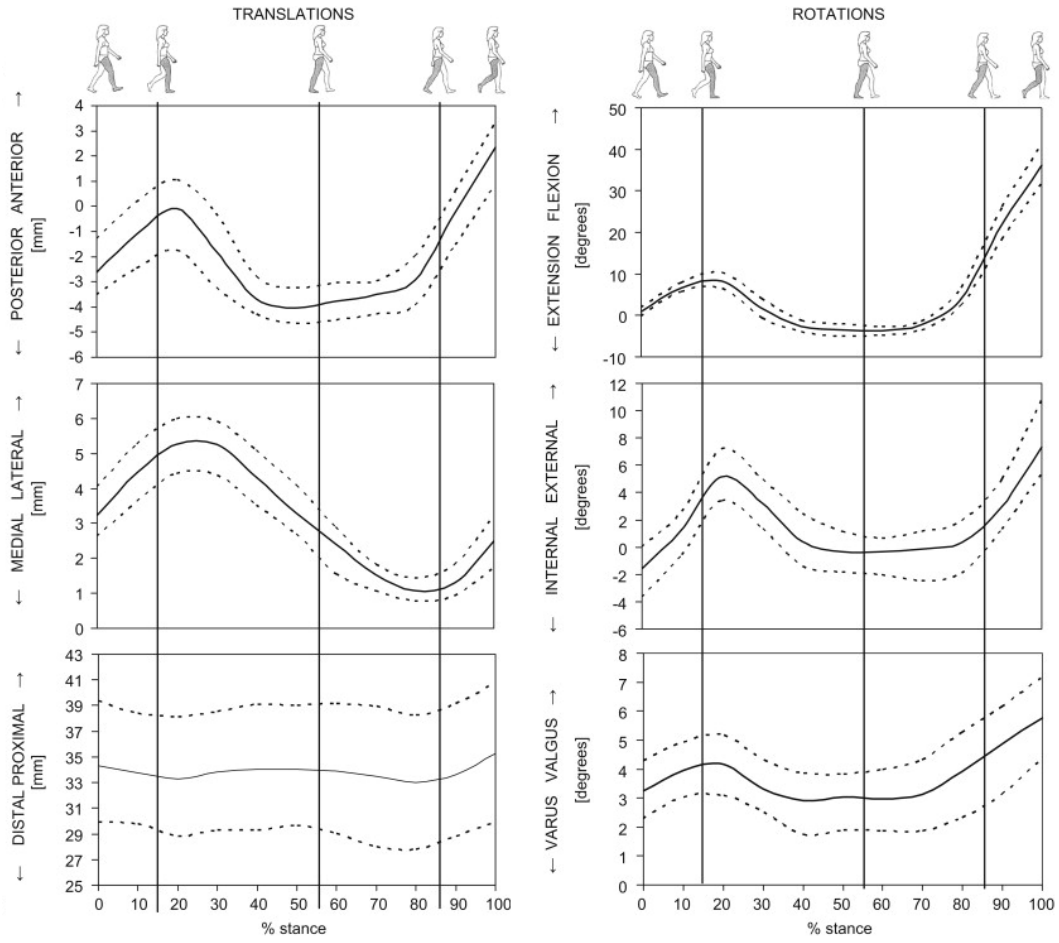


Figure 2.5: Active translations and rotations during stance phase of level walking. (Note: Femoral rotation shown.) ([85], permission to reproduce this (adapted) figure has been granted by Elsevier.)

on marker positions) and 7° (based on fluoroscopy) with small abduction-adduction rotations (2° based on fluoroscopy and 4° based on marker positions) observed during the activity [86].

The specific knee motions during this activity depend on the height of the stool as well as the locations of the subject's feet beneath the stool. These parameters likely vary between studies, making direct comparison of results between different studies complex.

2.1.4 Tibiofemoral contact points

While the main motions within the knee are well-established, there is still disagreement about where tibiofemoral contact occurs and how these contact locations change throughout knee flexion. If flexion and rotation are considered separately, contact point locations

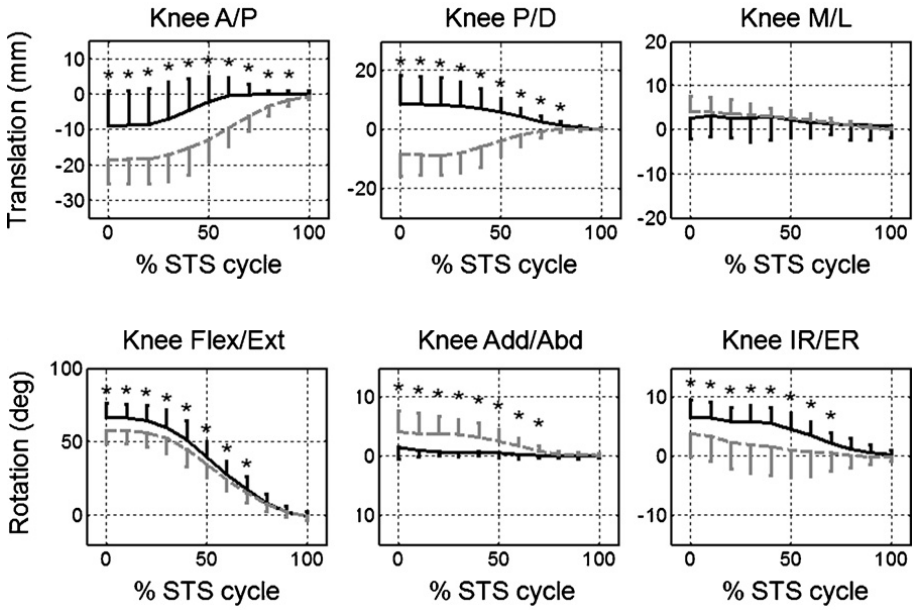


Figure 2.6: Active translations and rotations during rising from a stool. (Note: Data from markers shown in grey; data from fluoroscopy shown in black.) ([86], permission to reproduce this (adapted) figure has been granted by Elsevier.)

can be considered conceptually. With only sagittal flexion, tibial and femoral contact points move posteriorly. If only rotation is considered, internal tibial rotation causes the medial tibial contact point to move anteriorly and the lateral tibial contact point to move posteriorly. In reality, however, flexion and rotation occur simultaneously, complicating the determination of contact point location movement. Today, a central question seems to be whether the knee joint rotates about a point in the medial or in the lateral compartment, and the answer seems to depend on the activity being performed, in particular whether the activity is quasi-static or dynamic.

2.1.4.1 Studies involving quasi-static activities

Initially, it seemed clear that the knee joint rotated around a point in the medial compartment. Results of *in vivo* studies based on closed MRI scans [126, 127], open MRI scans [70], overlaid closed MRI and fluoroscopy scans [19, 27, 90], and overlaid computed tomography (CT) and fluoroscopy scans [80] supported this theory. In these studies, subjects performed a single-leg lunge, squat, or leg press while medical scans were acquired at multiple flexion angles ranging from 0° to 120°. The changes in the positions of the bones

and cartilage in the medial and lateral compartments were determined from the scans. The tibiofemoral contact areas were also segmented and the changes in the locations of these contact area centroids (the contact points) were determined throughout the motion.

The aims of these studies were to compare the locations and motions of the medial and lateral contact points as a function of flexion angle. Unfortunately, the studies reported contact point locations using different reference frames (distances from the posterior edge of the cartilage, from the anterior edge of the cartilage, and from the centre of the compartment were all used in at least one study to describe contact point location). Therefore, comparing contact point locations between studies is difficult. Some general comments on the locations can be made, however.

At full extension, the lateral contact point was generally cited as being anterior to the medial contact point [4, 27, 70, 80, 90]. As flexion angle increased to approximately 30°, both the medial and lateral contact points moved posteriorly. In some studies [19, 126, 127] this motion was nearly uniform between the medial and lateral contact points. Other studies reported that either the lateral contact point [4, 27, 44, 70] or the medial contact point [90, 128] had more posterior motion. This posterior motion varied from a minimum combination of 1 mm medial/2.5 mm lateral [4] to a maximum of 10 mm medial/10 mm lateral [126]. For flexion angles greater than 30°, the medial contact point was reported to remain relatively stationary while the lateral contact point continued to move posteriorly [4, 27, 44, 70, 90]. The exact magnitude of posterior motion cannot be compared between studies because the maximum flexion angles tested varied between studies. At the highest flexion angle tested, all research groups mentioned in this section reported that the lateral contact point was posterior to the medial contact point.

The easiest comparison to make between studies was to compare the overall contact location motion from smallest to largest tested flexion angles. With the exception of three studies by Scarvell *et al.* [126, 127, 128], the lateral contact points were found to have larger overall anterior-posterior motion than the medial contact points. Therefore, the research groups concluded that the knee had a medial centre of rotation because the lateral contact point continued to move posteriorly while the medial contact point remained relatively stationary. Figure 2.7 shows a typical example of reported contact

point motion during a range of flexion angles (mean results of a squatting activity shown).

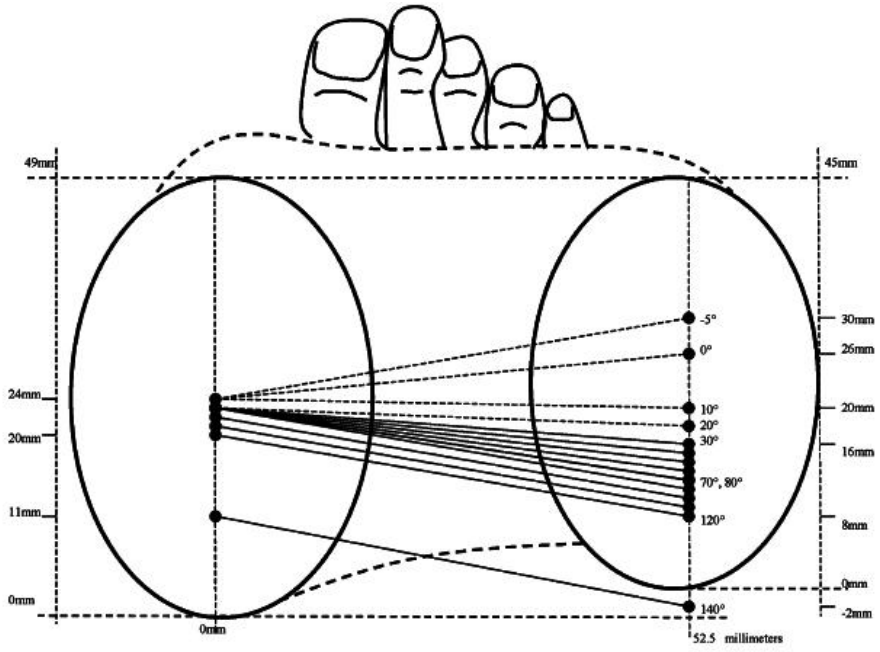


Figure 2.7: Medial centre of rotation reported for squatting activity. ([70], permission to reproduce this figure has been granted by Elsevier.)

Three studies by Scarvell *et al.* [126, 127, 128] reported relatively similar overall motion between the lateral and medial contact points. These were also the only studies tested using a loaded, supine leg press activity, which may account for the differences in results.

2.1.4.2 Studies involving dynamic activities

Recently, two research groups have begun to focus on tibiofemoral contact locations and motions during more dynamic activities such as walking (instead of the single-leg quasi-static activities reviewed in the previous section). These two groups have published results suggesting that the knee has a lateral centre of rotation.

In a 2008 paper, Koo and Andriacchi [82] showed that the knee does not always rotate around a medial contact point. Subjects performed normal walking trials in a gait lab. This gait data was then analysed using the point cluster technique to compare the percentage of stance phase with a medial versus lateral centre of rotation. The results showed that the knee rotates both around medial and lateral contact points but spends 75% of stance phase rotating around a lateral contact point (Figure 2.8). This conclusion

of a lateral centre of rotation clearly runs contrary to those conclusions reached by the researchers testing subjects in quasi-static flexion conditions.

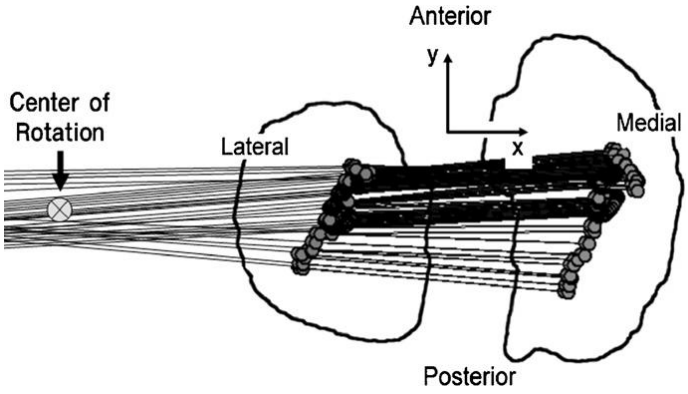


Figure 2.8: Lateral centre of rotation reported for stance phase of walking. ([82], permission to reproduce this figure has been granted by Elsevier.)

Koo and Andriacchi's findings were supported by a 2009 study by Kozanek *et al.* [85]. Subjects in Kozanek's study walked on a level treadmill within the imaging field of a fluoroscope. The scans from the dual fluoroscopy were then overlaid with 3D models based on MRI scans so that contact areas and points could be calculated. The study found that the medial contact point had more overall motion (9.7 mm) during the stance phase of walking than the lateral contact point (4.0 mm), again suggesting a lateral centre of rotation. The study also subdivided stance phase so that more detailed tibiofemoral contact information could be obtained (Figure 2.9). At heel strike (0% stance), the average lateral contact point was located 1.4 mm anterior to the medial contact point (located 1.9 mm and 3.3 mm posterior of the tibial plateau's medio-lateral centreline, respectively). For the next 10% of stance, both the medial and lateral contact points moved anteriorly on the tibial plateau, but from 10% to 20% stance, the medial contact point continued to move anteriorly while the lateral contact point reversed direction and returned approximately to its position at heel strike. From 20% to 50% stance, both contact points moved posteriorly, and from 50% to 70% stance, both contact points remained fairly stationary. From 70% until toe off (100% stance), both contact points moved anteriorly. In their final stance positions, the medial contact point was located 5.3 mm anterior and the lateral contact point was located 0.7 mm posterior to the centreline of the tibial plateau.

Considered together, the results of these two research studies suggest that the loca-

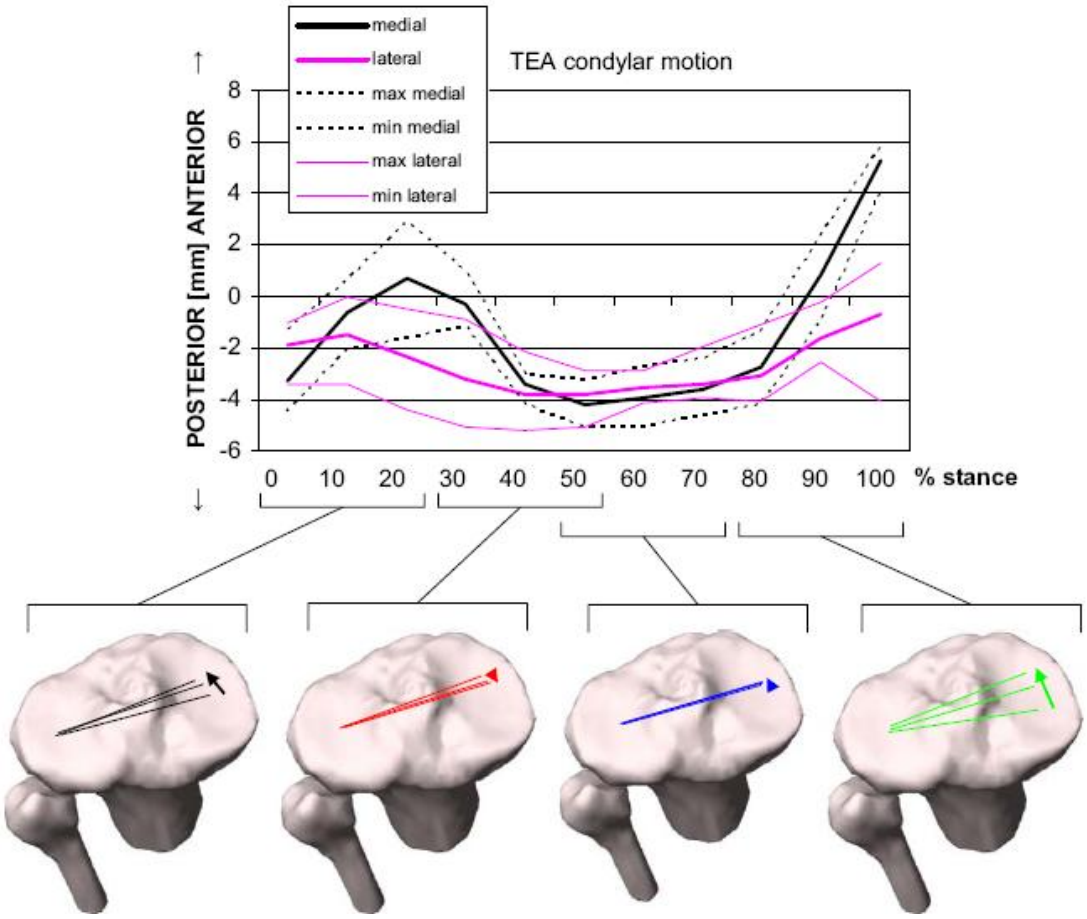


Figure 2.9: Contact point motion throughout stance phase of walking (8 subjects). (Note: Arrows on tibial plateau indicate direction of contact point motion.)([85], permission to reproduce this figure has been granted by Elsevier.)

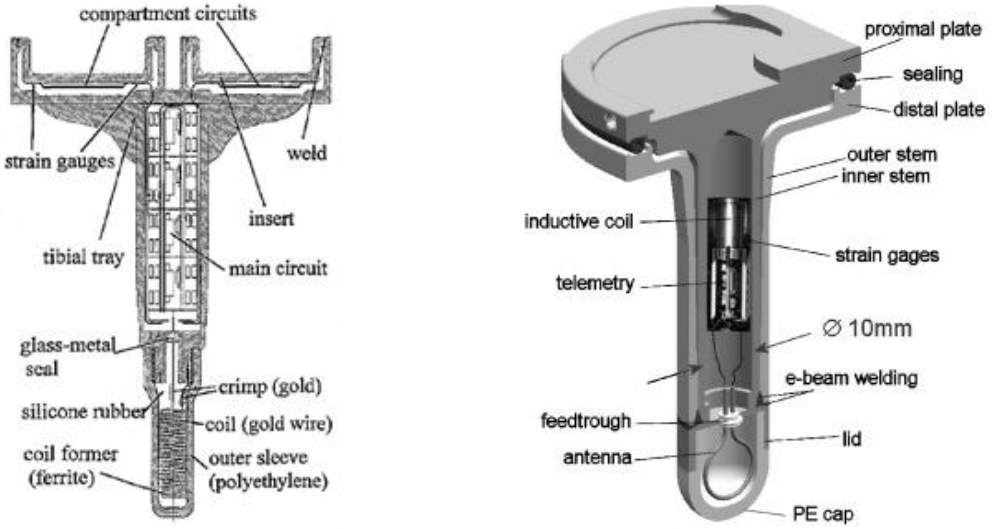
tions of medial and lateral contact points are dependent on the activity being performed. Therefore, it may be incorrect to assume contact points are solely a function of a given flexion angle and not also of a given activity. It should be noted, however, that Komistek *et al.* [80] also investigated contact point motion during walking and, contrary to these two studies, reported a medial centre of rotation.

2.1.5 Estimates of tibiofemoral contact forces from instrumented implants

Information about *in vivo* contact forces can be gathered using instrumented implants. Instrumented implants are joint replacements which fulfil the requirements of typical implants (functionally replacing bone and cartilage in a joint) but also contain internal

circuitry capable of recording and transmitting *in vivo* force data to electronic equipment located outside of the body. This data can then be used to analyse the forces within the joint.

There are currently two main types of instrumented knee implants [35, 59]. In both types, the tibial component is altered to allow for force measurements while the femoral component of the joint replacement remains identical to a normal joint replacement. The first design uses strain gauges placed around the inside of the implant stem (Figure 2.10), while the second design use transducers within the tibial tray (Figure 2.11) to measure forces.



(a) (b)

Figure 2.10: Cross-sectional views of strain gauge-based instrumented knees: (a) Frontal view of an early implant ([143], permission to reproduce this figure has been granted by Dr Taylor and IEEE ©1999.) and (b) sagittal view of a later implant. ([59], permission to reproduce this figure has been granted by Elsevier.)

Instrumented implants have recently been used to measure *in vivo* knee forces experienced during a variety of daily activities. Most studies measured forces during level walking, but forces during other common activities such as stair ascent and descent, stool rising and sitting, and squats as well as sports activities have also been measured.

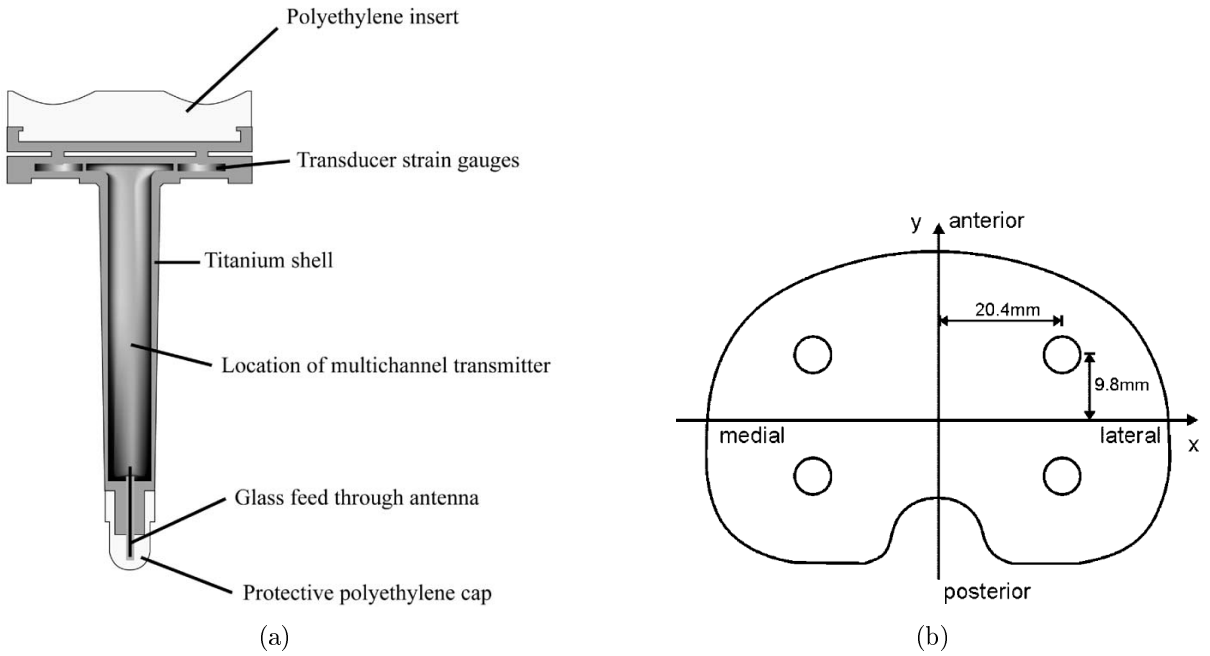


Figure 2.11: Cross-sectional views of transducer-based instrumented knees: (a) Frontal view of an implant ([35], permission to reproduce this figure has been granted by Elsevier.) and (b) superior view of typical transducer locations (circles represent transducers). ([106], permission to reproduce this figure has been granted by John Wiley and Sons.)

2.1.5.1 Level walking

Peak axial tibial forces during level walking performed at a comfortable pace ranged from 2.2 multiples of body weight (BW) to 2.8 BW [32, 33, 34, 38, 60, 77, 87, 106, 144, 162, 163]. The exact contact forces recorded were found to depend on the specific testing protocol, in particular the surface on which the subject walked [34], the speed at which the subject walked [34, 77, 163], and the time which had elapsed since the joint replacement operation [33, 34].

Taylor *et al.* [145] also calculated *in vivo* knee contact forces using data from four instrumented hip replacement patients. Gait trials were conducted, and contact forces at the hip and the knee were calculated using a model previously validated for the hip. Calculated and measured *in vivo* hip contact forces were similar; therefore, the forces in the knee calculated by the validated model were also expected to be physiologically accurate. Within this study, the peak tibiofemoral contact force was determined for each subject and then averaged, resulting in an average peak force of 3.1 BW and an absolute maximum force of 3.8 BW.

2.1.5.2 Rising from and sitting onto a stool

Various research groups also recorded *in vivo* knee forces while rising from a stool [32, 33, 38, 61, 87, 106, 144, 148] and sitting onto a stool [33, 38, 87, 106, 148]. Peak axial tibial forces while rising from a stool ranged from 1.8 BW to 3.3 BW; peak forces during sitting onto a stool ranged from 1.6 BW to 2.9 BW.

Maximum forces experienced during the two tasks should not simply be compared to determine which task results in larger tibiofemoral forces. The research group [61] which reported the largest maximum force (3.3 BW) for rising from a stool did not collect data on sitting onto a stool. If this study were not included, the maximum force for rising from a stool would have been 2.9 BW, the same maximum force reported for sitting onto a stool. Instead, forces for rising from and sitting onto a stool should only be compared within individual studies.

Within-study comparisons also occasionally led to conflicting results. Kutzner *et al.* [87] and Varadarajan *et al.* [148] reported higher forces experienced while rising from a stool than while sitting onto a stool; conversely, D'Lima *et al.* [33], Dyrby *et al.* [38], and Mündermann *et al.* [106] (please note: these three studies were all conducted by the same research group) reported higher forces while sitting onto a stool. Another study from D'Lima *et al.* [32] reported recording information for sitting onto a stool but then did not provide results for the task; therefore, the forces experienced in the two tasks could not be compared.

Peak axial forces varied more for stool activities than for level walking, perhaps again due to testing protocol variations. Some studies used stools at 95% [106, 162] tibial height, other studies at 100% [32] tibial height, and still other studies did not specify stool height. Since stool height affects kinetics [32], it should ideally be standardized between studies. Specific techniques used for rising from and sitting onto the stool could have also led to differences in results between studies. Some studies [32, 33, 87, 106, 144] stated that no arm support was used during testing; other studies [38, 61, 148] did not specify whether subjects could use arm supports. Yet another potential cause of the variability could be differences in elapsed time post-operation. For double-leg stance testing exercises in particular, it is important to specify time post-operation when reporting results. Subjects

compensate by placing less force on the operated leg immediately post-surgery; over time, however, force is gradually distributed more equally between the operated and non-operated leg [32, 106]. Elapsed time since operation was not always specified in the articles, however, and so could not always be taken into account.

2.1.5.3 Ascending and descending stairs

Research groups also reported *in vivo* tibiofemoral forces experienced while ascending [32, 38, 60, 61, 87, 106, 144, 162] and descending [33, 38, 60, 87, 106, 144, 162] stairs. Forces ranged from 2.0 BW to 3.6 BW while ascending stairs and from 2.8 BW to 3.5 BW while descending stairs.

As with the stool activities, these force ranges should not be directly compared to determine whether ascending or descending stairs results in larger tibiofemoral forces. The lower end of the force range for ascending stairs was reported by Heller *et al.* [61], a group which did not report forces experienced during stair descent. If this force were not included in the range, the lower end of the maximum force range for stair ascent would be 2.5 BW, which is similar to the lower end of the maximum forces for stair descent. Again, only within-study comparison should be made to gain insight into whether stair ascent or descent results in larger tibiofemoral forces.

The research groups were again divided on which of these two tasks resulted in larger tibiofemoral forces. Dyrby *et al.* [38], Mündermann *et al.* [106], and Zhao *et al.* [162] reported larger forces during stair ascent, while D'Lima *et al.* [33], Heinlein *et al.* [60], Kutzner *et al.* [87], and Taylor *et al.* [144] reported larger forces during stair descent.

Variations in peak axial forces during stair activities were also larger than in level walking. This variation was likely due to differences in testing protocols, for example, the speeds at which individuals moved up or down the stairs, the inclination (ratio of rise over run) of the stairs, and whether subjects used handrail support during the tasks. None of the studies regulated the speed at which subjects ascended or descended the steps, and faster stair ascent or descent would be thought to result in larger forces. Step inclinations also varied between studies. Larger step inclinations would be thought to result in larger forces due to the resulting larger knee flexion angles and required quadriceps muscle

forces. The availability of handrail support is yet another difference in testing protocol. Some studies [32, 144] allowed subjects to use handrails while completing the tasks, some studies did not provide handrail support [87, 106], and some studies did not specify whether handrails were provided [33, 38, 60, 61, 162].

Tibiofemoral forces during stair ascent were also calculated based on the instrumented hip data presented by Taylor *et al.* [145]. Similar to the level walking trials, *in vivo* hip data was recorded during stair ascent and then applied to a model validated for the hip to calculate forces in the knee. An average maximum tibiofemoral force of 5.4 BW was calculated for four individuals; the absolute maximum force reported was 6.2 BW.

2.1.5.4 Squatting

Some research groups [32, 38, 61, 87, 106] also reported tibiofemoral forces during squatting exercises. Comparing the results of these studies is difficult, however, because some authors did not specify whether the heels were kept on the ground or allowed to lift off during the activity. Some authors also did not specify whether forces were measured while the subject squatted from a standing position or while the subject stood from a squatting position. Only D'Lima *et al.* [32] reported results from both aspects of the squatting exercise; tibiofemoral forces experienced while standing from a squatting position were found to be slightly larger than the forces experienced during squatting from a standing position. Forces reported during squatting ranged from 2.1 BW to 3.6 BW. Caution should be taken when considering the lower maximum force (2.1 BW), however, as this study [32] noted that the subject was still favouring the operated knee by applying less load to it. If this force were not included in the range, the lowest maximum force value would then be 2.3 BW.

2.1.5.5 Other recreational activities

Tibiofemoral forces experienced during a number of other, more strenuous activities were also reported. These tasks focused on rehabilitation- or exercise-based activities and included (in order of increasing tibiofemoral force) rowing on an indoor ergometer [34], cycling on a stationary bicycle [33, 34], performing a leg extension [34], performing a lunge [148], using an elliptical machine [34], performing a leg press [34], using a stair

climbing machine [33, 34], swinging a golf club [34, 38, 106], and serving a tennis ball [34]. These activities resulted in forces ranging from 0.85 BW for the indoor rowing ergometer to 3.9 BW for serving a tennis ball.

2.1.5.6 Summary

Instrumented implants have been used to measure *in vivo* tibiofemoral forces experienced during a variety of activities. These activities ranged from daily tasks such as level walking to exercises such as serving a tennis ball. Of the activities considered, the activity which resulted in the lowest maximum tibiofemoral force (0.85 BW) was rowing on an indoor ergometer; the highest maximum tibiofemoral force (3.9 BW) was reported for serving a tennis ball. Between this range of tibiofemoral forces were more common activities such as level walking, rising from and sitting onto a stool, ascending and descending stairs, and performing a squat. The range of maximum tibiofemoral forces reported for each of these activities is provided in Table 2.1. As shown, maximum forces varied slightly between studies, likely due to differences in testing protocols.

Table 2.1: Maximum reported tibiofemoral forces for activities of daily living, based on the studies cited in Section 2.1.5.

Activity	Forces (BW)
Level walking	2.2 - 2.8
Rising from stool	1.8 - 3.3
Sitting onto stool	1.6 - 2.9
Ascending stairs	2.0 - 3.6
Descending stairs	2.8 - 3.5
Squatting	2.1 - 3.6

2.2 The osteoarthritic knee

2.2.1 Definition and types

OA is a degenerative, chronic, non-inflammatory disease of the cartilage. Ordinarily, cartilage covers the articulating surfaces of bone, but cartilage can wear away, resulting in painful bone-on-bone contact. OA is most commonly associated with cartilage lesions or

fibrillation as well as osteophytes, joint space narrowing, and subchondral bone sclerosis. Although an individual can have OA in multiple joints, OA generally initially develops in a single joint; it may then later develop in other joints, perhaps from an individual changing motion patterns to avoid loading a painful joint.

OA can develop in multiple locations within the knee. Patellofemoral OA develops at the articulation between the patella and femur whereas tibiofemoral OA develops in regions where the tibia and femur articulate. Tibiofemoral OA can be further categorized into medial tibiofemoral OA and lateral tibiofemoral OA depending on whether the medial or lateral compartment is affected. While it is possible for each of these three classifications of OA to affect a knee simultaneously (tri-compartmental OA), each of these classifications can also exist alone (uni-compartmental OA) or in any combination with each other (bi-compartmental OA). This thesis focused on uni-compartmental medial tibiofemoral OA and uni-compartmental lateral tibiofemoral OA, hereafter shortened to medial OA and lateral OA.

2.2.2 Theorized causes

The past few decades have seen much research focused on determining the cause of OA. Unfortunately, not many conclusive results have been reached, and researchers are still divided as to the exact cause or causes of OA initiation.

2.2.2.1 Genetic

One proposed cause of OA is genetics. Twin and sibling studies have been popular methods of testing family inheritance of OA. A 2005 study by Spencer *et al.* [138] found that individuals with siblings suffering from hip OA were 3.5 times more likely to develop OA than the average individual. A similar risk factor (3.05) was found in a 2000 study of hip OA inheritance conducted by Ingvarsson *et al.* [68]. This study, based on Iceland, collected family histories of individuals with hip OA who had undergone hip replacement surgery between 1972 and 1996. Risk factors of developing hip OA for siblings, cousins, and spouses of these hip replacement patients were then calculated. Significantly higher risks were found for siblings (3.05) and cousins (1.52) but not for spouses (1.29).

Groups are currently trying to discover whether specific chromosomes, genes, and/or single nucleotide polymorphs (SNPs) are linked to higher incidences of OA initiation. Relatively small cohorts have generally been studied, and the combined results suggest that the genes likely responsible for initiating OA are joint-specific. The genes (oestrogen receptor α gene (ESR1), interleuken-1 gene cluster, frizzled-related protein 3 gene (FRZB), and interleukin-4 receptor α gene (IL4R) [114]) currently considered most probable to cause OA initiation are linked to signalling proteins, not structure. Therefore, some groups conclude that genetics may cause OA initiation by predisposing an individual to have signalling proteins which result in over-resorption of the cartilage matrix.

Recently, research groups have been pooling information collected from genome-wide association studies in order to gather data from larger cohorts. Kerkhof *et al.* [75] collected information on 1,341 Dutch Caucasians either with OA of the hip, knee, or hand as well as on 3,496 control subjects without OA. The authors searched for a general OA gene instead of a joint-specific gene. Three points of interest were originally identified, two of which were on chromosome 7 and one on chromosome 20. The gene found most likely to be associated with OA initiation was a component of oligomeric Golgi complex 5 gene (COG5) on chromosome 7. The authors decided to further investigate five other genes located in close proximity to COG5 and discovered that G protein–coupled receptor protein 22 (GPR22) was not present in normal cartilage but was present in osteoarthritic cartilage. Therefore, it was proposed that a SNP located near COG5 in chromosome 7 might affect the functioning of GRP22, and either a decrease or increase in the functioning of this G-coupled receptor may lead to OA initiation.

Evangelou *et al.* [41] combined data from four genome-wide association studies to see which SNPs were most common specifically in knee OA. SNPs on chromosome 7q22 were most often affected, with six genes (protein kinase, cAMP-dependent, regulatory, type II, β (PRKAR2B), HMG-box transcription factor 1 (HPB1), dihydrouridine synthase 4-like (DUS4L), B cell receptor-associated protein 29 (BCAP29), COG5, and GPR22) being likely candidates. Of these six genes, DUS4L was involved in both cartilage development and metabolism and was reported the most likely initiator. In addition, the authors noted that these SNPs and genes were likely OA initiators regardless of subject gender,

age, or BMI.

2.2.2.2 Biochemical

A second theory is that biochemical compounds in the knee joint cause OA initiation. These biochemical compounds affect the functioning of the chondrocytes and therefore can cause cartilage degradation. Proteins cited as potential biochemical causes for OA initiation include interleukin-1 [46], metalloproteinase [46, 135], and hydroxyproline [52].

These proteins attract additional fluid into the cartilage matrix, and if the collagen network cannot support the increased amount of fluid, the matrix could be damaged. This increase in fluid flow within the cartilage may also affect the metabolic properties of the chondrocytes. These changes are thought to be especially evident in the deeper zones of the cartilage [135]. Since chondrocytes move from the deep zone to the superficial zone as they age, changing the base-level chondrocytes will eventually affect all the layers within the cartilage matrix.

2.2.2.3 Biomechanical

A third theory is that biomechanical changes in loading within the knee joint alter the magnitudes and locations of stresses experienced by the cartilage, leading to OA. Increasing or decreasing the stresses normally experienced by the cartilage will change the amount of fluid within the cartilage, again potentially damaging the collagen fibres and cartilage matrix.

The motion and stability of the knee is typically regulated by the internal structures (ligaments, menisci, muscles). If any of these structures are damaged, the motion of the knee as well as the magnitude and direction of loading may change. The body must then adapt to these changes in motion and loading to maintain relatively low stress levels. If the body cannot adapt, damage is likely to occur. Damage may also occur if the body adapts to these changes but in ways which result in higher stresses being experienced within the knee.

Other examples of how loading can lead to damage can be seen throughout the body. For example, if an individual experiences repetitive, excessively high stresses within bone, the body must adapt to the loading to remain healthy; otherwise the individual may

develop a stress fracture. It is possible that cartilage follows a similar trend. If the knee cannot adapt to the loads being experienced within the joint, an injury may occur, possibly in the form of a cartilage lesion or a meniscal tear.

Possible reasons for loading changes There are multiple reasons why loading within the knee may change. Three commonly-cited reasons include ligament injury, meniscectomy, and weight gain.

Since ligaments help maintain stability within the knee, ligament injuries can result in knee instability with potentially harmful consequences. Lohmander *et al.* [95] considered the prevalence of OA in female football players who had injured their ACL at an average age of 19 years. Within 12 years of injury, 51% of these athletes had developed OA and 80% of the athletes had either osteophytes or joint space narrowing. Despite over half of these athletes having undergone an ACL reconstruction surgery, the individuals still had abnormally large internal tibial rotations and posterior translations during stance phase over a decade after the initial injury and operation. These abnormal mechanical changes were proposed as causes of the resulting OA.

Injury is not the only reason ligaments may be unable to maintain knee stability. Other reasons include aging [8] and pregnancy [37]. Both of these factors result in increased ligament laxity.

Mensical injury or removal also affects loading within the knee. Three studies considered the effects of meniscectomy. Bolbos *et al.* [21] performed meniscectomies on guinea pigs and then compared their cartilage thicknesses to a group of control guinea pigs. After three months, cartilage thickness was the same for both groups. The meniscectomized group, however, had developed osteophytes, which the research group considered a sign of OA initiation (Buckwalter & Lane [23] stated in an earlier paper that osteophytes do not always indicate OA).

Song *et al.* [137] performed medial meniscectomies on sheep and then investigated how cartilage material properties changed after 16 weeks. This group found that the cartilage in the centre of the medial compartment now experienced larger forces, had softened, and showed signs of fibrillation. The peripheral cartilage, however, experienced less loading and developed osteophytes.

Seedhom [130] considered the locations of OA initiation post-meniscectomy. He theorized that regions of cartilage which had formerly been covered by menisci would experience larger concentrated forces post-meniscectomy. These locations of larger forces were suggested to be the most probable sites of OA initiation.

The effects of a torn meniscus on loading patterns in the knee have also been investigated. A torn meniscus (especially a radial tear [99]) may affect the ability of the menisci to distribute forces to the underlying cartilage. A tear may cause some areas of cartilage to experience abnormally high loadings while other areas experience no loading. A torn meniscus may also fail to stabilize knee motion and maintain proper tibiofemoral orientation. Any of these changes may lead to OA.

The third commonly-provided reason for loading change is weight gain. When an individual gains weight, the contact force between the femur and tibia also increases. The menisci then distribute this additional force to the cartilage [6, 7]. Ideally, the additional force will be distributed equally over the cartilage surface so that stress levels remain low. If the force is not equally distributed, however, some areas of cartilage will experience disproportionately large increases in loading, potentially damaging the cartilage as well as the menisci.

Support for biomechanical initiating factors Just as informative as considering the conditions under which OA develops, one can consider the conditions under which OA does not develop. For example, if OA were caused by proteins in the synovial fluid, then all of the compartments within a joint would be expected to be affected by OA (the same proteins and synovial fluid would be present in all compartments within a joint). Uni-compartmental OA is common, however; cartilage degeneration is observed in one compartment of a joint while cartilage in another compartment of the same joint remains normal. Therefore, it would seem the biomechanical loading within the joint compartment (not the biochemicals in the synovial fluid) is more likely to be an initiating factor of OA.

Results of sham surgeries also support the argument for biomechanical initiating factors. Chaudhari *et al.* [24] cited a comparison of the long-term effects of actual ACL transection surgeries and sham surgeries in cats. Both groups had identical surgeries and tissue damage, but the ACL was left intact in the animals that had sham surgeries. The

sham animals did not develop OA; the ACL-deficient animals did. This result indicates that any biochemical changes related to the incision or soft tissue damage incurred during surgery did not cause OA; OA was more likely caused by the biomechanical loss of the ACL.

Research studies [95] have also shown that OA is still likely to develop after an ACL reconstruction. The purpose of the reconstruction is to replace the functioning of the original ACL. Most ACL reconstructions are therefore designed primarily to limit anterior tibial translation. The normal ACL also limits tibial rotation, however, and reconstructions typically fail to correctly mimic this function [8, 24, 142]. Studies [142] have shown that patients with ACL reconstructions walk with persistently larger internal tibial rotations even after surgery. Therefore, the natural mechanics of the knee are not accurately reproduced by the ACL replacements, changing loading and potentially leading to OA.

Summary In summary, a biomechanical change in one of the internal knee structures will lead to changes in the magnitude, direction, and application location of loading experienced by the other tissues. The body must adapt to these changes to remain healthy. Otherwise, changes in loading or accumulation of damage within the cartilage may lead to cartilage degradation and OA initiation.

2.2.2.4 Combination of factors

Although it is simpler to assume a single factor results in OA initiation, a combination of factors is likely involved.

Felson *et al.* [43] investigated the combined effects of body weight and knee malalignment on OA progression. The heights, weights, and joint space widths of over 200 subjects with symptomatic OA were measured at 0, 15, and 30 months; knee alignment (three categories of absolute measures of varus/valgus were used: 0-2°, 3-6°, and more than 7°) was measured at 15 months. The progression of OA over the 30 months was then considered in relation to BMI and knee alignment. The results showed that increased BMI increased the risk of OA progression in moderately malaligned knees; the risk of OA in severely malaligned or neutral knees was not affected by BMI. The reason for this trend was unclear in the article, but perhaps the individuals with severely malaligned knees were

physically less active, leading to less frequent loading of the knee and smaller changes in joint space width over the course of the study. It is also possible that the severely malaligned knees indicated end stage OA whereas the moderately malaligned knees were still developing OA and therefore had the potential for more joint space narrowing during the course of the study.

Theories on the probable interplay between biomechanical and biochemical factors have also been published. In 2008, Brandt *et al.* [22] hypothesized that OA is the end result of a joint which has attempted unsuccessfully to reduce abnormally high levels of stress. These elevated stress levels may be caused by an increase in the load experienced within the joint or a decrease in joint contact area. The remaining paragraphs in this section summarize the mechanism proposed by Brandt *et al.*

One of the roles of cartilage is to distribute forces over a larger contact area to reduce stress levels. High stress levels can damage cartilage, however, and the body then sends metalloproteinases, aggrecans, and other proteins to repair the matrix. During this process, the damaged matrix is first removed, initially weakening the overall matrix, before the collagen network is repaired. If the matrix is subjected to additional high stresses during this rebuilding phase, cartilage fibrillation may result. These fibrillations can be vertical as well as horizontal, and if the fibrillations connect, fragments of cartilage may detach and enter the synovial fluid. This cartilage debris can then cause inflammation, which also leads to thicker synovial fluid and increased friction between cartilage surfaces.

High stress levels may also result in microfractures in the subchondral bone. The body repairs these microfractures by increasing the density and thickness of the trabeculae. During this remodelling, the deepest layers of cartilage may be replaced by subchondral bone, shifting the tidemark farther into the cartilage and reducing cartilage thickness.

Impulse loads due to quickly bringing articulating surfaces into contact can also damage the internal structures of the knee. The body can reduce these impulse loads by contracting the muscles to bring the surfaces into contact before the external load is experienced. Then the load is transmitted through the already-in-contact joint, resulting in larger damping of the applied load. If, however, an unexpected loading such as a sudden step down or stumbling occurs (especially if this loading is quickly repeated), the muscles

will not contract to bring the joint into contact, and the bone and cartilage will experience an impulse load with low damping. Muscles may also fail to contract due to a condition known as micro-incoordination. This condition, which is thought to affect one in three individuals, is characterized by slightly delayed muscle contraction timing.

Perhaps, although not stated explicitly by Brandt *et al.*, some of the mechanical changes hypothesized to lead to OA can be explained through genetics. An individual may be genetically predisposed to anatomy resulting in concentrated cartilage loading or looser ligaments that allow for more joint instability. It is also possible that genetics determine the maximum load that cartilage or subchondral bone can experience before damage occurs or how effectively these structures can remodel or repair after damage occurs. Reaction time, muscle signal propagation, or presence of micro-incoordination could also be genetically determined. Therefore, it is possible that a combination of factors is involved in OA initiation and progression.

2.2.3 Typical cartilage lesion locations

The phenotype of typical medial compartment lesion locations was first described by White *et al.* [154]. This group resected tibial cartilage samples from 46 patients during uni-compartmental knee replacement surgeries and then considered the locations of the full-thickness cartilage lesions. Medial tibial cartilage lesions were located in the antero-central region; from this information, the term 'antero-medial OA' was derived.

Since 1998, three main groups of studies [53, 56, 151, 152] have investigated the typical locations of osteoarthritic cartilage lesions. Comparing the results of the studies is difficult, however. One study [56] did not include information on femoral lesion locations. Another study [53] only included information for full-thickness cartilage lesions instead of including information on different grades of OA. Patient inclusion criteria also varied between studies and in some cases were not fully reported.

Harman *et al.* [56] investigated lesion locations for varus (medial OA) and valgus (lateral OA) knees; ACL-intact, ACL-deficient, and previously meniscectomized patients were all included in the study. Tibial plateau slices were resected during knee replacement surgeries and then examined for cartilage lesion locations. Lesion locations were

measured relative to the edges of the tibial plateau and were normalized to the length of the compartment in which the lesion was located. For varus knees with intact ACLs, lesions were located an average of 37% and 55% from the medial tibial plateau's medial and posterior edges, respectively. Cartilage damage affected 39% of the medial tibial plateau and was concentrated 5 mm medial to the centre of the compartment. Lesions in ACL-intact valgus knees were located an average of 43% and 51% from the lateral tibial plateau's lateral and posterior edges. Lateral compartment cartilage damage affected 47% of the lateral tibial plateau and was found 2 mm lateral to the compartment centreline. In other words, varus knees had central lesions and valgus knees tended to have more peripheral lesions.

The next set of studies was conducted by Weidow *et al.* [151, 152]. Again, cartilage was resected during total knee replacement surgery and later analysed for locations of damage. The results showed that both medial OA and lateral OA had predominantly central wear patterns on the tibial plateau; medial OA was characterized by increasingly anterior wear while lateral OA lesions progressed posteriorly. On the femur, medial OA lesions were evenly spread throughout the condyle; lateral OA lesions were located along the posterior periphery of the condyle. These results supported the findings of Keyes *et al.* [76] and White *et al.* [154], both of which found that early medial OA was associated with anterior tibial lesions. A disadvantage of the Weidow *et al.* studies was that inclusion criteria related to the health of the ACL was not provided.

The final study describing typical cartilage lesion locations was conducted by Gulati *et al.* [53]. Only patients with intact ACLs were included in this study, and instead of grading cartilage lesions based on severity, only full-thickness cartilage lesions were considered. Both tibial and femoral lesions were measured intraoperatively and referenced according to their distance from the centreline of the respective compartment.

In medial OA, the centroids of tibial lesions were an average of 1.9 mm or 3.4% anterior of the tibial cartilage centreline. Lesions started either centrally or anteriorly and then progressed posteriorly. On the femur, medial lesions were located an average of 10.1 mm posterior to the centreline and progressed posteriorly. The femur and tibia were then flexed to bring the tibial and femoral cartilage lesions into contact. The resulting flexion angle

was hypothesized to represent the angle at which contact resulted in medial compartment cartilage lesions. Tibial and femoral cartilage lesions contacted at a knee flexion angle of approximately 10.9°. The smallest lesion extended from 1° extension to 7° flexion with the largest lesion contacting at a maximum of 37° flexion.

In lateral OA, the centroids of tibial lesions were on average 3.2 mm or 7.1% posterior to the centreline. These lesions did not start in any specific location but once formed, spread both anteriorly and posteriorly. Lateral femoral lesions were an average of 24.6 mm posterior to the centreline and expanded anteriorly and posteriorly. Tibial and femoral cartilage lesions in the lateral compartment contacted when the knee was flexed to approximately 40.5°. The smallest lesion contacted the tibia from 14° to 65° flexion with the largest lesion contacting from 0° to 84° flexion.

In general, cartilage lesions in the lateral compartment occurred in more posterior locations and expanded to contact over a larger range of flexion angles than cartilage lesions in the medial compartment. Also of note, the knee flexion angles at which the lateral cartilage lesions contacted were larger than the flexion angles commonly experienced in the stance phase of walking, suggesting that loading during an activity other than walking results in lateral OA.

It should be noted, however, that the flexion angles at which the tibiofemoral cartilage lesions contacted were measured intraoperatively during passive knee flexion. The review of typical motions within the knee (see Section 2.1.3) showed that translations and rotations within the knee were dependent on whether an activity was passively or actively performed. It would therefore be interesting to also investigate the flexion angles at which these tibiofemoral cartilage lesions contacted during active activities such as level walking or rising from a stool.

2.3 Modelling the knee using FE analysis

This review is divided into two sections. A brief background on FE modelling in general as well as FE modelling specifically of contact is provided in the first section. The second section contains a review of FE models previously constructed to model contact in the knee.

2.3.1 Background

FE modelling began in the 1940s and involved three key individuals. Two of them, Hrennikoff (from the Massachusetts Institute of Technology) and Courant (from New York University), separately developed the concept of dividing an object into small pieces (finite elements) in order to get a more detailed idea of how loads affect the finite elements (instead of the object as a whole). Zienkiewicz (from Imperial College London) then combined the ideas of Hrennikoff and Courant to create what is now known as the FE method.

Since the 1940s, FE modelling has become a popular way to model behaviours described by differential equations. In this modelling method, loads (which can exist in a variety of forms, such as thermal, electrical, or mechanical within solid or fluid objects) are applied to a model and cause deformations within an object. For simple situations, the relationship between these loads and deformations can be calculated directly using differential equations, but real-life situations typically involve multiple differential equations and direct analytical solution may not be feasible.

FE modelling allows for these complex differential equations to be approximated by simpler (linear) equations. For the linear equations to appropriately approximate the differential equations, the linear equations must be solved over small (spatial) increments of the object. These spatial increments are often described using the terms 'mesh', 'element', and 'node' (Figure 2.12).

The mesh approximates the geometry of the model and is made up of elements, which can be 1D, 2D, or 3D. A mesh with a larger number of elements will better approximate the geometric detail of the real object of study. Tetrahedral meshes are comprised of tetrahedral-based elements (see Figure 2.12 for an example); hexahedral meshes are comprised of hexahedral-based elements. Tetrahedral-based and hexahedral-based elements can be combined to create mixed meshes.

Elements are defined by nodes and are classified according to the number of nodes along each side of the element. Linear elements have two nodes per element side; therefore, a linear deformation approximation is calculated for linear elements. Higher-order elements have more than two nodes per element side and allow for higher-order defor-

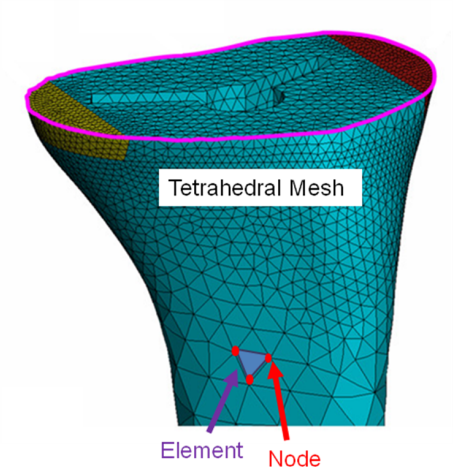


Figure 2.12: Illustration of terms frequently-used to describe FE model meshes: The (teal) mesh is comprised of (purple) elements, which are defined by (red) nodes.

mation approximations. A quadratic element, for example, has three nodes per side and results in a quadratic deformation approximation.

Within the FE modelling method, simpler linear equations are solved over a large number of geometrically small finite elements. Once the deformations of these small individual elements have been calculated, the individual deformations are combined to calculate the deformation of the entire object. Based on these deformations, additional model results such as strain, stress, and energy can be derived.

2.3.1.1 Two main solution approaches

There are two main approaches used by software packages to solve FE models: Standard (also called Implicit) and Explicit approaches (Figure 2.13 gives an outline of the steps within an increment of each approach). Both methods aim to calculate nodal displacements, but the two methods use different equations to accomplish this task [1].

The Standard method solves the equation $F = kx$, seeking to find a balance between the loads applied (F) and the displacements (x) of the element nodes. A stiffness matrix (k) is a key feature in determining the displacements. This matrix is re-calculated at frequent, user-defined intervals (generally with each time increment) during the solution process and must be inverted to solve the inverse equation $x = k^{-1}F$. Calculating and inverting the stiffness matrix can be computationally expensive because matrix dimensions

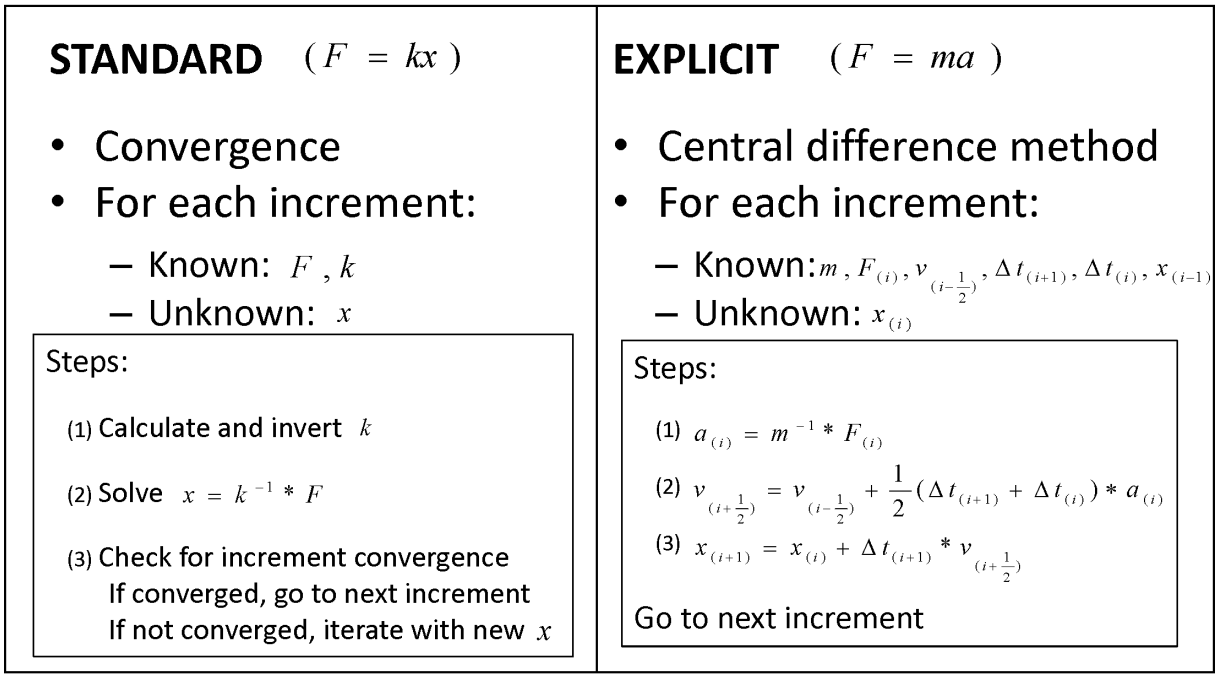


Figure 2.13: Outline of steps within a Standard and Explicit FE model solution increment. F, k, x, m, a, v, and Δt stand for applied force, stiffness matrix, displacement, mass, acceleration, velocity, and time increment size, respectively. Subscripts (i) and $(i \pm \frac{1}{2})$ indicate values in the current and mid- increments, respectively.

are determined by the number of elements in the model. Consequently, a large model will involve calculating and inverting a large stiffness matrix.

The Explicit method solves the equation $F = ma$, applying a load (F) to an object and then considering how that object moves (a) to calculate the final locations (x) of the centre of masses of the elements. Instead of using a stiffness matrix and aiming for convergence, the Explicit method uses central difference integration to calculate element positions based on data in current and previous (or initial) time increments. In comparison to the Standard method, each time increment of the Explicit method is computationally less expensive because there is no need to invert a stiffness matrix. An Explicit solution, however, typically includes a larger number of increments than a Standard solution; in an Explicit solution, the specific number of necessary increments is determined by the size of the smallest element. Each element has a characteristic increment size, Δt, calculated using the equation:

$$\Delta t = \min(\frac{L_e}{c_d}) \tag{2.1}$$

where L_e is associated with element size and c_d represents the wave propagation speed through the material. An Explicit model is conditionally stable on the condition that it is solved in increments smaller than the smallest characteristic increment size in the model [1].

In general, the Standard method is frequently used to model static load conditions and the Explicit method is used to model dynamic events. It is also possible to model quasi-static conditions using the Explicit method. This is accomplished by applying the load slowly enough (using a small Δt) that the resulting kinetic energy is very small ($<$5% typically) in comparison to the internal energy [3] (Figure 2.14).

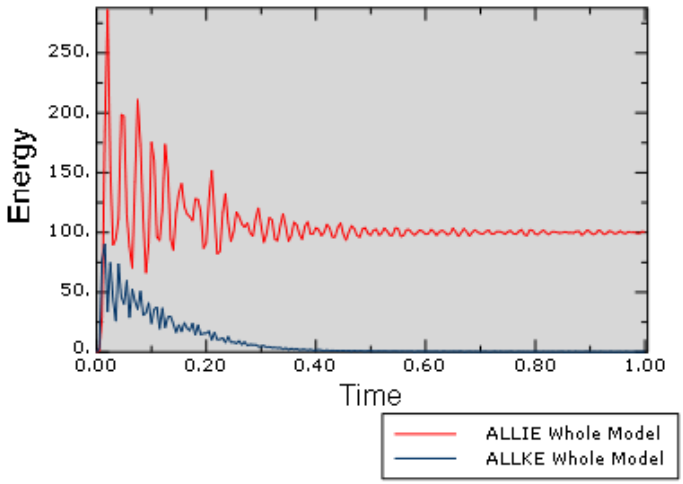


Figure 2.14: Verification of quasi-static conditions in an Explicit FE model. Internal energy (red, approximately 100 N*mm) » Kinetic energy (blue, approximately 0 N*mm).

2.3.1.2 Common difficulties associated with modelling contact

There are multiple difficulties commonly associated with modelling contact between objects in an FE model. The main issue faced when using the Standard approach is convergence. The applied load must be balanced by the stiffness matrix and displacements of the elements for convergence to occur. To improve convergence, the load is applied in increments instead of instantaneously, and iterations of each increment (Figure 2.13) are run to try to gradually bring the model into convergence. Even when the load is applied incrementally, convergence may still be difficult, especially if the geometries of the contacting surfaces are not smooth.

There are a number of reasons an FE model of contact may fail to converge. When modelling contact, the user can specify certain parameters to help the FE model determine which elements to bring into contact with each other. One of these parameters is called the pinball or tolerance region. This parameter tells the FE program how close in location two elements need to be before the elements are assumed to be in contact (Figure 2.15). If elements on two different bodies are within the pinball or tolerance region of each other, then those elements are defined as being 'in contact'; if they are not within the pinball or tolerance region of each other, they are defined as being 'out of contact'. This parameter must be carefully specified. If the region is too small (Figure 2.15a), few (if any) elements will be considered 'in contact', resulting in either no contact between the objects or the entire contact force acting through a limited number of contacting elements. If the region is too large (Figure 2.15c), many elements will be considered 'in contact' and the computational cost of running the model may become too large for the computer memory, causing the solution to stop. A compromise, such as shown in Figure 2.15b, is only including elements likely to come into contact in the region.

Another reason an FE model of contact may fail to converge is chattering. Chattering refers to elements continually switching between being 'in contact' and 'out of contact' in consecutive iterations of model solution. When chattering occurs, the model solution continues to iterate until the maximum number of iterations is reached, but convergence does not occur. Altering the size of the pinball or tolerance range may decrease chattering. Smoother model geometry may also decrease chattering.

Explicit models of contact do not rely on convergence for solution so pinball or tolerance region specifications and chattering do not result in Explicit models failing to solve. An Explicit model may fail, however, due to excessive distortion of relatively small mesh elements. To understand why smaller elements are more likely to undergo excessive distortion, consider an exaggerated case in which a deformation (say 0.1 mm) occurs in two elements, one of a 'typical' size (say an element with 10 mm long sides) and one of a relatively smaller size (say an element with 1 mm long sides). The same 0.1 mm deformation results in a larger per cent deformation in the smaller element and might result in the smaller element becoming excessively distorted. Therefore, it is necessary to

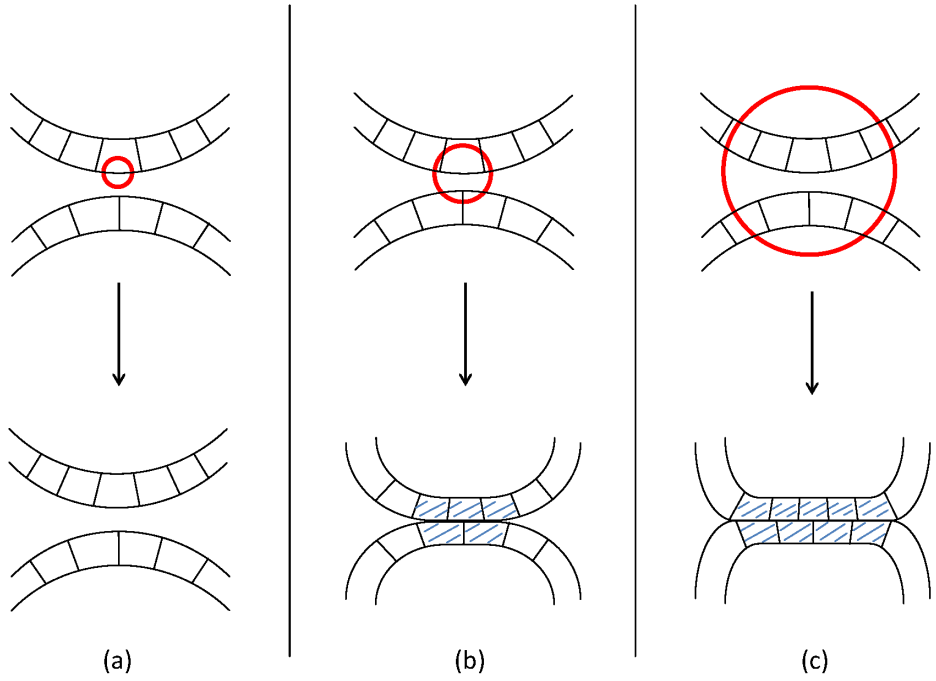


Figure 2.15: Effect of pinball or tolerance region on Standard FE model results: (top) Specified pinball or tolerance region indicated by red circle; (bottom) resulting contact conditions (elements 'in contact' indicated by blue hash marks).
Note: (a) Small region results in no contact between surfaces; (b) reasonable region results in contact only between closest pairs of elements on surfaces; (c) large region results in distorted and extensive contact between surfaces.

find and remove relatively small elements from the mesh (of course, the size classified as 'relatively small' depends on the average size of the elements in the mesh and therefore will vary between FE models).

Small elements also result in a reduction in solution speed for Explicit models. Explicit models should be solved in time increments smaller than the smallest characteristic increment size in the model. Therefore, even one significantly smaller element will cause a significant reduction in solution speed for the entire model.

Small elements in an Explicit FE model can be automatically identified by the FE software. Each element has a characteristic time increment determined by its size (smaller elements result in smaller time increments); therefore, the mesh can be queried for elements resulting in time increments smaller than a user-defined lower limit. Then these small elements can be removed by combining smaller elements with neighbouring elements.

Both Standard and Explicit models of contact may fail due to computational require-

ments. Data from each iteration (only used in Standard models) or load application increment (used in both Standard and Explicit models) is typically stored throughout the solution process. A larger number of elements, iterations, and increments will all lead to more stored information. It is possible that this amount of information will become too large for a standard computer to store; in this case, use of a computer with more memory (perhaps even a supercomputer) may be necessary.

Even after an FE model has solved, it is very important to check that the calculated results are reasonable and cover the entire area of contact. For both Standard and Explicit models, contact results are only calculated for elements pre-assigned as being in the contact area. Occasionally, elements which do contact are not initially included within the pre-assigned expected contact area. In this case, contact results will not be calculated for these elements and the FE model will need to be re-solved with the contact region correctly defined.

2.3.2 Previous FE knee models

This section provides a short literature review on FE models of the human knee which have been previously created. Methods of geometry acquisition are discussed first. Then a description of which internal structures were typically included in the models, as well as the material properties assigned to those structures, is provided. Detailed information on image modalities and structure material properties is provided in Table 2.2. Next, the types of load cases applied to the models are discussed. Two types of load cases predominate in the literature; examples of these load cases are given in Table 2.3 and Table 2.4. Finally, two current trends in FE modelling are presented: increasing the complexity of the cartilage and menisci material properties and using motion analysis data to tailor FE model load cases to a particular subject.

2.3.2.1 Image modalities used in model geometry acquisition

A search of the literature showed three types of imaging modalities commonly used to create FE models of the human knee.

The first modality, x-ray, is the most basic image modality. This type of medical

image uses radiation to capture a 2D image of bone and is not particularly well-suited to imaging soft tissues such as cartilage, menisci, and ligaments. X-ray was only used in one older study [20].

Two other image modalities, CT and MRI, were used in the remaining studies. Both of these image modalities collect multiple slices of information (similar to taking a series of x-rays) during scanning; these slices are then combined to create a 3D image. Like x-ray, CT scans require radiation and are not well-suited to imaging soft tissues. MRI scans, however, do not involve radiation and can be used to image bone as well as soft tissues.

When acquiring geometry for FE models of the knee, some studies used just CT scans or just MRI scans, whereas other studies combined data from CT and MRI scans. When both image modalities were used, CT scans were used to capture the geometry of the bones and MRI scans captured geometry of the soft tissues.

A few studies found other methods of acquiring soft tissue geometry. One method used laser digitization to capture soft tissue surface geometry [57, 58]; another method approximated soft tissue geometry from data available in the literature [25]. (Another study [100] relied solely on parameters reported in the literature to create their FE model geometry.)

2.3.2.2 Internal knee structures modelled

The first FE knee models included the femur, tibia, and sometimes patella as well as their associated cartilages with the knee in full extension. There was some disagreement about how to model the material properties of bone. Most studies considered the relative stiffness of bone and cartilage and modelled bone as a rigid material (Table 2.2). A few studies [54, 57, 119], however, modelled the bone as a deformable material and assigned specific material properties.

How to model cartilage has also been extensively debated. Although cartilage is a viscoelastic material with deformation properties dependent on duration of stress application, the elapsed loading time of the knee during dynamic activities such as walking or rising from a stool is less than the viscoelastic constant (1500 s) of cartilage [25, 54, 55,

57, 58, 65, 115, 116, 118, 159]. Therefore, fluid does not have time to move within the cartilage, and cartilage is frequently modelled as a linear elastic isotropic material. Popular values of Young's moduli used were 5 MPa, 9 MPa, 12 MPa, or 15 MPa. Typically, values of 0.45, 0.46, or 0.475 were used for Poisson's ratio.

Next, menisci were added to the FE models. Menisci were modelled as linear elastic isotropic homogeneous materials in ten studies, linear elastic transversely isotropic materials in eight studies, and a fibre-reinforced composite in five studies. Meniscal-tibial attachment sites were modelled by either assigning higher stiffness values to the meniscal horns [36, 55, 57, 58, 159] or tying the menisci to the tibia [25, 65, 73, 74, 103, 115, 117, 119, 161].

Haut Donahue *et al.* [58] conducted a parameter study on meniscal material properties. Pressure film was inserted into a cadaver knee, and pressure readings were recorded while the knee was loaded with a known axial load. FE models were then created based on the cadaver geometry, the model parameters were altered, and the pressure results were compared to those recorded by the pressure film. The study showed that the menisci could not be accurately modelled using a linear elastic isotropic material. FE model results were sensitive to the meniscal Young's moduli in the circumferential and axial/radial directions but relatively insensitive to Poisson's ratio. The authors suggested assigning menisci a Young's modulus between 100 MPa and 200 MPa in the circumferential direction and between 40 MPa and 60 MPa in the axial/radial directions.

Ligaments were one of the later structures to be added to FE models and were not included in six of the studies. Most studies modelled ligaments as uniaxial nonlinear elastic materials for lower strains (strains within the toe region of the stress-strain curve) and as linear elastic materials for larger strains beyond the toe region. The upper boundary of the toe region was defined by a nonlinear strain level parameter. This ligament definition is denoted as 'two-part uniaxial' in Table 2.2. One study [12] modelled ligaments as purely nonlinear springs (omitting the linear region of the 'two-part uniaxial' condition). Often, reference or initial strains were assigned to the ligaments, and ligaments were modelled as bundles of multiple springs instead of single units [10, 12, 15, 20, 25, 91, 94, 102, 118, 133, 159]. This bundle modelling was especially prevalent for the ACL

and PCL (both of which twist during normal gait) as well as for the MCL (which has both a femur-tibia attachment bundle and a femur-medial meniscus attachment bundle). Ligaments were also occasionally modelled as deformable 3D hyperelastic transversely isotropic [30, 36, 54, 115, 116, 117] or fibre-reinforced [73, 74, 118] materials. In general, the models which included ligaments included the ACL, PCL, MCL, and LCL.

Table 2.2: Image modalities used and material properties assigned to previously-published FE models of the knee (N/A = not included in model; HETI = hyperelastic transversely isotropic).

STUDY	IMAGE MODALITY	BONE	CARTILAGE	MENISCI	LIGAMENTS
Bae *et al.* 2011 [10]	CT + MRI	Rigid	E = 12 MPa, v = 0.45	E = 59 MPa, v = 0.49	Two-part uniaxial
Baldwin *et al.* 2009 [12]	MRI	Rigid	Rigid	N/A	Nonlinear 1D springs
Beillas *et al.* 2004 [14]	CT + MRI	Rigid	E = 20 MPa, v = 0.45	E = 250 MPa, v = 0.45,	Springs in parallel
Bendjaballah *et al.* 1995 [15]	CT	Rigid	E = 12 MPa, v = 0.45	Fibre-reinforced	Two-part uniaxial
Blankevoort *et al.* 1991 [20]	X-ray	Rigid	E = 5 MPa, v = 0.45	N/A	Two-part uniaxial
Checa *et al.* 2008 [25]	CT + literature	Rigid	E = 12 MPa, v = 0.45	E = 80 MPa, v = 0.3	Two-part uniaxial
Dhaher *et al.* 2010 [30]	MRI	Rigid	E = 12 MPa, v = 0.45	E_{cir} = 120 MPa, v_{cir} = 0.45, E_{other} = 20 MPa, v_{other} = 0.3	HETI
Dong *et al.* 2011 [36]	CT + MRI	Rigid	E = 5 MPa, v = 0.46	E = 59 MPa, v = 0.49	HETI
Guo *et al.* 2009 [54]	CT	Deformable	E = 5 MPa, v = 0.46	E = 59 MPa, v = 0.49	HETI
Hao *et al.* 2007 [55]	MRI	Rigid	E = 15 MPa, v = 0.475	E_{cir} = 140 MPa, v_{cir} = 0.3, E_{other} = 20 MPa, v_{other} = 0.2	N/A
Haut Donahue *et al.* 2002 [57]	CT + laser	Deformable	E = 15 MPa, v = 0.475	E_{cir} = 140 MPa, v_{cir} = 0.3, E_{other} = 20 MPa, v_{other} = 0.2	Two-part uniaxial
Haut Donahue *et al.* 2003 [58]	CT + laser	Rigid	E = 15 MPa, v = 0.475	* see Section 2.3.2.2	Two-part uniaxial
Hopkins *et al.* 2010 [65]	CT	Rigid	E = 12 MPa, v = 0.45	E = 80 MPa, v = 0.3	N/A
Kazemi *et al.* 2011, 2012 [73, 74]	MRI	Rigid	Fibre-reinforced	Fibre-reinforced	Fibre-reinforced
Li *et al.* 1999, 2001 [91, 94]	MRI	Rigid	E = 5 MPa, v = 0.45	Represented by springs	Two-part uniaxial
Meakin *et al.* 2003 [100]	Literature	N/A	E = 50 MPa, v = 0.3	E_{cir} = 200 MPa, v_{cir} = 0.3, E_{other} = 20 MPa, v_{other} = 0.03	N/A
Moglo *et al.* 2005 [102]	CT	Rigid	E = 12 MPa, v = 0.45	Fibre-reinforced	Two-part uniaxial
Mononen *et al.* 2012 [103]	MRI	N/A	Fibre-reinforced	E_{cir} = 140 MPa, v_{cir} = 0.3, E_{other} = 20 MPa, v_{other} = 0.2	N/A
Pena *et al.* 2006 [115]	CT + MRI	Rigid	E = 5 MPa, v = 0.46	E = 59 MPa, v = 0.49	HETI
Pena *et al.* 2006 [117]	CT + MRI	Rigid	E = 9 MPa, v = 0.46	E = 59 MPa, v = 0.49	HETI
Pena *et al.* 2008 [116]	CT + MRI	Rigid	E = 9 MPa, v = 0.46	E = 20 MPa, v = 0.45	HETI
Penrose *et al.* 2002 [118]	MRI	Rigid	E = 12 MPa, v = 0.45	Fibre-reinforced	Fibre-reinforced
Perie *et al.* 1998 [119]	MRI	Deformable	E = 5 MPa, v = 0.45	E = 5 MPa, v = 0.4	N/A
Shirazi & Shirazi-Adl 2009 [133]	CT	N/A	* see Section 2.3.2.4	* see Section 2.3.2.4	Two-part uniaxial
Yang *et al.* 2010 [159, 160]	MRI	Rigid	E = 15 MPa, v = 0.45	E_{cir} = 120 MPa, v_{cir} = 0.3, E_{other} = 20 MPa, v_{other} = 0.2	Two-part uniaxial
Yao *et al.* 2008 [161]	MRI	Rigid	E = 13 MPa, v = 0.49	E_{cir} = 133 MPa, v_{cir} = 0.325, E_{other} = 20 MPa, v_{other} = 0.325	N/A

2.3.2.3 Load cases applied

In most FE models, the femur was axially loaded in compression while the tibia was held fixed. Applied load cases varied between groups. Generally, forces represented multiples of body weight, but in some cases, reasons for applying a given force were not explicitly stated. Groups decided to apply axial loads ranging from 100 N to 3600 N (Table 2.3). One group [54] applied three different load cases to model the forces experienced at heel strike, single-leg stance, and toe-off.

Table 2.3: Applied load cases: Axial compressive force only.

Axial Load	Rationale	Study
100 N	not stated	Meakin *et al.* 2003 [100]
300 N	0.5 x BW	Kazemi *et al.* 2011 [74]
300 N	0.5 x BW	Kazemi *et al.* 2012 [73]
400 N	0.5 x BW	Haut Donahue *et al.* 2003 [58]
400 N	0.5 x BW	Li & Lopez 1999 [93]
570 N	0.83 x BW	Bae *et al.* 2011 [10]
800 N	1 x BW	Haut Donahue *et al.* 2002 [57]
1000 N	based on Fukubayashi & Kurosawa 1980 [47]	Bendjaballah *et al.* 1995 [15]
1000 N	1 x BW	Mononen *et al.* 2012 [103]
1150 N	not stated	Pena *et al.* 2006 [117]
1150 N	force at full extension in level walking	Pena *et al.* 2008 [116]
1150 N	based on Pena *et al.* 2008 [116]	Dong *et al.* 2011 [36]
1200 N	1.5 x BW	Haut Donahue *et al.* 2003 [58]
1202 N	1.85 x BW	Guo *et al.* 2009 [54]
1400 N	2.2 x BW	Li *et al.* 2001 [94]
1462 N	2.25 x BW	Guo *et al.* 2009 [54]
2000 N	5-6 x BW	Shirazi & Shirazi-Adl 2009 [133]
2275 N	3.5 x BW	Guo *et al.* 2009 [54]
3600 N	6 x BW	Hao *et al.* 2007 [55]

The knee experiences loads both in the form of forces and moments, however. Therefore, FE models next included load cases representing these combinations. Forces included both axial compressive and anterior-posterior shear forces; moments included both internal-external moments and varus-valgus moments (Table 2.4). These combination load cases were typically applied to FE models which included ligaments. In these models, ligaments were relied upon to constrain motion. The results of the models, therefore, gave additional information about the ligaments' contributions to stability in the knee. Parametric studies on quantities such as ligament stiffness and attachment sites were also

conducted to investigate the effect the level of uncertainties in these parameters had on model calculations.

Table 2.4: Applied load cases: Combinations of forces and moments (AP = anterior-posterior; IE = internal-external; VV = varus-valgus).

Axial Load	AP Load	IE Moment	VV Moment	Study
150 N	-	3 Nm	-	Blankevoort *et al.* 1991 [20]
50 N	134 N	10 Nm	-	Baldwin *et al.* 2009 [12]
-	100 N	10 Nm	-	Li *et al.* 1999 [91]
-	100 N	10 Nm	15 Nm	Checa *et al.* 2008 [25]

Some studies also included results of identical FE models solved with different combinations of load cases. Shirazi and Shirazi-Adl [132] solved models with load cases of (a) 1500 N axial compressive force, (b) 200 N anterior-posterior shear force, and (c) 1500 N axial compressive force combined with 200 N anterior-posterior shear force. The results for models with each of these load cases were then compared to investigate how the load case affected the stresses in the cartilage, forces in the ligaments, and contact loads in the joint. Pena *et al.* [115] also solved FE models with different combinations of loads. Load cases included (a) 1150 N axial compressive force and 134 N anterior-posterior shear force, (b) 1150 N axial force and 10 Nm varus-valgus moment, and (c) 1150 N axial compressive force, 134 N anterior-posterior shear force, and 10 Nm varus-valgus moment. This research group chose to apply these three specific load case sets to match load cases used in other studies in order to allow for comparison of results.

A more recent trend is calculating load cases based on forces generated by specific muscles. This load case calculation method likely developed later because of the difficulty of ethically measuring *in vivo* muscle forces and because of the variation in muscle anatomy and physiology between individuals [39]. Muscle origin and insertion points vary between humans. Even within an individual the strength of a muscle depends on its length, temperature, and speed of contraction. With so many unknown parameters, calculating muscle forces presents an optimization problem that is difficult to validate without implanting force sensors into live subjects and then having subjects perform an activity.

Due to these modelling challenges, relatively few groups have considered forces from specific muscles in their FE models. Muscle forces in the quadriceps and hamstrings muscle groups were considered in a 2011 study by Quatman *et al.* [121]. Justification for the specific forces assigned to each muscle group was unclear; it appears a 1000 N compressive load was divided between the two muscle groups. Similarly, Dhaher *et al.* published a 2010 study [30] in which FE model load cases were calculated based on forces generated by eight muscles acting about the knee. These muscle forces were calculated using a generic (not subject-specific) musculoskeletal model (SIMM, Software for Interactive Musculoskeletal Modeling [29]). Muscle forces from the quadriceps and hamstrings muscle groups were also applied in a 2002 study by Penrose *et al.* [118]. These forces were manipulated to mimic compressive tibiofemoral forces experienced during level walking, stair descent, a frontal car crash, and car-pedestrian impact.

Muscles were also included in a lower limb FE model created by Bae *et al.* [10]. Twelve 1D linear spring elements represented the muscles of the quadriceps muscle group and those muscles acting at the hip. In contrast to other FE models, these muscles were not used to directly load the FE model; instead the function of the muscles was similar to that of ligaments: to provide stability to the model.

2.3.2.4 Current trends in FE knee models

A review of FE modelling of the knee would be incomplete without more fully discussing two current trends: creating material models reflecting the different properties of the spatial zones of cartilage and menisci, and creating models with load cases reflecting loads experienced during a specific subject's motion.

Creating more complex material models Shirazi and Shirazi-Adl are working on increasing the physiological accuracy of the material properties used in FE knee models by modelling the different zones in cartilage and menisci [132, 133]. Cartilage has three distinct zones which can be classified according to the general shapes of the chondrocytes and orientations of the collagen fibres (Figure 2.16). The chondrocytes and collagen fibres in the deep zone of cartilage are closest to the calcified cartilage and bone. These chondrocytes are generally round and the fibres are predominantly perpendicular to the calcified

cartilage layer. The middle zone is called the intermediate or transitional zone. In this zone, chondrocytes have a more squashed appearance; fibres have a random orientation. The top zone, or superficial zone, includes the free surface of the cartilage. Chondrocytes are very thin in this zone and fibres are oriented parallel to the free surface.

Likewise, meniscal fibres have characteristic orientations. Fibres are classified as either circumferential (fibres running from anterior to posterior of meniscus, creating semi-lunar shapes congruent with the peripheral edge of the meniscus) or axial/radial (fibres running perpendicular to the circumferential fibres, connecting the middle inner edge and peripheral outer edge of the meniscus).

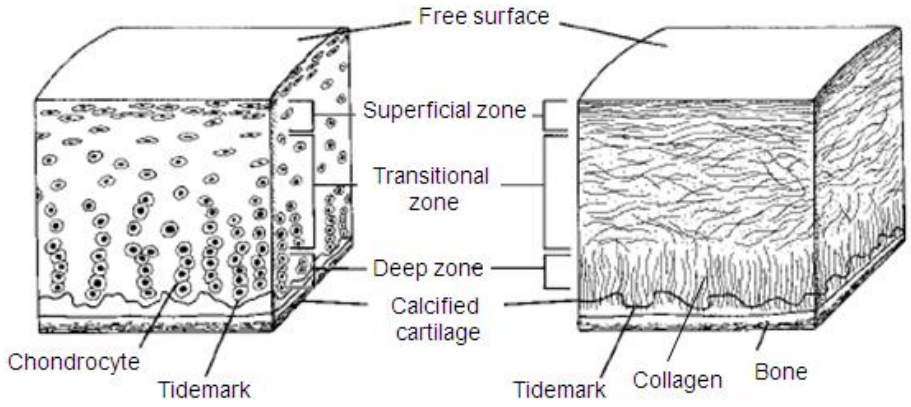


Figure 2.16: (left) Chondrocyte shapes and (right) collagen fibre orientations in different cartilage zones. ([107], permission to reproduce this (adapted) figure has been granted by SAGE Publications.)

Shirazi and Shirazi-Adl have created FE models which take these characteristic cartilage zones and meniscal fibre orientations into consideration. Their FE models (example shown in Figure 2.17 (top)) include the femoral cartilage, tibial cartilage, menisci, and ligaments (all but ligaments shown as solid bodies; ligaments are uniaxial spring elements). Both the cartilage and menisci have been modelled using solid matrix and membrane elements. In the cartilage (Figure 2.17 (centre)), membrane elements have been used to model the three distinctive zones of cartilage (superficial, random, and vertical fibres represent the superficial, transitional, and deep zones, respectively). It is believed that the random fibrils are solid instead of membrane elements because random fibrils will not align with the mesh grid and therefore must occupy the space between the grids (only occupied by solid elements). In the menisci, membrane elements have been used to model

the circumferential and radial fibres on the top and bottom free surfaces (top/bottom fibrils), periphery free surfaces (peripheral fibrils), and inside the menisci (mid fibrils) (Figure 2.17 (bottom)).

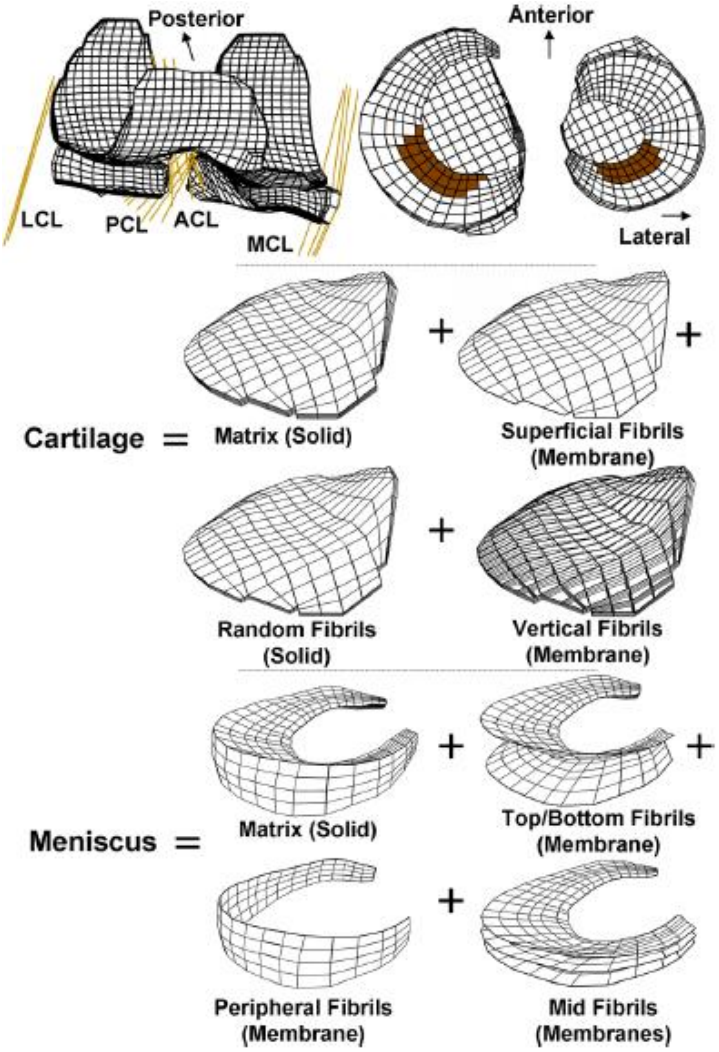


Figure 2.17: Modelling the zones of cartilage and menisci in FE models: (top) FE knee model, (centre) elements used to represent cartilage layers, (bottom) elements used to represent meniscus layers. ([132], permission to reproduce this figure has been granted by Elsevier.)

Other groups have created fibre-reinforced models of the cartilage and menisci. A 2012 study by Mononen *et al.* [103] focused on modelling the split lines (fibre orientation in the superficial zone) of cartilage. In this zone, fibres are parallel to the free surface but can run in a variety of directions (for example, medial-lateral, anterior-posterior, or random orientations). This study solved FE models of knees with normal cartilage split lines (Figure 2.18) as well as cartilage with abnormal split lines to try to simulate

osteoarthritic conditions.

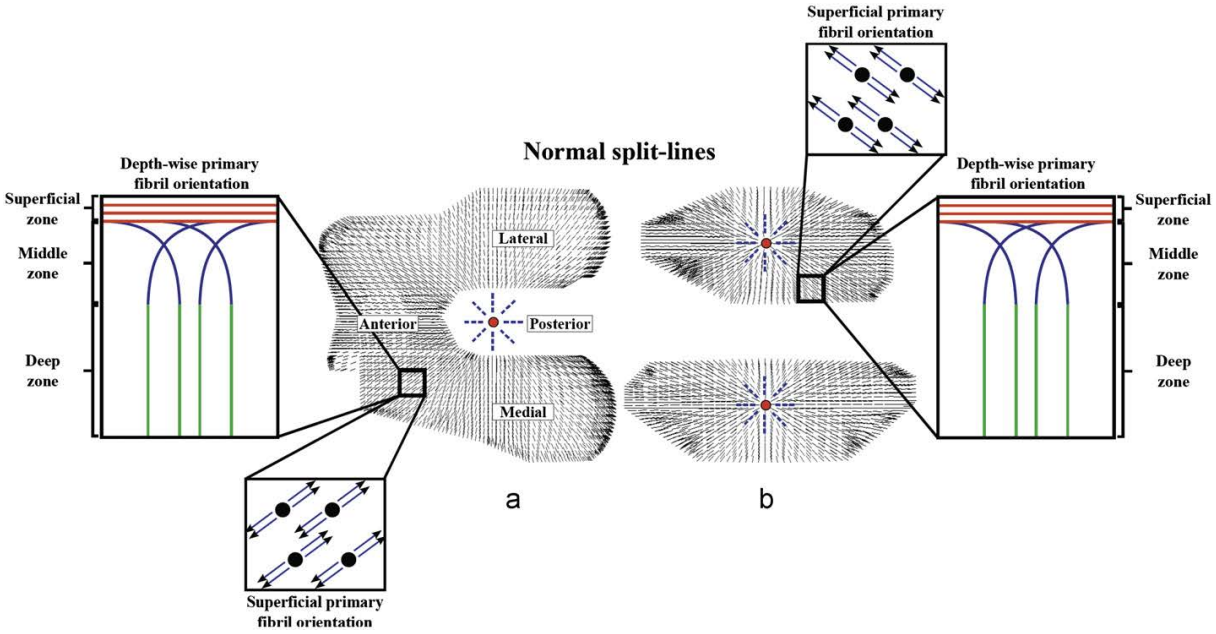


Figure 2.18: Normal split lines in (a) femoral cartilage and (b) tibial cartilage. ([103], permission to reproduce this figure has been requested from Elsevier.)

Creating more subject-specific load cases Another research group whose work should be mentioned is Yang *et al.* In 2010, this group published a protocol for developing subject-specific FE models of the knee [159]. This protocol used MRI scans of the knee in full extension to provide model geometry and motion analysis trials of level walking to calculate load cases. In the proposed method, the external joint moments were calculated first using inverse dynamics; these external joint reaction forces were counter-acted by internal joint moments due to muscle activation. Which muscle (hamstrings, quadriceps, or gastrocnemius) to activate was determined based on expected muscle activation patterns based on EMG results published by other research groups.

Although this group provided contact results calculated in different stages of the gait cycle [160], it is not clear whether the geometry used in the models was altered to reflect the different orientations of the internal structures during the various flexion angles. Instead it appears that geometry of the knee in full extension was used in all models, with only the load cases changing to reflect the various stages of the gait cycle. If this were the case, then the load conditions for a flexed knee were being applied to geometry of a fully-extended knee, bringing into question how well the models can predict contact pat-

terns for times in which the *in vivo* knee is in flexion. Using EMG patterns derived from other subjects to calculate load cases also means the model was not fully subject-specific.

2.4 Project overview

2.4.1 Introduction

OA is a debilitating disease of the articular cartilage that can have devastating effects on an individual's quality of life. In the knee, OA can begin either medially (medial OA) or laterally (lateral OA) before potentially spreading to multiple knee compartments. Most research studies have not separately investigated medial OA and lateral OA but have either focused solely on medial OA or combined medial OA and lateral OA into a single category when reporting results.

Most researchers approached investigating possible biomechanical causes of knee OA from one of two different directions. The majority of groups focused on the internal knee structures and how changes or injuries in these structures may lead to OA (see Section 2.2.2.3). These studies focused on loading distribution after injury or removal of ligaments or menisci. The second approach was to focus on the locations of cartilage lesions to determine whether loading at specific knee flexion angles results in OA (see Section 2.2.3). By determining the locations and flexion angles at which femoral and tibial cartilage lesions contact, theories about possible OA initiation mechanisms were developed.

This thesis aligns primarily with the second investigative approach. Previous research [53] has shown that medial OA and lateral OA have distinct phenotypes. Medial cartilage lesions contact at an average knee flexion angle of 11°, so it was theorized that activities that load the knee in low flexion angles (such as heel strike in walking) are most likely to lead to medial OA. Lateral OA seems to have a different cause, however. Lateral cartilage lesions contact at approximately 40° knee flexion, an angle larger than that reached during stance phase of walking. Consequently, lateral OA was predicted to be caused by higher flexion activities, possibly rising from or sitting onto a stool or walking up or down stairs. This thesis investigated subject-specific contact loading in the

knee during both common low flexion (level walking) and mid-range flexion (rising from a stool) activities to gain insight into potential mechanisms of medial OA and lateral OA initiation.

2.4.2 Description of steps

Subject testing consisted of collecting two types of data: knee geometry and motion analysis data. These two types of data were separately pre-processed (Figure 2.19) before being combined to create subject-specific FE models of the knee. Three normal subjects were tested in this project.

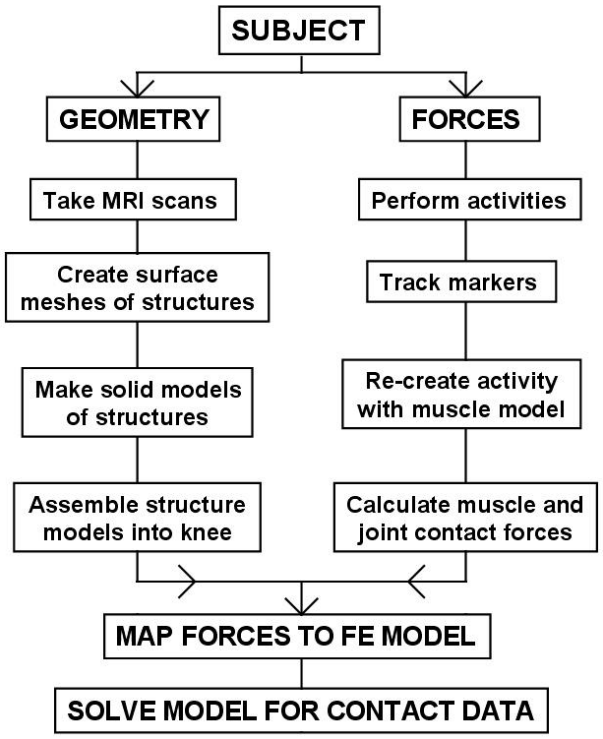


Figure 2.19: Flow map of FE model creation method.

Obtaining the knee geometry was the first step. MRI scans were taken with the knee fully extended as well as in the maximum flexion angle achievable within the MRI scanner. These flexion angles were chosen because low (full extension) and mid-range (maximum achievable) knee flexion angles are cited for medial and lateral tibiofemoral lesion contact, respectively. The MRI scans were then processed to create 3D objects of the internal structures of the knee. Intra- and inter-observer tests were performed to quantify the

repeatability with which the bone and cartilage structures could be segmented and with which the registration marker centre points could be identified. Locations of differences were then considered since differences within the tibiofemoral contact region influence contact results more than differences in locations far from the contact region.

The load cases experienced in the lower limb were then calculated and applied to the model geometry. These forces were calculated from motion analysis data collected during level walking and rising from a stool. Markers placed on the subject allowed for subject motion during the activities to be recorded. This data was then used as input to a lower limb musculoskeletal model, which calculated the muscle forces necessary to re-create the recorded motion. Joint reaction forces, segment positions, and segment orientations were also calculated. Verification studies were then conducted which compared these calculated joint reaction and muscle forces to contact forces and expected muscle activation patterns cited in the literature.

The lower limb musculoskeletal model could not, however, account for the specific surface geometries or deformations and stresses in the internal knee structures. An FE model was necessary to model and calculate this information. The FE model combined subject-specific geometry with subject-specific load cases and then calculated the resulting deformations, von Mises stresses, and contact pressures in the knee. A validation study tested the FE model creation method. This validation study involved placing pressure film within porcine knees and applying known loads to the knees. FE models which reflected the experimental conditions were then created. The contact data recorded by the pressure film and calculated by the FE models were then compared.

In the final steps of the thesis, the FE models of normal human knees were altered to simulate mechanical changes hypothesized to be associated with OA initiation. Load cases and both global and local cartilage material properties were altered in these simulated mechanical change models. The calculated patterns of tibiofemoral contact were then compared to the contact patterns calculated for the normal models as well as to locations of typical OA cartilage lesions. The magnitudes of displacement, von Mises stress, and contact pressure were also calculated in the mechanical change models; these magnitudes were compared to the results calculated for the normal models to investigate trends asso-

ciated with the mechanical changes. These contact results were used to develop theories of potential mechanisms of medial OA and lateral OA initiation.

It is important to note that while FE knee models have been created before, this research is novel because it combines subject-specific MRI-derived geometry and motion analysis-derived load cases from the same individual to calculate contact information. No other group is known to have previously created subject-specific FE models of different knee flexion angles in order to investigate the role of tibiofemoral contact in both medial OA and lateral OA initiation.

2.5 Conclusions

This chapter provided a review of the structures and functions of the normal knee before providing reviews on the current literature on both OA and FE modelling of the knee. After presenting this information, a project which fills a gap in the current knowledge was introduced. The rationale as well as description of the steps necessary to complete this project were then outlined and explained.

The next chapters discuss the methods used to create the subject-specific geometry and to calculate the subject-specific load cases.

Chapter 3

Creating the FE Model Geometry

The first half of data collection and processing involved creating the geometry used in the FE models. This geometry was derived from MRI scans, which were segmented and processed to create solid 3D models of the internal structures of the knee. To investigate the repeatability of the 3D object creation, intra- and inter-observer tests were conducted.

3.1 Methods

Ethics approval (Rec Number 07/H0604/151) and informed consent were given for this study. Data was collected on three healthy subjects (2 female, 1 male; age 23-30 years; height 1.57-1.66 m; mass 54.8-65.7 kg; body mass index 21.0-23.7). Information was collected for both left and right knees of each subject; therefore, information about a total of six knees was available.

All data processing described in this chapter was completed using the same computer (Intel®Core™2 Duo processor workstation running at 3.2 GHz with 3.25 GB of RAM).

3.1.1 Collecting the MRI scans

Preparation for testing began by verifying an absence of MRI contra-indications. Registration markers (MM3002 Multi-Modality Fiducial Markers, IZI Medical, Owings Mills, Maryland, USA) were then placed on the subject over seven specific bony landmarks: medial femoral epicondyle, lateral femoral epicondyle, mid thigh superior to patella, superior lateral patella, tibial tuberosity, medial tibial condyle, and fibular head (Figure 3.1).

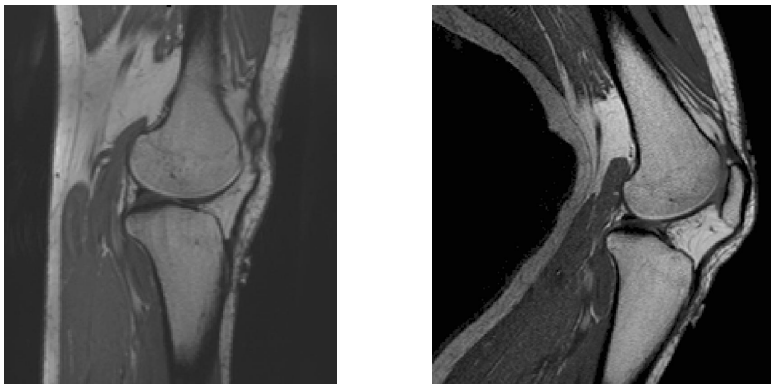
These markers were used to identify the upper and lower leg segments and to later register the MRI and motion analysis data.



Figure 3.1: Registration marker locations (right knee shown).

After placing the registration markers, MRI scanning began. Scans were acquired using a closed 3T MRI scanner (MobiView Philips Medical Systems/Achieva, Best, The Netherlands). A T1-weighted scanning protocol (sagittal view, slice interval 2 mm, slice thickness 0.05 mm) was used because this protocol showed both the soft (cartilage and menisci) and hard (bone) tissues within the knee.

All scans were taken using the same scanner and protocol and with subjects lying supine with knees unloaded. Multiple scans were taken for each subject. Separate scans of the left and right knees were taken with the knees fully extended. Two additional scans were taken with both knees simultaneously flexed to the maximum knee flexion angle achievable within the MRI scanner. This flexion angle was limited by the dimensions of the scanner. For the subjects tested, maximum knee flexion angles of 48°, 51°, and 56° (measured from a sagittal slice of the MRI scan) were achieved. These two categories of flexion angles (0° and maximum attainable, see Figure 3.2) were chosen to be scanned because they represented the orientations of the knee during low and mid-range flexion activities, respectively.



(a) (b)

Figure 3.2: MRI scans of (a) full extension and (b) mid-range knee flexion.

3.1.2 Creating 3D objects of the internal structures

Once the MRI data was available, the internal knee structures were semi-automatically segmented (Mimics 13.0, Materalise, Leuven, Belgium). Segmentation involved assigning pixels in the MRI scans to bone, cartilage, and menisci based on pixel greyscale intensity value and location within the knee. Using segmentation, the outer surfaces of the femur, femoral cartilage, tibia, tibial cartilage, and menisci were identified in each scan. The surfaces and centre point locations of the registration markers were also identified. Figure 3.3 shows an example of the segmented internal structures and registration markers.

The surface data of each internal structure was separately inspected and processed (Geomagic Studio 11, Geomagic, Inc., Research Triangle Park, North Carolina, USA) before further analysis was completed. The first step in processing was reducing the number of polygons used to represent the surfaces. This reduction resulted in more manageably-sized data files without visibly altering surface geometry. After polygon reduction, each surface was described by approximately 3,000 triangles.

Next, the surfaces were manually smoothed. Discontinuous greyscale pixel intensities between slices of the MRI scans resulted in irregular rather than smooth surfaces. Particular care was taken to fill holes and smooth spikes along the surfaces while maintaining the maximum possible amount of original data.

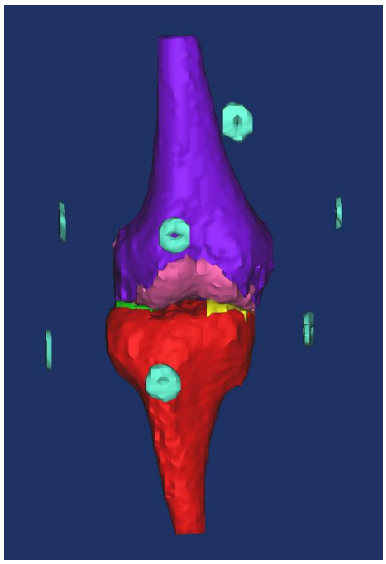


Figure 3.3: Surface geometry created from segmentation (femur = purple; tibia = red; femoral cartilage = pink; medial tibial cartilage = yellow; lateral tibial cartilage = green; registration markers = blue; menisci not shown to allow for cartilage visualization).

3.1.3 Defining the surface contours of the 3D objects

After the surfaces had been smoothed, grids were created to depict the surface contours of the 3D objects. Surfaces were defined using multiple levels of grids (Figure 3.4). The largest grids are panels (shown in red), the panels are made up of patches (shown in black), and the patches are made up of finer grids (shown in blue). The patches were later used as a template for the FE model mesh.

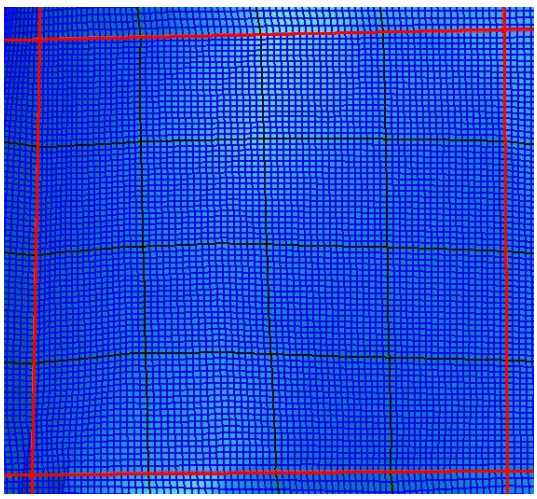
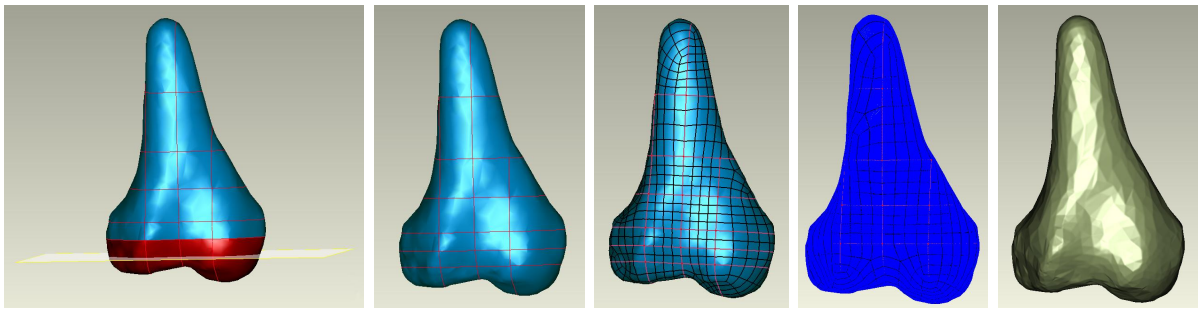


Figure 3.4: Hierarchy of grids used to define the surface contours.

The same processing steps were used to create the grids for each internal knee structure (Geomagic). First, the panels were created by taking section cuts (Figure 3.5a) through the anatomical plane in which the largest dimension of the 3D object was visible. Sagittal and axial plane section cuts were made from the frontal view for the bones; frontal and sagittal plane section cuts were made from the axial view for the cartilage and menisci. Additional section cuts were made in areas of expected soft tissue contact to increase the number of panels (Figure 3.5b) and consequently future FE model mesh density in these areas.

The panels were then subdivided into patches (Figure 3.5c). Each panel was individually examined to ensure that the number of patches was sufficient to accurately describe the geometry within the panel. Again, additional patches were included in panels near expected contact areas to increase control over the future FE model mesh density.

Once the patches were constructed, the final layer of the hierarchy, the finer grids (Figure 3.5d), was created inside each patch. The finer grids were then used to define the surface geometry (Figure 3.5e) used in the FE models.



(a) (b) (c) (d) (e)

Figure 3.5: Steps in defining the surface contours: (a) Section cuts, (b) panels, (c) patches, (d) finer grids, and (e) solid model.

3.1.4 Creating the knee model assembly

The process of creating a 3D object was repeated for each of the internal structures in the knee. The individual solid structures were then assembled to create the knee model (SolidWorks 2010, Dassault Systèmes SolidWorks Corp., Concord, Massachusetts, USA). When creating the assembly, each structure was automatically positioned in the same

location and orientation as in the original MRI scan; therefore, expected contact regions in the knee assembly matched those in the original MRI scan.

In some cases, small gaps or overlaps existed between structures. These gaps could later cause convergence problems in the FE model so the structures were brought into contact using an 'interference detection' tool (SolidWorks). While this tool permits structures to be moved in any direction, it is important to note that the tool was constrained to only allow axial motion in this study. In other words, structures could be moved in the superior-inferior direction but not in anterior-posterior or medial-lateral directions. This constraint ensured that closing small gaps did not change expected contact areas.

Once all processing of the knee assembly model had been completed, model geometry was stored for later input into the FE software (example of completed knee assembly shown in Figure 3.6).



Figure 3.6: Example of completed knee assembly for FE model.

3.2 Intra- and inter-observer segmentation and registration marker centre identification study

3.2.1 Introduction

The 3D objects representing the internal knee structures were created through segmentation. This segmentation was semi-automatic, meaning that some user discretion was

involved when assigning the individual pixels in the MRI scans to objects. Since these objects would later be used to create the FE model geometry, it was important to establish the repeatability with which the same individual and different individuals assigned pixels to the 3D objects. Intra- and inter-observer tests were conducted to collect this information.

Another step in the 3D object creation process was segmenting the registration markers and identifying their centre point locations. The markers were later used to register the geometry and calculated load cases; therefore, it was also important to conduct intra- and inter-observer tests to estimate the repeatability associated with determining the marker centre locations.

Similar to a study by Koo *et al.* [83], the intra-observer tests were completed by one individual on five different non-consecutive days while four additional individuals participated in the inter-observer tests.

3.2.2 Methods

Each participant in the intra- and inter-observer tests started with the same materials: an MRI scan of a normal knee, reference anatomical diagrams showing the expected locations of femoral cartilage and tibial cartilage, and a document explaining the testing procedures. The document (Appendix Section A) provided background information on the purpose of the testing, explained the basics of the segmentation software (Mimics), and listed the steps that should be followed during testing.

The segmentation portion of testing was completed first. In this section, participants used greyscale intensity values to select the pixels in each MRI scan slice that represented the femur, tibia, femoral cartilage, medial tibial cartilage, and lateral tibial cartilage. Interpolation was then used to create 3D objects from the selected pixels.

Five quantities were recorded for each 3D object: the volume, surface area, and length of object in the x (anterior-posterior), y (superior-inferior), and z (medial-lateral) directions. After analysing the numerical data, solid modelling Boolean subtraction and interaction operations were used to investigate the locations of differences between the 3D objects. These visual inspections were particularly useful in gaining insight into whether the

discrepancies occurred in regions of expected tibiofemoral contact.

The second half of testing involved determining the registration marker centre locations. Participants were asked to first locate the seven registration markers within the MRI scan and then pan through the MRI slices to determine the x, y, and z coordinates of the centre locations of each marker.

3.2.3 Intra-observer test results

3.2.3.1 Segmentation of structures

First, the average results of the 3D objects were considered (Table 3.1). The femur and tibia had the largest volumes; the volume of the femoral cartilage was larger than the volume of either the medial or lateral tibial cartilage. These results agree with the physiological anatomy of the normal knee.

Next, the variability between segmentation test results was examined. The largest standard deviation for volume was calculated for the tibia. A visual inspection showed that most of this variation occurred along the anterior surface of the tibia, at the distal end of the tibia, and near the tibial spine.

Of the cartilage segments, the femoral cartilage standard deviations were larger than the standard deviations of either of the tibial cartilage results. This trend is likely explained by the femoral cartilage including cartilage in both medial and lateral compartments. If the standard deviations are considered in relation to the average results, the results suggest more variability in creating 3D objects of the tibial cartilage. Visual inspection showed that these variations were not isolated to particular regions of the tibial cartilage surfaces but were spread across the entire surface.

For all structures, the variability of the lengths of the 3D objects was relatively small. The largest standard deviation was 2.0 mm in the lateral tibial cartilage.

3.2.3.2 Identification of registration marker centres

The registration marker centre locations were analysed next (Table 3.2). The average coordinate values served only to locate the markers in the MRI scan; therefore, no comparison was made between average values of different marker coordinates. Standard deviations

were compared, however. Standard deviations were small for each of the registration markers, suggesting that the centre point locations were consistently identified.

3.2.4 Inter-observer test results

3.2.4.1 Segmentation of structures

Similar to the intra-observer results, the average volumes were largest in the femur and tibia, with the femoral cartilage volume being larger than either of the tibial cartilage volumes (Table 3.1).

In terms of variability, the largest standard deviation for volume was calculated for the femoral cartilage. The standard deviations of the volume of the femur and tibia were similar, and the variation of the medial tibial cartilage volume was approximately twice that of the lateral tibial cartilage.

The femoral cartilage also had the largest variation in surface area. The remaining structures had approximately equal standard deviations in surface area, although there was slightly more variation in the medial tibial cartilage than in the lateral tibial cartilage.

Variations were also observed in the lengths of the 3D objects. In most cases, the standard deviations of length were larger in the cartilage segments than in the bone.

3.2.4.2 Identification of registration marker centres

The registration marker centre locations for the inter-observer participants were then analysed (Table 3.2). As with the intra-observer study, the average centre locations of the markers were not compared. An investigation of the standard deviations, however, showed good general agreement for all marker centre locations.

3.2.5 Comparing the intra- and inter-observer results

After analysing the intra- and inter-observer results separately, the results of the two studies were compared. As the true volumes, surface areas, lengths of the 3D structures, and marker centre locations were not known, the differences between the average variables in the two studies were calculated (difference = inter-observer average − intra-observer average) (Table 3.1).

3.2.5.1 Segmentation of structures

Most of the differences calculated between the intra- and inter-observer studies were negative, indicating the 3D objects from the intra-observer study had larger volumes, surface areas, and lengths than the inter-observer 3D objects.

All structures had larger average volumes in the intra-observer study than in the inter-observer study. The largest difference in volume was in the tibia. This difference was almost double the second-largest difference (the volume of the femur). The differences in volumes for the cartilage structures were approximately equal.

The largest difference in surface area was also in the tibia. This difference was again almost double the difference in the femur. In both of these structures, average intra-observer surface areas were larger than those in the inter-observer study. The surface area of the tibial cartilage structures was also larger in the intra-observer study. Conversely, the femoral cartilage surface area was larger in the inter-observer study.

The dimensions of the 3D objects were also larger in the x and y directions in the inter-observer study; shorter lengths were reported in the z direction.

Following numerical comparisons, the intra- and inter-observer structures were visually compared. The largest differences were calculated in the tibia, but visual inspection showed that these differences mainly occurred at areas removed from the tibia-tibial cartilage interface. In the inter-observer study, the tibia structures frequently extended further in the anterior and lateral directions than in the intra-observer study; the inter-observer tibial plateaux also extended further in the medial and lateral directions. Some differences also occurred within the expected contact region, however. Pixels representing subchondral bone were occasionally assigned to tibial cartilage rather than bone in the inter-observer study.

Intra- and inter-observer differences in the cartilage structures were also visually inspected. These differences were user-dependent and commonly involved segmenting different thicknesses of cartilage. For example, medial tibial cartilage structures were thinner in the extreme anterior and posterior regions in the inter-observer study than in the intra-observer study. Similarly, lateral tibial cartilage thickness was frequently reduced in the extreme anterior and posterior regions.

3.2.5.2 Identification of registration marker centres

The registration marker centre locations recorded in the intra- and inter-observer studies were also compared. Good agreement was found between the two studies for all markers (Table 3.2).

3.3 Discussion

The intra-observer study results showed that the volume, surface area, and dimensions of the 3D structures could be consistently segmented by the same individual, even when segmentation was performed on different days.

The largest differences occurred in the tibia. Most of these differences occurred outside the expected contact area and were likely caused by poor pixel resolution in regions far from the centre of the MRI scan. Some differences also occurred along the tibial spine. These differences were relatively small but could affect the results of the FE models; therefore, extra care was taken when later segmenting near the tibial spine.

Differences in the intra-observer cartilage structures should also be discussed as contact results on the cartilage surfaces were calculated by the later FE models and so differences in cartilage geometry will affect model results. Most of the differences in the geometry could be explained by the difficulty of identifying the border between the tibial cartilage and femoral cartilage, particularly in areas where these surfaces were in contact. More variability was associated with segmenting the femoral cartilage than the tibial cartilages because the femoral cartilage included both medial and lateral compartment cartilage. The chance of misidentifying femoral cartilage pixels was therefore twice as large as in the smaller tibial cartilage structures. If variability is considered relative to the average values, the percentage variation was larger in the tibial cartilage structures.

Similar greyscale intensity values of pixels in the bone-cartilage interface region also contributed to variations in tibial cartilage structures. The pixels representing subchondral bone had greyscale intensity values which were intermediate to the intensity values of either bone or cartilage; therefore, user discretion was introduced when assigning these subchondral pixels to either the tibia or tibial cartilage.

After analysing the potential sources of differences involved in segmenting the femoral and tibial cartilages, a better understanding of where these differences commonly existed was gained. In future segmentations, extra care was taken when segmenting the cartilage structures in these interface regions.

Inter-observer differences were larger than intra-observer differences, but the locations where these differences occurred were similar. Differences again existed in the tibia in areas away from the expected contact area as well as in the thickness of the cartilage structures. These results show that while the same individual may consistently assign the same pixels to the same structures, different individuals may assign those pixels to different structures, resulting in an increase in segmentation variability.

Interestingly, comparing intra- and inter-observer tests showed that the intra-observer structures generally had larger volumes, surface areas, and length dimensions than the structures created in the inter-observer tests. The dimension information as well as visual inspections provided useful information on potential reasons for some of these differences. In the inter-observer structures, the thicknesses of the tibial cartilages were underestimated due to not segmenting the furthest superior or inferior articulating layers of pixels. Determining the anterior-posterior and medial-lateral extents of the cartilage segments was another source of variation. These differences may have been caused by poor scan resolution, relatively similar greyscale intensity values of pixels, or a fear of incorrectly assigning pixels representing ligaments to the cartilage.

Another potential reason the intra-observer study structures were larger may be that the intra-observer participant had previous experience with the model geometry creation process. During this process, structure surfaces are smoothed, which involves removing spikes caused by the pixelated geometry of the MRI scan; therefore, the structures become progressively smaller during processing. The intra-observer participant had experience with the later data processing steps; the inter-observer participants did not. It is therefore possible that the intra-observer participant segmented initially larger structures knowing that the structures would likely decrease in size during subsequent processing steps.

The centre locations of the registration markers were also recorded and compared in the intra- and inter-observer studies. Good agreements between marker locations were

found both within each study and between the two studies. The maximum variation between intra-observer marker locations was 1.0 mm; the maximum variation between inter-observer marker locations was 1.3 mm. Both of these maximum variations occurred in the medial-lateral direction and were smaller than the MRI scan slice interval (2 mm).

The conclusions reached from these intra- and inter-observer studies are similar to those reached by Koo *et al.* [83]. They also found that intra-observer variation was smaller than inter-observer variation. The group also stated that different segmentation approaches led to different 3D structures; this conclusion supports the theory from the current study that the more experienced intra-observer participant may have used slightly different approaches when segmenting and therefore created larger structures. Koo *et al.* also found that variations were largest in locations where cartilage thickness was smallest. The authors therefore suggested using higher scan resolution and smaller scan slice thicknesses to decrease variations in segmentation.

3.3.1 Limitations

A main limitation affecting model geometry creation was the resolution of the MRI scans. The scans were acquired using a 3T scanner and a general body coil, a standard combination in medical imaging. Cartilage is as few as three pixels thick in the sagittal plane using this resolution scan, however, and the greyscale intensity values of cartilage, menisci, and the underlying bone are relatively similar. This similarity in pixel intensity values increases the likelihood of assigning pixels to the incorrect structures. Since the cartilage is only a few pixels thick, misassigning one pixel can lead to large per cent errors in segmented cartilage thickness. Studies [94] have shown that FE model results are sensitive to tibiofemoral cartilage thickness, with 8% increases in von Mises stress and 9% increases in pressure when cartilage thickness is decreased by 10%.

Better resolution scans using a 7T MRI scanner, knee coil, and/or a contrast agent would therefore be recommended for future studies. A 7T MRI scanner uses a stronger magnetic field than a 3T scanner and therefore is capable of capturing images with better signal-to-noise ratios. Eliminating noise improves scan clarity, allowing for more accurate delineation of cartilage, menisci, and bone borders. Also, a 7T MRI scan represents the

imaged object using a larger number of pixels so misassigning a pixel would have less effect on per cent error. In addition to the strength of the MRI scanner, the type of MRI coil used in data collection determines the volume of area considered to be 'of interest'. The general body coil is larger than the knee coil and therefore images a larger volume of interest; the knee coil gives more detailed information about a smaller volume, improving resolution and the ability to delineate structure borders. Contrast agents can also be used to allow for better imaging of cartilage. These contrast agents must be injected into subjects, however, introducing an invasive aspect to the medical scans.

Better resolution scans would improve multiple aspects of the current study. The per cent differences in the intra- and inter-observer tests would decrease as the borders between structures became clearer. The resulting segmented geometry would then more accurately represent the actual subject-specific knee geometry, leading to more subject-specific FE model results. On the other hand, more detailed scans contain more pixels, and finer meshes can retain more of the original pixelated geometry and lead to stress concentrations in FE model results (see Section 8.3).

3.4 Conclusions

This chapter described a method for creating subject-specific FE model geometry from MRI scans. MRI scans were first segmented based on pixel greyscale intensity values before being smoothed and made into solid objects. The solid objects of the bones, cartilages, and menisci were then used to create the model geometry of the normal knee.

Since the segmentation process has a direct effect on the FE model geometry and therefore the calculated FE model results, intra- and inter-observer studies were conducted to investigate the variation associated with segmenting the bones and cartilage. The study found that the segmentation process was user-dependent; the structures could be fairly consistently created in the intra-observer study but differences in structure geometry were larger in the inter-observer study. Some of these differences occurred in areas outside the expected contact region (anterior and lateral distal surfaces of the tibia), but other differences were within the contact region (superior and inferior surfaces of the tibial cartilages). This second category of differences likely resulted from poor pixel resolution

in the cartilage-cartilage and bone-cartilage interfaces. These test results highlighted the importance of carefully identifying the structures to which the pixels located near cartilage interfaces belong. Extra care was taken in all subsequent segmentations when assigning pixels located in these interface regions.

Intra- and inter-observer tests were also conducted on the repeatability of determining the centre locations of the seven registration markers. These markers were later used to register the FE model geometry and load cases so it was important to investigate if these registration marker positions could be consistently determined. The x, y, and z locations of these centres were found to be repeatable to within less than 1.3 mm.

After conducting the intra- and inter-observer studies, the proposed model geometry creation method was used to create the geometry of each of the six normal knee models. The centre locations of each registration marker were also determined.

After creating the FE model geometry, the load cases to apply to the FE models were calculated. The next chapter describes the methods used to calculate these load cases.

Table 3.1: Intra- and inter-observer segmentation results (base unit = mm; Aver. = average; St. Dev. = standard deviation; M. = medial; L. = lateral; in-plane pixel resolution = 0.0918 mm^2; 3D voxel resolution = 0.184 mm^3).

	Intra-Observer		Inter-Observer		Difference
	Aver.	St. Dev.	Aver.	St. Dev.	
FEMUR					
Volume	148024	478	141271	7446	-6753
Surface Area	19688	72	19246	901	-442
X Length	67.4	0.5	66.2	1.5	-1.2
Y Length	123.6	0.0	122.9	0.9	-0.7
Z Length	70.9	1.0	74.8	9.0	3.9
FEMORAL CARTILAGE					
Volume	17700	505	15577	11883	-2123
Surface Area	10090	281	10679	4377	589
X Length	70.3	0.5	67.0	6.9	-3.3
Y Length	41.4	0.4	39.0	8.1	-2.4
Z Length	62.1	1.0	62.7	2.2	0.6
TIBIA					
Volume	117054	5551	104669	6187	-12385
Surface Area	15730	459	14773	655	-957
X Length	55.2	0.9	52.7	1.6	-2.5
Y Length	106.9	0.5	106.1	0.9	-0.8
Z Length	66.9	1.2	69.9	2.8	3.0
M. TIBIAL CARTILAGE					
Volume	3393	225	2039	1040	-1354
Surface Area	2311	79	2086	636	-225
X Length	48.7	1.6	42.5	5.2	-6.2
Y Length	16.1	0.8	16.0	5.3	-0.1
Z Length	20.7	1.2	23.1	5.5	2.4
L. TIBIAL CARTILAGE					
Volume	3424	233	1703	575	-1721
Surface Area	1966	123	1889	428	-77
X Length	39.3	1.0	38.8	7.0	-0.5
Y Length	17.6	2.0	13.2	4.6	-4.4
Z Length	20.3	1.0	24.8	4.2	4.5

Table 3.2: Intra- and inter-observer registration marker centre results (base unit = unit; Aver. = average; St. Dev. = standard deviation; M. = medial; L. = lateral; in-plane pixel resolution = 0.0918 mm^2; 3D voxel resolution = 0.184 mm^3).

	Intra-Observer		Inter-Observer		Difference
	Aver.	St. Dev.	Aver.	St. Dev.	
M. FEMORAL EPICONDYLE					
X Location	126.0	0.0	125.9	0.4	-0.1
Y Location	-216.1	0.7	-215.8	0.9	0.3
Z Location	-45.2	1.0	-45.3	1.1	-0.1
L. FEMORAL EPICONDYLE					
X Location	127.0	0.0	126.9	0.2	-0.1
Y Location	-216.5	0.5	-217.0	0.7	-0.5
Z Location	-170.1	0.0	-169.0	1.3	1.1
MID THIGH					
X Location	58.0	0.0	57.6	0.4	-0.4
Y Location	-172.0	0.0	-171.6	0.5	0.4
Z Location	-93.1	0.0	-93.3	0.3	-0.2
SUPERIOR-L. PATELLA					
X Location	67.0	0.5	67.3	0.4	0.3
Y Location	-222.6	0.4	-222.3	0.8	0.3
Z Location	-121.3	1.0	-121.6	0.2	-0.3
TIBIAL TUBEROSITY					
X Location	84.8	0.0	84.9	0.3	0.1
Y Location	-288.4	0.9	-287.9	0.3	0.5
Z Location	-127.9	1.0	-127.5	1.1	0.4
M. TIBIAL CONDYLE					
X Location	129.8	0.0	129.3	0.5	-0.5
Y Location	-267.3	0.5	-267.9	0.5	-0.6
Z Location	-60.1	0.0	-60.1	0.1	0.0
FIBULAR HEAD					
X Location	140.4	0.0	140.1	0.4	-0.3
Y Location	-273.6	0.0	-273.6	0.3	0.0
Z Location	-176.3	1.0	-175.1	1.1	1.2

Chapter 4

Calculating the FE Model Load Cases

The second half of data collection and processing involved calculating the loads to apply to the FE models. Motion analysis trials provided the data describing the movements of the subjects during various functional activities. This data was then used as input to a lower limb musculoskeletal model, which calculated the forces generated by the lower limb muscles during the functional activities. The calculated activation timings of the muscles and forces of the muscles and hip joint were then compared to on-off EMG-derived muscle activation trends and to maximum forces reported in other studies.

4.1 Methods

All data processing described in this chapter was completed using the same computer (Intel®Core™2 Duo processor workstation running at 3.2 GHz with 3.25 GB of RAM).

4.1.1 Collecting the motion analysis data

The data used to calculate the FE model load cases was collected using motion analysis. Motion analysis allows quantitative description of motion. The motion, which is performed within a capture volume defined by peripheral cameras, is recorded when infrared light emitted from the cameras reflects off retro-reflective markers placed on a subject and returns to the cameras. Each camera records the 2D locations of each marker within its viewing field. A computer then uses the 2D data from each camera as well as the known relative orientations of the cameras to reconstruct the 3D locations of each marker

throughout the motion trial.

Force plates are also frequently used during motion analysis. These plates are located in the floor within the capture volume of the cameras and record a subject's ground reaction forces and moments during the motion trial. When recorded simultaneously, data from gait markers and force plates can be combined to calculate joint kinetics and kinematics. Although predominantly associated with level walking, motion analysis is also used to quantify motion during other activities.

Motion analysis testing was performed in the Oxford Gait Laboratory. Prior to data collection, the motion capture equipment (Vicon 612, Vicon Motion Systems Ltd., Oxford, UK) was used to calibrate the capture volume in the centre of the motion analysis laboratory. The force plates (OR6 platform, Advance Mechanical Technology Inc., Watertown, Massachusetts, USA) were also checked to ensure proper functioning (see Appendix B) and then zeroed to eliminate any erroneous forces recorded due to drift.

Following laboratory set-up, subjects were prepared for data collection. The heights, weights, lower limb lengths, distances between anterior-superior iliac spine prominences, and widths of the ankles and knees were measured and recorded. Retro-reflective markers were then placed over bony landmarks on the subjects. An adapted Helen Hayes marker set [72] was used in this project; additional markers were included to give more information on the 3D positions of the feet and knees (Figure 4.1). Retro-reflective markers (represented by black circles) were placed over the sacrum as well as the posterior superior iliac spine, anterior superior iliac spine, greater trochanter, thigh (wand), tibia (wand), shin, ankle, medial mallelous, heel, toe, distal first metatarsal, and distal fifth metatarsal of both the right and left limbs. Retro-reflective markers also replaced the seven registration markers (represented by green circles) used in the MRI scanning. The medial mallelous (represented by blue circle) was only used in the static trial and then removed. In total, 37 gait markers were used for each subject during motion analysis.

Once the markers had been placed on the subjects, a static trial was recorded so that the pelvis, thigh, shank, and foot segments could be defined. This static trial involved subjects standing with both feet on a single force plate (data capture rate: 1000 Hz) while 12 cameras (data capture rate: 100 Hz) recorded the positions of the markers.

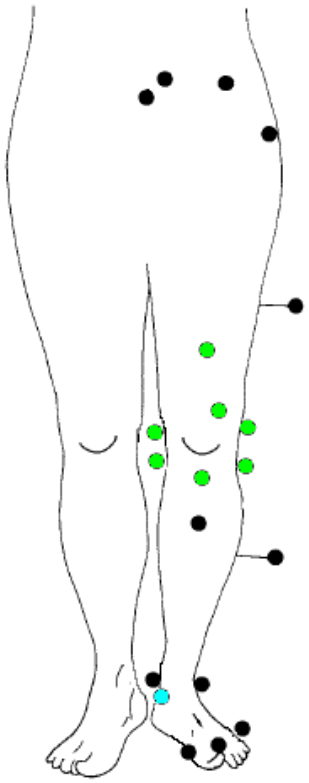


Figure 4.1: Marker set used in motion analysis (registration markers = green; marker only used in static trial = blue; markers only shown on one leg for clarity). ([72], permission to reproduce this (adapted) figure has been granted by John Wiley and Sons.)

Motion analysis testing began after the static trial. Data was collected while subjects completed two functional activities: level walking (a lower knee-flexion activity) and rising from a stool (a higher knee-flexion activity). Subjects were allowed to practice each task before data collection began.

During level walking, subjects walked at self-selected speeds down a 10 m walkway, passing through the capture volume of the cameras and across two force plates, until eight successful foot strikes (four right and four left) were collected. A successful foot strike was defined as one foot landing entirely on a force plate. If any part of the opposite foot also touched that same force place or if any marker was not seen by the cameras during the gait trial, the foot strike was not considered successful.

Subject motion was then recorded while rising from a stool (Figure 4.2). The stool was placed to the side of the force plates and positioned so that no part of the stool contacted the plates. Subjects sat on the stool with both feet flat on the ground, arms crossed across the chest, and knees flexed to approximately 90°. One foot was placed in the centre of

one of the force plates and the other foot was placed in the centre of the other force plate. Subjects were then instructed to stand up from the stool, without using the arms as an aid, while maintaining as natural a motion as possible. This task was repeated until four successful trials were collected. A successful trial was defined as one in which only a single foot contacted each force plate and all markers were visible throughout the motion.

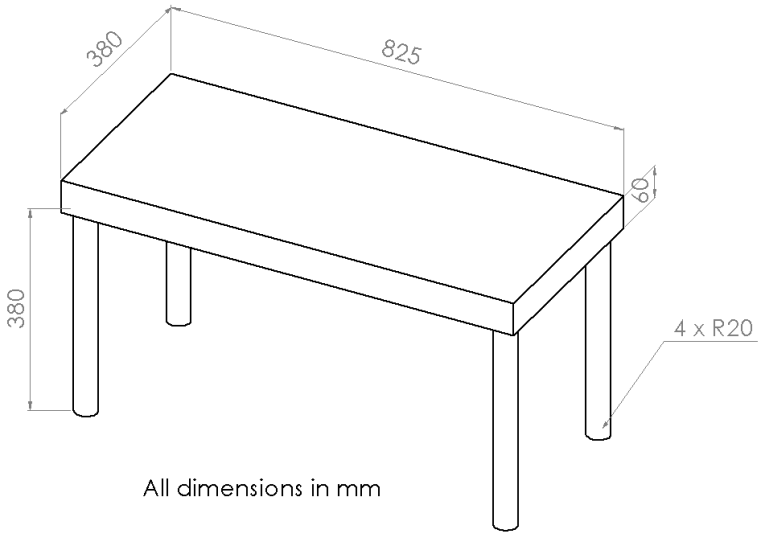


Figure 4.2: Dimensions of stool.

4.1.2 Processing the motion analysis data

After data collection, each successful trial was processed. The first processing step was reconstructing the desired task in the motion analysis software (Vicon Nexus 1.4.115, Vicon Motion Systems Ltd., Oxford, UK). This reconstruction allowed the marker and force plate data to be visualized for each time frame, or instance of recorded data, throughout the trial. The marker data was then filtered using a Woltring filter ([158], MSE = 10) to decrease the noise and effects of skin movement artifact in the data.

The next processing step was identifying the locations of the markers throughout the task. A single time frame was randomly selected from the trial, and each marker in the time frame was manually assigned a label indicating its location on the lower limbs. The software then used this manually-created marker label template to automatically label the markers in the remaining time frames of the trial. This automatic labelling assumed that marker positions changed minimally between time frames and that marker trajectories

followed continuous paths.

Occasionally, the automatic labelling resulted in incorrectly-labelled markers. Therefore, the last processing step involved investigating when these errors occurred and determining whether it was necessary to correct them. Errors occurring within the cycle of interest required manually re-labelling mislabelled markers; errors outside the cycle of interest were ignored. Cycles of interest were defined as the gait cycle beginning with the successful foot strike for level walking trials and as the time during which the subject was actively moving from the sitting to standing position during the rising from a stool activity.

After correcting any mislabelled markers, processing was complete (Figure 4.3 shows an example of a processed level walking trial). The processed marker labels and locations throughout the cycles of interest were saved for future input to a lower limb model. Ground reaction forces as well as centres of pressures recorded by the two force plates were also saved.

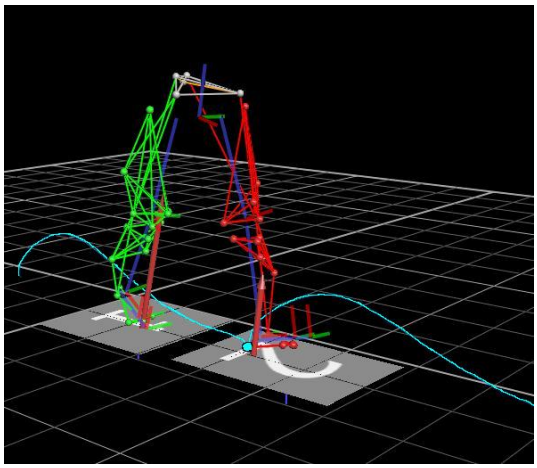


Figure 4.3: Example of processed level walking trial (left heel strike; heel marker and heel trajectory shown in light blue).

4.1.3 Applying data to the lower limb model

A lower limb model (AnyBody Version 3.0, AnyBody Technology A/S, Aalborg, Denmark) calculated the muscle and joint reaction data which was used to calculate the load cases to apply to the FE models of the knee. This lower limb model contained limb segments,

joints, and muscles which reflected the anatomy of the human lower body. The model was driven by marker data recorded during motion analysis; this data determined the positions and therefore motions of the segments throughout a trial. Force plate data, also collected during motion analysis, was used to calculate the inverse dynamics of the lower limb during the re-created motion. Finally, an optimization was used to calculate the muscle forces necessary to re-create the motion.

The lower limb model was created using a combination of two types of files: body and application files. Body files defined subject geometry; application files described the expected motion for a particular task. A modified version of GaitUniMiami ([11], adapted from AnyBody Repository7.1) was used in this study. These body files defined a seven segment (one pelvis and a thigh, shank, and foot segment on each side of the body) lower limb model with eighteen kinematic degrees of freedom. The pelvis had six degrees of freedom (three translations and three rotations). The hip was permitted to rotate, flex-extend, and abduct-adduct (spherical joint); the knee was permitted to flex-extend (hinge joint); the ankle was permitted to plantarflex-dorsiflex and invert-evert (universal joint).

Initially, the lower limb model represented a generic human performing an arbitrary task. It was therefore necessary to change certain parameters within the body and application files before the lower limb model could compute subject- and task-specific muscle and joint reaction loads.

First, the generic lower limb model was scaled to reflect the height and weight of the subject. This information (recorded during motion analysis data collection) was updated in the lower limb model's body files. Subject height and weight were used in standard anthropometric ratios provided within the body files to calculate the lengths and weights of the limb segments.

Next, force plate data was imported into the lower limb model's application files. This data included the 3D ground reaction forces and moments measured by the force plates as well as the locations of the centres of pressures on the two force plates. Both of these types of data were important for the inverse dynamics calculations.

The final step in setting up a subject- and task-specific model was transferring the motion of the subject to the lower limb model. Marker data was first imported into the

application files. These markers reflected the specific trial and task being performed. Marker positions were matched to pre-defined expected marker positions on the lower limb model, and then an optimization was performed. This optimization calculated the 18 variables necessary to define the position of the body throughout the motion cycle by minimizing the difference between the subject marker positions and the expected lower limb model marker positions throughout the motion cycle.

4.1.4 Calculating the muscle and joint reaction load cases

Muscles have optimal lengths at which they most efficiently generate force, and these lengths are dependent on the muscle origin and insertion locations, which in turn depend on limb length. Therefore, muscle and tendon lengths were calibrated to the limb lengths of each subject before calculating the muscle forces.

Following calibration, inverse dynamics was used to calculate the muscle forces generated during the functional tasks. In these calculations, the measured ground reaction forces and positions of the model lower limbs were used to calculate the muscle forces necessary to re-create the recorded motion. There were more unknown muscle forces than equations describing muscle force distribution and model motion, however, making the lower limb model an indeterminate system. Therefore, an optimization technique was required to calculate the individual muscle forces. A min-max optimization was chosen.

The min-max optimization approach minimizes muscle fatigue by dividing the total muscle force required to re-create the model's motion between the available muscles in such a way that each muscle exerts the smallest proportion of its own maximum force [146]. This approach, therefore, is designed to avoid any single muscle generating its maximum force. To keep muscle loads to a minimum, co-contractions of opposing muscles spanning a single joint are not permitted; co-contractions of opposing muscles spanning multiple joints, however, are allowed since these muscles may be simultaneously responsible for multiple types of motion (for example, the semimembranosus can extend and/or rotate the hip as well as flex the knee).

Figure 4.4 shows an inverse dynamics calculation for a time frame in a level walking trial (right heel strike shown). The left skeleton shows the orientation of the body at heel

strike; the right skeleton, orientation at toe off. The magenta colour indicates a currently activated muscle. Inverse dynamics calculations were only made for time frames within the cycles of interest to reduce computation time and the size of the resulting files. The final outputs of the lower limb model were muscle forces and joint reaction forces and moments; these results were then used to calculate the FE model load cases.

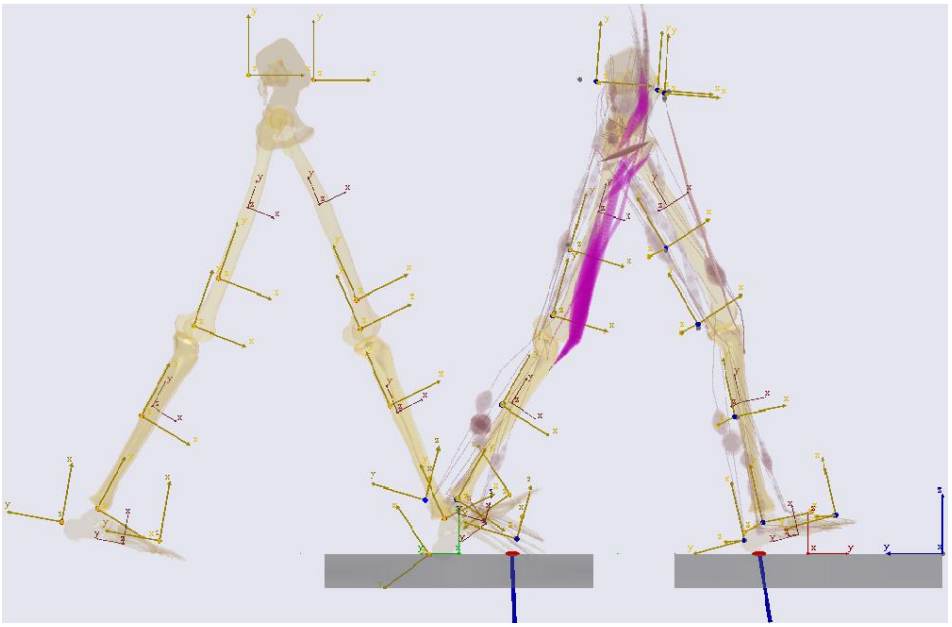


Figure 4.4: Illustration of a result from the muscle activation calculations.

4.1.5 Selecting a representative motion cycle

A separate set of muscle and joint reaction loads was calculated for each motion cycle. Each cycle had slightly different peak muscle forces and patterns, but it was not feasible to create separate FE models with load cases representative of each motion cycle. Therefore, an objective, consistent method for selecting the most representative cycles was necessary.

Representative cycles were selected based on root mean square (RMS) differences between muscle forces calculated for an individual motion cycle and the mean muscle forces calculated for the set of task-specific motion cycles. Each cycle was first normalized to 100 time points per motion cycle. The mean force value at each time point was then calculated for each individual muscle. Individual muscle forces in each cycle were compared to the calculated mean values at each of the 100 time points, and RMS differences were

calculated using the following formula:

$$\text{RMS Difference for Muscle } m \;=\; \sqrt{\frac{\sum_{i=1}^{n}(F_{mi} - \overrightarrow{F}_{mi})^2}{n}} \tag{4.1}$$

where F_{mi} represented muscle forces in a given motion cycle, $\overrightarrow{F}_{mi}$ the calculated mean forces, and n the number of time points in the motion cycle. RMS differences for all muscles spanning the hip joint ($j = 1 : m$) during a cycle were summed to calculate the overall RMS difference for each cycle. The motion cycle with the minimum RMS difference from the mean (all muscles considered) was selected as the most representative cycle. Most representative cycles were selected for each subject, task, and leg.

4.1.6 Calculating equivalent forces and moments to apply to FE models

After selecting representative motion cycles, the data from these cycles was used to calculate the load cases to apply to the FE model. Load cases were calculated from the lower limb model results, which included individual muscle and joint reaction loads acting at their own specific attachment or application locations. The FE model, however, required the load cases to be applied to a single point (also referred to as either the reference node or pilot node). Therefore, it was necessary to calculate the equivalent forces and moments acting at a single point. This single point was chosen to be the centre of mass of the FE model femur.

Calculating equivalent loads at this single point required first registering the coordinate systems used in the lower limb model (based on motion analysis data) and in the model geometry (based on MRI scans). Registration was accomplished using the registration markers, which were included during both types of data collection.

First, the location of each registration marker was identified in both the lower limb model and FE model coordinate systems. Next, the location of the centre of mass of the femur in the model geometry was determined (SolidWorks). A computer code ([153], Matlab R2007a, MathWorks, Natick, Massachusetts, USA) using least-squares error minimization [66] then registered the two coordinate systems. The resulting transformation

matrix was used to transform the coordinates of the FE model's femoral centre of mass into the lower limb model coordinate system. Equivalent loads could then be calculated at this single point.

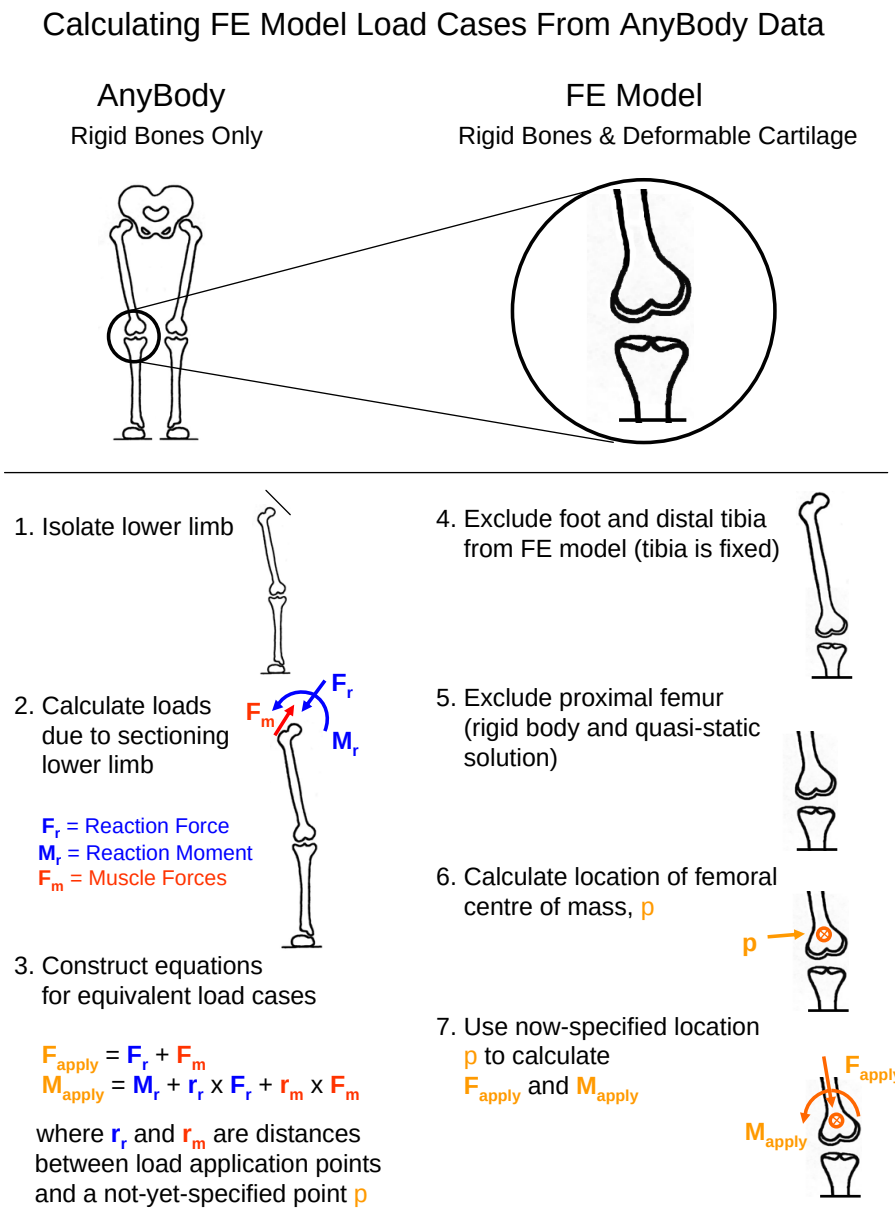


Figure 4.5: Rationale for muscle and joint reaction data included in equivalent load cases.

Equivalent load cases were calculated from loads experienced in the muscles crossing the hip and from the joint reaction data calculated at the hip. The rationale for combining these muscle and joint reaction data to calculate equivalent load case is provided in Fig-

ure 4.5. Twenty-nine muscles crossed the hip in the lower limb model: rectus femoris; semitendinosus; semimembranosus; biceps femoris caput longum; sartorius; gracilis; iliopsoas; gluteus maximus, medius, and minimus in nine total muscles; tensor fasciae latae; piriformis; adductor longus; adductor magnus in three muscles; quadratus femoris; adductor brevis; obturator internus; obturator externus; pectineus; gemellus inferior; and gemellus superior.

4.1.6.1 Calculating equivalent force and moment for muscle data

The first step in calculating equivalent muscle loads was determining which muscle force and attachment location to use in the calculations. Each muscle had multiple attachment locations: an origin, an insertion, and at least one intermediate point known as a via point (via points ensure muscles wrap around bones, see Figure 4.6). The magnitudes of the muscle forces at the origin and insertion locations were the same; this magnitude represented the force generated by the muscle. The magnitude of the force reported at via points, however, did not represent the tensile force within the muscle but instead the compressive contact force between the muscle and underlying bone. Since via nodes were located near joints, each muscle had a via node on at least one side (proximal or distal) of a joint.

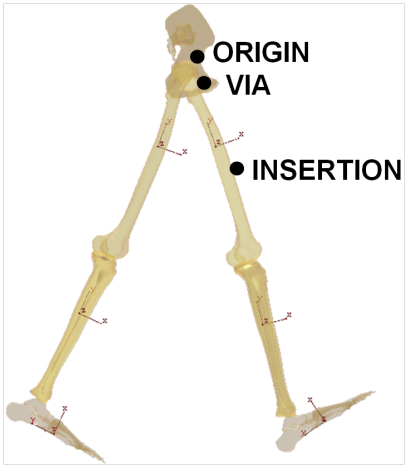


Figure 4.6: Example of different locations of muscle attachments.

Only the tensile muscle forces (not compressive via node forces) were included when calculating the equivalent muscle forces and moments. The via point locations were

important, however, when calculating the line of action of each muscle force. The steps used to calculate the equivalent muscle data were:

1. Calculate magnitude of muscle force at muscle insertion

$$Fm_i = \sqrt{(Fm_{ix})^2 + (Fm_{iy})^2 + (Fm_{iz})^2} \tag{4.2}$$

where F stands for force and m_i stands for individual muscle.

2. Identify closest muscle attachment locations (origin, insertion, or via point) on both sides (upper and lower) of the hip

$$\overrightarrow{Loc_p} = \text{ most distal muscle attachment on pelvis} \tag{4.3}$$

$$\overrightarrow{Loc_f} = \text{ most proximal muscle attachment on femur} \tag{4.4}$$

where Loc stands for location, p stands for pelvis, and f stands for femur.

3. Calculate the unit vector $\hat{n}$ along the muscle line of action.

$$\hat{n} = \frac{\overrightarrow{Loc_p} - \overrightarrow{Loc_f}}{|\overrightarrow{Loc_p} - \overrightarrow{Loc_f}|} \tag{4.5}$$

4. Calculate muscle force along line of action.

$$\overrightarrow{Fm_i} = (Fm_i)\hat{n} \tag{4.6}$$

After the force of each muscle as it crossed the hip was known, the equivalent force and moment acting at the femoral centre of mass could be determined. The following steps were used:

1. Identify location of centre of mass in lower limb model coordinate system (use registration algorithm [153]). $\overrightarrow{p}$ is taken to be the location of the centre of mass of the femur.

2. Calculate equivalent muscle force by adding force components from each individual muscle

$$\overrightarrow{Fm_{total}} = \sum_{i=1}^{k} (\overrightarrow{Fm_i}) \tag{4.7}$$

where i stands for each of the k individual muscles crossing the hip.

3. Calculate distances between centre of mass and muscle attachment locations.

$$\overrightarrow{rm_i} = \overrightarrow{Loc_f} - \overrightarrow{p} \tag{4.8}$$

4. Calculate moments caused by moving each muscle force to centre of mass.

$$\overrightarrow{Mm_i} = \overrightarrow{rm_i} \times \overrightarrow{Fm_i} \tag{4.9}$$

5. Calculate total equivalent moment due to muscles

$$\overrightarrow{Mm_{total}} = \sum_{i=1}^{k} (\overrightarrow{Mm_i}) \tag{4.10}$$

where i stands for each of the k individual muscles crossing the hip.

4.1.6.2 Calculating equivalent force and moment for joint reaction data

Next, the equivalent loads due to moving the hip joint reaction data to the femoral centre of mass were calculated. The procedure was similar to calculating the equivalent loads due to muscle data, except that both a force and moment were reported for the lower limb model joint reaction data (in contrast to just a force for muscles). The steps used to calculate the equivalent joint reaction data were:

1. Identify joint reaction force, moment, and application location directly-reported by lower limb model

$$\overrightarrow{Fr_{dir}} = [Fr_x, Fr_y, Fr_z] \tag{4.11}$$

$$\overrightarrow{Mr_{dir}} = [Mr_x, Mr_y, Mr_z] \tag{4.12}$$

$$\overrightarrow{Loc_{dir}} = \text{ location of directly} - \text{reported joint reaction loads} \tag{4.13}$$

where F stands for force, M for moment, Loc for location, r for reaction, and dir for directly-reported data.

2. Identify location of centre of mass in lower limb model coordinate system (use registration algorithm [153]). As before, $\overrightarrow{p}$ is taken to be the location of the centre of mass of the femur.

3. Reassign directly-reported joint reaction force to joint reaction equivalent force (this is the only joint reaction force acting at the hip).

$$\overrightarrow{Fr_{total}} = \overrightarrow{Fr_{dir}} \tag{4.14}$$

4. Calculate distance between femoral centre of mass and directly-reported joint reaction application location.

$$\overrightarrow{rr} = \overrightarrow{Loc_{dir}} - \overrightarrow{p} \tag{4.15}$$

5. Calculate moment caused by moving directly-reported joint reaction force to centre of mass.

$$\overrightarrow{Mr_{move}} = \overrightarrow{rr} \times \overrightarrow{Fr_{total}} \tag{4.16}$$

6. Calculate total equivalent moment due to both directly-reported joint reaction moment and moving joint reaction force to centre of mass.

$$\overrightarrow{Mr_{total}} = \overrightarrow{Mr_{dir}} + \overrightarrow{Mr_{move}} \tag{4.17}$$

4.1.6.3 Calculating total equivalent force and moment

Both muscle and joint reaction loads contributed to the load cases applied to the FE models. Therefore, the muscle and joint reaction equivalent load cases were combined to calculate the total equivalent load case.

$$\overrightarrow{F_{apply}} = F\overrightarrow{m_{total}} + F\overrightarrow{r_{total}} \tag{4.18}$$

$$\overrightarrow{M_{apply}} = M\overrightarrow{m_{total}} + M\overrightarrow{r_{total}} \tag{4.19}$$

4.2 Results

Muscle forces and joint reaction forces and moments were calculated for each time frame of each motion cycle. It is not feasible to present the loads calculated for each of the 29 muscles and for the hip joint in each time frame, however. Therefore, the maximum muscle forces in six muscles (rectus femoris, semitendinosus, semimembranosus, biceps femoris caput longum, sartorius, and gracilis) commonly included in knee studies [40, 92, 129, 131] as well as the maximum hip joint reaction data are presented.

Maximum muscle forces generated during each cycle were determined first. Average maximum muscle forces for all subjects were then computed (Table 4.1). For ease of comparison, these maximums have been provided both in absolute values (N) as well as multiples of body weight.

Table 4.1: Maximum muscle forces calculated for level walking and rising from a stool (All subjects included; Average ± Standard Deviation; BFC = biceps femoris caput).

	Level Walking		Rising from a Stool	
	(N)	(BW)	(N)	(BW)
Rectus Femoris	624 ± 225	1.1 ± 0.4	186 ± 159	0.3 ± 0.3
Semitendinosus	231 ± 53	0.4 ± 0.1	165 ± 120	0.3 ± 0.2
Semimembranosus	661 ± 173	1.1 ± 0.3	281 ± 208	0.5 ± 0.3
BFC Longum	271 ± 105	0.5 ± 0.2	450 ± 160	0.8 ± 0.2
Sartorius	135 ± 46	0.2 ± 0.1	78 ± 28	0.1 ± 0.0
Gracilis	104 ± 51	0.2 ± 0.1	27 ± 33	0.0 ± 0.1

Average maximum muscle forces were larger in level walking than in rising from a stool. This trend may be explained by the types of motion performed in the two tasks as well as by the optimization criterion used to calculate the muscle forces. In level walking, muscle groups activated individually to decelerate the body at heel strike and accelerate the body at toe off; maximum forces in the hamstrings occurred soon after heel strike, whereas

maximum forces in the quadriceps occurred just before toe off. Simultaneous activations of the hamstrings and quadriceps were necessary to control motion during rising from a stool, however, and maximum muscle forces might have been lower than those calculated in level walking due to the min-max optimization method used to calculate the muscle forces. The optimization criterion did not allow for co-contraction of muscles unless the muscles were activated to perform different roles at different joints (for example, the quadriceps could be activated to provide a motion at the knee while the hamstrings were activated to provide a motion at the hip - but the quadriceps and hamstrings could not both be activated to provide a motion at the knee). It is possible that muscles which co-contract *in vivo* during rising from a stool were not calculated to co-contract in the lower limb model, resulting in underestimations of maximum muscle forces during this activity.

Standard deviations of muscle forces were similar between the two tasks, but if the standard deviations are considered relative to the maximum values, there was more relative variability during rising from a stool than during level walking. Larger standard deviations in rising from a stool may again be partially due to the min-max optimization method. Calculating muscle forces generated by simultaneously contracting muscle functional groups is more complex than calculating muscle forces generated during level walking when contraction alternates between muscle functional groups. The added complexity in muscle force calculations during rising from a stool may have contributed to larger standard deviations of calculated muscle forces in this activity.

Differences in relative muscle force standard deviations between the two tasks may have also been caused by differences in familiarity with the tasks. Although level walking and rising from a stool are both completed on a regular basis, walking within the laboratory environment was probably more similar to daily conditions than rising from a stool with arms crossed over the chest. Perhaps subjects commonly use their hands when rising from a stool, or perhaps the height of the stool did not match the stool height commonly used by the subjects. These potential variations from normal daily activities might explain why standard deviations (relative to absolute muscle forces) were larger in rising from a stool than in level walking.

The joint reaction forces were considered next. The maximum joint reaction force at the hip was determined for each motion cycle completed by the subjects. The average and standard deviation of these maximum joint reaction forces were then calculated for each subject (Table 4.2). Average maximum joint reaction forces have again been reported in both absolute values (N) and multiples of body weight.

Table 4.2: Maximum joint reaction forces calculated for level walking and rising from a stool (Average ± Standard Deviation).

	Level Walking		Rising from a Stool	
	(N)	(BW)	(N)	(BW)
Subject 1	2836 ± 281	5.3 ± 0.5	3801 ± 1197	7.1 ± 2.2
Subject 2	4078 ± 465	7.4 ± 0.8	3822 ± 379	7.0 ± 0.7
Subject 3	3835 ± 326	6.0 ± 0.5	4503 ± 1098	7.0 ± 1.7

Maximum joint reaction forces during level walking were lower than those during rising from a stool for two of the three subjects; between-subject differences in joint reaction forces were relatively small, especially for rising from a stool. Standard deviations of joint reaction forces were again typically larger for rising from a stool than for level walking.

4.3 Verification studies

4.3.1 Comparing calculated muscle forces to forces applied in other FE models

Only four research groups (Pandy *et al.* [111], Penrose *et al.* [118], Riemer *et al.* [123], and Yang *et al.* [159, 160]) are known to have created FE models of the knee which applied forces representative of individual muscles. Only Pandy *et al.* [111] reported the magnitudes of the applied muscle forces; this group based their muscle forces on peak isometric muscle forces reported by Delp [28]. (Delp calculated peak isometric muscle forces from physiological muscle cross-sectional areas reported by Friederich & Brand [45] and Wickiewicz *et al.* [155]; Pandy *et al.* then scaled these peak isometric muscle forces to individual subjects using muscle torques before using this information to calculate maximum muscle forces.) The peak isometric muscle forces reported by Delp

and Pandy *et al.* have been included in Table 4.3 to allow for comparison with the average of the level walking maximum muscle forces calculated in this thesis.

Table 4.3: Comparison of maximum muscle forces (N) calculated in the current study for level walking and reported by Delp and Pandy *et al.* (BFC = Biceps femoris caput).

	Current Study	Delp [28]	Pandy *et al.* [111]
Rectus Femoris	624 ± 225	780	1682
Semitendinosus	231 ± 53	328	640
Semimembranosus	661 ± 173	1030	1480
BFC Longum	271 ± 105	717	960
Sartorius	135 ± 46	104	187
Gracilis	104 ± 51	108	194

The maximum muscle forces calculated in the Current Study were generally smaller than the maximum muscle forces reported by Delp and Pandy *et al.* This result was not surprising since the lower limb model used in this thesis used a min-max optimization method (see Section 4.1.4) to prevent loading any individual muscle to its peak muscle force. Therefore, it would not be expected that the calculated muscle forces would exceed peak isometric muscle forces.

The exception to this trend was the sartorius. The force calculated by the lower limb model (135 N) was slightly larger than the peak isometric force (104 N) reported by Delp but was still lower than that reported by Pandy *et al.* (187 N). The differences between these three maximum forces were small, however.

4.3.2 Comparing joint contact forces with instrumented implants and other mathematical models

The maximum hip joint contact forces calculated for the three subjects were then compared to *in vivo* contact forces measured using instrumented hip implants. Similar to the instrumented knee replacements described in Section 2.1.5, instrumented hip replacements have also been used to measure *in vivo* joint contact forces. Contact forces measured during level walking (Table 4.4) and rising from a stool (Table 4.5) are provided below. The average maximum hip joint contact forces calculated for this study ('Current Study') have also been included in the tables.

Table 4.4: Measured and calculated maximum joint contact forces (BW) during level walking.

Instrumented Implants		Mathematical Models	
Force	Reference	Force	Reference
2.4	Bergmann *et al.* [17]	3.3	Stansfield *et al.* [139]
2.7	Kotzar *et al.* [84]	4.3	Crowninshield *et al.* [26]
2.8	Stansfield *et al.* [139]	4.8	Paul [113]
3.5	Bergmann *et al.* [18]	5.5	Röhrle *et al.* [124]
		6.2	Current Study

Table 4.5: Measured and calculated maximum joint contact forces (BW) during rising from a stool.

Instrumented Implants		Mathematical Models	
Force	Reference	Force	Reference
1.2	Kotzar *et al.* [84]	2.0	Crowninshield *et al.* [26]
1.6	Bergmann *et al.* [17]	2.3	Stansfield *et al.* [139]
2.0	Stansfield *et al.* [139]	7.0	Current Study

The joint contact forces measured by the instrumented hips were smaller than those calculated both using mathematical models and in the current study. This trend is not uncommon, however, as mathematical models commonly result in contact forces larger than those recorded by instrumented implants [81]. Stansfield *et al.* [139] reported that hip joint contact forces calculated by mathematical models were as much as 33% larger and 23% larger than contact forces measured by instrumented hips during level walking and rising from a stool, respectively. It should be noted that while the Current Study maximum joint contact force was relatively similar to (although still larger than) the contact forces reported by other mathematical models for level walking, the Current Study maximum joint contact force for rising from a stool was markedly higher than the forces calculated by other mathematical models.

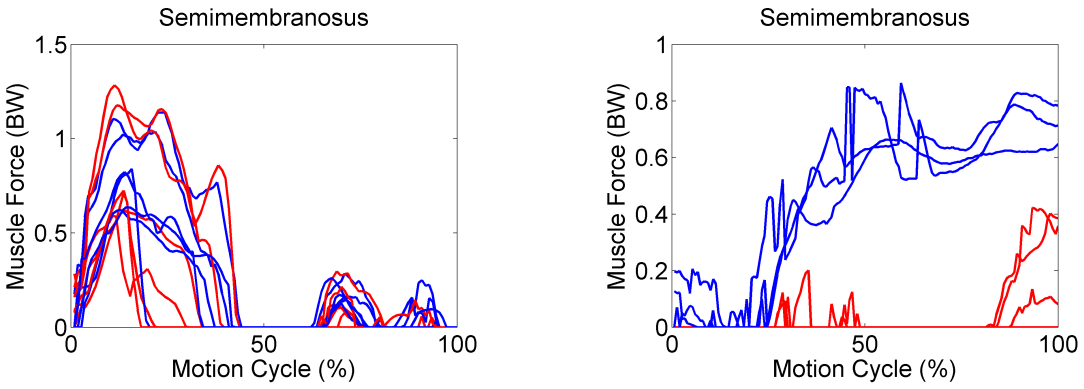
Suggested reasons for these overestimated forces include non-physiological distributions of forces between muscles in functional groups as well as non-physiological representations of the joints within the mathematical models (for example, modelling the knee as a hinge joint). Mathematical models may also specifically overestimate contact forces

if ligaments are not included in the models. Ligaments provide *in vivo* knee stability. Without ligaments, the mathematical models rely on muscle contractions to provide knee stability [110]; the additional muscle contractions lead to larger muscle forces which in turn lead to larger joint contact forces.

4.3.3 Comparing intra-subject muscle forces

Although the overall motion of the subjects was generally similar between consecutive cycles of the same activity, there were slight differences between trials. In this section, the forces calculated throughout each motion cycle were examined.

Each subject was first considered separately. Plots of muscle forces throughout the cycles of interest were generated for each subject, muscle, and task. Examples of calculated semimembranosus muscle forces calculated for a single subject during twelve cycles of level walking and seven cycles of rising from a stool are provided in Figure 4.7a and Figure 4.7b, respectively. Note that both motion cycles beginning with (blue) left and (red) right foot strikes have been included in these figures.



(a) (b)

Figure 4.7: Semimembranosus muscle forces for (a) twelve cycles of level walking and (b) six cycles of rising from a stool (one subject; left leg in blue; right leg in red).

Three important trends were seen in these graphs. First, muscle force trends were repeatable between different cycles of level walking collected from the same subject; trends were similar for left and right foot strike cycles. Muscle force trends were also repeatable within a given leg for rising from a stool; semimembranosus muscle forces were larger in the left leg than right leg. Closer inspection of the force plate data showed that the

magnitudes of the ground reaction forces were similar for the left and right legs, but that the anterior-posterior ground reaction force components differed in the two legs. The right and left legs had anterior and posterior ground reaction force components, respectively, leading to different muscle functional groups being activated during the activity. The hamstrings were predominantly active on the left leg; the quadriceps were predominantly active on the right leg.

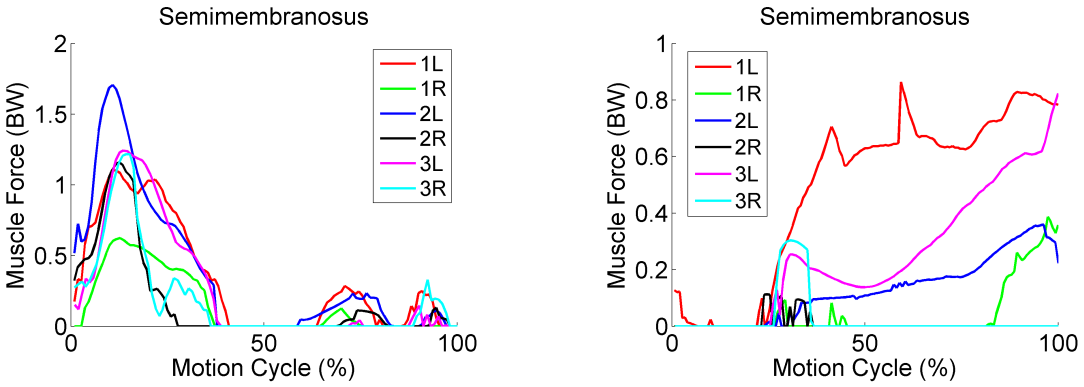
Second, different patterns were seen in muscle forces for the two tasks shown. Maximum semimembranosus muscle forces for level walking were generated earlier in the motion cycle during mid-stance, while maximum muscle forces for rising from a stool occurred later in the motion cycle when the knee was nearly extended.

Third, the magnitudes of the muscle forces varied between motion cycles regardless of the task being performed, particularly when different activation patterns were witnessed in the two legs.

4.3.4 Comparing inter-subject muscle forces

Muscle forces calculated for multiple subjects were then compared. Representative cycles of a left and a right foot strike of each activity were identified using the RMS difference method (see Section 4.1.5). The muscle forces calculated for these representative cycles were then plotted throughout the cycles of interest. Examples of semimembranosus muscle forces calculated for multiple subjects during level walking and rising from a stool are shown in Figure 4.8a and Figure 4.8b, respectively. Note that the cycles are labelled according to subject-foot strike; therefore, '1R' is a motion cycle from Subject 1 beginning with a right foot strike.

Good repeatability in muscle force trends was seen between subjects in level walking. Different muscle patterns were again calculated during rising from a stool based on whether the left or right leg was the leg of interest. Larger semimembranosus muscle forces were again calculated in the left leg during this activity, with a general pattern of increasing muscle force towards the end of the cycle. In general, there was more variability in inter-subject muscle forces than in intra-subject muscles forces, which is not surprising since different subjects might use slightly different motion patterns to complete the



(a) (b)

Figure 4.8: Semimembranosus muscle forces for (a) level walking and (b) rising from a stool (three subjects).

activities.

4.3.5 Comparing calculated muscle activation timings to expected EMG activation timings

The calculated muscle activation patterns were then compared to muscle activation patterns reported in EMG studies. Five studies [69, 140, 141, 149, 157] were available with which to compare the calculated muscle activation timings during level walking. The EMG sets did not include information on muscle activation timings of the sartorius or gracilius; therefore, these muscles are not included in the verification studies. The expected activation timings of the remaining four muscles are shown in Figure 4.9. The bars in the figure represent the expected activation periods for each muscle; the colours identify the EMG study which reported each activation trend. Please note that the EMG studies gave the same expected activation timings to each of the muscles comprising the hamstrings (semitendinosus, semimembranosus and biceps femoris caput longum).

Each EMG set provided slightly different expected muscle activation trends (Figure 4.9). Instead of selecting a single set of EMG data with which to compare the calculated muscle activation trends, an overall set of on-off patterns from the different EMG sets was created. This overall set considered a muscle to be activated or 'on' if any of the five sets of EMG data expected the muscle to be 'on' (for example, if EMG set 1 listed a muscle as activated from 15-35% motion cycle and EMG set 2 listed activation from

20-40% motion cycle, the overall 'on' trend was considered to be 15-40% motion cycle). These expected on-off timings were then compared to the calculated muscle force timings (a muscle with a force greater than 0 was classified as 'on') for each time frame.

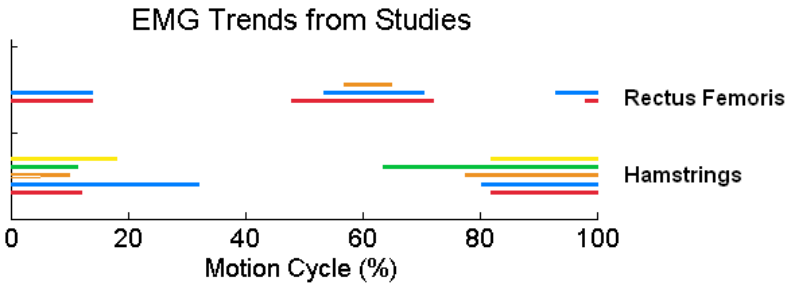


Figure 4.9: Expected muscle activation trends from five EMG studies (yellow = Inman *et al.* [69]; green = Vaughan *et al.* [149]; orange = Sutherland *et al.* [141]; blue = Sutherland [140]; red = Winter [157]).

Four studies were conducted to investigate the agreement between the calculated and EMG-predicted muscle activation timings. Visual assessments of the muscle activation trends were made first. Bars indicating when the EMG studies expected muscle activation were added above the muscle force data, and the locations of these bars were then compared to the activation trends of the calculated data.

Next, three quantitative studies were conducted which calculated the per cent differences between the calculated and expected muscle activation timings. The first two studies (Unweighted Differences and Weighted Differences) compared the two sets of activation trends directly: each time frame of the calculated muscle force was compared to its corresponding time frame in the EMG predictions. Any discrepancies between the two sets were considered differences. In the Unweighted Differences study, all differences were given the same weight (difference = 0 if calculated and expected timings match; difference = 1 if calculated and expected timings do not match). In the Weighted Differences study, differences were weighted based on the number of EMG studies which predicted muscle activation in the specific time frame. The third study (Percentage Activation Differences) considered the percentage of the motion cycle during which the calculated muscle force data showed muscle activation. This percentage was then compared to the percentage of the motion cycle during which the EMG studies predicted muscle activation.

4.3.5.1 Study A: Visual assessment

The Visual Assessment study involved placing EMG activation bars above the calculated muscle activation periods and qualitatively describing the relationship between the two sets of timings.

Two categories of discrepancies or differences between the two sets of timings were found. The first category involved a time shift between the calculated and expected muscle activation patterns. This trend was generally caused by a slightly early or late muscle activation that then shifted subsequent muscle activation patterns by similar amounts. The second category involved augmented calculated activation periods which both began before and ended after the EMG-predicted activation periods.

The rectus femoris (Figure 4.10a) was expected to have three activation periods. The first and third activation periods were absent in every motion cycle, however. Instead, the second activation began early and shifted the timings so that the second activation also ended prematurely.

The hamstrings (Figure 4.10b, c, d) were expected to have two activation periods. There was good agreement between the calculated and expected timings during the first activation period. Two distinct patterns of differences were found in the second activation period. In the semimembranosus and semitendinosus, the calculated activation period was divided into two shorter activation periods separated by a brief period of non-activation. The first of these divided activation periods was augmented and shifted earlier in the motion cycle, resulting in calculated activation beginning before expected. The second activation pattern was absent in the biceps femoris caput longum.

4.3.5.2 Study B: Unweighted differences

The Unweighted Differences study directly compared the calculated muscle force timings to the expected EMG-derived activation timings. Any discrepancies between the two sets were considered differences, and all differences were given the same weight.

Differences were classified as one of two types: Type A when the EMG set expected a muscle to be 'on' but the calculated data showed the muscle as 'off' or Type B when the calculated data showed a muscle to be 'on' but the EMG trends expected the muscle to

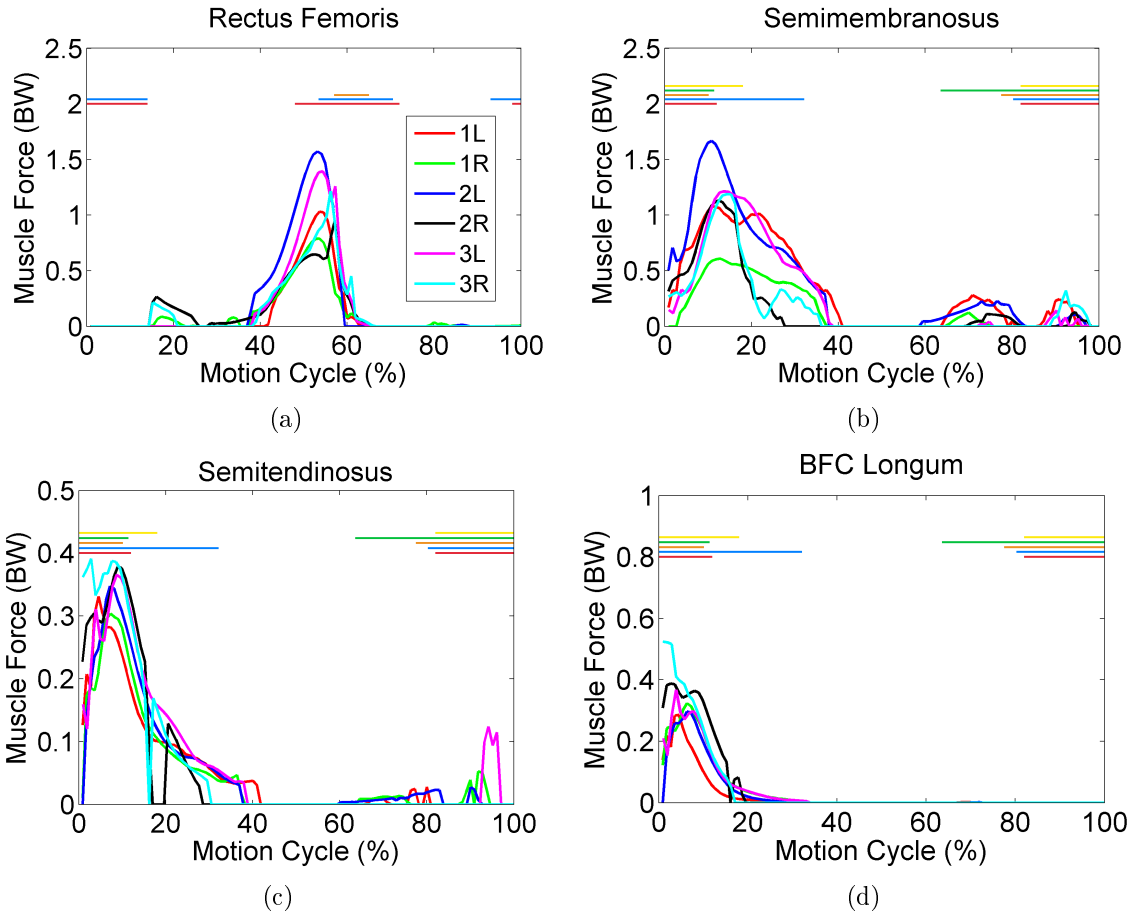


Figure 4.10: Calculated and expected activation timings during level walking: (a) Rectus femoris, (b) semimembranosus, (c) semitendinosus, and (d) biceps femoris caput longum.

be 'off'. The percentage of time frames with each type of difference was found for each motion cycle. Average per cent differences were then calculated for each subject using leg of foot strike as a variable, for all subjects using leg of foot strike as a variable, and for all level walking cycles.

Type A differences were larger than Type B differences for all muscles (Table 4.6). This result was not surprising; Type A differences were expected to be inherently more prominent due to the method of combining EMG sets to create an overall EMG set with maximum muscle activation timings.

More surprising, however, were the relative percentages of Type A and Type B differences for the different groups of muscles. The hamstrings (involved in knee flexion) had consistently lower Type B differences (range: 1.3% to 4.2%) than the rectus femoris (involved in knee extension, with a difference of 18.4%). It is unlikely that model geometry,

Table 4.6: Unweighted per cent differences (Type A = calculated muscle 'off' when EMG expected muscle 'on'; Type B = calculated muscle 'on' when EMG expected muscle 'off'; BFC = biceps femoris caput).

	Type A (%)	Type B (%)
Rectus Femoris	29.7	18.4
Semitendinosus	30.7	3.4
Semimembranosus	23.7	4.2
BFC Longum	41.1	1.3

marker placement, or the method of representing muscles within the lower limb model can explain this result. Instead, this trend may represent a systematic weakness in the ability of the lower limb model to calculate quadriceps muscle activation timings which are consistent with EMG studies.

4.3.5.3 Study C: Weighted differences

The Weighted Differences study was identical to the Unweighted Differences study except that weights were assigned to the Type A differences. These weights reflected the varying levels of agreement between individual EMG sets (which were compiled to create the overall EMG set used in the Unweighted Differences study) about muscle activation timings.

Weights were assigned to each time frame with a Type A difference based on the ratio of the number of individual EMG sets expecting activation in a muscle to the total number of EMG sets which included activation timings for the muscle (not all of the EMG studies included data for each muscle). For example, if five EMG sets provided activation timings for a muscle and a Type A difference occurred in a time frame where all five individual EMG sets indicated activation, a full weighting of 1 was assigned to the Type A difference; if only three EMG sets showed activation for the time frame, however, a weighting of 3/5 or 0.6 was assigned to the Type A difference. Using this method of weighting, new average weighted Type A differences were calculated for each muscle (Table 4.7). Type B differences were unaffected by the weighting but are included in the table for comparison.

Comparing the Type A differences from the Unweighted Differences and Weighted

Table 4.7: Weighted per cent differences (Type A = calculated muscle 'off' when EMG expected muscle 'on'; Type B = calculated muscle 'on' when EMG expected muscle 'off'; BFC = biceps femoris caput).

	Type A (%)	Type B (%)
Rectus Femoris	17.8	18.4
Semitendinosus	18.4	3.4
Semimembranosus	15.1	4.2
BFC Longum	22.5	1.3

Differences studies gave some interesting insight. Large differences between the two values indicated large numbers of Type A differences occurring in time frames during which EMG studies disagreed about muscle activation; differences during time frames of questionable muscle activation could be considered less significant. On the other hand, similar Unweighted and Weighted Type A differences would indicate that these differences occurred during time frames in which EMG studies agreed a muscle should be activated. Differences in these time frames could be considered more significant.

The biceps femoris caput longum had the largest decrease in Type A difference - from 41.1% in the Unweighted Differences study to 22.5% difference in the Weighted Differences study. These results suggested a large number of Type A differences occurred during time frames in which the EMG sets disagreed about muscle activation; the recorded differences, therefore, could be disputed as not actually representing differences but instead disagreements between published EMG sets.

Type A and Type B differences in the Weighted Differences study were then compared. Muscles associated with knee flexion continued to have larger Type A than Type B differences, meaning that most differences resulted from the muscles being calculated as 'off' when expected to be 'on'. Meanwhile, the weighted Type A difference in the muscle associated with knee extension reduced to be lower than the Type B difference, indicating that the rectus femoris was commonly 'on' when expected to be 'off'. This distinction between the two muscle functional groups again suggests a systematic difficulty within the lower limb model to calculate quadriceps muscle activation timings which match EMG study predictions.

The standard deviations of the Weighted Type A differences were also calculated for

each muscle (Table 4.8). These values indicated whether there was a large variability between per cent differences calculated for different subjects and motion cycles. A relatively small range of standard deviations was calculated: from 2.6% in the biceps femoris caput longum to 5.7% in the semitendinosus. These results suggested that the percentage of Type A differences for each muscle were similar both between subjects and motion cycles.

Table 4.8: Averages and standard deviations (St. Dev.) of weighted Type A differences (BFC = biceps femoris caput).

	Average (%)	St. Dev. (%)
Rectus Femoris	17.8	3.0
Semitendinosus	18.4	5.7
Semimembranosus	15.1	4.9
BFC Longum	22.5	2.6

4.3.5.4 Study D: Percentage activation differences

The Percentage Activation Differences study considered whether the percentage of the motion cycle during which muscle activation was calculated matched the percentage of the motion cycle during which muscle activation was predicted by the EMG studies.

Each motion cycle was first analysed to determine the percentage of the cycle during which each muscle was calculated to be activated. These percentages were then compared to the expected percentage activation of the overall EMG set used in the Unweighted Differences study. The difference between the calculated muscle activation timings and expected EMG timings was then computed for each muscle (Table 4.9). Negative differences indicated that the muscle was activated for a shorter percentage of the motion cycle than expected; positive differences indicated that the calculated percentage activation was longer than expected.

All of the muscles were activated for a smaller percentage of the motion cycle than expected. Again, this result was unsurprising given the method of compiling the overall EMG set.

The results of this study supported those of the Visual Assessment study, which found some activation periods absent in particular muscles. For example, the Visual Assessment

Table 4.9: Percentage activation differences (BFC = biceps femoris caput).

	Difference (%)
Rectus Femoris	-20.7
Semitendinosus	-39.0
Semimembranosus	-27.2
BFC Longum	-58.2

study showed that the second activation period was frequently absent in the biceps femoris caput longum. This absent-but-expected activation period resulted in this muscle having the largest percentage activation difference. The semitendinosus (another hamstrings muscle with an occasionally absent second activation period) also had a relatively large percentage activation difference.

The percentage activation difference was smallest in the rectus femoris. Although the first and last expected activation periods were frequently absent, the muscle was also activated during the first expected period of non-activation. The combined effect of these two trends led to smaller percentage activation differences in this muscle.

4.4 Discussion

In addition to subject-specific geometry, a subject-specific FE model also requires subject-specific load data. This chapter outlined a method for calculating these loads. A lower limb model was used to calculate the muscle loads generated and joint reaction loads experienced while performing two functional tasks. This data was then combined to calculate the loads to apply to the FE models. Since the applied loads directly influence the FE model results, verification studies were conducted to investigate the validity of the calculated muscle and joint reaction loads as well as their variability between motion cycles.

Muscle force activation trends were found to be similar between motion cycles of level walking and rising from a stool. Variations in maximum values of force magnitudes were seen, however, and may reflect slight adaptations in individual motion.

Muscle activation timings were then compared to previously-published results from

EMG studies to investigate the validity of the calculated muscle timings. The Visual Assessment study showed that the level of agreement between these two sets of activation timings varied between muscles. In some muscles (such as the semimembranosus and semitendinosus) there was relatively good agreement; in other muscles (such as the rectus femoris and biceps femoris caput longum) some predicted muscle activation periods were absent in the calculated muscle forces.

Three numerical verification studies were also conducted. The first of these studies (Unweighted Differences) compared the calculated and EMG-predicted muscle activation timings. A wide range of differences was calculated. Type A differences, related to a muscle not being activated when the EMG studies predicted activation, ranged from 23.7% (semimembranosus) to 41.1% (biceps femoris caput longum); Type B differences, related to a muscle being activated when the EMG studies predicted non-activation, were smaller and ranged from 1.3% (biceps femoris caput longum) to 18.4% (rectus femoris). All muscles had larger Type A than Type B differences.

Since the individual EMG studies used to create the combined EMG set did not always agree about whether a muscle should be activated in a specific time frame, the differences found in the Unweighted Differences study were then weighted in a second study (Weighted Differences). Type A differences were weighted according to the proportion of EMG studies contradicted by a difference in the calculated muscle activation trends. Type A differences, therefore, decreased in this study. The largest decrease (from 41.1% to 22.5%) was found for the biceps femoris caput longum, indicating that the differences calculated in the Unweighted Differences study may not have been as significant because they occurred in time frames when the EMG studies were uncertain about expected activation timings. Type A differences decreased by approximately 10% in the remaining muscles.

Finally, the percentages of the motion cycle during which muscle activation was calculated and predicted were considered. All of the muscles were activated for smaller proportions of the motion cycle than expected by the EMG studies. This trend was particularly apparent in muscles in which predicted activations were absent. The biceps femoris caput longum and rectus femoris, for example, typically did not show activation in the final expected activation period. This final expected activation period occurred

during swing phase, however, and so would not affect the load cases applied to the FE models. Of more importance, the rectus femoris also did not show activation in the first expected activation period, which occurred during stance phase. The remaining muscles in the quadriceps functional group were activated during these predicted activation periods (data not included as vasti muscle forces were not included in load case calculations) so it is possible that the lower limb model divided the total activation of the functional group in a manner different from that measured by the EMG studies.

In general, muscle force trends were repeatable both between motion cycles from the same subject and from different subjects (though trends were leg-specific in rising from a stool). There were varying levels of agreement between calculated and expected muscle activation timings for the various muscles, but many of these discrepancies were due to absent-but-expected activation periods during swing phase. Also, if one muscle in a functional group had an absent activation period, the remaining muscles in the functional group were generally activated; therefore, the expected overall muscle patterns still existed but were simply being created by different muscles within the functional group.

4.4.1 Potential sources of differences

A potential source of differences between the calculated and EMG-expected muscle activation timings could be the subjects used in testing. Only three subjects were included in this study, and if any of these individuals showed unusual muscle activation patterns, these abnormalities could significantly affect the calculated Type A and Type B differences. To limit the potential for this source of difference, only subjects with normal motion patterns were tested and all data was inspected for anomalies in motion.

Another possible source of differences could be the method used by the lower limb model to determine which muscles to activate. The optimization technique did not attempt to smooth muscle activations from time frame to time frame. Instead, muscles could switch between being 'on' and 'off' in consecutive time frames. Therefore, seemingly unusual rapid changes between activation and non-activation (such as were seen in the hamstrings) can be at least partially explained by the optimization method.

It should also be noted that some of the differences in muscle activation occurred

during swing phase of level walking. Load cases for the FE model were only calculated based on data during stance phase so differences during swing phase did not affect the calculated load cases or FE model results. Noticeable differences occurred, however, during stance phase in the rectus femoris: the muscle was calculated as being 'off' during its first expected activation period. The optimization method activated the remaining muscles in the muscle functional group during this phase to compensate for the rectus femoris being 'off'.

4.4.2 Limitations

Some assumptions and limitations of the lower limb model should be addressed. First, though the lower limb model was scaled to the height of each subject, the locations of muscle origins and insertions were not identified specifically for each subject so it is possible these muscle locations were not representative of the individual subjects. In the future, subject-specific muscle origin and insertion locations could be identified in the MRI scans and used in the lower limb model.

A second assumption made by the lower limb model involved the optimization criterion used to decide how to divide required muscle forces between the muscles. A min-max optimization criterion was used. This criterion assumes that multiple muscles activate when performing a motion and that the relative contribution of each muscle is proportionate to the maximum possible force which can be generated by each muscle; this criterion limits muscle fatigue and avoids overloading any single muscle. Other optimization criteria (such as minimum muscle stress or minimum metabolic energy expenditure [39, 120]) have also been proposed, however, and different optimization criteria are likely to result in different muscles being activated with different muscle forces. Therefore, the calculated load cases were likely affected by the min-max optimization criterion used by the lower limb model.

A third assumption and limitation of the lower limb model was modelling the knee as a hinge joint. The hinge joint only allowed flexion-extension within the knee (despite the *in vivo* knee having six degrees of freedom - see Section 2.1.3). Other motions such as internal-external rotation also occur during level walking and rising from a stool, however, and the lower limb model would not have activated muscles to re-create these motions.

Modelling the knee as a hinge joint therefore likely affected the distribution of forces between the muscles, particularly within a functional group, and may explain why the calculated muscle activation timings did not always match the EMG-derived expected activation timings. More physiological models of the knee which allow for additional knee motions are currently being developed [40] and should be used in future studies.

A fourth limitation of the lower limb model was a lack of ligaments. Although ligaments restrict excessive motion in the *in vivo* knee, they were not included in the lower limb model. Any excessive motions were instead constrained by activating the muscles. These additional activations would increase the calculated load cases, perhaps providing another explanation of why calculated mathematical model contact forces are frequently larger than measured instrumented implant contact forces.

A fifth assumption which affected specifically the level walking load cases was determining the time frame in which to calculate the load cases (the time frames in which to calculate rising from a stool load cases were determined based on knee flexion angles). Level walking load cases in this thesis were calculated in the first time frame with a non-negligible (greater than 10 N, representing a noise threshold) ground reaction force. This time frame was selected to represent heel strike, a feature of the motion cycle hypothesized to be linked with medial OA development. Load cases could also have been calculated in other time frames, for example, the time frame with the first peak of the ground reaction force. Though not occurring at heel strike, these other time frames may also have represented loading with the knee in approximately 11° flexion. Ground reaction forces would have been larger in these other time frames, resulting in larger calculated load cases which would have subsequently affected the FE model results.

4.5 Conclusions

This chapter described a method for calculating FE model load cases from forces and moments experienced in the lower limb. Motion analysis data was collected and processed before being applied to a lower limb model. This lower limb model then used marker locations and force plate data recorded during the motion cycles, assumptions about muscle function, and an optimization method to calculate muscle forces and joint reaction

loads throughout the motion cycles.

Muscle forces calculated both from the same subject and from different subjects were then compared for cycles of level walking and rising from a stool. Muscle activation patterns were similar both between motion cycles from the same subject and between motion cycles from different subjects. Activation patterns were similar regardless of leg of interest during level walking but differed according to leg during rising from a stool.

Muscle activation timings calculated by the lower limb model were then also compared to level walking muscle activation timings reported by EMG studies. Most of the muscle activation patterns matched EMG timings, especially during stance phase. In instances when activation patterns of a muscle did not match (such as for the rectus femoris), other muscles within the functional group were activated.

After creating the subject-specific model geometry and calculating the subject-specific load cases, the FE model creation method was developed. The next chapter explains the steps involved in creating an FE model and then provides examples of preliminary models created while developing the proposed model creation method.

Chapter 5

Creating the FE Knee Models

This chapter begins by describing the steps involved in setting up FE models. Some of the preliminary FE models created to establish and fine-tune the procedural steps are then presented. The first models created for this thesis were of simple sphere-on-cuboid Hertzian contact. The geometry and load cases were then changed to progressively make the models more representative of the human knee.

All FE models in this thesis were created using the same computer (Intel®Core™2 Duo processor workstation running at 3.2 GHz with 3.25 GB of RAM). The models were then all solved using a separate computer (Intel core i5 processor workstation running at 3.2 GHz with 16 GB of RAM).

5.1 Steps in model set-up

5.1.1 Importing geometry and defining material properties

The first steps in creating the FE models were importing the geometry and defining the material properties of the structures. The solid geometries of the structures (created as described in Chapter 3) were imported as individual parts into the FE software (Abaqus 6.11, Dassault Systemes, Velizy-Villacoublay Cedex, France).

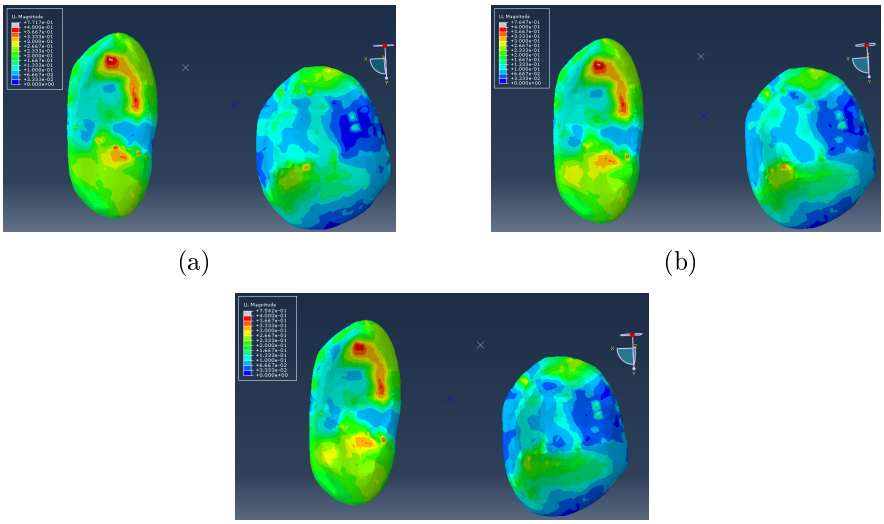
Material properties were assigned to each structure based on values commonly used in the literature (see Section 2.3.2.2). Bone was modelled as a rigid material; a 2002 study by Haut Donahue *et al.* [57] reported that modelling bone as a rigid rather than de-

formable material resulted in less than 2% change in contact variables while decreasing model solution time by 50%. Cartilage was modelled as linear elastic isotropic (E = 12 MPa, ν = 0.45) and menisci as linear elastic transversely isotropic (circumferential: E = 120 MPa, ν = 0.2; axial/radial: E = 20 MPa, ν = 0.3). Although these are physiologically viscoelastic materials, the elapsed loading times during level walking and rising from a stool are less than the viscoelastic constants [57, 115] so fluid does not move within the tissues during these activities and a linear elastic approximation is commonly used. It should be noted that the meniscal material properties were consistent with Yang *et al.* [159, 160] but not with Haut Donahue *et al.* [58], who suggested using an axial/radial meniscal Young's modulus of between 40 MPa and 60 MPa.

To investigate the effects of different axial/radial meniscal Young's modulus values, a sensitivity test was conducted as part of this thesis. Three FE models, identical with the exception of the meniscal axial/radial Young's modulus (values of 20 MPa, 40 MPa, and 60 MPa were used) were created and solved. The calculated displacement, von Mises stress, and contact pressure patterns on the articulating tibial cartilage surfaces of the three models were then compared (only the effects on the cartilage surface were investigated as these are the surfaces of primary interest in OA). The assigned axial/radial meniscal Young's modulus had no effect on the main areas of tibial cartilage contact and minimal effect on the calculated results (Figure 5.1). Therefore, the meniscal axial/radial Young's modulus value from Yang *et al.* was used so that results of the current study could be compared to results published by another group trying to create subject-specific FE models.

5.1.2 Generating mesh

The next step in setting up FE models was generating the mesh. The patches created as described in Section 3.1.3 were used as templates for the meshes and allowed for better control of mesh density (smaller patches were created in expected contact regions so that finer meshes were generated in these areas). Controlling mesh density allowed for detailed results to be calculated only in areas of expected contact. Models with fine meshes required longer computation times; therefore, using a coarse mesh in areas outside the expected



(a) (b)

(c)

Figure 5.1: Displacements (thresholds 0 - 0.4 mm) calculated on articulating tibial cartilage surfaces for FE models with axial/radial meniscal Young's moduli of (a) 20 MPa, (b) 40 MPa, and (c) 60 MPa.

contact area reduced the necessary computation time of the models.

Due to the patch geometry, the FE software only allowed tetrahedral meshes to be generated. Two commonly-used tetrahedral mesh elements are linear (C3D4) and quadratic (C3D10) mesh elements (these are the only two tetrahedral mesh element types available for Explicit model types). As second-order tetrahedral elements are not recommended for contact [1], linear tetrahedral mesh elements (C3D4) were generated for the FE models.

5.1.3 Assigning boundary conditions

After generating the meshes, boundary conditions were assigned. To avoid unrestrained motion of the model, one of the bones needed to be held fixed. Some researchers held the femur [57, 94, 111, 123], while others held the tibia [13, 15, 54, 102, 112, 115, 133, 150, 159]. The decision as to which bone to hold fixed seemed to be a matter of convenience. This study held the tibia fixed.

Displacement constraints were also applied to the femur. Preliminary FE models were created with different combinations of femoral boundary conditions (translations and rotations) to gain insight into the effect of constraining certain boundary conditions. (Heavily

constrained models may be more likely to solve because displacement and therefore excessive motion in some planes is prohibited - but the additional constraints may also fail to represent the physiological knee.) In some of the preliminary models, the femur was only allowed axial translation (to move along the proximal-distal axis). In other models, the femur was allowed axial translation as well as varus-valgus rotation in the frontal plane. Frontal plane rotation was allowed in some models to investigate the effect this additional model degree of freedom had on model solution difficulty.

No displacement conditions were applied to the cartilage or menisci. These structures were allowed to deform in all directions.

5.1.4 Defining interactions between structures

In addition to boundary constraints, nine contact constraints or interactions between structures were created for each model. The following tie constraints and contact interactions were defined:

- Tie Constraints
    1. Bottom of Femur - Top of Femoral Cartilage
    2. Bottom of Lateral Tibial Cartilage - Top of Lateral Tibia
    3. Bottom of Medial Tibial Cartilage - Top of Medial Tibia
- Contact Interactions
    1. Bottom of Lateral Femoral Cartilage - Top of Lateral Tibial Cartilage
    2. Bottom of Medial Femoral Cartilage - Top of Medial Tibial Cartilage
    3. Bottom of Lateral Femoral Cartilage - Top of Lateral Meniscus
    4. Bottom of Medial Femoral Cartilage - Top of Medial Meniscus
    5. Bottom of Lateral Meniscus - Top of Lateral Tibial Cartilage
    6. Bottom of Medial Meniscus - Top of Medial Tibial Cartilage

Tie constraints were used to ensure the contacting bone and cartilage surfaces did not move relative to each other. These constraints represented the physiological bonded contact between the deepest cartilage layer (calcified cartilage) and the subchondral bone. Contact interactions were created between the contacting soft tissues. Frictional contact ($\mu = 0.02$) [93, 94] represented the physiological nearly frictionless cartilage-cartilage and

cartilage-menisci interactions.

Another parameter used when defining contact interactions was the 'Separation' parameter. This parameter determined whether contacting surfaces could separate after coming into contact during model solution. FE models were solved both with and without allowing separation between contacting soft tissue surfaces.

5.1.5 Applying load cases

Load cases were applied to the model using the 'Concentrated Load' option. This option allowed for 3D forces and moments to be applied at a specific point. Since the tibia was chosen to be held fixed, the load cases were applied to the rigid femur. The single point at which the loads were applied (hereafter called 'the reference point') was chosen to be the femoral centre of mass.

The loads applied to the reference point were a combination of the joint reaction and muscle forces as calculated in Chapter 4. It should be noted that the applied boundary constraints nullified some components of the applied load cases (for example, a medial-lateral component of an applied force had no effect on the model if medial-lateral motion was constrained).

5.1.6 Setting model solution parameters

FE model solution can be attempted in a single increment (the entire load is applied instantaneously) or over multiple increments (the applied load is ramped to the total load over multiple increments). Models involving multiple contact pairs typically fail if solution is attempted in a single increment; therefore, the FE models in this study were set to solve in multiple increments.

In Standard models, the FE software continually calculates the optimal number of increments over which to apply the load based on the difficulty of solving the convergence equations. If convergence is becoming more difficult, the number of increments used is increased; if convergence is improving, the number of increments used is decreased. For Explicit models, the user defines the number of increments based on the size of the smallest element in the model (the load must be ramped over enough increments that

the resulting deformation wave through the material does not exceed wave propagation speed). Consequently, the specific number of increments used for both the Standard and Explicit FE models was model-specific.

All models were solved using an augmented Lagrangian contact method. This method allows some penetration between surfaces within a contact pair [2]. If penetration exceeds a given tolerance value, the load applied in that increment is decreased so that smaller penetrations between surfaces occurs; the additional load is then applied in following increments.

The final parameter set only pertained to Explicit models. The models were created to reflect quasi-static loading situations; therefore, over two million increments were used when solving the Explicit models. Single precision calculations would have resulted in significant round-off errors so double precision calculations were made.

5.2 Preliminary FE models

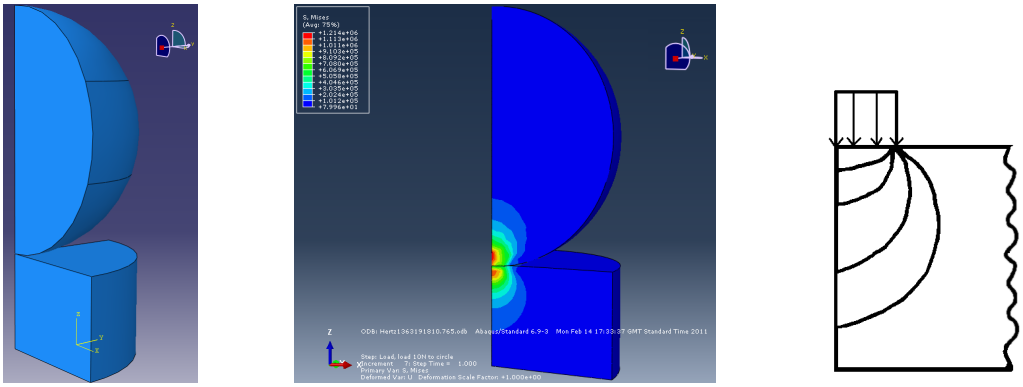
The steps just described were used to create multiple preliminary FE models. The first models involved relatively simple geometry and load cases. The simple geometry was then replaced by subject-specific geometry, continually building the geometric complexity and physiological accuracy of the knee models. Then the generic load cases were replaced with subject- and task-specific load cases.

5.2.1 Solving Hertzian contact model with generic geometry

The first model was of Hertzian contact: a sphere being pushed into a cuboid. This geometry represented simplified knee geometry - the sphere being a femoral condyle and the cuboid being a tibial plateau. Since the sphere and cuboid were symmetrical, it was only necessary to model a quarter of the geometry (Figure 5.2a). Well-established analytic and experimental solutions were available for this model [71], allowing the accuracy of the FE model results to be checked.

Both structures were modelled as deformable structures with identical material properties. The bottom surface of the cuboid was held fixed and a 100 N axial force was applied to the top surface of the sphere. The first models were created without boundary

constraints applied to the sphere; these models failed due to excessive unconstrained motion of the sphere. Various approaches (springs attached to the sphere, increased friction between the sphere and cuboid) were used to try to prevent excessive side-to-side motion of the sphere, but the model only solved when the sphere was constrained to axial (down)-only motion. Figure 5.2b shows the von Mises stresses calculated by the FE model; these results matched the expected Hertzian contact pattern (Figure 5.2c).

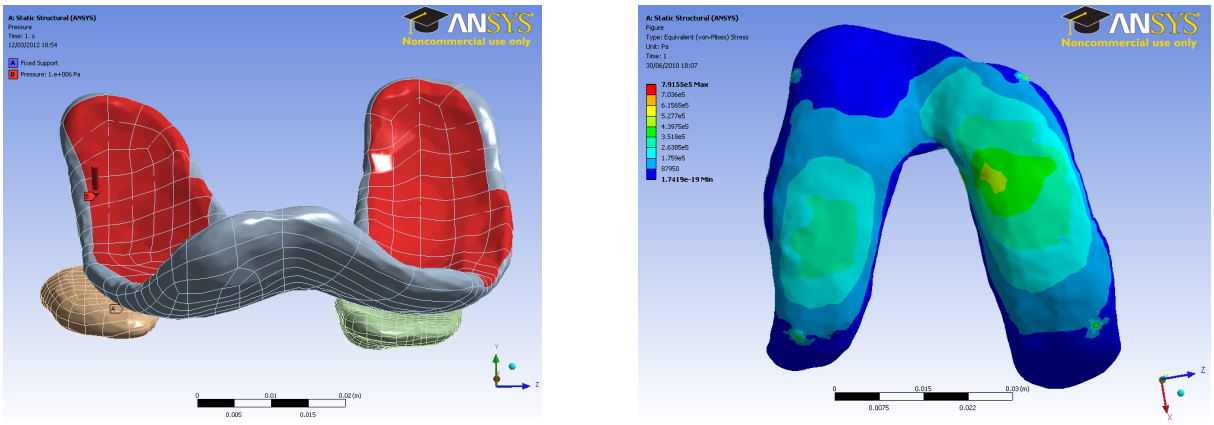


(a) (b) (c)

Figure 5.2: Hertzian contact FE model: (a) Sphere-on-cuboid geometry; (b) calculated von Mises stresses (threshold 80 Pa - 1.2 MPa); (c) expected Hertzian stress pattern on cuboid.

5.2.2 Progressing towards models with subject-specific bone and cartilage geometry

After solving the sphere-on-cuboid FE model, the sphere-on-cuboid geometry was changed to more accurately reflect the geometry of the knee. The sphere and cuboid were replaced by subject-specific femoral cartilage and tibial cartilage, respectively (Figure 5.3a). Material properties representative of human cartilage were assigned to the structures. The bottom surfaces of the tibial cartilage segments were held fixed while an axial 1 MPa pressure was applied to the top surface of the femoral cartilage (load application area shown in red). Von Mises stresses calculated on the articulating surface of the femoral cartilage are shown in Figure 5.3b. (Note that a second FE software program (ANSYS 12.1, ANSYS, Inc., Canonsburg, Pennsylvania, USA) was used to solve some of the preliminary FE models, including the cartilage-only models.)

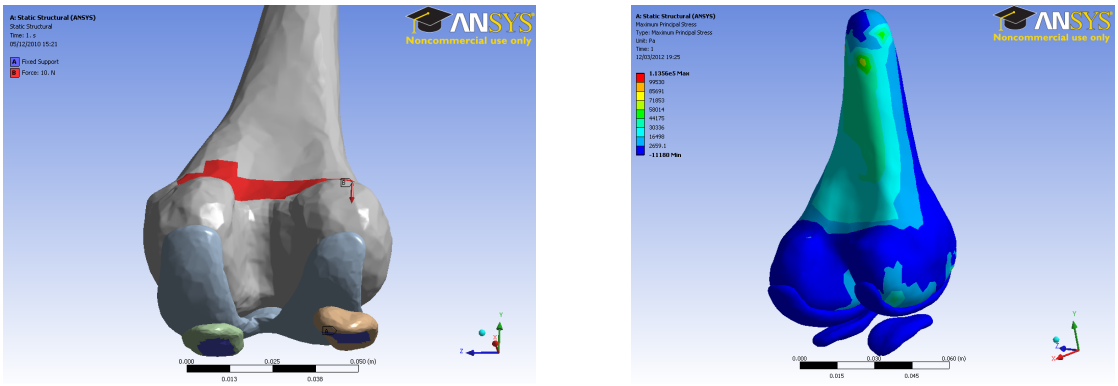


(a) (b)

Figure 5.3: Cartilage-only FE model: (a) Anterior view of model geometry; (b) calculated von Mises stresses (threshold 0 - 0.8 MPa) on articulating surface of femoral cartilage (anterior at top; lateral at left).

Next, the femur (modelled as a deformable material) was included in the FE model geometry (Figure 5.4a). A 10 N axial load was applied to the bone (load application area shown in red) instead of directly to the femoral cartilage. While applying the load to the femur represented a more physiological loading mechanism, it also increased the difficulty of convergence. Instead of simply pushing two objects together, there was now a chain of events with the femur contacting the femoral cartilage which then contacted the tibial cartilage. In an effort to improve convergence, models with different pinball region sizes were created. Relatively small pinball regions resulted in no femoral cartilage-tibial cartilage contact (Figure 5.4b); relatively large pinball regions resulted in excessive contact between structures and the models failed due to unmanageably large computations and file sizes.

Finally, the tibia was included in model geometry (Figure 5.5), resulting in FE models with subject-specific geometry of all of the tibiofemoral bone and cartilage structures within the human knee. The femur and tibia were modelled as rigid bodies; the femoral cartilage and tibial cartilage were modelled as deformable structures with identical material properties. Bone-cartilage interfaces were tied. The tibia was held fixed while a 1 kN load was applied to the femoral centre of mass. Boundary conditions constraining the femur to axial-only translation were necessary for model solution; cartilage was



(a) (b)

Figure 5.4: Cartilage and femur FE model: (a) Posterior view of model geometry; (b) calculated maximum principal stresses (threshold 0 - 0.1 MPa). (Note: No contact between femoral cartilage and tibial cartilage.)

allowed to deform in all directions. Figure 5.5 shows calculated von Mises stresses in a sagittal cut through the lateral compartment.

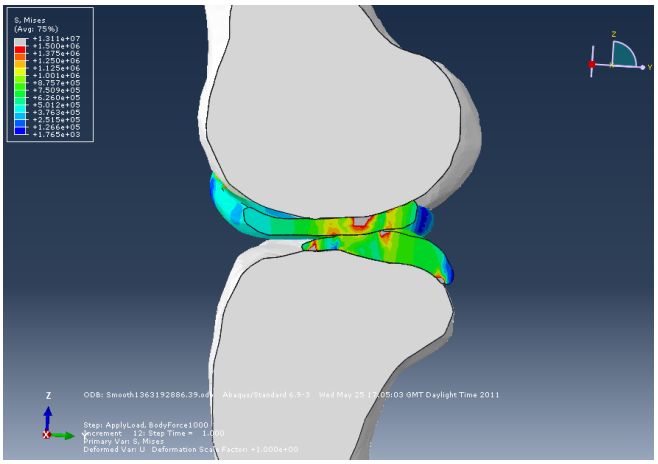


Figure 5.5: Cartilage, femur, and tibia FE model: Sagittal cut of model geometry and calculated von Mises stresses (threshold 1.8 kPa - 1.5 MPa) (anterior at left).

5.2.3 Creating subject- and task-specific models of the extended and flexed knee

After solving models with subject-specific geometry, FE models with subject- and task-specific load cases were created. Two models were created, one with the knee in extension and one with the knee in flexion. Both models were based on data from the same subject.

The load (532 N) applied to the FE model of the extended knee represented forces at heel strike during level walking; the load (126 N) applied to the FE model of the flexed knee represented forces experienced at that knee flexion angle during rising from a stool.

These models were originally created to gain preliminary insight into the different contact patterns during activities of knee extension and flexion. A main insight gained from the models, however, was how specific and in some cases inflexible some of the model parameters were. The pinball region and mesh densities were two such parameters. The size of the pinball region affected which elements in the contact pairs came into contact, in turn affecting the contact area and forces calculated by the model. Only a limited range of pinball region sizes (different ranges for different models) resulted in model convergence; models with too small or too large a pinball region failed to converge with either no or most elements, respectively, coming into contact.

Mesh density was another relatively inflexible parameter. The models were originally created with relatively coarse meshes. Attempts to refine the mesh led to distorted elements which resulted in models no longer solving. Both global and local mesh refinement were attempted without success. It was thought that requiring simultaneous convergence in two tibiofemoral compartments was perhaps too complex. The model of the extended knee was therefore temporarily simplified to include contact only in the medial tibiofemoral compartment (Figure 5.6). This simplification offered limited improvements; only one medial-compartment-only model solved.

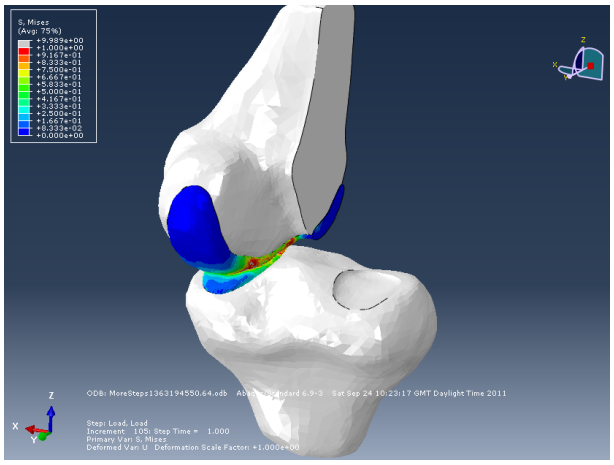
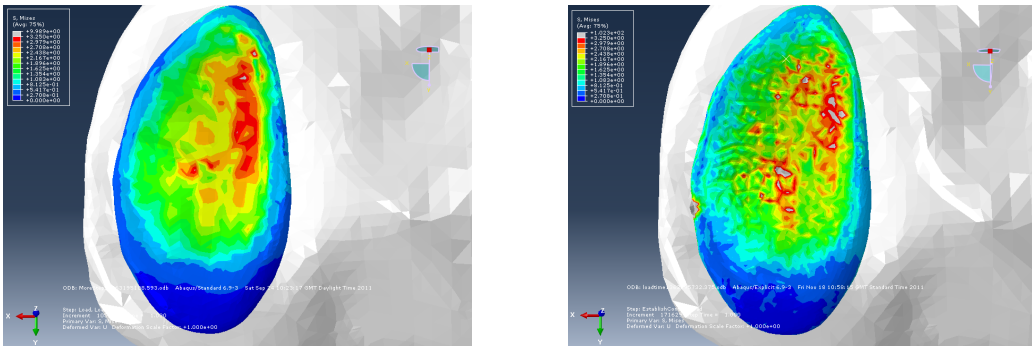


Figure 5.6: Medial compartment-only FE model: Posterior view of model geometry and calculated von Mises stresses (threshold 0 - 1.0 MPa).

The preliminary FE models created until this point were Standard General FE models. Since this type of model was proving sensitive to pinball region size and mesh density, the possibility of using other model types began to be explored. In particular, using Explicit General models was investigated. This model type is considered to be very good at solving complex contact problems and can be used to model quasi-static situations [3].

The first models created using the Explicit model type were medial-compartment-only models. Solving this model allowed for comparison of the Standard and Explicit model results. Each of three Explicit medial-compartment-only models solved. The displacements and von Mises stresses calculated by the two types of models gave similar results (Figure 5.7).



(a) (b)

Figure 5.7: Von Mises stresses (thresholds 0 - 3.25 MPa) calculated on the articulating medial tibial cartilage surface of (a) Standard and (b) Explicit FE models.

The lateral compartment was then added back into the model geometry, and Explicit FE models of the whole knee in extension and flexion were created. Both of these models also solved, and the mesh densities could be controlled to allow for mesh convergence tests.

5.2.4 Incorporating menisci into the models

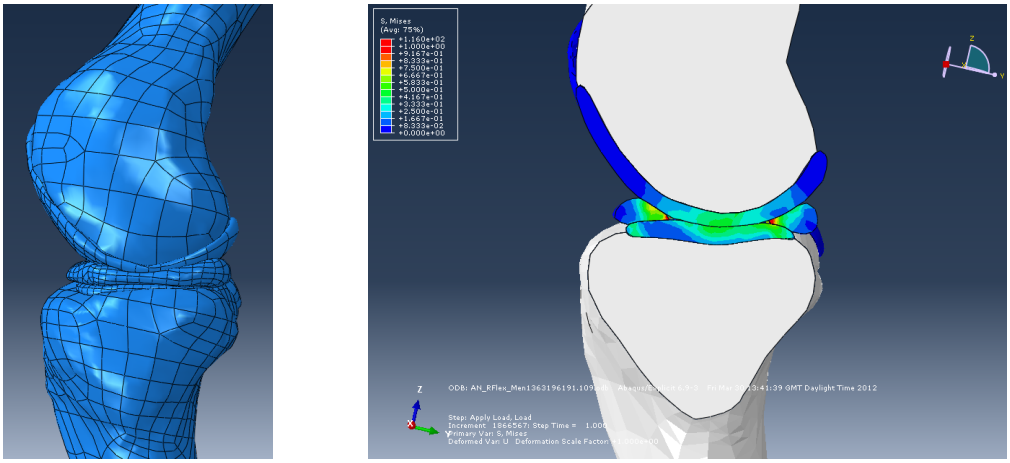
Models were originally created without the menisci in an effort to reduce model complexity. Once models began routinely solving, the menisci were included to make the models more representative of the physiological knee.

Including menisci initially increased the number of distorted elements and reduced

model solution speed. The first issue (distorted elements) was mandatory to address as distorted elements automatically caused model solution to stop. The second issue did not prohibit model solution but sometimes resulted in models requiring weeks to solve. Both issues were associated with small elements in the mesh (see Section 2.3.1.2 for details on how mesh size affects distorted elements and solution speed) and were alleviated by removing these smallest elements.

To remove the small elements, the mesh was queried to identify elements resulting in characteristic time increments less than a user-defined lower limit (smaller elements result in smaller time increments). These smaller elements were then combined with neighbouring elements to create typical-sized elements.

Once the smallest elements were identified and removed, FE models with subject-specific geometry of the femur, tibia, cartilage, and menisci and subject- and task-specific applied loads were able to be solved in both extension and flexion. An example of full model geometry and calculated von Mises stresses is shown in Figure 5.8.



(a) (b)

Figure 5.8: Full subject-specific FE model: Sagittal view of (a) model geometry and (b) calculated von Mises stresses (threshold 0 - 1.0 MPa) (anterior at left).

5.3 Conclusions

This chapter described the steps involved in creating FE models. The steps were then implemented to create preliminary FE models of the knee. The first models used sphere

and cuboid primitives as well as generic applied loads to model Hertzian contact. These generic geometries were then replaced by subject-specific geometry of the human knee. Subject- and task-specific load cases were then applied to these subject-specific geometries. Through this progression of increasingly complex and physiologically representative models, some of the common difficulties associated with modelling contact were encountered. Methods of overcoming these difficulties were found, and subject- and task-specific models of the knee in both extension and flexion were then solved.

The steps and methods described in this chapter are next used to create FE models of porcine knee specimens in a validation study.

Chapter 6

Validating the FE Model Creation Method

For results from a FE model to be meaningful, the accuracy of the results should be validated. Previous researchers [58] have inserted pressure film into cadaver joints and recorded the pressures experienced in the joint during loading. FE models of the experimental set-up were then created and solved for pressure data, and the experimentally-measured and calculated FE pressures were compared.

This chapter describes a validation study conducted on porcine knee specimens. The study comprised two parts: a *preliminary study* which determined the number of preconditioning load cycles necessary to avoid hysteresis effects and a *main study* which involved collecting data from pressure film and comparing these measured values to pressures calculated by FE models.

Both studies were conducted on porcine knees loaded in compression in full extension. In the preliminary study, one porcine specimen was cyclically loaded to 100 N while the axial displacement of the femur was recorded (data capture rate: 100 Hz; Zwick/Roell Z005, Zwick Testing Machines Ltd., Leominster, UK). This displacement data was then used to determine the number of preconditioning loops necessary for each successive load cycle to result in less than 5% change in displacement.

Two porcine knee specimens were used in the main study. For each specimen, pressure film (data capture rate: 100 Hz; K-Scan System Model 4201, Tekscan, Inc., South Boston, Massachusetts, USA) was inserted into both tibiofemoral compartments and three known

compressive loads (100 N, 200 N, and 300 N) were applied (Zwick/Roell Z005) to the femur. Following load testing, the relative positions of the femur and tibia were fixed, and the specimens were imaged using a 3T MRI scanner (MobiView Philips Medical Systems/Achieva, Best, The Netherlands). The geometry from the MRI scan was then combined with the known load data to create subject-specific FE models (Abaqus 6.11). FE models were created using a number of user-defined inputs (for example, boundary conditions and contact conditions). In the main study, multiple FE models with variations of inputs were created for each specimen and load condition. These models were then solved for the displacement of the femur and the contact pressure on the articulating surface of the tibial cartilage. The following calculated results from each model were then compared to each other as well as to the experimental data:

- *Experiment:* Axial displacement of femur (Zwick crossbeam).
  FE Model: Axial displacement of femur.
- *Experiment:* Maximum pressure on film.
  FE Model: Maximum pressure on matched articulating tibial cartilage nodes.
- *Experiment:* Average pressure on film.
  FE Model: Average pressure on matched articulating tibial cartilage nodes.
- *Experiment:* Pressure pattern on film.
  FE Model: Pressure pattern on articulating tibial cartilage surface.

6.1 Preliminary study

Before collecting the validation study data, each pressure film sensor was first equilibrated. Equilibration is important because the initial measurement sensitivity of each sensel (the pressure-sensing element within the pressure film, sensel size: 1.9 mm x 1.9 mm, film thickness: 0.2 mm) is not identical. If a uniform pressure were applied to an un-equilibrated pressure film, some sensels would measure slightly higher pressures and some sensels would measure slightly lower pressures. Therefore, the pressure films needed to be equilibrated so that, under a uniform pressure, all sensels would measure the same pressure.

Equilibration was conducted in accordance with Tekscan manufacturer guidelines. A load of 350 N was distributed uniformly over the surface of the pressure film so that each sensel experienced the same pressure. The difference between the measured and

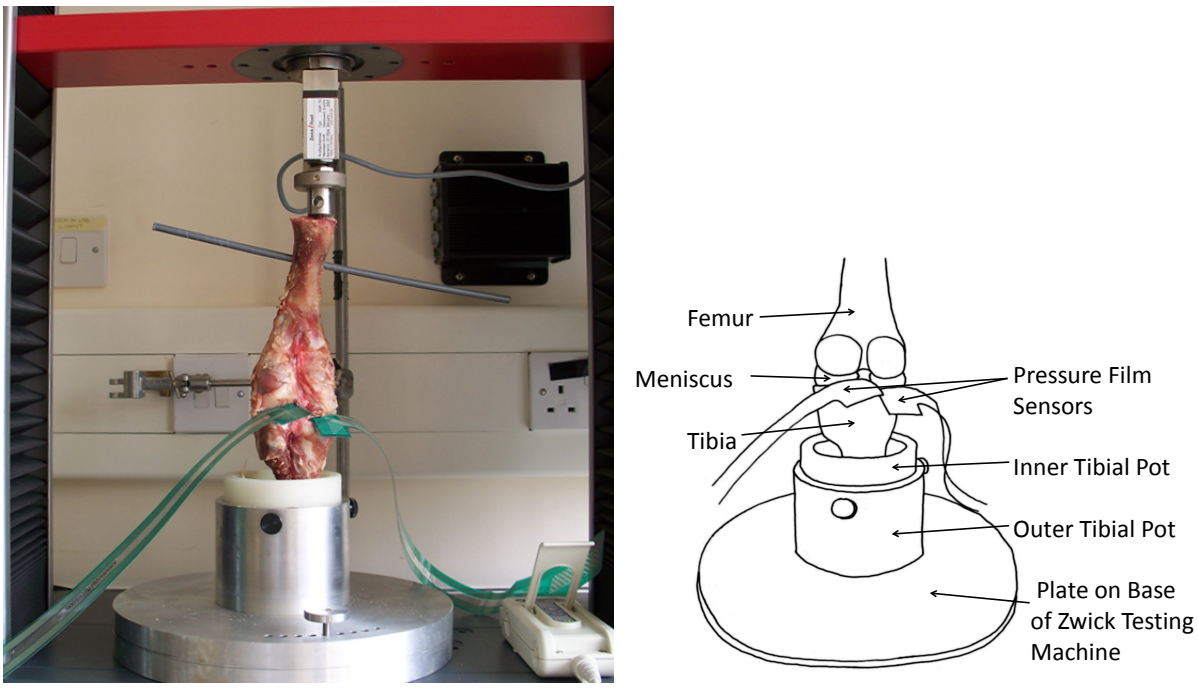
expected uniform pressures was then used to adjust the sensitivity of each sensel. A load of 350 N was selected because it represented a load slightly larger than the maximum load which would be applied in the experiment.

Next, each pressure film was calibrated, again in accordance with Tekscan manufacturer guidelines. Calibration involved applying uniformly distributed loads to the pressure films, measuring the raw output from the sensels, and then using this data and the known applied load to calculate two constants in an exponential power law equation ($Y = Ax^b$ where Y is the known applied load, x is the raw sensel output, and A and b are constants). Two loads (100 N and 240 N) were applied to create two-point exponential power law equations. A separate equation was created for each pressure film.

After equilibration and calibration, a preliminary study was conducted to determine the number of preconditioning load cycles necessary to avoid hysteresis. A porcine knee specimen was obtained from a local butcher on the day of delivery from the abattoir and was kept frozen at -20°C until testing. The knee was then put in a refrigerator at 4°C 36 hours prior to testing and allowed to thaw. After thawing, the femur and tibia were cut to approximately 15 cm above and below the tibiofemoral joint line [89, 101]. The patella and excess muscle tissue obstructing the posterior border between the menisci and tibial cartilage were then also removed. Ligaments and tendons were left intact to maintain the physiological stability of the knee.

After preparing the specimen, the distal end of the tibia was placed in a nylon inner tibial pot (Figure 6.1). Bone cement was poured into the inner tibial pot and allowed to harden. Next, the inner tibial pot was secured inside a metallic outer tibial pot (a removable non-metallic inner pot was necessary for later MRI testing), and the validation rig was then placed within the testing machine (Zwick/Roell Z005) with the knee positioned in the maximum extension achievable in the porcine specimen.

The femur was then axially loaded in 30 continuous, force-controlled cycles. In each cycle, the applied force was ramped from 0 N to 100 N and then back to 0 N at a rate of 10 mm/min [147]. The load was applied to the proximal end of the femur without a rigid connection between the femur and testing machine. This loading method allowed the femur some natural physiological rotation. The vertical location (and therefore ax-



(a) (b)

Figure 6.1: Posterior view of rig used during validation study as (a) figure and (b) diagram.

ial displacement) of the proximal end of the femur was recorded throughout the load cycles (Figure 6.2).

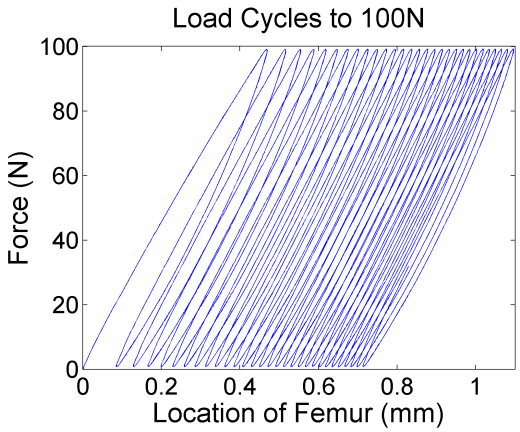


Figure 6.2: Displacement of femur during 30 preconditioning load cycles.

After data collection was completed, the location of the proximal femur at the beginning of each load cycle was determined. Next, the differences in proximal femur location (displacement) were calculated for each set of consecutive load cycles. The first load cycle resulting in less than 5% change in femoral displacement was then identified.

The results of the preliminary study showed that 14 continuous preconditioning load

cycles were necessary for less than 5% change in displacement between consecutive load cycles (Figure 6.3).

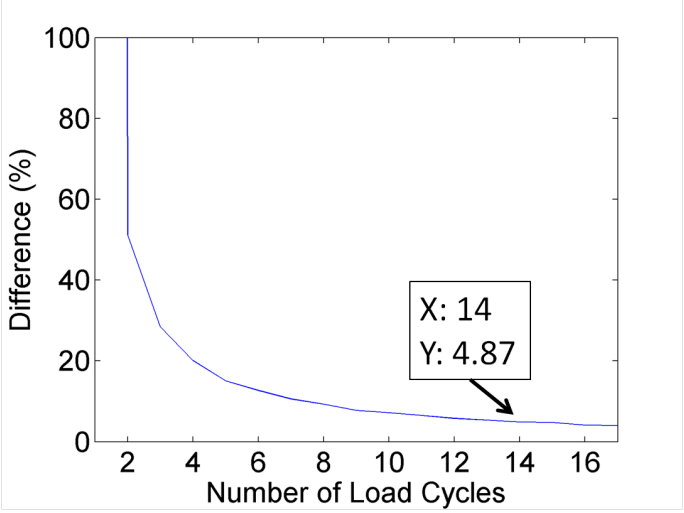


Figure 6.3: Per cent change in displacement between consecutive load cycles.

6.2 Main study

6.2.1 Methods

6.2.1.1 Collecting the experimental data

The main study was conducted on two porcine knee specimens (hereafter referred to as Pig 1 and Pig 2). The specimens were obtained and prepared as in the preliminary study. In the main study a medial-lateral hole was also drilled through the proximal femur before potting the tibia; this hole was later used to lock the relative position of the femur and tibia.

After positioning the validation rig and specimen within the testing machine, pressure film was inserted posteriorly [64, 89, 101] below each meniscus [89]. (Pressure film was inserted posteriorly because an anterior insertion required removing a larger amount of soft tissue. Also, pressure film was positioned beneath the menisci because there was less error associated with fitting the flat pressure film to the relatively flat tibial plateaux than to the relatively curved femoral condyles.) A slight (less than 5 N) preload was applied to the proximal femur to hold the specimen in place. This preload force was then

zeroed before testing continued (so a force reported as 100 N was actually 100 N plus the preload).

The knee was then preconditioned to the first load condition: 100 N. In accordance with the results of the preliminary study (see Section 6.1), 14 preconditioning loops with ramped force from 0 N to 100 N at a rate of 10 mm/min were first applied. Then eight individual load cycles to 100 N were conducted. In each load cycle, both force-displacement data from the Zwick and pressure data from the pressure film were collected. Data could only be collected from one pressure film (and therefore one tibiofemoral compartment) at a time because of limitations with the number of available channels in the pressure sensor system. Therefore, medial compartment pressure data was collected in the first four cycles and lateral compartment data was collected in the second four cycles. (Data from a fifth medial compartment load cycle was collected after all lateral load cycles were completed, and no difference was found between the first four and the fifth medial load cycle so the order of compartment testing did not affect results.) After all 100 N load cycles were complete, the specimen was sprayed with water to avoid drying out.

Three preconditioning cycles were then conducted with a ramped force from 0 N to 200 N, again at a rate of 10 mm/min. (These additional preconditioning cycles allowed the specimen to settle into a new position given the new, higher load.) Eight load cycles were then conducted at 200 N. Again, force-displacement data and pressure data were collected for each cycle. Lateral compartment pressure film data was collected for the first four cycles; medial compartment data was collected for the second four cycles. The specimen was again sprayed with water after all 200 N load cycles were complete.

The specimen was then preconditioned with three cycles ramped from 0 N to 300 N at a rate of 10 mm/min. Eight load cycles to 300 N were conducted. Medial compartment pressure film data was collected for the first four cycles; lateral compartment data was collected for the second four cycles. The specimens were sprayed with water following load testing.

Next, the relative position of the pressure film within each tibiofemoral compartment was recorded. Eight locations on the tibial plateaux were used to later map the locations of the two pressure films to the FE model mesh. Four locations (one anterior and three

posterior) were selected on the medial tibial plateau, and four locations (all posterior) were selected on the lateral tibial plateau. A fluid-filled marker was placed at each location. Pressure was then applied to the pressure film sensors at each of these individual marker locations. The pressure film did not directly contact some of the posterior markers due to the slope of the posterior tibial plateaux (the pressure film is relatively flat and therefore was located above the posterior markers on the slope); in these cases, the pressure film was carefully flexed down to the marker and then pressure was applied at the marker location.

After completing all load testing, the relative position of the femur and tibia was locked (Figure 6.4) so that the orientation of the knee during the experimental load testing would be replicated in the MRI scan. To lock the relative position, a non-metallic rod was inserted through a medial-lateral hole drilled through the proximal femur. Wooden supports were then slid onto either end of the rod and attached to the inner, non-metallic tibial pot. This fixation rig was assembled while the specimen was still loaded with the slight preload applied during testing.

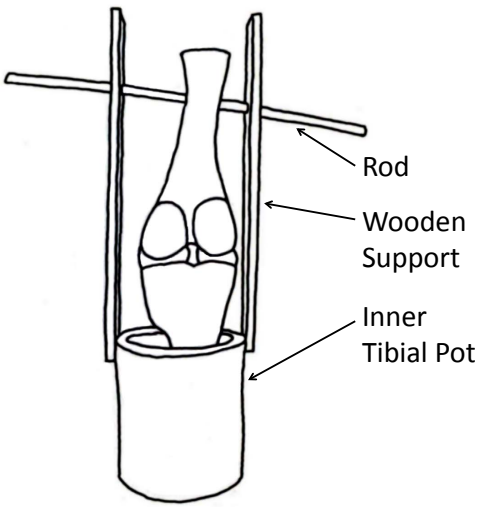


Figure 6.4: Posterior view of rig with relative positions of femur and tibia locked.

The preload was then removed from the femur, the pressure films removed from the tibiofemoral compartments, and the specimen placed in a plastic bag and taken to the MRI scanner (MobiView Philips Medical Systems/Achieva, Best, The Netherlands). Each specimen was scanned (T1-weighted sagittal view, slice interval 2 mm, slice thickness 0.05 mm)

in its locked full knee extension position. Care was taken to ensure both that the fluid-filled markers did not move between load testing and MRI scanning and that the markers were visible in the MRI scans. Following MRI scanning, the specimens were returned to the -20°C freezer in case further information about them was required.

6.2.1.2 Modelling the experiment using FE models

FE models were created which reflected the experimental set-up of the validation study. Model geometry was derived from the MRI scans using the procedure described in Chapter 3. In brief, the femur, tibia, femoral cartilage, tibial cartilage, and meniscal surfaces were segmented from the MRI image data (Mimics 13.0) and exported as solid geometries (Geomagic Studio 11; SolidWorks 2010). An assembly of the knee was then created from the individual structures (SolidWorks). Within this assembly, a 0.5 mm overlap was created between the following sets of surfaces: distal femur and proximal femoral cartilage, distal femoral cartilage and proximal menisci, distal menisci and proximal tibial cartilage, and distal tibial cartilage and proximal tibia. Slight initial overlap between surfaces was found to aid in FE model solution.

These geometries were used to create the FE models (Abaqus 6.11). Eight types of FE models (Figure 6.5) were created for each specimen and load condition. Since 2 specimens were tested, each with 3 load conditions, a total of 48 models were created for this validation study. The following inputs were identical in all porcine FE models. The bones were modelled as rigid, cartilage as linear elastic isotropic (E = 3.4 MPa, ν = 0.45) [125], and menisci as linear elastic transversely isotropic (circumferential: E = 120 MPa, ν = 0.2; axial/radial: E = 20 MPa, ν = 0.3) (material properties for porcine menisci could not be found so human material properties [159] were used). These assigned material types (rigid, linear elastic isotropic, and linear elastic transversely isotropic) were consistent with the material types assigned to human structures in the literature (see Section 2.3.2.2). Loads of 100 N, 200 N, and 300 N were applied to the proximal femur. The tibia was fully constrained. Bone-cartilage interactions were tied; frictional contact (μ = 0.02) [93, 94] was assigned to cartilage-cartilage and cartilage-menisci interactions. Identical meshes (linear tetrahedral C3D4 elements) were used in all models of the same specimen (one mesh was

used for all Pig 1 models; a separate mesh was used for all Pig 2 models). Models were solved using an augmented Lagrangian algorithm.

Half the models were solved as Standard FE models; the other half were Explicit FE models (Figure 6.5). Explicit models are generally considered to be better at solving complex contact conditions but do not make the regular convergence checks used in the Standard FE models. Therefore, models of both types were created and solved to see if similar results were calculated.

Within each of these model types, the femur was allowed one of two boundary conditions. In the first condition (referred to as 'Axial'), the femur was only allowed axial translation; in the second condition (referred to as 'Rotate'), the femur was allowed axial translation as well as varus-valgus rotation. In the experimental set-up, femoral varus-valgus rotation was not restricted by the rig; therefore, FE models with both sets of boundary conditions were created to investigate the effects of allowing or restricting femoral varus-valgus rotation.

For each of these combinations, models were also created which either allowed separation (referred to as 'Sep') or did not allow separation (referred to as 'No Sep') between in-contact cartilage-cartilage or cartilage-meniscal surfaces. Prohibiting separation typically simplifies model solution because chattering (see Section 2.3.1.2 for description) is eliminated. Experimentally, however, separation between the soft tissue surfaces was possible. Therefore, models were run with both contact conditions to determine whether this simplification could still accurately reflect the physiological behaviour of the knee.

6.2.1.3 Comparing the experimental and calculated results

Once all FE models had been created, the models which solved were compared to the experimental results measured at the instant of maximum compressive load. The experimental results were obtained from the load cycle selected as most representative (see Section 4.1.5) of the four cycles measured for each load case and tibiofemoral compartment. Comparisons were made for the axial displacement of the femur as well as the maximum pressure, average pressure, and pressure distributions on the articulating tibial cartilage surfaces.

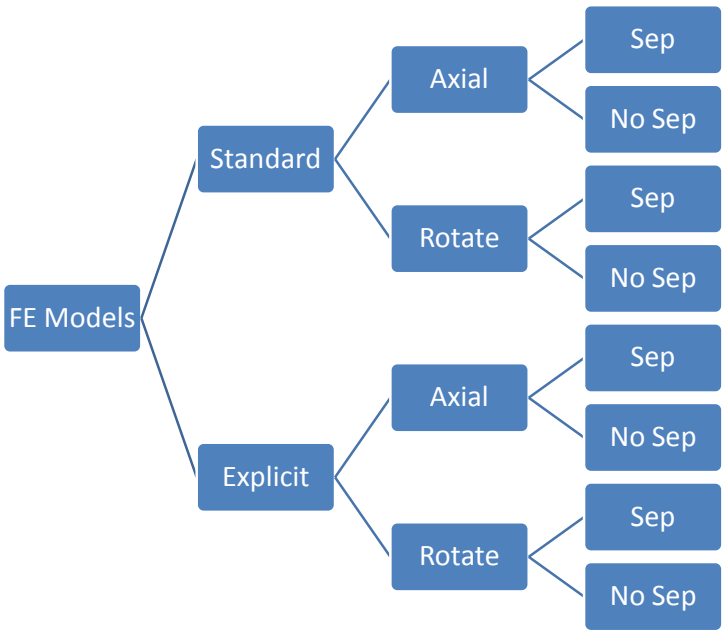


Figure 6.5: FE model types created for main validation study.

Axial displacements of femur For the femoral displacement results, the experimental displacement was calculated as the difference in the vertical position of the Zwick crossbeam at 0 N and at the final applied load (100 N, 200 N, or 300 N).

The calculated model femoral displacement was set as the axial displacement of the node closest to the location of experimental load application.

Maximum pressures The pressure on each pressure film sensel (the individual sensing elements on the pressure film) was recorded during the experiment. The maximum pressure measured by a sensel in the instant of maximum load application (100 N, 200 N, or 300 N) was designated as the maximum pressure on the film.

Determining the maximum calculated pressure required first mapping the pressure film sensels to the FE model mesh. (The pressure film did not cover the entire tibial cartilage surface, making it possible that the maximum pressure calculated on the tibial cartilage was outside the pressure film measurement area.) Mapping was accomplished by first determining the fluid-filled marker locations on the MRI scans (and therefore also on the FE model) and on the pressure films. The transformation matrix between these two sets of marker locations was then calculated (Matlab computer code based on [66]),

and the location of each pressure film sensel was transformed into the FE model mesh coordinate system. Only locations of sensels which recorded pressures were transformed. The transformed location of each sensel was then matched (purpose-specific Matlab code) to the nearest node on the articulating tibial cartilage surface. Once the matched mesh nodes were found, the pressures at each of these nodes was determined. The maximum pressure of these matched nodes was determined to be the maximum calculated pressure.

Average pressures The experimental average pressure was calculated as the average of all sensels which recorded a pressure at the instant of maximum load application (100 N, 200 N, or 300 N).

The calculated average pressure of the FE models was calculated from the pressures on the mesh nodes matched to the mapped pressure film sensels. Only pressures which were positive (not negative or zero) were included when calculating the average pressure.

Pressure patterns This comparison was a visual, qualitative comparison. The experimental pressure pattern was based on the pressures recorded by the pressure film.

The calculated pressure pattern was based on the contact pressures calculated by the FE models.

6.2.2 Results

Results are shown separately for the two porcine specimens. The results for Pig 1 are provided first; the results for Pig 2 are provided second. Unless stated otherwise, all results have been measured or calculated on the articulating surface of the tibial cartilage. In the result tables 'L' denotes the 'lateral' tibial compartment, 'M' denotes the 'medial' tibial compartment, and '*' indicates an FE model which did not solve. Concentrated higher pressures at individual nodes were calculated in some FE models; in these models, result calculations were made both including and excluding these concentrated higher pressures. Results excluding concentrated pressures are given in parentheses.

6.2.2.1 Axial displacements of femur

The femoral displacement results for Pig 1 and Pig 2 are provided in Table 6.1 and Table 6.2, respectively. In general, allowing rotation and allowing separation resulted in larger femoral displacement. Standard models generally underestimated displacement while Explicit models more commonly overestimated displacement. Overestimations were especially prevalent in Explicit-Rotate models (Standard-Rotate models typically did not solve).

Table 6.1: Pig 1: Experimental and calculated displacements of femur (unit = mm; * = FE model which did not solve).

		Standard-Axial		Standard-Rotate		Explicit-Axial		Explicit-Rotate	
	Experiment	Sep	No Sep	Sep	No Sep	Sep	No Sep	Sep	No Sep
100 N	0.40	0.27	0.33	*	*	0.54	0.43	*	0.72
200 N	0.65	0.67	0.60	*	*	0.90	0.74	*	1.09
300 N	0.86	0.92	*	*	*	1.20	1.04	*	1.66

Table 6.2: Pig 2: Experimental and calculated displacements of femur (unit = mm; * = FE model which did not solve).

		Standard-Axial		Standard-Rotate		Explicit-Axial		Explicit-Rotate	
	Experiment	Sep	No Sep	Sep	No Sep	Sep	No Sep	Sep	No Sep
100 N	0.40	0.33	0.32	0.37	0.35	0.49	0.44	0.52	0.46
200 N	0.73	*	0.64	*	*	0.86	0.77	*	0.80
300 N	1.22	*	0.94	*	*	1.20	1.04	*	1.10

6.2.2.2 Maximum pressures

Experimental and calculated maximum pressures for Pig 1 and Pig 2 are provided in Table 6.3 and Table 6.4, respectively.

Typically, calculated maximum pressures were larger than the experimentally-measured maximum pressures. This trend was particularly evident when larger loads were applied. Occasionally, concentrated higher pressures were calculated at a small number of nodes.

Experimentally, maximum pressures for Pig 1 were larger (approximately double) in the medial compartment than in the lateral compartment. Conversely, Axial FE models

calculated higher maximum pressures in the lateral compartment. When separation was restricted, this ratio was approximately double; when separation was allowed, lateral pressure was between two and four times higher than medial pressure. Only the Rotate FE models calculated higher medial pressures than lateral pressures, and only one type of Rotate model (Explicit-Rotate-No Sep) solved.

Experimentally, maximum pressures for Pig 2 were approximately the same in the medial and lateral compartments. The calculated pressures were also generally similar in the two compartments, especially for the Explicit-Axial models. Allowing separation tended to lead to higher pressure magnitudes but also decreased the incidence of calculated pressure concentrations. As in Pig 1, allowing rotation led to higher medial than lateral maximum pressures - as well as models which only occasionally solved for applied loads larger than 100 N.

Table 6.3: Pig 1: Experimental and calculated maximum pressures (unit = kPa; L. = lateral; M. = medial; * = FE model which did not solve).

			Standard-Axial		Standard-Rotate		Explicit-Axial		Explicit-Rotate	
		Experiment	Sep	No Sep	Sep	No Sep	Sep	No Sep	Sep	No Sep
100 N	L.	245	1180	657	*	*	597	406	*	147
	M.	441	373	319	*	*	700 (174)	271	*	556
200 N	L.	283	1180	1100	*	*	677	894	*	328
	M.	519	621	634	*	*	140	4020 (441)	*	9430 (956)
300 N	L.	325	2828	*	*	*	1520	1290	*	452
	M.	615	944	*	*	*	682	1550 (707)	*	9900 (1370)

Table 6.4: Pig 2: Experimental and calculated maximum pressures (unit = kPa; L. = lateral; M. = medial; * = FE model which did not solve).

			Standard-Axial		Standard-Rotate		Explicit-Axial		Explicit-Rotate	
		Experiment	Sep	No Sep	Sep	No Sep	Sep	No Sep	Sep	No Sep
100 N	L.	349	928 (552)	416	225	206	374	264	166	183
	M.	334	282	311	305	315	301	318	339	310
200 N	L.	417	*	595	*	*	840	1560 (576)	*	262
	M.	405	*	1730 (748)	*	*	928	881	*	1030
300 N	L.	417	*	1380 (811)	*	*	1180	3040 (914)	*	488
	M.	437	*	2050 (1070)	*	*	1320	1350 (999)	*	3560 (1120)

6.2.2.3 Average pressures

Experimental and calculated average pressures for Pig 1 and Pig 2 are provided in Table 6.5 and Table 6.6, respectively.

In Pig 1, the experimental average pressure was (consistent with the maximum pressure results) higher in the medial compartment than in the lateral compartment. The medial pressure was generally less than 1.5 times higher than the lateral compartment pressure. The Axial FE models continued to calculate higher lateral compartment average pressures, however. Of the Axial models, the Standard-Sep model matched the experimental medial compartment pressures best (but then overestimated the lateral compartment pressures); all Axial models overestimated medial pressures. The Rotate FE models again matched the experimental data in that higher medial than lateral compartment pressures were calculated; the calculated ratios between the pressures in the two compartments were larger than (approximately double) the experimental ratios, however.

In Pig 2, the experimental medial and lateral compartment pressures were again similar. In general, all FE models underestimated average pressures at lower applied loads (100 N) and overestimated average pressures at higher loads (300 N). Closer average pressure compartment ratio matches were found in the Explicit-Axial models than in the Standard-Axial models. The Rotate models again had relatively higher medial pressures.

Table 6.5: Pig 1: Experimental and calculated average pressures (unit = kPa; L. = lateral; M. = medial; * = FE model which did not solve).

			Standard-Axial		Standard-Rotate		Explicit-Axial		Explicit-Rotate	
		Experiment	Sep	No Sep	Sep	No Sep	Sep	No Sep	Sep	No Sep
100 N	L.	218	775	359	*	*	335	264	*	90
	M.	250	247	133	*	*	156 (79)	129	*	224
200 N	L.	237	828	747	*	*	334	491	*	239
	M.	305	275	257	*	*	51	530 (281)	*	1128 (420)
300 N	L.	261	1359	*	*	*	870	818	*	361
	M.	357	312	*	*	*	268	418 (379)	*	1350 (799)

Table 6.6: Pig 2: Experimental and calculated average pressures (unit = kPa; L. = lateral; M. = medial; * = FE model which did not solve).

			Standard-Axial		Standard-Rotate		Explicit-Axial		Explicit-Rotate	
		Experiment	Sep	No Sep	Sep	No Sep	Sep	No Sep	Sep	No Sep
100 N	L.	237	239 (182)	148	101	99	113	97	67	83
	M.	253	130	149	146	188	137	152	172	193
200 N	L.	266	*	234	*	*	283	335 (273)	*	151
	M.	257	*	530 (368)	*	*	337	374	*	446
300 N	L.	279	*	481 (415)	*	*	538	512 (418)	*	217
	M.	277	*	752 (453)	*	*	544	556 (512)	*	907 (697)

6.2.2.4 Pressure patterns

Due to space constraints, only the pressure patterns for the largest applied load (300 N) are provided. This load most closely matched the load magnitudes applied to the later human FE models; therefore, it was important to determine whether the calculated pressure patterns due to these magnitudes of loads matched experimental pressure patterns.

Figure 6.6 and Figure 6.7 show the (top) experimental and (centre, bottom) calculated contact pressures on the articulating tibial cartilage surfaces of Pig 1 and Pig 2, respectively. (Note: results only shown for models which solved.) The lateral compartment is always on the left for Pig 1 and always on the right in Pig 2. Experimental pressures are all shown with a maximum threshold of 750 kPa; calculated pressures were typically higher than the experimental pressures, however, so have all been shown with a maximum threshold of 1500 kPa. The pressure film measurement area for each compartment lies between the sets of parallel thick white lines; experimental pressure patterns have been sketched (also in white) onto the calculated pressure distributions to allow for easier comparison of results.

The pressure patterns for the Axial models were typically similar, regardless of whether the Standard or Explicit solution method was used. Axial models also tended to more closely match experimental pressure patterns. In Pig 1, higher pressure magnitudes were found in the lateral compartment while higher experimental pressures were in the medial compartment. In Pig 2, measured and calculated pressure magnitudes were approximately equal in the medial and lateral compartments.

The pressure patterns in the Rotate models were qualitatively different from the pres-

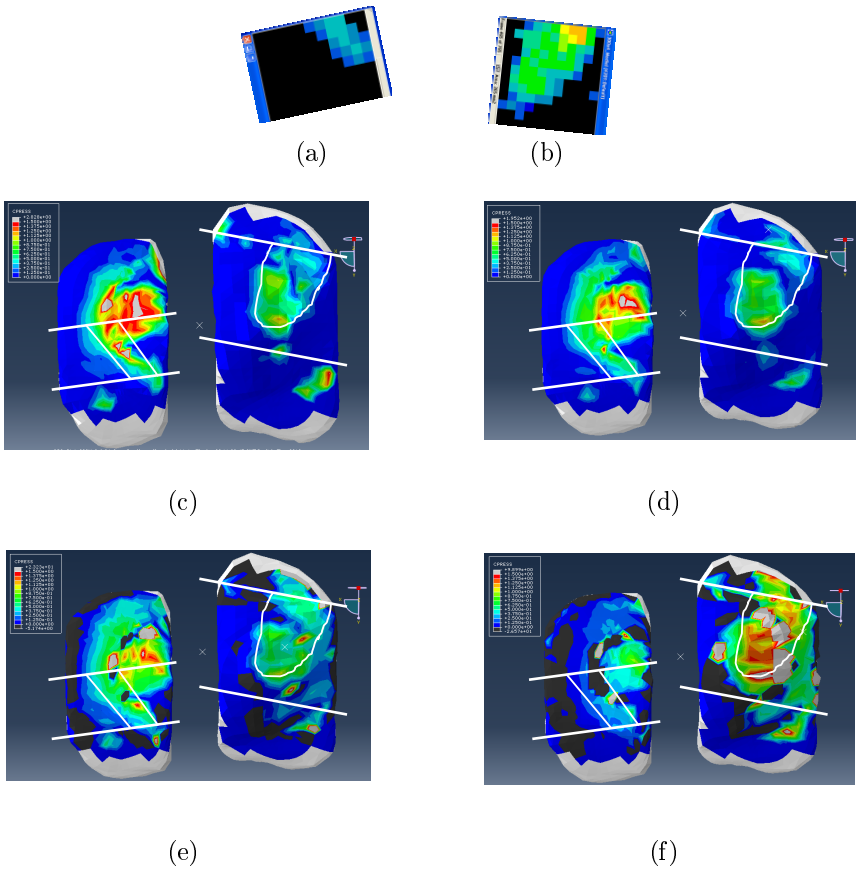


Figure 6.6: Pig 1: Experimental and calculated pressure patterns for 300 N load: (top) Experimental pressure patterns (thresholds 0 - 750 kPa) for (a) lateral and (b) medial tibial cartilage surfaces; (centre, bottom) calculated contact pressure patterns (thresholds 0 - 1500 kPa) in solved FE models of (c) Standard-Axial-Sep; (d) Explicit-Axial-Sep; (e) Explicit-Axial-No Sep; and (f) Explicit-Rotate-No Sep. Pressure film measurement areas are between the parallel white lines; experimentally-measured pressure patterns have been sketched (also in white) onto the calculated FE model pressure patterns for easier comparison of results.

sure patterns in the Axial models. For Pig 1, allowing femoral varus-valgus rotation led to higher medial compartment pressures; concentrated higher pressures are visible as silver-grey regions along the edge of femoral cartilage-tibial cartilage contact. In Pig 2, allowing rotation led to somewhat less significant changes in the medial compartment pressure - but decreased pressures in the lateral compartment.

Another aspect of the pressure results which should be mentioned can be seen when comparing Sep and No Sep model pressures. No Sep models generally had negative/tensile pressures (shown in black in Figures 6.6 and 6.7) along the edges of contact. These tensile pressures indicated regions in which two surfaces were initially in contact but would have later separated if contact definitions had allowed. The overall patterns of Sep and No Sep models were generally similar in the centre of contact regions. Higher pressure magnitudes

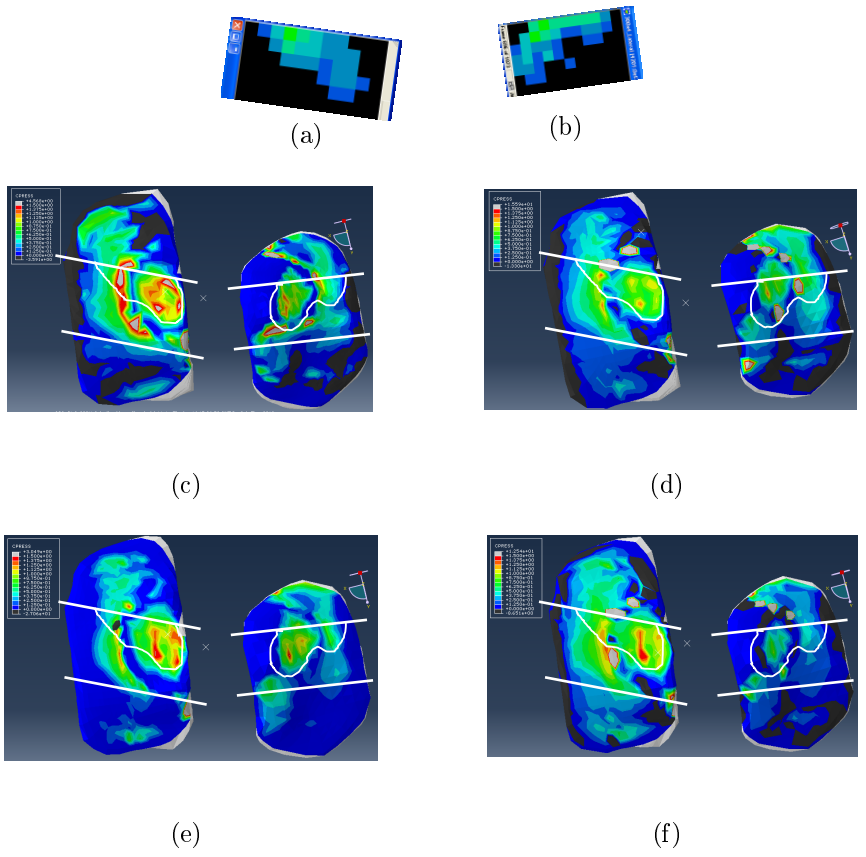


Figure 6.7: Pig 2: Experimental and calculated pressure patterns for 300 N load: (top) Experimental pressure patterns (thresholds 0 - 750 kPa) for (a) medial and (b) lateral tibial cartilage surfaces; (centre, bottom) calculated contact pressure patterns (thresholds 0 - 1500 kPa) in solved FE models of (c) Standard-Axial-No Sep; (d) Explicit-Axial-No Sep; (e) Explicit-Axial-Sep; and (f) Explicit-Rotate-No Sep. Pressure film measurement areas are between the parallel white lines; experimentally-measured pressure patterns have been sketched (also in white) onto the calculated FE model pressure patterns for easier comparison of results.

were occasionally calculated in the Sep models, however, because allowing separation resulted in smaller contact areas.

6.2.3 Discussion

This discussion section has been divided into two parts. Potential reasons that some FE models did not solve are discussed first; then the experimental and calculated results are compared and the most representative FE model type determined.

6.2.3.1 Potential reasons that some FE models did not solve

Modelling contact is considered one of the most difficult tasks done within FE analysis. Common reasons models fail to solve were presented in Section 2.3.1.2. This section

applies some of the already-discussed difficulties to the models in the validation study in particular.

Modelling contact between surfaces is often difficult, even in models with only two relatively simple, idealized geometries in contact. The knee presents a particular challenge, however. The geometry of the knee includes irregular surfaces, and the smaller geometrical details have been included in these subject-specific models. The knee also includes multiple contact pairs (cartilage-cartilage and cartilage-menisci contact pairs), and each of these contact pairs exist in two compartments (the medial and lateral tibiofemoral compartments).

The large number of contacting surfaces makes it difficult in particular for the Standard FE models to solve. Standard models make regular convergence checks for each set of contacting surfaces; if the applied loads and calculated displacements in any of the surface pairs cannot be balanced in the equation $F = kx$, then the entire FE model fails to solve. This convergence difficulty likely explains why the Standard models solved less frequently than the Explicit models (which do not make regular convergence checks). Also, larger applied forces result in additional deformation and larger contact areas, and larger contact areas lead to more elements being included in the Standard model convergence checks, which might explain why some Standard model types solved for the 100 N load case but failed for the 200 N and 300 N load cases.

Some Standard models did solve, however, as long as sufficient boundary constraints were applied. For example, the Standard-Axial models solved more frequently than the Standard-Rotate models. By only allowing axial translation of the femur, rigid body motion in the other planes was not possible and therefore did not hinder convergence.

Contact constraints (Sep or No Sep) were also found to affect Standard model convergence success. The No Sep models solved more frequently, likely because by not allowing elements previously in contact to separate, chattering in these models was avoided. Decreasing chattering leads to improved convergence rates.

The Explicit models, without their convergence checks, were able to solve for all model types except Explicit-Rotate-Sep. When separation between the cartilage and menisci structures was allowed, rigid body motion caused the models to fail. The cause of failure

can be investigated by considering the behaviour of the model at the instant before failure (Figure 6.8). The figure shows that the femur and femoral cartilage rotated towards the medial compartment, resulting in liftoff (separation between the femoral and tibial structures) in the lateral compartment. The femur, femoral cartilage, and medial meniscus then rotated to the outer edge of the medial tibial cartilage before separating from the tibia and tibial cartilage completely. Including ligaments in the Explicit-Rotate-Sep FE models may have prevented the rigid body motion while still allowing separation between the soft tissue surfaces; therefore, future studies could investigate the effect of including ligaments within the FE models.

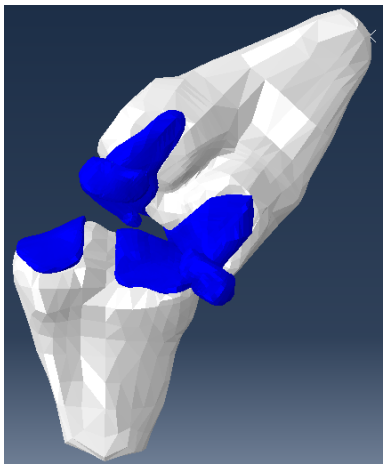


Figure 6.8: Explicit-Rotate-Sep failure mechanism: Lateral liftoff, excessive slide to edge of medial compartment, complete separation of (top bone) femur and (bottom bone) tibia.

6.2.3.2 Selecting representative FE model types

Representative FE models were selected from the FE model types which frequently solved. Separate representative FE model types were first selected for Pig 1 and Pig 2 because different user-defined inputs may have been necessary to model the two porcine specimens. The load applied to Pig 1 in the experiment was applied at a location medial to the central proximal femur (Figure 6.1a), resulting in a varus alignment of the femur and consequently higher pressures in the medial compartment than in the lateral compartment. (A more medial load application location was used in Pig 1 because this specimen both rotated and flexed during load application when the load was applied to a more central location on the proximal femur. The FE models in this project modelled quasi-static activities, however,

so the load was applied to a medial location in Pig 1 to avoid dynamic motion.) The load applied to Pig 2 in the experiment was applied to the central proximal femur, resulting in approximately equal medial and lateral compartment pressures. After selecting the most representative model type for each specimen, an overall most representative model type was selected.

Representative FE model type for Pig 1 In Pig 1, the Explicit-Rotate-No Sep model best represented the quantitative experimental data. Allowing the femur varus-valgus rotation resulted in higher pressures being calculated in the medial compartment than the lateral compartment - a trend also seen in the experimental data. The Axial models, however, calculated higher lateral compartment pressure and therefore did not reflect the experimental data as well. A disadvantage of the Explicit-Rotate-No Sep model was that it overestimated the displacement of the femur.

This overestimation of displacement could be due to at least two factors. First, the material properties used for the models were not subject-specific. The pigs were slaughtered at a relatively young age (between 3 months and 6 months of age), and skeletal immaturity was evident in the MRI scans. Limited information on the material properties of skeletally immature pigs was available in the literature, however, so it is possible the assigned material properties were not representative of the porcine specimens tested. (As part of this main validation study, additional FE models with cartilage Young's moduli of 4 MPa, 8 MPa, and 12 MPa were solved. Results showed this material property had a significant effect on the calculated femoral displacements and tibial cartilage pressures; stiffer cartilage led to less displacement and therefore higher pressure). The Standard models used the same material properties as the Explicit models, however, and typically underestimated displacement so the extent to which material properties may explain the Explicit models' overestimation of displacement is unknown. Another reason for overestimated displacement may be the absence of ligaments in the FE model. Ligaments were left intact during experimental load testing to maintain the physiological structure of the knee but were not included in the FE models. It is possible that the ligaments in the experimental specimen prevented at least some of the femoral rotation calculated by the FE models.

Qualitatively, the Explicit-Rotate-No Sep model did not reflect the experimental pressure distributions as well as the Axial models. A trend towards lateral compartment liftoff (the lateral meniscus and femoral cartilage lifting from the tibial cartilage) was calculated by the Rotate FE models, but evidence of this trend was not seen experimentally.

Considering both quantitative and qualitative data, it was difficult to select the overall most representative FE model type for Pig 1. If the medial to lateral compartment pressure ratio were not considered, the FE model which most closely matched experimental results was *Explicit-Axial-No Sep*. In addition to having a good match to experimental pressure patterns, this model did not result in large over- or underestimations of femoral displacements, maximum pressures, or average pressures (Standard models typically underestimated displacement and overestimated lateral compartment maximum and average pressures; Explicit-Axial-Sep typically underestimated medial compartment maximum and average pressures).

Representative FE model type for Pig 2 The selection process for Pig 2 was largely by elimination. The Standard-Rotate models frequently did not solve and the Explicit-Rotate models had medial to lateral compartment maximum and average pressure ratios which did not match experimental data. Therefore, only Axial models were further considered as potential representative model types. Of these four options, Standard-Axial-Sep also frequently failed to solve so was eliminated.

The three remaining model types gave similar results. Standard-Axial-No Sep tended to underestimate femoral displacement while Explicit-Axial-Sep generally overestimated displacement. Explicit-Axial-No Sep seemed to be a compromise of the two models. In terms of maximum pressures, Explicit-Axial-Sep did not result in the concentrated higher pressures seen in the two other models; it did, however, calculate slightly higher pressures than the other models (when the pressure concentrations were ignored). Maximum and average medial and lateral pressures were typically similar for all three model types, though Explicit-Axial-Sep matched experimental ratios slightly better.

Considering the quantitative and qualitative data, it was decided that Standard-Axial-No Sep, Explicit-Axial-Sep, or Explicit-Axial-No Sep model types would give reasonable matches to the experimental data but *Explicit-Axial-Sep* was the closest match.

Overall most representative FE model type for both pigs For both pigs, the Explicit-Axial models were selected as most representative of the experimental data. Different separation conditions were selected for the two pigs, however. The No Sep condition was selected for Pig 1; the Sep condition was selected for Pig 2. Since the Sep and No Sep Explicit-Axial models gave similar results for Pig 2, a compromise between the model types selected for the two pigs was made. The overall most representative FE model type for both pigs was chosen to be *Explicit-Axial-No Sep*.

The Explicit-Axial-No Sep model type matched the experimental pressure patterns, avoided the overestimated femoral displacements common in the Rotate models, and solved for the range of loads applied. Some discrepancies between the calculated results for this model and the experimental data are acknowledged, however. The pressures calculated by this model type were - like all FE model types tested - higher than the experimentally-measured pressures. The No Sep condition also led to concentrated higher pressures along the edges of contact. These characteristics were considered when evaluating results calculated by the FE models of the human knee.

6.2.3.3 Limitations

Although this thesis focused on loading within the human knee, it was not possible to test a human cadaver in the validation study so porcine specimens were used instead. There are obvious differences in human and porcine morphology and material properties, so not being able to conduct the study on a human specimen was a limitation. Regardless, the pressure patterns calculated by the FE models and measured by the pressure film were similar so the model creation method was validated and important decisions about the model type (for example, Standard or Explicit, and Separation or No Separation) to use were guided by the porcine work. Ideally, the validation study should be extended to include testing of a human cadaver knee.

6.3 Conclusions

This chapter detailed a validation study conducted using porcine specimens. First, experimentally-measured data was collected for each specimen. Known axial loads (100 N,

200 N, and 300 N) were applied to the femur while pressure film recorded the resulting pressures experienced in the knee. Each specimen was then imaged using a 3T MRI scanner. The acquired geometry was combined with the known axial loads to create specimen-specific FE models which reflected the experimental conditions (applied loads, certain boundary constraints).

Multiple types of FE models were constructed for each specimen and load condition. The models used different combinations of model (Standard versus Explicit), boundary (femoral axial translation versus femoral axial translation plus varus-valgus rotation), and contact definitions (soft tissue separation versus no separation). The displacements and pressures calculated by the various FE model types were then compared to the experimentally-measured data to determine which model type best matched the experimental data.

For model and boundary definitions, the best match between experimental and calculated results for both specimens was the Explicit model which allowed only femoral axial translation. The contact definitions in the most representative model types differed between specimens. In one specimen, not allowing soft tissue separation gave a better match between measured and calculated data; in the other specimen, allowing separation gave a marginally but not significantly better match. Therefore, a compromise between the two most representative FE model types was made, and the overall most representative FE model type for both specimens was chosen to be the *Explicit-Axial-No Sep* model type.

Having chosen this as the best model type to use in the FE models of the human knee, the next step was to conduct a parameter study to investigate whether the FE models could be simplified to decrease the necessary computation time. Then, after making these last decisions about model set-up, mesh convergence tests were conducted.

Chapter 7

Last Stages of FE Model Set-Up

7.1 Introduction

The FE model type to use when modelling the human knee (Explicit-Axial-No Sep) was selected using the results of the validation study. Two steps remained before creating and solving the models of the normal human knee. The first step was a *parameter study*, conducted to determine whether the model geometry could be streamlined to decrease model computation time. The second step was conducting *mesh convergence tests* to ensure that further mesh refinement would not change calculated results.

7.2 Parameter study

7.2.1 Introduction

The FE models solved in Chapters 5 and 6 modelled the femur and tibia as rigid bodies. Although the motion of each bone was determined based on the motion of a single reference point, the model included the geometries of the entire bone. This model set-up required a mesh to also be generated for the geometries of the entire bone. Although coarse meshes were created for the bones (the femur and tibia were not directly involved in cartilage-cartilage or cartilage-menisci contact so a dense mesh was unnecessary), the overall size of the bones was relatively large. Each bone required a mesh of approximately 13,000 to 20,000 elements.

It was hypothesized that models with more elements would require longer solution times; therefore, methods of reducing the numbers of elements in the models were investigated. This parameter study tested whether the rigid femur and/or tibia could be replaced by equivalent systems of model definitions and boundary conditions in order to decrease both the number of elements in the model and the required model solution time.

7.2.2 Methods

Six FE models were solved as part of the parameter study. All models were created based on data from the right knee of the same subject. Three models were of an extended knee; three models were of a flexed knee. Within each of these conditions (knee extension or knee flexion), identical geometry, material properties, boundary conditions, contact conditions, and mesh densities were used for the femoral cartilage, tibial cartilage, and menisci. The model parameters of the femur and tibia, however, varied between models. Within each condition (knee extension or knee flexion), models classified as full models, no-tibia models, and no-femur models were created and solved. The descriptions of each model type follow.

Full models were created first. These models included the entire femur and tibia with both bones modelled as rigid bodies. The rigid tibia was held fixed while loads were applied to the rigid femur's centre of mass.

No-tibia models were created next. These models were created by deleting the tibia geometry from the full models. In the full model, the tibia had been held fixed, and the tibia-tibial cartilage interface had been tied. Therefore, the boundary conditions assigned to the rigid tibia in the full model had also indirectly been applied to the tied bottom surface of the tibial cartilage. In the no-tibia models, the elements representing the tibia were deleted, and the bottom surfaces of the tibial cartilage were held fixed.

No-femur models were also created based on the full models. In these models, the tibia was modelled as a rigid body, but instead of modelling the entire solid femur as a rigid body, only the surface elements directly contacting the femoral cartilage were included in the models. This femur-femoral cartilage interface was modelled as a rigid surface (first the femur was changed from a solid body to a shell without internal elements, and

then femoral elements not contacting the femoral cartilage were deleted from the model). Before removing the non-contacting femoral elements, however, the location of the centre of mass of the entire solid femoral body was recorded. Load cases in no-femur models were applied to this same location to maintain consistency of load application location in all three models.

All models were solved for the following results:

- Displacement patterns on the articulating tibial cartilage surfaces.
- Von Mises stress patterns on the articulating tibial cartilage surfaces.
- Contact pressure patterns on the articulating tibial cartilage surfaces.
- Time required for model solution.

If the pattern results of the full model *matched* those of the no-tibia model and/or the no-femur model, then the model which required the shortest amount of time for model solution should be used in future models.

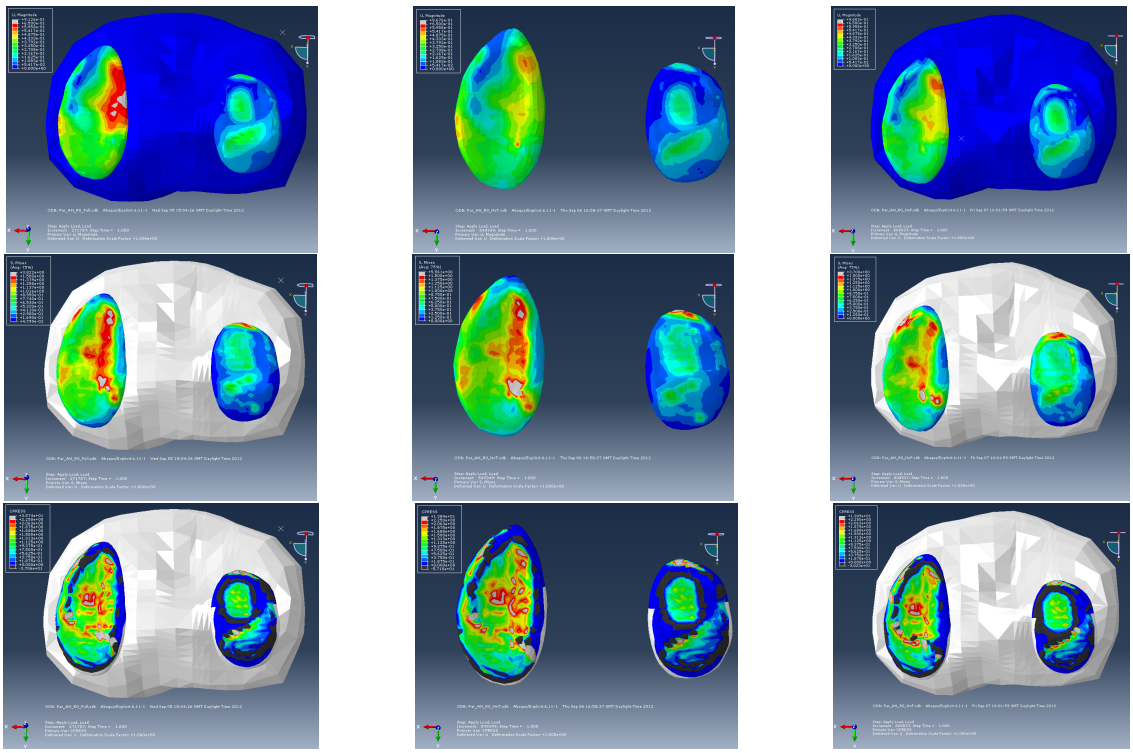
If the pattern results of the full model *differed* from the pattern results of the no-tibia model or the no-femur model, then the full model should be used for the remainder of the FE models in this thesis (the full model most closely represents the anatomical knee).

7.2.3 Results

The calculated displacement, von Mises stress, and contact pressure patterns for the extended and flexed knee models are shown in Figures 7.1 and 7.2, respectively. The same colour thresholds were used for all models to allow for easier comparison of model results.

For the models of the extended knee, displacement patterns (Figure 7.1 (top)) in the full model and no-femur model were similar; the largest displacements on the medial tibial cartilage occurred along the edge of the tibial spine. In the no-tibia model, the largest displacements were farther from the tibial spine, approaching the centre of the medial tibial cartilage. Displacement magnitudes calculated for the full model were larger than those calculated by the no-tibia and no-femur models.

The von Mises stress patterns (Figure 7.1 (centre)) for the full model and no-tibia model of the extended knee were similar. The von Mises stresses in the no-femur model,



(a) (b) (c)

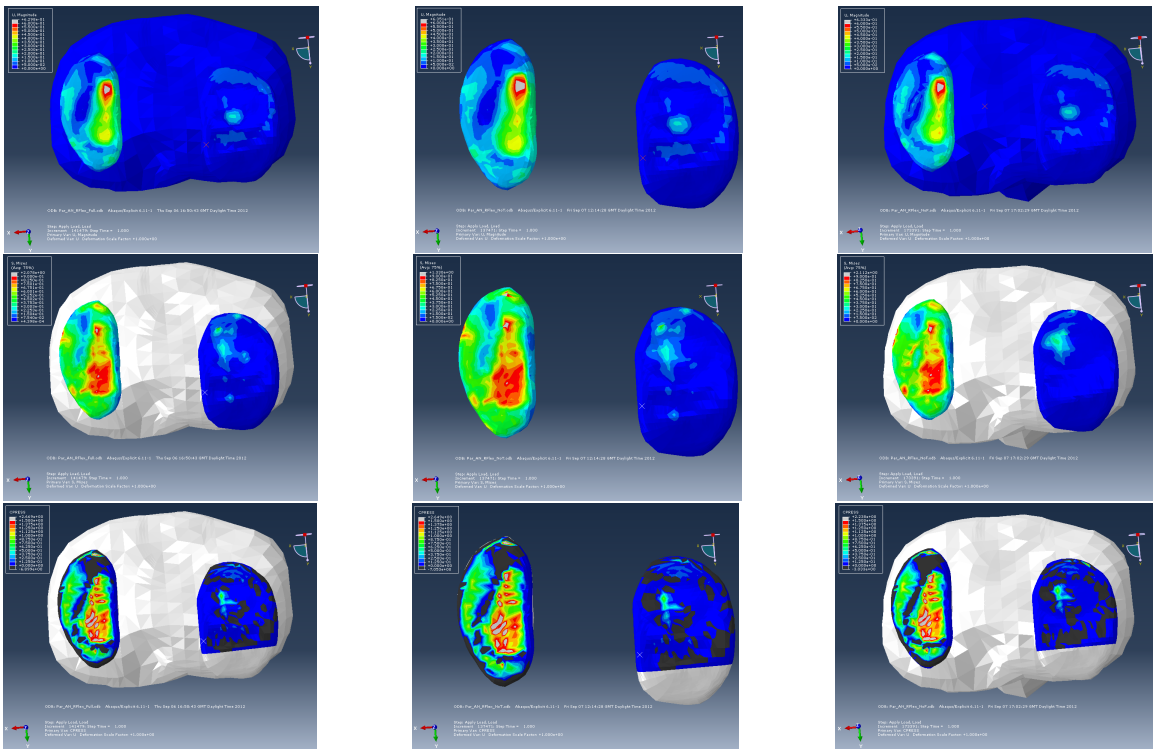
Figure 7.1: Parameter study results: Extended knee models: (top) Displacements (thresholds 0 - 0.65 mm), (centre) von Mises stresses (thresholds 0 - 1.5 MPa), and (bottom) contact pressures (thresholds 0 - 2.25 MPa) calculated on the articulating surfaces of the tibial cartilage by the (a) full models, (b) no-tibia models, and (c) no-femur models.

however, were slightly lower in magnitude on the medial tibial cartilage and slightly more distributed on the lateral tibial cartilage.

Contact pressure patterns were similar for all three models of the extended knee (Figure 7.1 (bottom)).

For the models of the flexed knee, no significant differences were found in the displacement, von Mises stress, or contact pressure patterns on the articulating surfaces of the tibial cartilage (Figure 7.2).

The required solution times for each model are shown in Table 7.1. For the models of the extended knee, the full model solved the fastest. For the models of the flexed knee, all models required approximately equal amounts of time to solve.



(a) (b) (c)

Figure 7.2: Parameter study results: Flexed knee models: (top) Displacements (thresholds 0 - 0.60 mm), (centre) von Mises stresses (thresholds 0 - 0.90 MPa), and (bottom) contact pressures (thresholds 0 - 1.5 MPa) calculated on the articulating surfaces of the tibial cartilage by the (a) full models, (b) no-tibia models, and (c) no-femur models.

7.2.4 Discussion and conclusions

For the models of the extended knee, differences in displacement and von Mises stress patterns and necessary solution time were found between the models. The models were created to represent equivalent systems of boundary conditions so differences in result patterns were not expected.

Boundary conditions and contact conditions are known to affect Explicit model solution time [1]. Identical lower limits of time increment size were used in all models. Model time increments were permitted to increase, however, if the time increment calculated for the smallest element was larger than the assigned time increment. The time increments used in the extended knee full model were indeed larger than the time increments used in the no-tibia and no-femur models. Differences in time increments will affect the calculated velocities and accelerations of the elements, potentially affecting which elements come into contact, which then also affects the displacement, von Mises stress, and contact

Table 7.1: Required times for parameter study FE model solution (time = HH:MM)

	Extension	Flexion
Full	4:47	2:55
No-tibia	10:30	2:51
No-femur	15:45	3:05

pressure patterns. Also, if a relatively small element came into contact in the no-tibia or no-femur models (but not in the full model), the time increment used in model solution would further decrease, with a corresponding increase in required model solution time.

Since different results were calculated from the various models, the model which most closely reflected the anatomical knee should be selected; this was the full model. The full model also required the least amount of time for model solution. *The full model set-up was used in the remaining models of the extended knee.*

For the models of the flexed knee, no differences in displacement, von Mises stress, or contact pressure patterns were found between models. There was also no significant difference in required solution time. Since removing the tibia and replacing the rigid body of the femur with a rigid surface did not improve model solution speed, *the full model set-up was used in the remaining models of the flexed knee.*

7.3 Mesh convergence tests

7.3.1 Introduction

The final stage of the FE model set-up was conducting mesh convergence tests. Continually increasing the number of elements in a coarse mesh should result in calculated results converging to a specific value. FE model meshes should contain at least as many elements as are necessary for results to converge, but using more elements generally increases required solution time. Therefore, mesh convergence tests can be used to determine the minimum number of elements required for results to converge.

Two sets of mesh convergence tests were conducted in this project: one on a model of an extended knee and one on a model of a flexed knee. Both sets of tests were conducted in case the different orientations of the knee resulted in different sizes of contact areas and

consequently different required mesh densities. All models were created based on data from the right knee of the same subject. Since the geometry of the knee structures were of relatively similar size for all subjects, the required mesh density of the knee structures should be similar regardless of the subject used in the mesh convergence test.

7.3.2 Methods

Models were created of the knee in extension as well as of the knee in flexion. In accordance with the results of the validation study and the parameter study, all models used the full model set-up with rigid bones and deformable cartilage and menisci. The tibia was held fixed while loads were applied to the femoral centre of mass.

The mesh convergence tests involved creating models with progressively denser meshes. The first model (called 'Model 1') in each set (knee extension or knee flexion) contained soft tissues with arbitrary mesh densities. Subsequent models included increasingly dense meshes of the femoral cartilage, tibial cartilage, and meniscus. Given the hypothesized links between loading during knee extension and medial OA and between loading during knee flexion and lateral OA, mesh density was only progressively increased in the relevant tibiofemoral compartment for each set (medial for the extended knee models, lateral for the flexed knee models). Within the relevant compartment, Model 2 contained twice as many elements as Model 1; Model 3 contained three times as many elements as Model 1, and so forth.

After model solution, the displacement, von Mises stress, and contact pressure at each node on the articulating surfaces of the femoral cartilage and tibial cartilage in the relevant compartment were recorded. (The mesh convergence test only tested for convergence of results on the femoral cartilage and tibial cartilage (not the menisci) because this thesis investigated links between mechanical loading and osteoarthritic cartilage lesions (not changes in the menisci).) The average displacement, von Mises stress, and contact pressure for each surface were then calculated. Models with increasingly dense meshes were created and solved until all three results (displacement, von Mises stress, and contact pressure) converged in the same consecutive three sets of models. Consecutive models were said to have 'converged' if the difference in their results was less than 5% of the result

calculated in the model with the finer mesh [63]. In other words, mesh convergence for a particular result was achieved when:

$$\left|\frac{x_n - x_{n-1}}{x_n}\right| < 0.05 \tag{7.1}$$

where x_n is a result from Model n (model with finer mesh) and x_{n-1} is a result from Model $n-1$ (model with coarser mesh). When a model structure (femoral cartilage or tibial cartilage) had converged for three consecutive sets of models, the model structure was said to be 'fully converged'. Different model structures could fully converge in different models (for example, femoral cartilage could fully converge in Model 4 and tibial cartilage fully converge in Model 5).

Once each structure was classified as 'fully converged', the number of elements and size of the elements in the first of the three models to converge were recorded. This element size was used when generating the meshes of the structures in the FE models of the normal knees and of the knees with simulated mechanical changes.

7.3.3 Results

The calculated (top) displacements, (centre) von Mises stresses, and (bottom) contact pressures as functions of number of elements are shown in Figure 7.3 (extended knee) and Figure 7.4 (flexed knee). Sets of consecutive models which have converged for a result are marked using a 'Δ'; fully converged models are shown with red circles.

For the models of the extended knee, the femoral cartilage fully converged when the mesh contained 17,292 elements. These elements were not equally distributed throughout the structure; a denser mesh was created in the medial tibiofemoral compartment. The medial compartment contained 12,290 of these elements; this number of elements corresponded to elements with sides of approximately 1.650 mm. The tibial cartilage fully converged when 98,782 mesh elements (sides of approximately 0.510 mm) were used. The medial meniscus (note: this structure was not tested to full convergence) was modelled using 25,161 elements (sides of approximately 0.780 mm) in the first of the three models to converge.

For the models of the flexed knee, the femoral cartilage fully converged when the

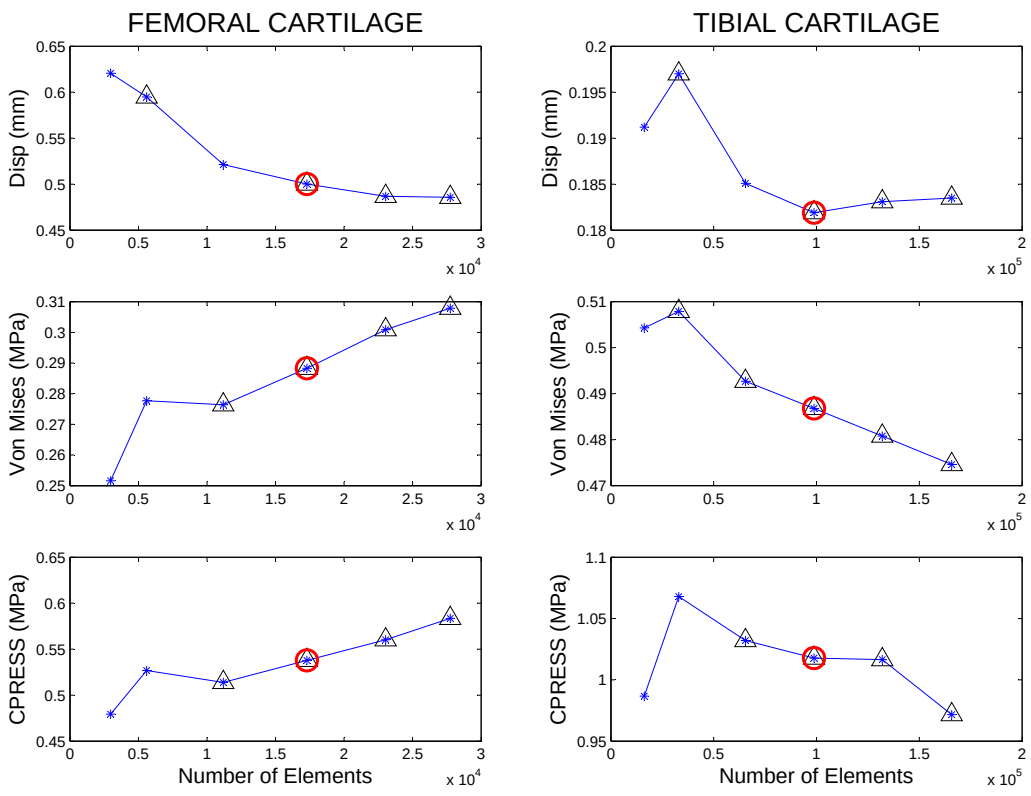


Figure 7.3: Convergence test results: Extended knee models: Average (top) displacements, (centre) von Mises stresses, and (bottom) contact pressures calculated on the (left) femoral cartilage and (right) tibial cartilage (Δ = convergence of consecutive models, red O = first model with full convergence).

mesh contained 104,830 elements. Similar to the extended knee models, elements were not equally distributed in this structure, and a denser mesh was created in the lateral tibiofemoral compartment. The lateral compartment contained 79,872 elements; this number of elements corresponded to elements with sides of approximately 0.984 mm. The tibial cartilage fully converged when 121,851 mesh elements (sides of approximately 0.567 mm) were used. The lateral meniscus (note: this structure was not tested to full convergence) was modelled using 66,994 elements (sides of approximately 0.375 mm) in the first of the three models to converge.

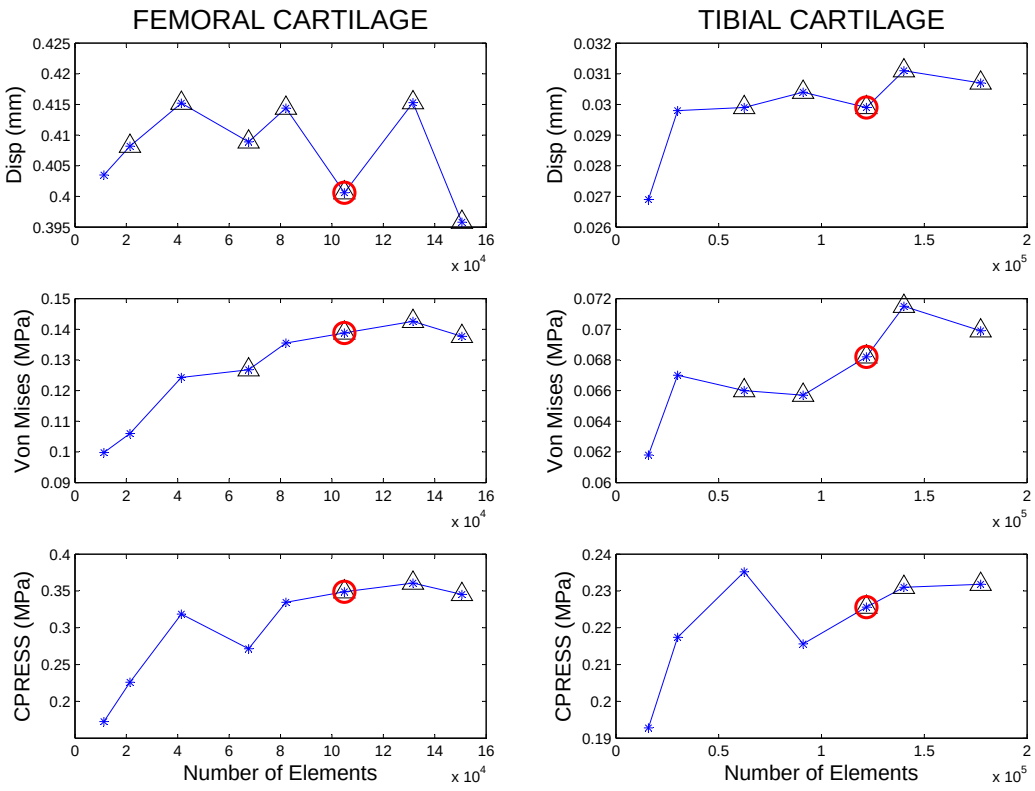


Figure 7.4: Convergence test results: Flexed knee models: Average (top) displacements, (centre) von Mises stresses, and (bottom) contact pressures calculated on the (left) femoral cartilage and (right) tibial cartilage (Δ = convergence of consecutive models, red O = first model with full convergence).

7.3.4 Discussion and conclusions

It is interesting to compare the required mesh densities of the femoral cartilage in the models of the extended and flexed knees. A denser mesh was necessary for the results of the flexed knee model to converge. There could be at least two reasons for this finding. Both explanations are associated with a smaller contact area in the lateral compartment (smaller contact areas typically require finer meshes in order to avoid concentrated stresses at a small number of nodes).

First, the shapes of the articulating surfaces of the medial tibial cartilage and lateral tibial cartilage are different. The medial compartment is concave, meaning there is a relatively large contact surface between the femoral cartilage and the medial tibial cartilage. Conversely, the lateral compartment is convex, resulting in a relatively smaller contact

surface between the femoral cartilage and the lateral tibial cartilage.

Second, the femoral condyle is not a perfect sphere. The most distal aspect of the femur (the region that contacts the tibial cartilage in full knee extension) is relatively flat in comparison to the posterior aspect of the femoral condyle (which contacts the tibial cartilage in knee flexion). Contact with a more-rounded object (as occurs in knee flexion) will result in a smaller contact area.

There are two aspects of the convergence criteria which should be considered. First, the criterion used to define 'convergence' was 'less than 5% difference between results of consecutive models'. Other convergence criteria could have been used, however, and might have resulted in different required mesh densities. For example, a convergence criterion of less than 2% difference between results of consecutive models might have required a denser mesh. Second, the required mesh densities may also have been affected by considering the average of results instead of a maximum result when checking for convergence. The average took into account a larger number of nodal results and was therefore a measure of the overall convergence of a contact surface mesh. Using maximum values would have only tested whether a mesh had converged at a single node (and the node at which this maximum result occurred may have changed between models).

7.4 Conclusions

This chapter discussed the last two stages of FE model set-up: a parameter study and mesh convergence tests.

The parameter study tested whether models could be streamlined by replacing the rigid femur and/or tibia with equivalent systems of model definitions and boundary conditions. The study found that neither removing the tibia nor using a rigid surface instead of a rigid body for the femur decreased the required time for model solution. Therefore, the full model (with rigid femur and rigid tibia included) was used for the remaining models in this thesis.

Mesh convergence tests were used to determine the minimum number of elements necessary to include in the femoral cartilage and tibial cartilage so that further increasing mesh density would not affect calculated results. It was found that medial femoral

cartilage and medial tibial cartilage in the extended knee model required 17,292 and 98,782 mesh elements, corresponding to elements with sides of approximately 1.650 mm and 0.510 mm, respectively. Lateral femoral cartilage and lateral tibial cartilage in the flexed knee model required 104,830 and 121,851 mesh elements, corresponding to elements with sides of approximately 0.984 mm and 0.567 mm, respectively.

After the final stages of setting up the FE model were complete, the FE models of the normal human knees could be created. Models of the entire knee were created in accordance with the results of the parameter study. The structures within the model were then assigned mesh densities based on the mesh convergence test results. Mesh density was controlled by assigning mesh element side lengths and then automatically generating the meshes.

Chapter 8

FE Models of the Normal Human Knee

After finalizing the model set-up and necessary mesh densities, subject-specific FE models of three healthy subjects were created and solved. In total, twelve FE models of the normal knee were created. Four models were created for each subject: two (one of the left knee and one of the right knee) with the knee in extension and two with the knee in mid-range flexion. Model geometry and load cases were derived as described in Chapter 3 and Chapter 4, respectively. These data sets were then combined as explained in Chapter 5 to create FE models.

Models were solved for displacements, von Mises stresses, and contact pressures on the articulating surfaces of the tibial cartilage and femoral cartilage. Given the hypothesized association between tibiofemoral flexion angle and OA type, only medial compartment results are reported for models of the extended knee and only lateral compartment results are reported for models of the flexed knee. These calculated compartmental results were then compared to diagrams of frequent cartilage degeneration and to intraoperative photos (where available) of typical cartilage lesion locations.

All results are shown on the articulating surfaces of the tibial cartilage and femoral cartilage in the same orientations. The orientation of tibial cartilage results is shown in Figure 8.1; femoral cartilage orientation has not been illustrated because orientation can be readily determined based on the location of the cartilage connecting the two compartments. Anterior is always at the top. Medial and lateral compartment cartilage surfaces are shown with the tibial spine to the right and left, respectively. Maintaining consistent orientations required reflecting half of the images; the images which have been

reflected are indicated in figure captions.

When describing medial-lateral locations within a single compartment, 'periphery' and 'inside' are used to describe the regions of the cartilage farther from and closest to, respectively, the tibial spine. 'Periphery' and 'inside' have been used to avoid confusion about whether 'medial' and 'lateral' within a compartment are defined relative to the centre of the joint or the centre of the human body.

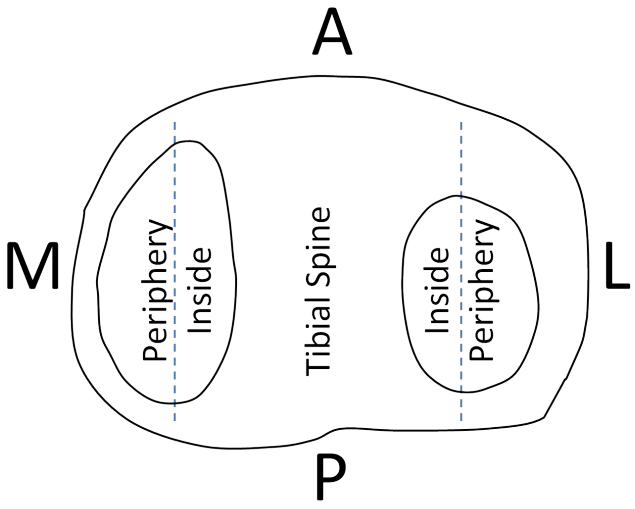


Figure 8.1: Knee orientation and terms used when illustrating and describing FE model results.

8.1 Cartilage lesion locations

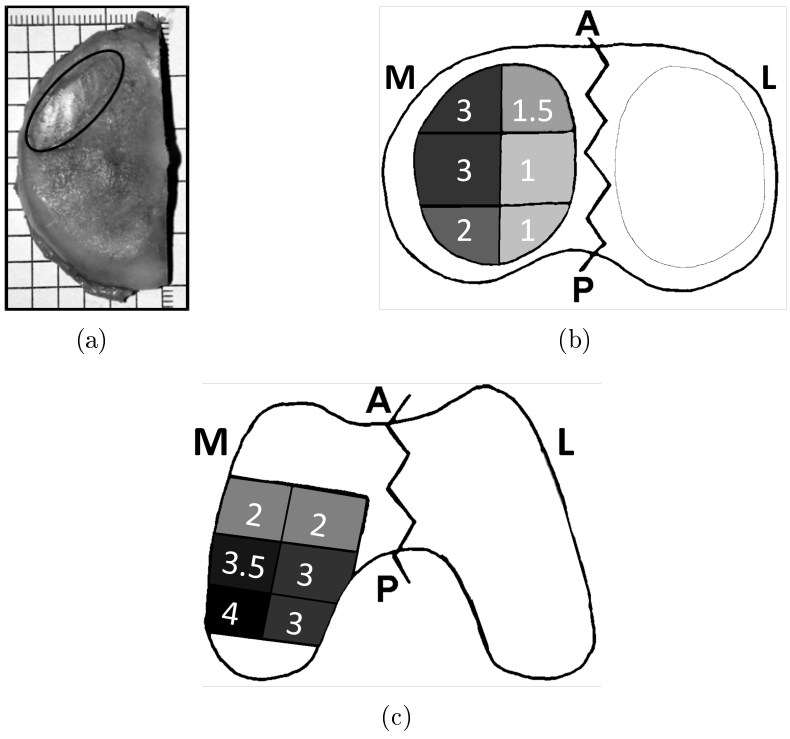
Weidow *et al.* [151, 152] created diagrams of frequent cartilage degeneration based on data from 42 patients (30 females, 12 males) undergoing knee replacement surgery due to uni-compartmental tibiofemoral OA. Medial OA was present in 32 patients; lateral OA was present in 10 patients. There were no significant differences in cartilage degeneration locations based on gender; no information was given on ligament health.

8.1.1 Medial tibiofemoral compartment

Intraoperatively, medial OA lesions are typically observed in the anterior-periphery region of the medial tibial cartilage (Figure 8.2a). Weidow *et al.* [151, 152] reported approxi-

mately equal degeneration along the entire periphery of the medial tibial cartilage, with noticeable degeneration also occurring in the anterior-inside region (Figure 8.2b).

While it is relatively easy (and for research purposes, common) to remove a fully-intact sample of tibial cartilage (example shown in Figure 8.2a) during a knee replacement operation, it is difficult to remove a fully-intact femoral sample due to the curvature of the femur. Therefore, an intraoperative example of medial OA femoral cartilage lesion locations was not available. Weidow *et al.* [151, 152] reported widespread degeneration throughout the entire medial compartment of the femoral cartilage (Figure 8.2c).



(a) (b)

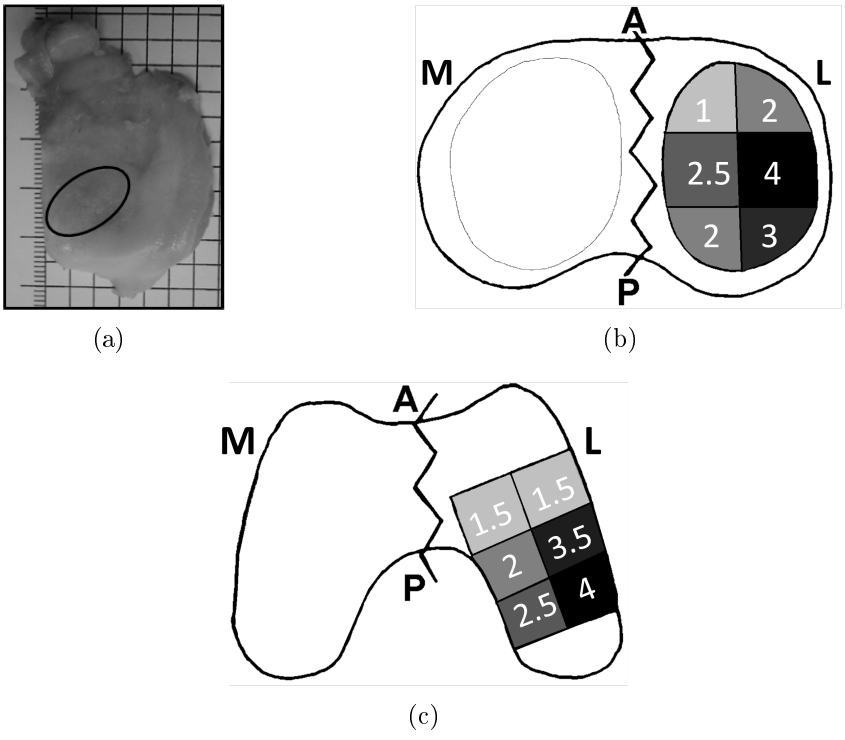
(c)

Figure 8.2: Expected cartilage lesion locations in the medial compartment: (top) Tibial cartilage and (bottom) femoral cartilage surfaces. (a) Lesion circled in intraoperative picture (provided courtesy of Dr Chethan Jayadev and the Nuffield Department of Orthopaedics, Rheumatology and Musculoskeletal Sciences). (b, c) Diagrams of frequent cartilage degeneration locations (darker colours and higher numbers (scale 0 - 4) indicate areas of increased cartilage degeneration) are based on data presented by Weidow *et al.* [151, 152].

8.1.2 Lateral tibiofemoral compartment

Intraoperatively, lateral OA lesions are frequently seen in the posterior and central regions of the lateral tibial cartilage, extending from the inside edge to the centre of the tibial cartilage (Figure 8.3a). Weidow *et al.* [151, 152] reported characteristic lateral OA degeneration affecting much of the surface of the lateral tibial cartilage (Figure 8.3b). Only the anterior-inside region had relatively less degeneration.

As with the medial femoral cartilage results, an intraoperative illustration of typical lateral OA femoral cartilage lesion locations was not available. Weidow *et al.* [151, 152], however, reported that while cartilage degeneration is present throughout the lateral femoral cartilage, degeneration is more severe in the peripheral central and posterior regions (Figure 8.3c).



(a) (b) (c)

Figure 8.3: Expected cartilage lesion locations in the lateral compartment: (top) Tibial cartilage and (bottom) femoral cartilage surfaces. (a) Typical location of lesion circled in intraoperative picture (provided courtesy of Dr Raj Rout and the Nuffield Department of Orthopaedics, Rheumatology and Musculoskeletal Sciences). (b, c) Diagrams of frequent cartilage degeneration locations (darker colours and higher numbers (scale 0 - 4) indicate areas of increased cartilage degeneration) are based on data presented by Weidow *et al.* [151, 152].

8.2 Results

8.2.1 Extension models

Maximum magnitudes of displacements, von Mises stresses, and contact pressures on the medial tibial cartilage and medial femoral cartilage surfaces are provided in Table 8.1. Von Mises stresses calculated on the tibial cartilage surfaces (Figure 8.4 and Figure 8.5) and the femoral cartilage surfaces (Figure 8.6) have also been provided. (Displacement and contact pressure patterns are not included due to space constraints.)

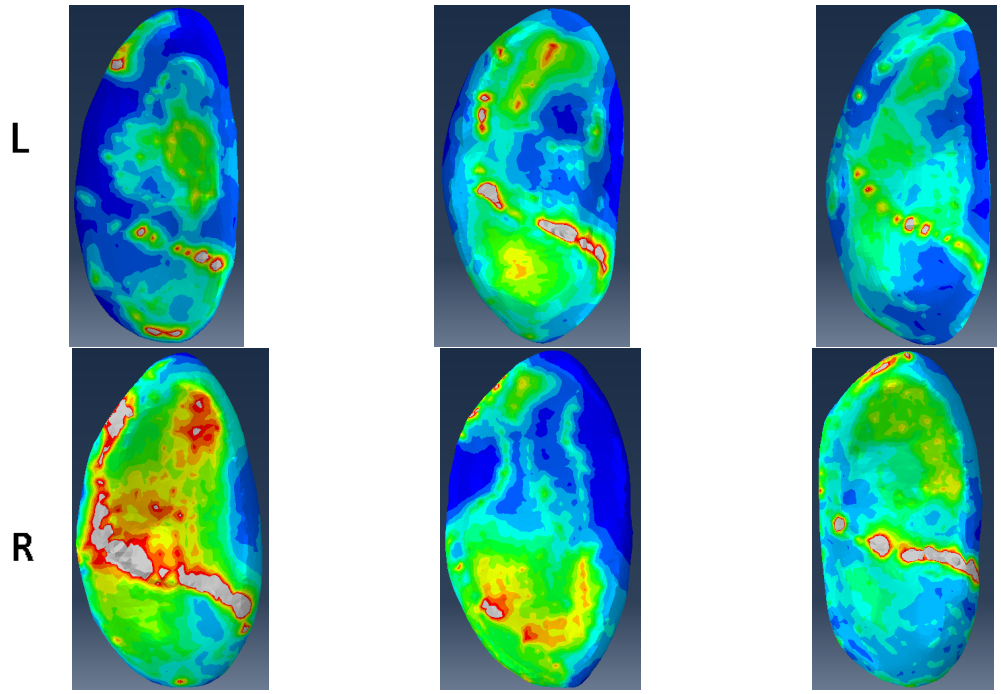
8.2.1.1 Medial tibial cartilage results

Maximum displacements ranged from 0.44 mm to 0.68 mm, von Mises stresses from 2.3 MPa to 4.1 MPa, and contact pressures from 3.0 MPa to 7.8 MPa (Table 8.1).

Table 8.1: Medial tibial and femoral cartilage results: Maximum magnitudes of displacements, von Mises stresses, and contact pressures.

Subject	Knee	Load (N)	Disp (mm)		Von Mises (MPa)		Contact Pressure (MPa)	
			Tibial	Femoral	Tibial	Femoral	Tibial	Femoral
1	Left	206	0.44	0.74	3.8	0.74	3.0	6.5
1	Right	532	0.68	1.0	2.3	1.5	7.4	2.2
2	Left	325	0.63	1.0	4.1	0.87	7.8	1.5
2	Right	396	0.48	0.77	2.4	0.89	5.9	3.2
3	Left	285	0.50	0.57	4.1	0.57	3.9	1.2
3	Right	424	0.48	0.84	2.5	1.0	5.5	3.2

Von Mises stress was distributed over most of the articulating surface of the medial tibial cartilage (Figure 8.4), with concentrations of stress frequently calculated along the border of the cartilage-meniscus interface (examples of the interface border stress concentrations are shown both with and without the menisci included in Figure 8.5). Magnitudes of stresses varied between models, likely because the subject-specific load cases varied between models. In all models, however, some level of von Mises stress was calculated in the anterior-periphery where intraoperative medial OA lesions are frequently observed; higher stresses were also always calculated elsewhere on the medial tibial cartilage surface.



(a) Subject 1 (b) Subject 2 (c) Subject 3

Figure 8.4: Medial tibial cartilage results: Von Mises stresses (thresholds 0 - 1.5 MPa) calculated for models of extended (top) left and (bottom) right knees. (Note: Anterior at top; tibial spine at right; left knee results have been reflected for easier comparison; grey indicates stresses above maximum threshold.)

8.2.1.2 Medial femoral cartilage results

As with the tibial cartilage results, the magnitudes of femoral cartilage contact results varied between models (Table 8.1). Maximum medial femoral cartilage displacements ranged from 0.57 mm to 1.0 mm. These femoral cartilage displacements were larger than the tibial cartilage displacements. Maximum von Mises stresses ranged from 0.57 MPa to 1.5 MPa; maximum contact pressures ranged from 1.2 MPa to 6.5 MPa. The magnitudes of the stresses and pressures were lower than those calculated on the medial tibial cartilage surfaces.

Von Mises stress patterns varied between models, but similar orders of magnitudes of stress were calculated for the models (Figure 8.6). An exception was Subject-1-Right-Knee (bottom, left image), which had stresses approximately twice that of the other models; the largest load case was also applied to Subject-1-Right-Knee, however. Concentrations of stress were less common on the femoral cartilage surfaces than on the tibial

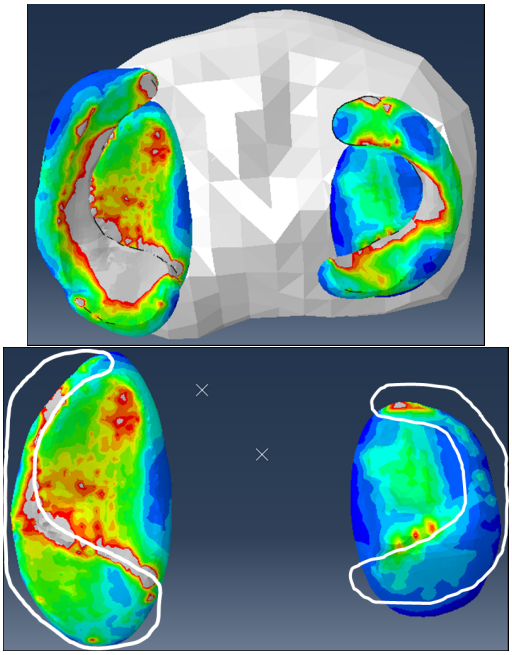


Figure 8.5: Concentrated von Mises stresses (threshold 0 - 1.5 MPa) calculated along cartilage-menisci interface border: Articulating tibial cartilage surface with menisci (top) included and (bottom) outlined in white.

cartilage surfaces.

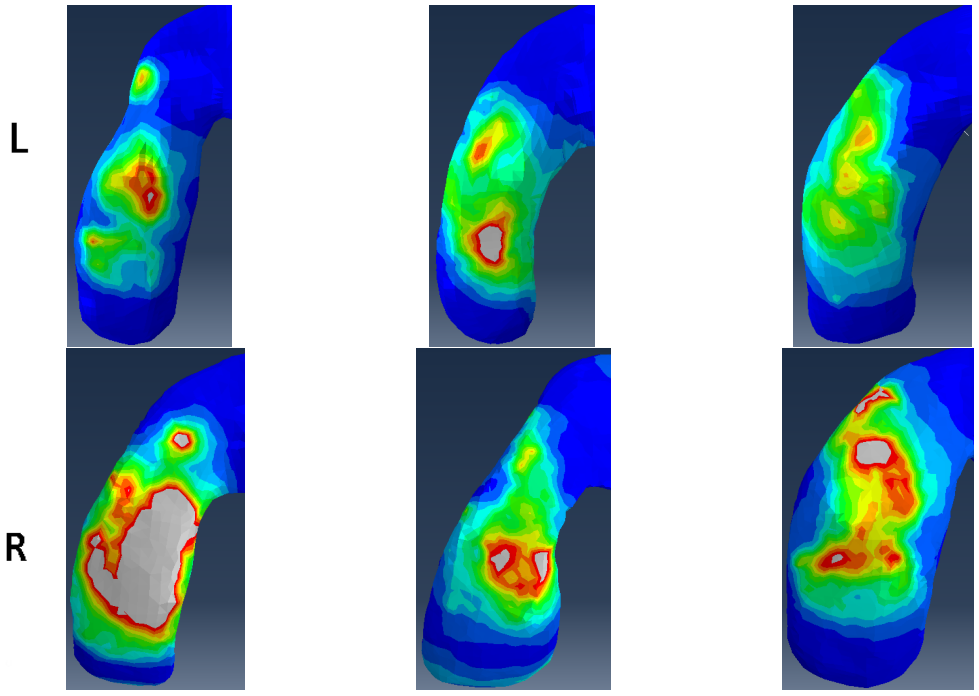
8.2.2 Mid-range flexion models

Maximum magnitudes of displacements, von Mises stresses, and contact pressures on the lateral tibial cartilage and lateral femoral cartilage surfaces are provided in Table 8.2. Von Mises stresses calculated on the lateral tibial cartilage and femoral cartilage surfaces are shown in Figure 8.7 and Figure 8.8, respectively. (Displacement and contact pressure patterns are not included due to space constraints.)

8.2.2.1 Lateral tibial cartilage results

Maximum displacements on the lateral tibial cartilage ranged from 0.19 mm to 0.43 mm, von Mises stresses from 1.0 MPa to 4.8 MPa, and contact pressure from 1.3 MPa to 3.1 MPa (Table 8.2). In comparison to the medial tibial cartilage results, the displacements and contact pressures in particular were lower on the lateral tibial cartilage.

With the exception of the Subject 1 models (which had relatively smaller loads), the



(a) Subject 1 (b) Subject 2 (c) Subject 3

Figure 8.6: Medial femoral cartilage results: Von Mises stresses (thresholds 0 - 0.7 MPa) calculated for models of extended (top) left and (bottom) right knees. (Note: Anterior at top; inter-compartment cartilage at right; right knee results have been reflected for easier comparison; grey indicates stresses above maximum threshold.)

stresses calculated by the FE models were distributed across much of the articulating surface of the lateral tibial cartilage (Figure 8.7). Typically, there were two areas of higher stress: the central region where femoral cartilage-tibial cartilage contact occurred and along the periphery where cartilage-meniscus contact occurred. As with the medial tibial cartilage results, concentrations of increased stress were occasionally calculated along the cartilage-meniscus interface, and magnitudes of stresses varied between models, likely because of subject-specific load cases.

8.2.2.2 Lateral femoral cartilage results

Displacements on the lateral femoral cartilage ranged from 0.32 mm to 1.3 mm, von Mises stresses from 0.52 MPa to 1.8 MPa, and contact pressures from 1.5 MPa to 6.0 MPa (Table 8.2). Consistent with the medial compartment results, lateral femoral displacements were larger and lateral femoral von Mises stresses were smaller than the results calculated

Table 8.2: Lateral tibial and femoral cartilage results: Maximum magnitudes of displacements, von Mises stresses, and contact pressures.

Subject	Knee	Load (N)	Disp (mm)		Von Mises (MPa)		Contact Pressure (MPa)	
			Tibial	Femoral	Tibial	Femoral	Tibial	Femoral
1	Left	73	0.24	0.32	4.1	0.52	1.3	2.3
1	Right	126	0.26	0.72	1.0	0.96	1.9	5.9
2	Left	270	0.40	1.3	3.8	1.8	2.8	2.8
2	Right	196	0.39	1.1	3.5	1.5	3.1	6.0
3	Left	518	0.42	1.0	4.8	1.4	3.0	2.5
3	Right	296	0.19	0.64	2.1	0.96	2.0	1.5

on the lateral tibial cartilage surface.

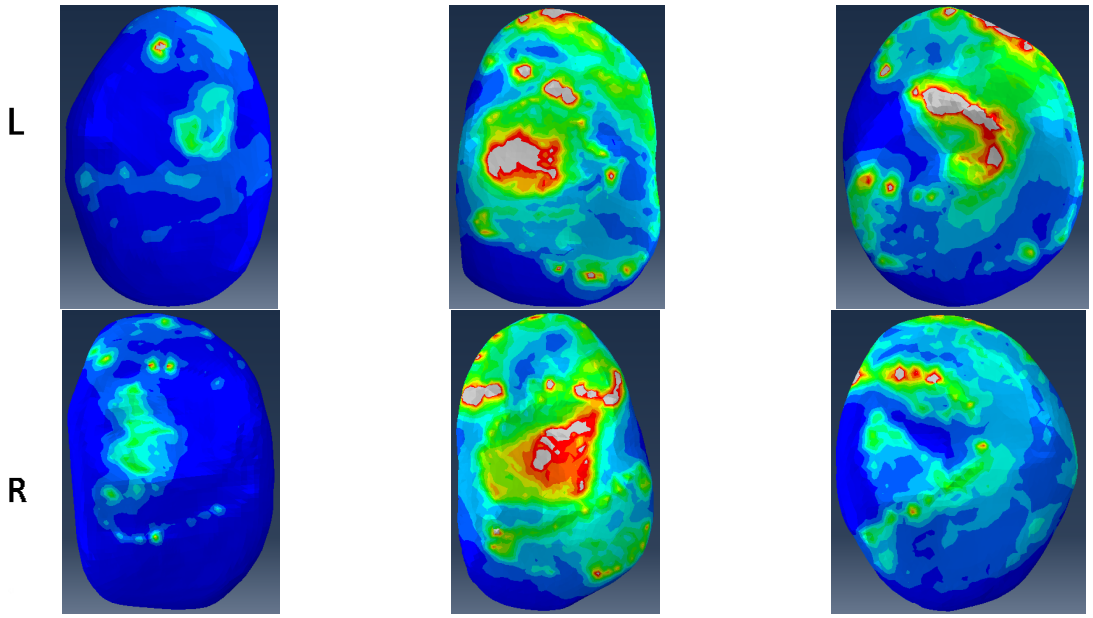
The locations of von Mises stresses calculated on the lateral femoral cartilage seem to match the locations of frequent cartilage degeneration. Stresses occur frequently and in larger magnitudes in the posterior aspect of the femoral cartilage, in particular peripherally.

8.3 Discussion

This section first discusses some trends in the data and then provides some potential causes of those trends. Then locations of calculated contact results are compared to the expected lesion locations in medial OA and lateral OA.

Perhaps the most intuitive trend was that larger load cases resulted in larger displacements. This trend was seen both in models of the knee in extension and mid-range flexion. For example, two mid-range flexion models with relatively small load cases (Subject 1 in Figure 8.7a and Figure 8.8a) had relatively small lateral tibiofemoral contact regions and displacements. (These models also had limited lateral compartment contact because a larger proportion of the applied load case passed through the medial compartment.)

Another trend was that the maximum magnitudes of von Mises stress and contact pressure were generally larger and higher, respectively, on the tibial cartilage surfaces than the femoral cartilage surfaces. Larger femoral cartilage displacements may have led

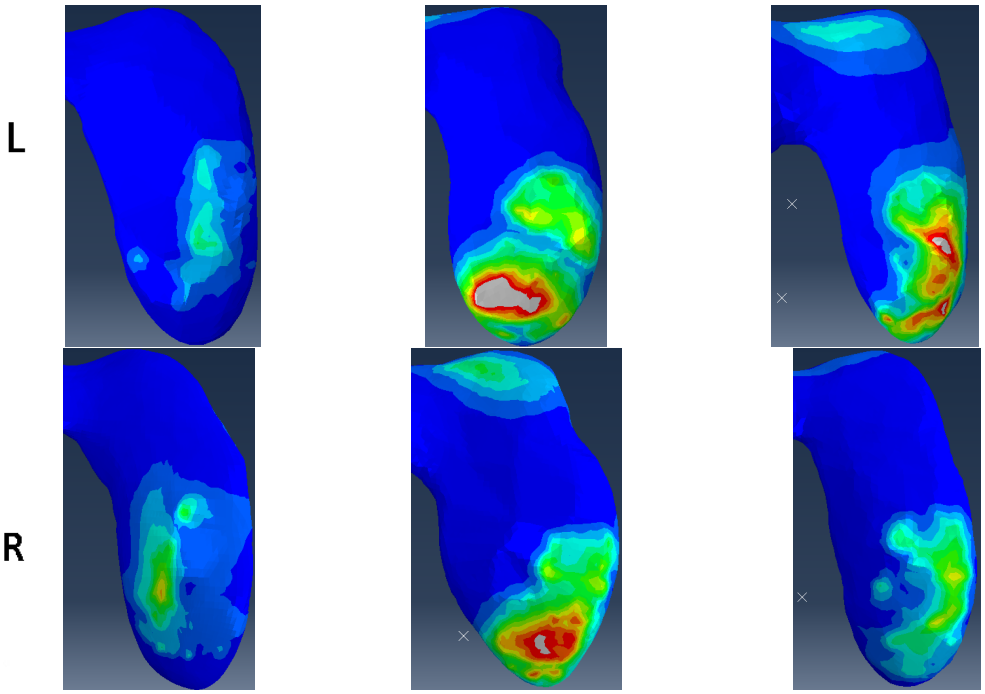


(a) Subject 1 (b) Subject 2 (c) Subject 3

Figure 8.7: Lateral tibial cartilage results: Von Mises stresses (thresholds 0 - 1.0 MPa) calculated for models of flexed (top) left and (bottom) right knees (Note: Anterior at top; tibial spine at left; left knee results have been reflected for easier comparison; grey indicates stresses above maximum threshold.)

to increased femoral cartilage contact area and consequently lower stresses and contact pressures on the femoral cartilage. It is also possible that differences in mesh density contributed to this trend. Finer meshes were used for the tibial cartilage than for the femoral cartilage. Finer meshes give more detailed approximations of underlying geometry - and the original model geometry was derived by segmenting pixels in relatively coarse MRI scans. It is possible that the finer-meshed tibial cartilage retained a greater degree of this pixelated geometry, resulting in loads occasionally passing through a single pixel or point on the tibial cartilage surface and creating stress concentrations.

Another trend, concentrations of high stresses were most common along the edges of the tibial cartilage-meniscus interfaces (Figure 8.5). Contact status between these two surfaces is likely to change during motion in the *in vivo* knee. In the FE model, however, surfaces originally out-of-contact could come into contact during model solution, but (due to the No Separation contact condition selected during the validation study) surfaces originally in-contact were not allowed to separate during model solution. Prohibiting sep-



(a) Subject 1 (b) Subject 2 (c) Subject 3

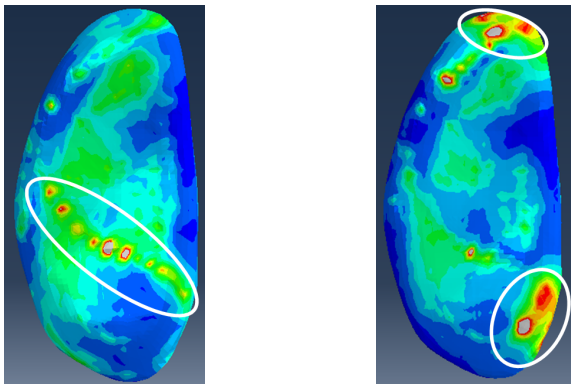
Figure 8.8: Lateral femoral cartilage results: Von Mises stresses (thresholds 0 - 1.2 MPa) calculated for models of flexed (top) left and (bottom) right knees (Note: Anterior at top; inter-compartment cartilage at left; right knee results have been reflected for easier comparison; grey indicates stresses above maximum threshold.)

aration in the FE model led to stress concentrations in the nodes most likely to switch between in-contact and out-of-contact: the nodes along the tibial cartilage-meniscus borders.

A short study was conducted to test the effect of the No Separation constraint on the calculated stress concentrations. Models were altered to allow the cartilage and menisci to separate during model solution and then re-solved. In these models, the menisci displaced to the medial and lateral edges of the knee and then completely separated from the knee. This solution was not physiological so it was necessary to add constraints to limit the motion of the menisci. Meniscal motion was limited by tying the meniscal horns to the articulating tibial cartilage surface. Stress concentrations were no longer frequently calculated along the tibial cartilage-meniscus interface borders (circled in white in Figure 8.9a), but there were new concentrated stresses at the tibial cartilage-meniscal horn tie locations (circled in white in Figure 8.9b). As stress concentrations were calculated

using both model set-ups, it was decided to continue using the No Separation constraint since this model set-up was used in the validation study, parameter study, and mesh convergence tests.

It should be noted that previous studies [51, 103, 119, 161] also tied the meniscal horns to constrain excessive meniscal motion, but these studies did not tie the meniscal horns to the tibial cartilage but instead to the tibia, resulting in a more physiological representation of the knee. Stress concentrations calculated in the current study may have been avoided if tibia-meniscal horn ties had been modelled. The error of using tibial cartilage-meniscal horn rather than tibia-meniscal horn ties was only noticed after completion of the thesis so it was no longer possible to alter the contact constraints used in the models.



(a) (b)

Figure 8.9: Von Mises stresses (thresholds 0 - 1.5 MPa, areas of concentrated stresses circled in white) calculated on articulating medial tibial cartilage when the same FE model was solved with (a) No Separation and (b) Separation-allowed constraints (meniscal horns tied to tibial cartilage).

The final trend to consider was whether the locations of the calculated contact results matched expected lesion locations. For the models of the extended knee, the calculated von Mises stresses and contact pressures generally spanned the entire tibial cartilage surfaces. Higher stresses typically occurred in the anterior-periphery region of the medial tibial cartilage, matching the location of typical intraoperative medial OA lesions; high stresses were also calculated elsewhere on the articulating surface. Calculated stresses also spanned much of the medial femoral cartilage surface. This result was consistent with the wide-spread locations of degeneration reported by Weidow *et al.* [151, 152].

For the models of the flexed knee, higher stresses were frequently calculated in the posterior and central regions of the lateral tibial cartilage, the typical location of lateral OA tibial cartilage lesions. Areas of higher stress also existed in other areas on the cartilage surfaces. On the lateral femoral cartilage surface, contact generally occurred posteriorly, consistent with expected lateral OA lesion locations.

8.3.1 Limitations

There were three main limitations associated with the FE model set-up: not including ligaments, not allowing separation between the meniscal and cartilage surfaces, and not using subject-specific material properties.

Ligaments contribute to *in vivo* knee stability by restricting excessive motion and are an integral part of the four-bar linkage system used to describe motion within the knee [49]. Ligaments were not included in these FE models, however, due to their probable addition in model complexity and solution time (the required solution time for the current models ranged from 9 hours to 150 hours). Instead of including ligaments, displacement constraints were used to prevent excessive motion within the knee. Replacing ligaments with these additional boundary constraints was deemed permissible because the FE models represented quasi-static conditions so noticeable translations and rotations within the knee were not expected.

In vivo, ligaments also create a physical barrier which prohibits the menisci from excessive medial or lateral translation. Without ligaments in the model, the menisci slid to the medial and lateral edges of the knee and dislocated, making a No Separation contact constraint between the cartilage and meniscal surfaces necessary. Physiologically, it is unlikely that the menisci as structures would separate from the cartilage surfaces, but it is possible that individual elements on the meniscal surfaces would separate from the cartilage surfaces. Since individual elements were not allowed to separate in the FE models, it could be argued that the No Separation contact constraint did not reflect physiological conditions and was a limitation. The validation study models used this No Separation contact constraint, however, and the calculated contact patterns were similar to the contact patterns measured by the pressure film. Therefore, the contact

constraint was deemed allowable for the current study. In future studies, models could be made more physiological by including ligaments instead of applying additional boundary constraints and contact constraints.

Another limitation of the subject-specific FE model set-up was using literature-derived rather than subject-specific material properties for the cartilage and menisci. Ideally, subject-specific properties would be used but these properties cannot currently be determined non-invasively. The material properties used in the models, however, match values commonly cited in the literature for other FE models of the normal knee.

8.4 Conclusions

Twelve FE models of normal knees were created and solved in this chapter: six models of the knee in extension and six models of the knee in mid-range flexion. Subject-specific load cases during level walking and rising from a stool, respectively, were applied to these models. Displacements, von Mises stresses, and contact pressures were calculated on the articulating cartilage surfaces, and then areas of higher stresses and pressures were compared to typical OA cartilage lesion locations.

In general, contact was fairly wide-spread over the cartilage surfaces. Higher stresses were typically calculated in areas of expected cartilage lesions - but high stresses were also calculated in areas not typically affected by osteoarthritic cartilage lesions. In the next chapter, specific model parameters are altered to investigate how these parameters affect the calculated displacements, stresses, and contact pressures, in particular in areas where cartilage lesions typically occur.

Chapter 9

FE Models with Simulated Mechanical Changes

After solving the subject-specific models of normal, healthy subjects, three studies were conducted to investigate how changing various parameters affected model results. These studies considered the effects of:

- increasing the load case applied to the models.
- assigning cartilage a globally decreased stiffness.
- simulating a cartilage defect via locally decreased cartilage stiffness.

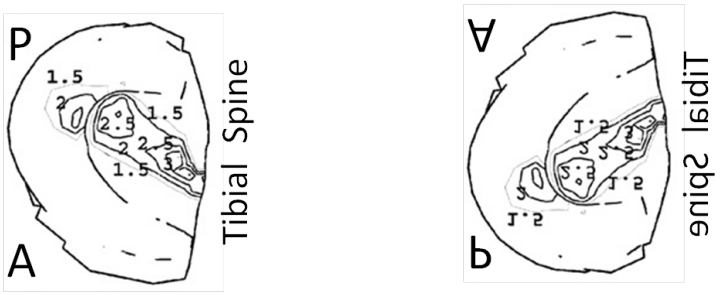
For each model, the displacements, von Mises stresses, and contact pressures on the articulating surfaces of the tibial cartilage and femoral cartilage were calculated. These patterns and magnitudes were then compared to the results calculated for the FE models of the normal knee; locations of relatively large displacements and high stresses and contact pressures were also compared to locations of characteristic OA cartilage lesions.

9.1 Increased load case

9.1.1 Methods

Increased body weight and obesity are commonly associated with increased risk of OA [67]. The effect of increased body weight on calculated contact results was investigated by increasing the load case applied to the models. Axial load cases applied to the normal

extended knee models (see Chapter 8) ranged from 206 N to 532 N. A study by Shirazi *et al.* [134] applied 2000 N to an FE model of the normal extended knee and calculated the resulting contact pressures (Figure 9.1). Load cases in the current study's extended knee models were therefore increased to 2000 N (called 'increased-load' models), both to investigate the effect of increasing the applied load and to compare the results of the current study to previously-published data.



(a) (b)

Figure 9.1: Medial tibial cartilage contact pressures reported by Shirazi *et al.*: Image in (a) original orientation and (b) reflected to maintain consistency with orientation of other figures in thesis. ([134], permission to reproduce this (adapted) figure has been granted by Elsevier.)

Von Mises stress or contact pressure patterns for FE models of knees in mid-range flexion could not be found. Therefore, the load cases applied to the current study's increased-load models of the flexed knee were not increased to a standard load case. Instead, the load cases which had been applied to the normal models were doubled in these increased-load models.

9.1.2 Results

Increasing the applied load case increased the maximum displacements, von Mises stresses, and contact pressures in the models of the extended knee and of the flexed knee (Figure 9.2). Larger increases were calculated in the extended knee models (load increased to 2000 N) than in the flexed knee models (load doubled). The slopes of the contact results were typically similar in the extended and flexed knee models, with the exception of the femoral cartilage displacements (larger displacement increase per unit load increase was observed in the flexed knee models).

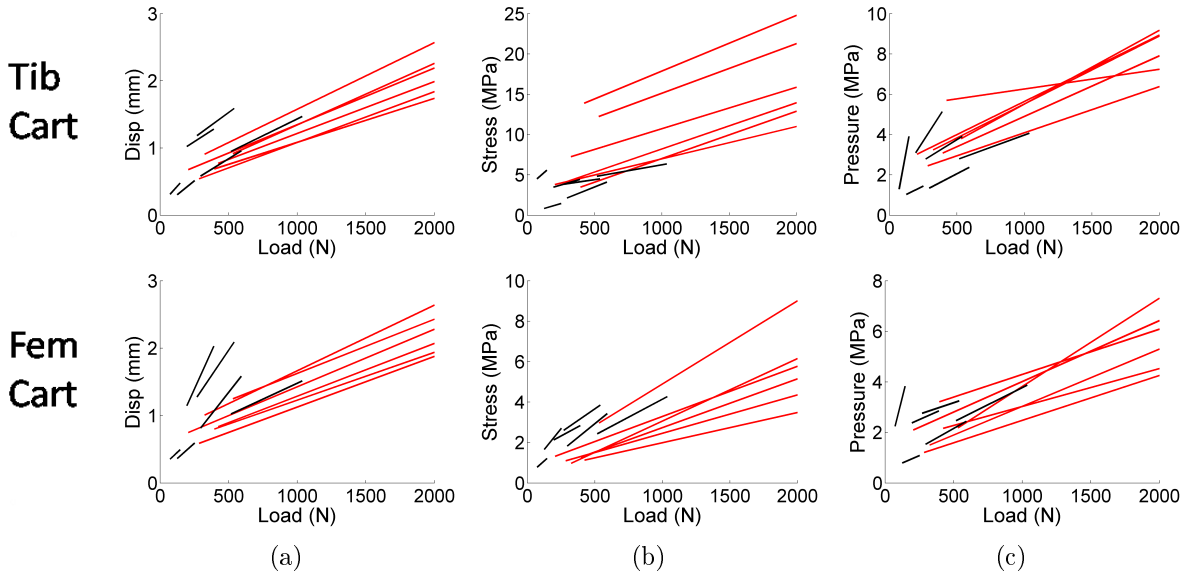


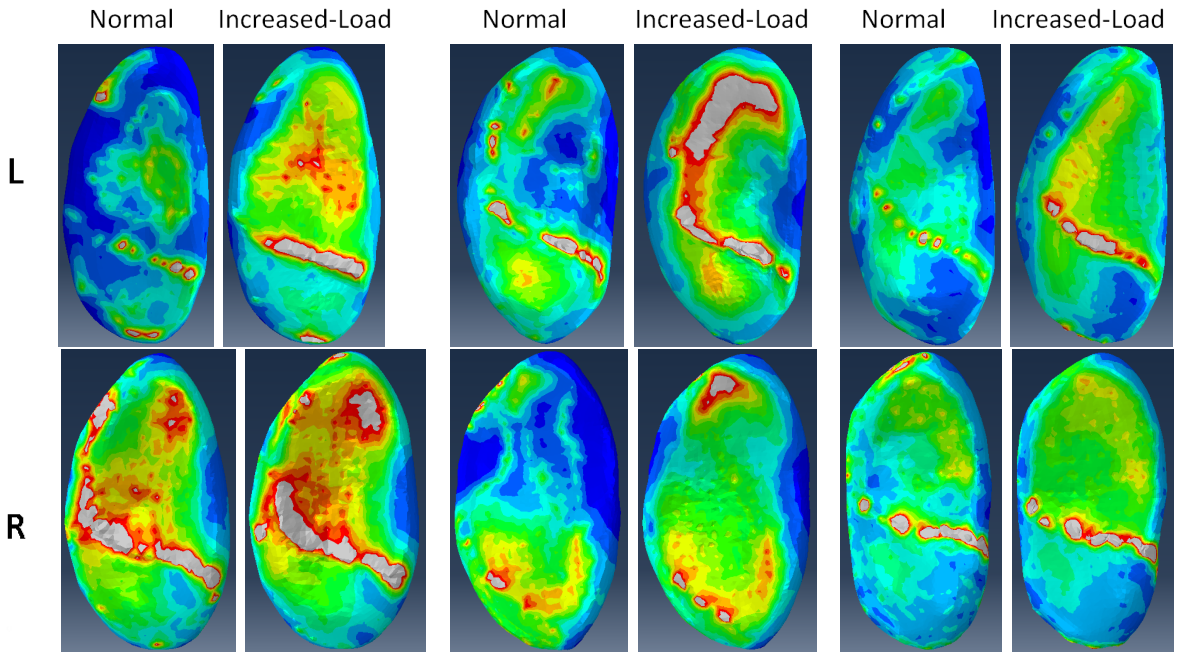
Figure 9.2: Increased load case trends: Maximum magnitudes on (top) tibial cartilage and (bottom) femoral cartilage surfaces: (a) Displacements, (b) von Mises stresses, and (c) contact pressures (extended knee models increased to 2000 N in red; flexed knee models with doubled load cases in black).

After comparing trends of maximum magnitudes, the distribution of von Mises stresses (Figures 9.3, 9.4, 9.5, and 9.6) in the normal models (left image in each pair) and increased-load models (right image in each pair) were examined.

There were two patterns of tibial cartilage stress increase in the extended knee increased-load models (Figure 9.3). The first pattern was of stress increase along the tibial cartilage-meniscus interface border; the second pattern was of stress increase in the anterior cartilage region (the region typically associated with medial OA tibial cartilage lesions). Examples of these patterns, particularly of increased anterior stress, are visible in the FE model results for Subject 1 and Subject 2.

Increasing the load applied to the extended knee models noticeably increased the femoral cartilage contact areas and stresses (Figure 9.4). Stresses in the increased-load models were frequently higher than the threshold stress values set using the normal models. These areas of high stresses in the increased-load models included the areas of high stress in the normal models and extended anteriorly to cover most of the medial femoral cartilage surface.

The two patterns of tibial cartilage stress increase seen in the extended knee models

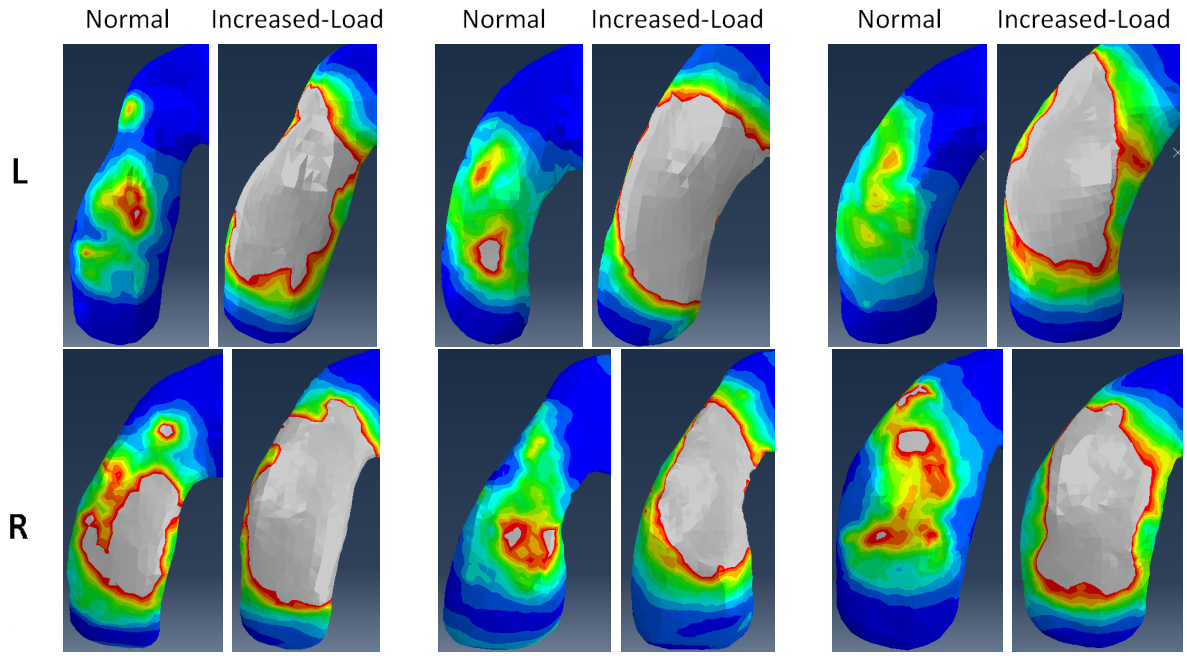


(a) Subject 1 (b) Subject 2 (c) Subject 3

Figure 9.3: Increased load case results: Medial tibial cartilage: Von Mises stresses (thresholds 0 - 1.5 MPa) calculated for extended (top) left and (bottom) right knees. (Note: Anterior at top; tibial spine at right; left knee results reflected for easier comparison; grey indicates above-threshold stress.)

were also seen in the flexed knee models (Figure 9.5). Stress again increased along the tibial cartilage-meniscus interface border but was not as pronounced as in the extended knee models. This increased cartilage-meniscus interface stress was most noticeable in Subject 3. The second trend, that of increased stress at the femoral cartilage-tibial cartilage interface, was particularly evident in Subject 2. Increased stresses typically occurred in the central region of the lateral tibial cartilage (an area commonly associated with lateral OA cartilage lesions). Doubling the applied load had little effect in models of Subject 1.

Increasing the applied load led to increased femoral cartilage stress in the flexed knee models for Subject 2 and Subject 3 (again with little effect in Subject 1) (Figure 9.6). Contrary to the extended knee model results, there was limited expansion of the femoral cartilage contact area in the increased-load flexed knee models (likely because of a smaller increase in load than in the extended knee models); the general patterns and centre locations of higher stress remained constant. Above-threshold stresses in the increased-load models expanded in all directions from these centre locations, which were posterior-central for Subject 2 and posterior-periphery in Subject 3. Lateral OA femoral cartilage



(a) Subject 1 (b) Subject 2 (c) Subject 3

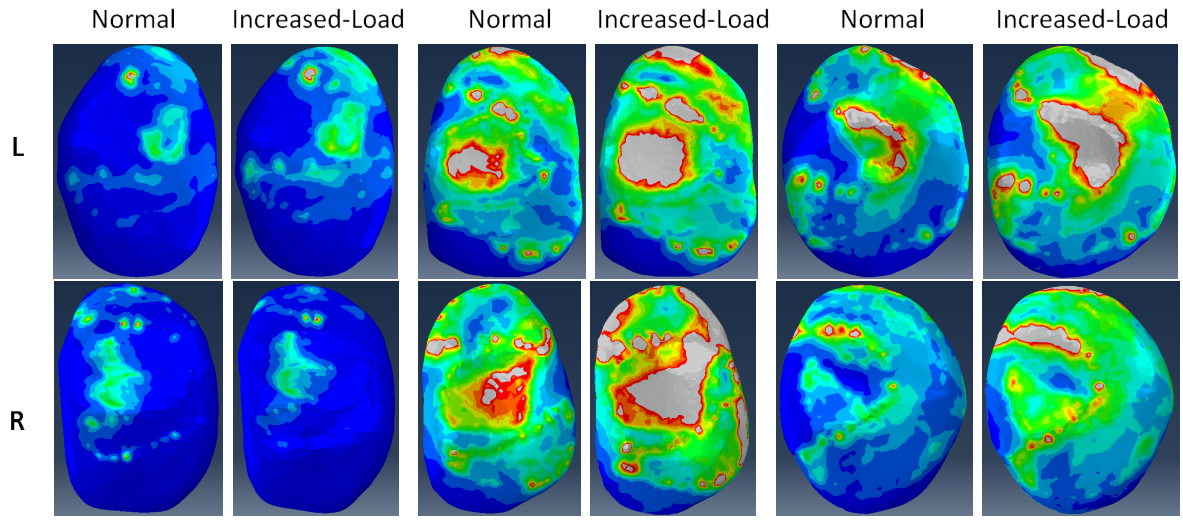
Figure 9.4: Increased load case results: Medial femoral cartilage: Von Mises stresses (thresholds 0 - 0.7 MPa) calculated for extended (top) left and (bottom) right knees. (Note: Anterior at top; inter-compartment cartilage at right; right knee results reflected for easier comparison; grey indicates above-threshold stress.)

lesions typically occur in the posterior region of the femoral cartilage.

The contact pressures calculated on the medial tibial cartilage surfaces have also been provided (Figure 9.7) for comparison with the contact pressures published by Shirazi *et al.* (Figure 9.1). Contact pressures in the current study's increased-load models spanned the majority of the articulating medial tibial cartilage surface with maximum contact pressures ranging from 6.4 MPa to 9.2 MPa. In comparison, the results presented by Shirazi *et al.* show a band of contact pressures from the centre-inside edge to the posterior/central-periphery of the medial tibial cartilage; maximum contact pressures were less than 4 MPa.

9.1.3 Discussion

In this section, the medial tibial cartilage contact pressures calculated in this study and reported by Shirazi *et al.* are compared first. Then, a short discussion on the relationships between applied load, displacement, von Mises stress, and contact pressure is provided.



(a) Subject 1 (b) Subject 2 (c) Subject 3

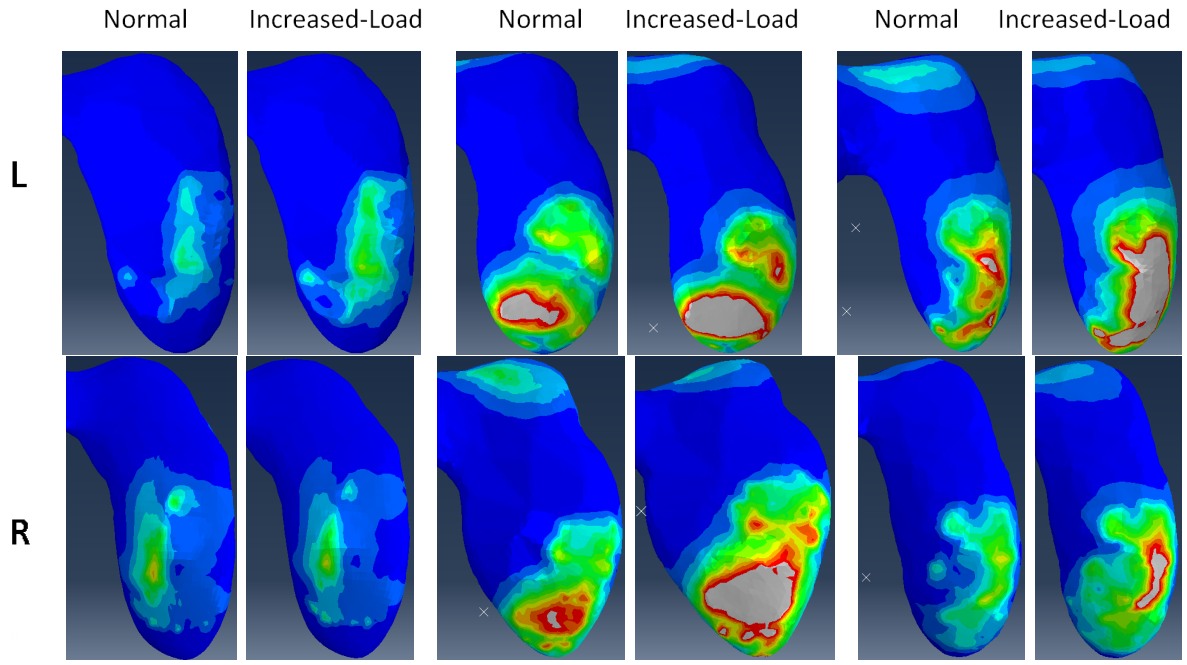
Figure 9.5: Increased load case results: Lateral tibial cartilage: Von Mises stresses (thresholds 0 - 1.0 MPa) calculated for extended (top) left and (bottom) right knees. (Note: Anterior at top; tibial spine at left; left knee results reflected for easier comparison; grey indicates above-threshold stress.)

Finally, the results of the normal and increased-load models are compared, with potential links between increased load and OA initiation being proposed.

The contact pressure patterns calculated in this study and reported by Shirazi *et al.* differed, with distributed contact pressures in this study but a band of pressures reported in the previously-published study. It is possible that different cartilage material properties (the three cartilage zones were modelled separately by Shirazi *et al.* – see Chapter 2.3.2.4) and/or the inclusion of ligaments (the FE model created by Shirazi *et al.* included ligaments) contributed to differences in contact pressure patterns. It is encouraging, however, that the contact pressure magnitudes were similar between the two studies.

This study showed that applying larger load cases resulted in increased displacements, von Mises stresses, and contact pressures on the articulating cartilage surfaces.

It is logical to predict that applying a larger load to an object causes the object to deform or displace by a larger amount. All of the models had increased displacement with increased load case. In addition, displacement increases were larger in the extended knee models, the models with the largest increases in applied loads (the smallest load case increase in the extended knee models was 276% versus the doubled or 100% load increases in the flexed knee models).

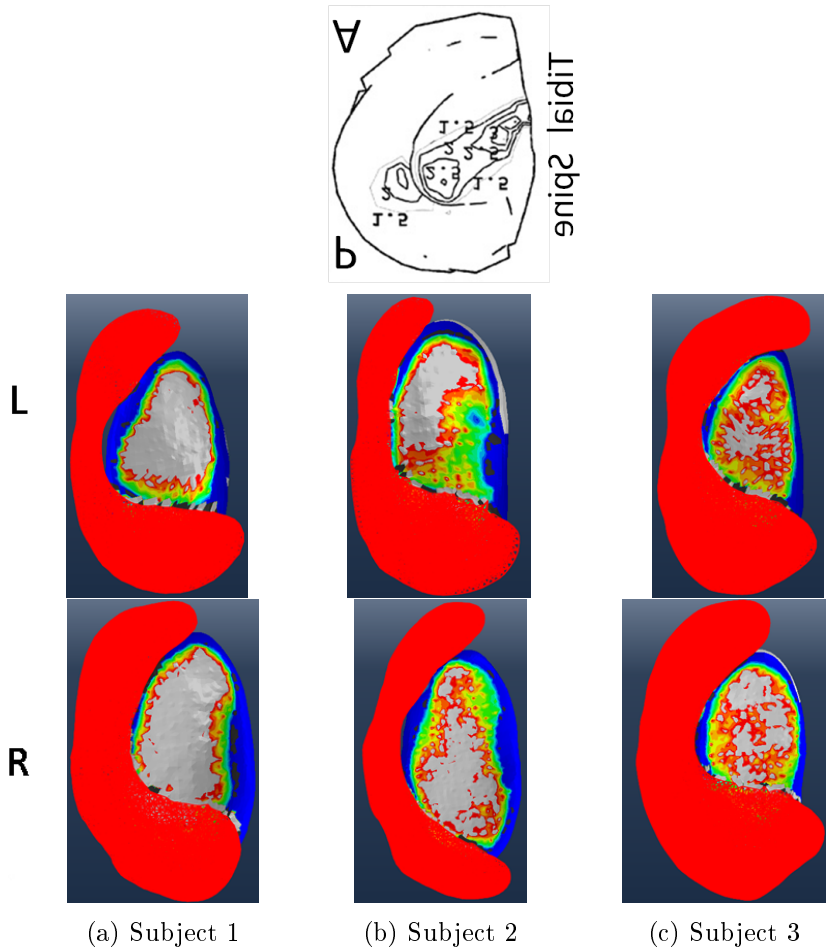


(a) Subject 1 (b) Subject 2 (c) Subject 3

Figure 9.6: Increased load case results: Lateral femoral cartilage: Von Mises stresses (thresholds 0 - 1.2 MPa) calculated for extended (top) left and (bottom) right knees. (Note: Anterior at top; inter-compartment cartilage at left; right knee results reflected for easier comparison; grey indicates above-threshold stress.)

It is also not surprising that increased loads led to increased stresses and pressures. These quantities are defined as force per unit area. Therefore, stress or pressure must increase if the increase in applied load is more than the resulting increase in contact area. All of the increased-load models had higher maximum stresses and contact pressures than their corresponding normal models, and larger stress and pressure increases were again calculated for the extended knee models than for the flexed knee models (due to larger increases in loads applied to the extension models). Although contact area increased in the increased-load models, this increase was not enough to balance the increased load applied. Explanations of this increased stress and pressure can be given both from the perspective of a model as a whole (the general stress and pressure patterns) and of elements specifically (the maximum stress and pressure magnitudes).

For the model as a whole: increasing the applied load increases deformation and therefore expands model contact area. Most of the normal models already had significant contact areas, however, limiting the potential for further increases. Consider, for example, the results of the flexed knee normal and increased-load (doubled load case) models. To



(a) Subject 1 (b) Subject 2 (c) Subject 3

Figure 9.7: Increased load case results: Medial tibial cartilage: Contact pressures (top) reported by Shirazi *et al.* [134] and calculated (thresholds 0 - 3.5 MPa) for increased-load models of the extended (centre) left and (bottom) right knees. (Note: Anterior at top; tibial spine at right; left knee results reflected for easier comparison; grey indicates above-threshold pressure; meniscus included in red for spatial orientation.)

maintain the stress and pressure values of the normal model, the contact area of the increased-load models would need to also double, but if more than half of the cartilage surface had been in contact in the normal model, it would be impossible to double the contact area in the increased-load model and so the stress and pressure must increase.

For elements specifically: if two elements were already in-contact in the normal model, those elements will have already deformed under the normal applied load. If a larger load were then applied to those elements in the increased-load model, it is unlikely the elements would be able to undergo significant further deformation to increase the contact area. In this case, a larger load is applied to a similar contact area - and again, the stress and pressure must increase (as was seen in both tibial cartilage stress increase patterns).

This explanation is illustrated in the Subject 2 flexed knee models (Figures 9.5 and 9.6). Elements in the central-inside edge region were already in-contact with higher stresses and pressures in the normal models; these stresses and pressures only increased further when a larger load was applied.

After considering the effects of increased load case on displacement, stress, and contact pressure, it is useful to consider the locations of these increased contact results. For the models of the extended knee, contact area and stresses on the posterior region of the medial tibial cartilage surface did not change noticeably between the normal and increased-load models. Instead, contact increased anteriorly, particularly in Subject 1 and Subject 2. The locations of these increased stresses were especially noteworthy as medial OA cartilage lesions are typically located in this anterior region. Femoral cartilage contact area and stress also extended anteriorly in the increased-load models. Contact spanned nearly the entire medial femoral cartilage surface, correlating well with the diagram from Weidow *et al.* [151, 152] showing widespread medial OA femoral cartilage degeneration.

Using this information, a potential link between increased body weight and medial OA initiation can be proposed: the increased load not only increased the stresses experienced in the cartilage but also changed the locations of contact. Cartilage is known to have regional material properties, with stiffer cartilage in areas of frequent contact and loading [9]. Changing the location of contact, therefore, could lead to less-stiff cartilage being loaded and degenerative diseases such as OA.

For the models of the flexed knee, the centres of the contact areas remained fairly constant between the normal and increased-load models; stresses increased and contact areas expanded without noticeable shifts in contact locations. The locations of higher stresses in the tibial cartilage and femoral cartilage were central and posterior, respectively. These locations correlate with locations of frequent lateral OA cartilage lesions.

Given the results in this study, if increased body weight were a factor in lateral OA initiation, the cause of initiation is unlikely to be a shift in contact location or loading new regions of less-stiff cartilage. Instead, the increased load might simply increase the stresses experienced in the lateral cartilage beyond the threshold for cartilage damage and disease. It is possible, however, that the increase in load case was not enough for the main

areas of contact to shift. It would therefore be interesting to increase the applied load cases to 2000 N to see if contact area shifts similar to those calculated in the extended knee models would then also be calculated in the flexed knee models.

9.1.4 Conclusions

Increasing the applied load led to increased displacements, von Mises stresses, and contact pressures. In the extended knee models, the contact areas on the tibial cartilage and femoral cartilage shifted anteriorly. In the flexed knee models, the centres of the contact area remained stationary while the contact area expanded in all directions. The anterior medial tibial cartilage contact and posterior lateral tibial cartilage contact in the increased-load models match typical OA cartilage lesion locations.

9.2 Globally decreased cartilage stiffness

9.2.1 Methods

Early OA is characterized by a damaged cartilage matrix with disorganized collagen fibres and a decreased number of proteoglycans [105]. Typically, collagen fibres help maintain the structural integrity of the matrix and proteoglycans maintain the fluid levels within the matrix. If the fibres are damaged, however, additional fluid can enter the matrix, resulting in cartilage swelling [22, 31, 62, 78] and decreased cartilage stiffness [78, 105]. A stiffness reduction of at least 20% is seen in early stages of OA [79].

In this study, the effect of damaged cartilage matrix was investigated by incrementally and uniformly decreasing the global Young's modulus of the tibial cartilage and femoral cartilage. Two sets of models were created and solved, one in which the stiffness modulus was decreased by 10% (10.8 MPa) and another in which the stiffness modulus was decreased by 20% (9.6 MPa). All other parameters remained constant.

The effects of decreasing cartilage stiffness were then compared to trends published by Meakin *et al.* [100]. This group created FE models of the femur, femoral cartilage, tibial cartilage, and meniscus. After identifying material properties commonly used in FE models, the group created two sets of FE models: one with 10% decreased material

properties and one with 10% increased material properties. The effect changing these material properties had on the femoral displacement was then determined (Figure 9.8). Note: although the displacement trend was calculated for the femur and not the tibial cartilage, the direction of the trend (increase or decrease) was expected to be the same for both structures.

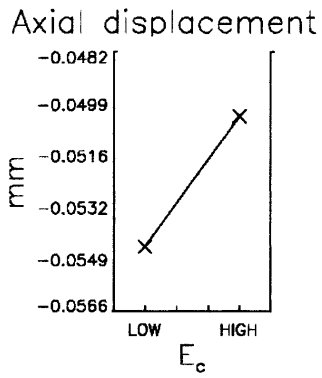


Figure 9.8: Effect of changing ((LOW) decreasing and (HIGH) increasing) the Young's modulus of cartilage and menisci on axial femoral displacement as reported by Meakin *et al.* ([100], permission to reproduce this figure has been granted by Elsevier.)

9.2.2 Results

There were negligible differences between the displacement, von Mises stress, and contact pressure patterns calculated for the normal models, 10% decreased Young's modulus models, and 20% decreased Young's modulus models. Therefore, figures of these results are not presented. Maximum magnitudes of the contact results varied with stiffness modulus, however.

For all models, there was an indirect relationship between Young's modulus and maximum displacement (Figure 9.9a). Maximum tibial cartilage displacement increased between 3.5% and 10% when cartilage Young's modulus was decreased by 10% and between 6.0% and 19% when the modulus was decreased by 20%. On the femoral cartilage surface, displacement increased between 1.7% and 30% for a 10% decreased modulus and between 6.7% and 120% for a 20% decrease in modulus.

The effect of decreasing Young's modulus on von Mises stress was not as consistent between models, though stress typically decreased with decreased modulus (Figure 9.9b).

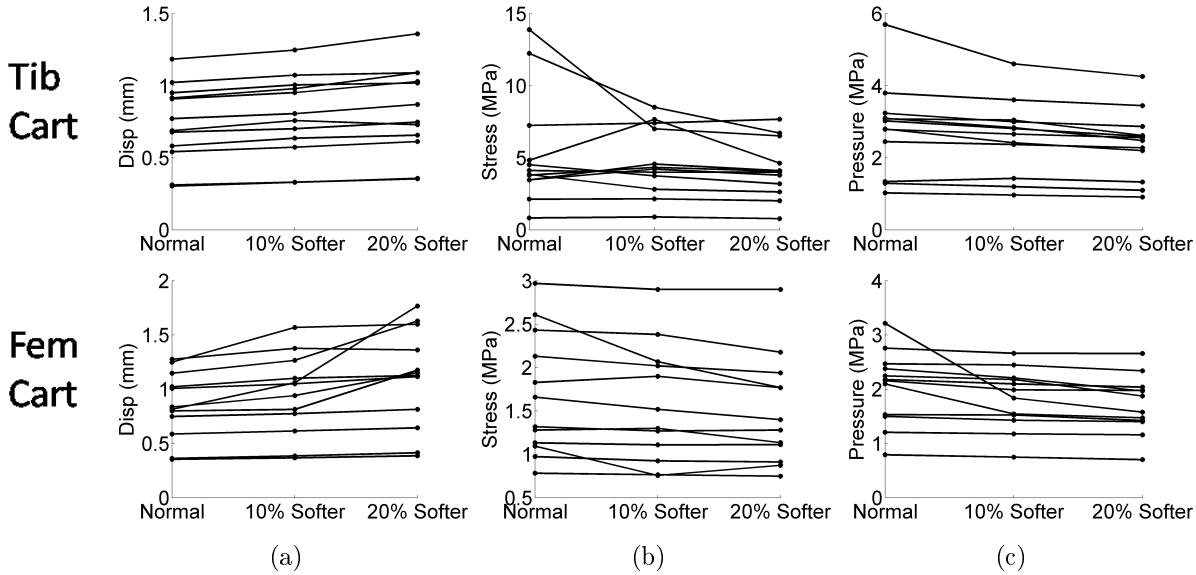


Figure 9.9: Globally decreased cartilage stiffness trends: Maximum magnitudes on (top) tibial cartilage and (bottom) femoral cartilage: (a) Displacements, (b) von Mises stresses, and (c) contact pressures for normal, 10% decreased cartilage stiffness, and 20% decreased cartilage stiffness FE models.

On the tibial cartilage surface, decreasing the modulus by 10% resulted in decreased stress in five of twelve models (range: 50% decrease to 59% increase). A 20% decreased modulus led to decreased tibial cartilage stresses in eight models (range: 53% decrease to 18% increase). On the femoral cartilage surface, decreases of 10% and 20% in modulus led to decreased stress in ten and twelve of the twelve models, respectively. Femoral cartilage stress in models with 10% modulus decrease ranged from 31% decrease to 3.9% increase; stress decreases ranged from 1.9% to 32% in models with 20% modulus change.

Contact pressure typically decreased with decreased Young's modulus (Figure 9.9c). On the tibial cartilage surface, pressure decreased in eleven of the twelve models with a 10% lower Young's modulus (range: 19% decrease to 6.7% increase) and in all twelve models with a 20% lower Young's modulus (range: 0.70% to 25% decrease). Contact pressure on the femoral cartilage decreased in all models of lower Young's modulus. In models with 10% lower modulus, pressure decreases ranged from 0.30% to 43%; in models with 20% lower modulus, pressure decreases ranged from 3.6% to 51%.

9.2.3 Discussion

As expected, maximum displacement increased as cartilage stiffness decreased, and larger changes in displacement were calculated for models with larger decreases in stiffness. These results agreed with the trend presented by Meakin *et al.* [100].

The relationship between Young's modulus and stress varied between models. In most models, decreased stiffness led to decreased stress because the decreased stiffness also led to increased displacement and therefore increased contact area. As in the increased-load models, stresses were larger in the tibial cartilage than in the femoral cartilage. This trend could again be explained by the more pixelated geometry represented by the denser tibial cartilage meshes. It should be noted that stress increased in some models, however. In these models, decreasing cartilage stiffness changed contact locations, with the contact area in the decreased-stiffness models being smaller than that in the normal models.

Contact pressure typically decreased with decreased stiffness, likely for the same reasons that von Mises stress decreased. In agreement with the other results, tibial cartilage contact pressures were typically higher than femoral cartilage contact pressures.

Although trends were seen in the maximum magnitudes of the contact results, changes in the overall distributions of these results were generally not apparent between the normal models and models with decreased cartilage Young's modulus. This observation suggested that a 20% change in cartilage stiffness was not sufficient to observe significant differences in cartilage displacement, von Mises stress, and contact pressure trends. Twenty per cent is the lower bound of cartilage modulus changes associated with early-stage OA; stiffness modulus decreases of up to 80% have also been reported in early-stage OA [79].

It is also possible that a global change in cartilage Young's modulus does not result in osteoarthritic-like changes. Matrix damage and cartilage lesions ordinarily initiate in specific locations rather than affecting the entire cartilage structure. Therefore, it is perhaps more physiological to decrease cartilage stiffness modulus locally (as was done in a study by Shirazi & Shirazi-Adl [133]), creating a stiffness gradient which may then lead to local cartilage matrix damage.

9.2.4 Conclusions

Decreasing the Young's modulus of the entire cartilage surfaces by 10% and 20% did not lead to noticeable changes in patterns of displacements, von Mises stresses, or contact pressures. Changing cartilage stiffness did, however, affect the maximum magnitudes of the contact results. Decreasing cartilage stiffness increased maximum displacement magnitudes and generally (but not always) decreased maximum magnitudes of von Mises stress and contact pressure.

A 20% decrease in stiffness was hypothesized to have a more significant, consistent effect on the contact results, but perhaps larger decreases in cartilage stiffness modulus or local as opposed to global decreases in cartilage stiffness are necessary for these effects to be seen.

9.3 Locally decreased cartilage stiffness

In the final study, the Young's modulus was changed locally in specific locations rather than globally throughout the cartilage. Local changes in stiffness were expected to better reflect the physiological conditions during which OA lesions form.

In the early stages of OA, the stiffness moduli of normal and osteoarthritic cartilage are approximately equal. As OA progresses, the diseased cartilage becomes increasingly less stiff. Mechanical tests show that stiffness decreases by approximately 20%, 45%, and 85% in mild OA, moderate OA, and severe OA, respectively [79]. Relatively small areas (less than 10 mm in diameter, [108]) of cartilage are initially affected; larger regions of cartilage are affected as OA progresses.

9.3.1 Methods

Ten models were created and solved in this study: five models of the extended knee (medial compartment stiffnesses decreased) and five models of the flexed knee (lateral compartment stiffnesses decreased). Each model within the sets represented a different grade of OA severity (normal, mild OA, mild-moderate OA, moderate OA, and severe OA).

The OA grades were modelled by changing two parameters: the per cent decrease

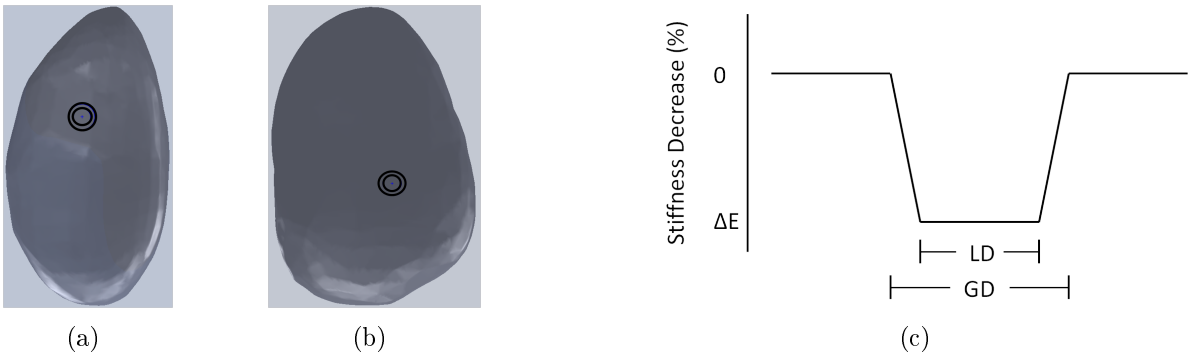
in local cartilage Young's modulus and the diameter of the cartilage region assigned the decreased Young's modulus (Table 9.1). (Severe OA models had larger areas of more decreased Young's modulus.) Note: a model representing mild-moderate OA (the smallest lesion size and moderate OA cartilage Young's modulus decrease) was created to investigate which parameter change had more effect on the contact results.

Table 9.1: Parameters used in locally decreased cartilage stiffness study. See Figure 9.10 for definitions of lesion and gradient diameters.

Grade	Stiffness Decrease (%)	Lesion Diameter (mm)	Gradient Diameter (mm)
Normal	0	0	0
Mild OA	20	1	2
Mild-Moderate OA	45	1	2
Moderate OA	45	2	3
Severe OA	85	3	4

These parameters were changed at typical locations of cartilage lesions [53]. After identifying the lesion location centres (Figure 9.10a, b), a purpose-specific computer code (Python 2.6.2, Python Software Foundation, Delaware, USA) assigned material properties to each tibial cartilage element according to the element's 3D distance from the lesion centre (Figure 9.10c). Elements within the 3D lesion diameter (including internal elements not on the articulating tibial cartilage structure) of the lesion centre were assigned a constant decreased Young's modulus. Elements located outside the lesion diameter yet within the gradient diameter of the lesion centre were assigned stiffness values based on the distance between the element and lesion centre. A linear gradient between the uniformly decreased Young's modulus and normal Young's modulus (12 MPa) was used in this region. Elements located outside the gradient diameter of the lesion centre were assigned a normal cartilage Young's modulus (12 MPa).

The magnitudes and patterns of displacements, von Mises stresses, and contact pressures were calculated for each model. In this study, the normal axial and anterior-posterior shear strains were also calculated. These local strains were considered to gain additional insight into potential mechanisms of cartilage lesion development.



(a) (b) (c)

Figure 9.10: Cartilage lesion locations and Young's modulus values used in locally decreased cartilage stiffness study: Typical lesion locations in (a) medial OA and (b) lateral OA; (c) cartilage stiffness decrease (ΔE) values assigned to elements located within the lesion diameter (LD), between the lesion diameter and the gradient diameter (GD), and beyond the gradient diameter.

9.3.2 Results

Decreasing local cartilage Young's modulus led to increased maximum displacement (Figure 9.11a) in the lesion locations in both the models of the extended (Figure **??**) and flexed (Figure 9.13) knees (lesion locations circled in black). For each grade of OA, displacements were larger in the flexed knee models than in the extended knee models. Displacements increased as the grade of OA worsened; the largest increases in displacement occurred in the severe OA models. In the extended knee models, local changes in cartilage stiffness also decreased displacement in a location (circled in white, Figure **??**) remote to these local changes in stiffness.

In agreement with the displacement results, axial and shear strain magnitudes also increased with decreased cartilage stiffness. Strains in the flexed knee models were larger than in the extended knee models, and strains increased with more severe grades of OA. Again, the largest increases in strain were in the severe OA models. When comparing axial and shear strains, axial strains were larger in the extended knee models and shear strains were larger in the flexed knee models.

Decreased von Mises stress was calculated in the areas of decreased cartilage stiffness. Stresses calculated for the extended and flexed knee models were approximately equal for a given grade of OA, with a slightly larger stress magnitude calculated in the extended knee model of mild OA. The largest changes in stress again occurred in the models rep-

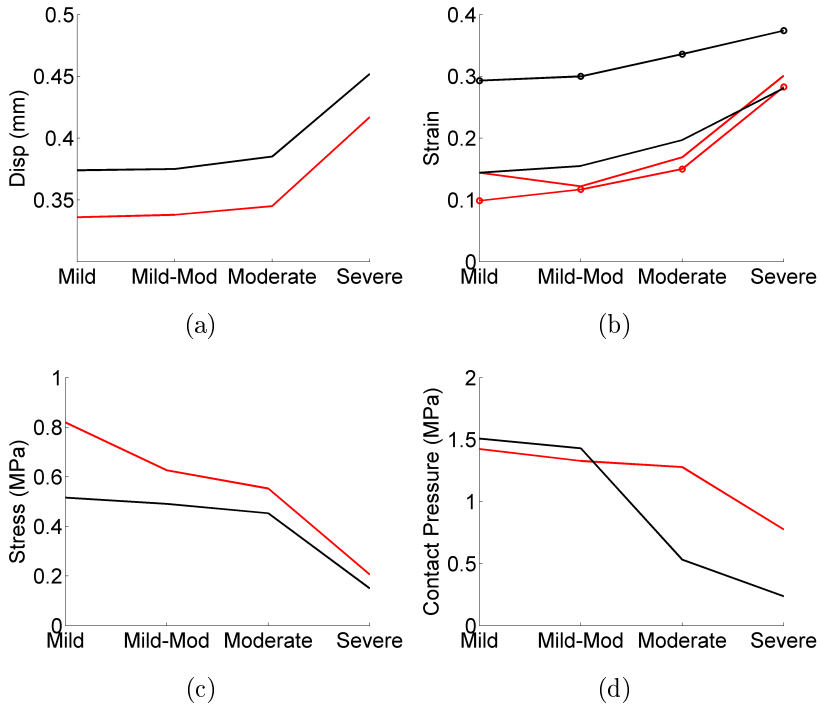


Figure 9.11: Locally decreased cartilage stiffness trends: Magnitudes of (a) displacements, (b) strains (shear strain shown with 'o'), (c) von Mises stresses, and (d) contact pressures (extended knee model results in red; flexed knee model results in black).

resenting severe OA. In agreement with the displacement results, extended knee model stress increased in the area (again circled in white) remote from the decreased cartilage stiffness.

Contact pressure also decreased locally with the locally decreased cartilage stiffness. Contact pressures in the extended and flexed knee models were initially approximately equal, with higher magnitudes of contact pressures calculated for the extended knee models of moderate OA and severe OA.

Results of the mild OA, mild-moderate OA, and moderate OA models were then compared to investigate whether lesion size or cartilage stiffness had a larger effect on the results. Although both parameter changes affected the results, the results calculated for the models of mild OA and mild-moderate OA were more similar than the results for the models of mild-moderate OA and moderate OA. This comparison suggested that lesion size affected the results more than the per cent decrease in local cartilage stiffness.

9.3.3 Discussion

Locally decreasing the Young's modulus of the cartilage led to local changes in both the extended knee models and the flexed knee models. The displacements, axial strains, and shear strains increased locally while the von Mises stresses and contact pressures decreased locally. These results were reasonable as the increased displacements led to increased contact areas and therefore decreased stresses and contact pressures. These changes were relatively small for the mild OA and mild-moderate OA models but became more noticeable in the moderate OA and especially severe OA models. Small stiffness changes in small regions of the cartilage were therefore less likely to lead to OA than either larger changes in stiffness or larger-sized lesions.

Decreased cartilage stiffness also led to changes in other areas of the extended knee models: displacement decreased and stress increased in an area near the periphery of the medial tibial cartilage. In these models, the decreased anterior cartilage stiffness caused the main area of contact to shift anteriorly. The increased anterior displacement of the femoral cartilage resulted in femoral cartilage lift off in the posterior region of the tibial cartilage, decreasing contact area and increasing stress in this removed periphery region.

It is also interesting to consider the axial and shear strains in more detail. As expected, strain magnitudes (calculated from displacement) increased as cartilage stiffness decreased. Perhaps of more interest, axial strains were larger than shear strains in the extended knee models, and, conversely, shear strains were larger than axial strains in the flexed knee models. These results can be explained by the mechanical axes of the tibia and femur in the two sets of models. In the extended knee models, the mechanical axes of the two bones were aligned so the majority of the displacement and therefore strain occurred axially. The mechanical axes of the tibia and femur were not aligned in the flexed knee models, however, resulting in larger non-axial displacements and strains.

The results of this study were then used to propose potential mechanisms of OA initiation and development. Model results showed that a decrease in cartilage stiffness (even by as little as 20%) increased both local axial and shear strains. Higher strains could damage the cartilage matrix, affecting the orientations of the fibres in the different cartilage zones as well as the functional ability of the matrix. If the damaged matrix continued

to experience higher strains, this damage might expand to affect larger regions of the matrix, resulting in further increases in cartilage swelling and further decreases in cartilage stiffness. This process can then repeat, resulting in larger lesions with increasingly decreased cartilage stiffness until osteoarthritic cartilage lesions develop. Comparing the predominant types of strain in the extended and flexed knee models, fibre damage in the extended knee models might be linked to compressive axial loads and matrix fibrillations extending through the zones of cartilage, whereas fibres in the flexed knee models might be damaged by shear tensile loads, perhaps overstretching and breaking the superficial zone fibres.

9.3.4 Conclusions

Locally decreased cartilage Young's modulus led to locally increased displacements, axial strains, and shear strains as well as decreased von Mises stresses and contact pressures. Changes in results became more noticeable in the models of moderate and severe OA: when cartilage stiffness was decreased by at least 45% and cartilage lesion diameters increased to at least 2 mm. In the extended knee models, local cartilage stiffness changes also resulted in decreased displacements and increased von Mises stresses in removed locations.

A theory of OA initiation and development was proposed using these results. Within this theory, decreases in cartilage stiffness lead to increased strain, which then leads to cartilage matrix damage, cartilage swelling, and further decreases in cartilage stiffness. Therefore, even small initial decreases in cartilage stiffness could lead to cartilage lesions and OA.

9.4 Discussion

Three studies were included in this chapter. These studies considered the effects of increased load case, globally decreased cartilage stiffness, and locally decreased cartilage stiffness as occurs in cartilage defects.

In the increased load case study, increasing the applied load resulted in increased displacements, von Mises stresses, and contact pressures. The area of contact generally

shifted anteriorly in the extended knee models and remained stationary for the flexed knee models.

In the globally decreased cartilage stiffness study, applied loads matched those applied to the normal models but cartilage stiffness was decreased. Decreasing cartilage stiffness by 10% and 20% had minimal effect on the calculated patterns of results. Trends were seen in the maximum magnitudes of results, however. Magnitudes of displacement increased while magnitudes of von Mises stress and contact pressure decreased.

These results were supported by the results of the locally decreased cartilage stiffness study. Locally decreasing cartilage stiffness again led to local increases in displacement (and strain) and decreases in von Mises stress and contact pressure. An addition, FE models representing more severe grades of OA were also created. As in the globally decreased cartilage stiffness study, the result patterns calculated for the mild OA models (20% local decrease in cartilage stiffness) were very similar to those of the normal knee models. Visual differences in result distributions were seen in models of more advanced stages of OA, particularly in the models representing moderate OA (45% decrease in cartilage stiffness) and severe OA (85% decrease in cartilage stiffness). In the extended knee models, there were some indications that decreasing stiffness caused contact to shift anteriorly to the area of the modelled cartilage defects.

Displacement increased in all studies for both the extended and flexed knee models. An anterior shift in contact area was also observed in the extended knee models in the increased load case and locally decreased cartilage stiffness studies. Shifting contact to previously infrequently-loaded areas of cartilage could be one mechanism leading to medial OA cartilage lesions (especially since the contact shifted to typical locations of medial OA lesions). Contact shifts were not observed in the flexed knee models, but stress magnitudes increased in the contact areas and might eventually exceed the threshold value for cartilage damage. Both increased stresses and strains (derived from displacements) could lead to cartilage matrix damage, with high stresses resulting in compressive damage and high strains breaking the collagen fibres in the matrix.

9.4.1 Limitations

The limitations of the FE model set-up mentioned in the previous chapter also applied to models in this chapter. Again, ligaments were not included, the No Separation constraint was used to restrain excessive motion, and literature-derived material properties were used for the cartilage and menisci. The aim of this chapter, however, was to investigate how changing various mechanical parameters affected the contact results. Since limitations were consistent between models, comparative results between models should give valid effects of increasing the applied load or decreasing the cartilage stiffness.

9.5 Conclusions

This chapter considered the effects of altering three mechanical parameters hypothesized to lead to OA initiation. Increased load case and locally decreased cartilage stiffness most noticeably affected the displacements, von Mises stresses, and contact pressures on the articulating cartilage surfaces. The next chapter provides a summary of the contributions, assumptions, and limitations of the work described in this thesis. Potential improvements to overcome some of these limitations are suggested. Then future work to improve upon and/or use the method of creating subject-specific FE models is proposed.

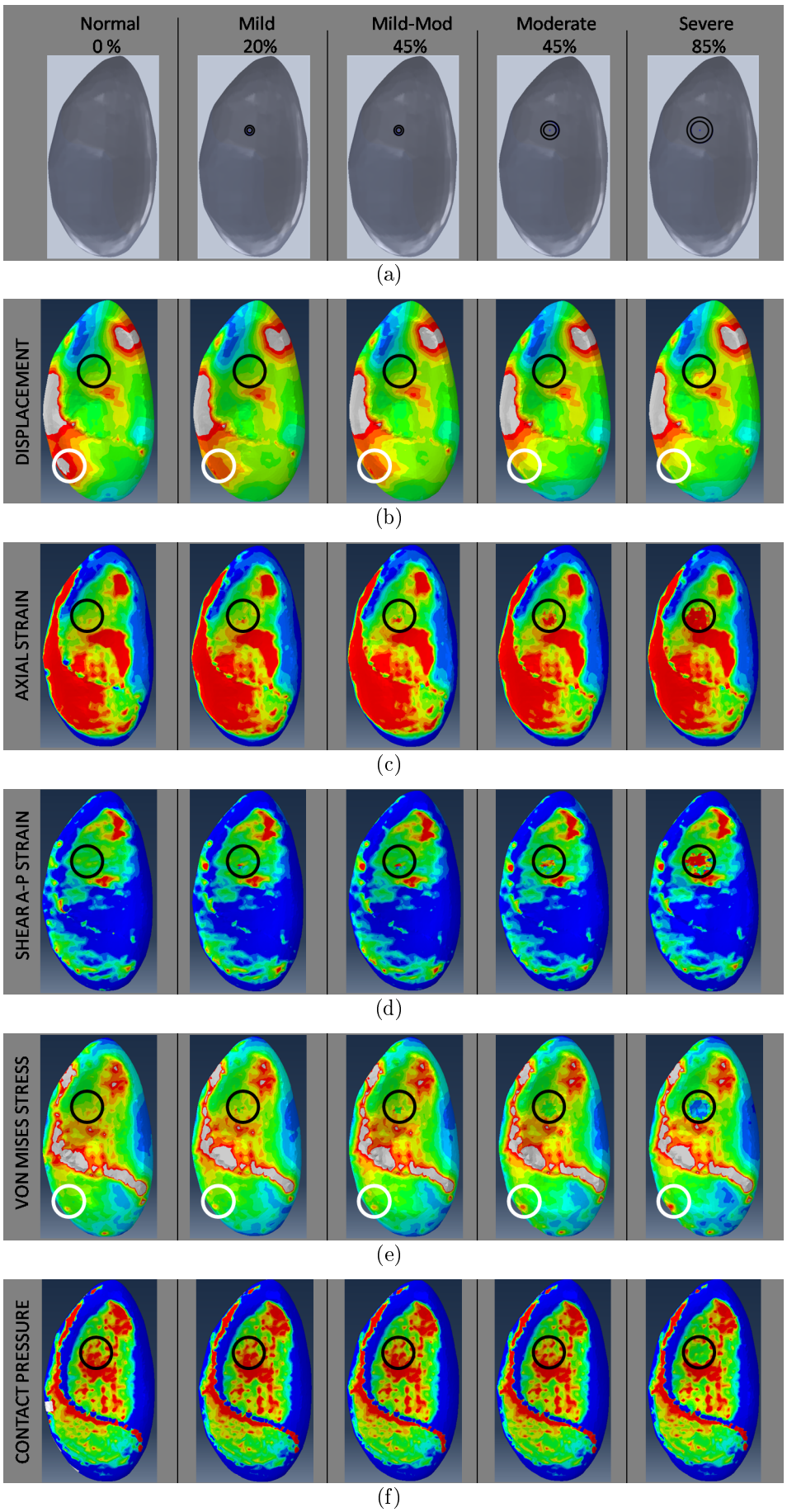


Figure 9.12: Locally decreased cartilage stiffness results: Medial tibial cartilage: (a) Lesion locations and sizes, (b) displacements, (c) axial strains, (d) shear anterior-posterior strains, (e) von Mises stresses, and (f) contact pressures. (Note: Circles in (b-f) not drawn to scale; changes removed from stiffness change location circled in white.)

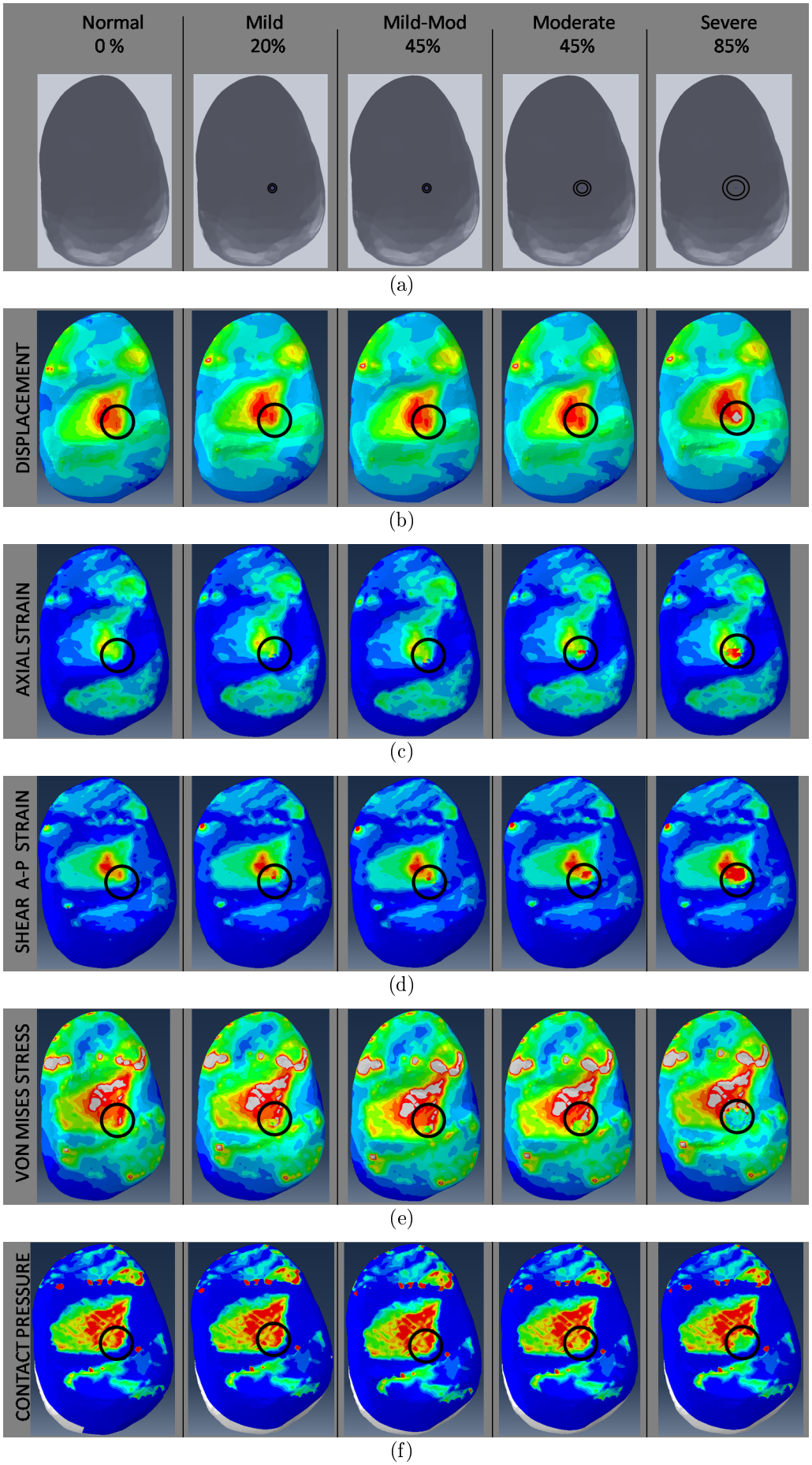


Figure 9.13: Locally decreased cartilage stiffness results: Lateral tibial cartilage: (a) Lesion locations and sizes, (b) displacements, (c) axial strains, (d) shear anterior-posterior strains, (e) von Mises stresses, and (f) contact pressure. (Note: Circles in (b-f) not drawn to scale.)

Chapter 10

Contributions and Future Work

10.1 Contributions

This thesis presented two novel contributions to the engineering and medical fields: developing a method of creating subject- and task-specific FE models and utilizing the subject-specific FE models to investigate potential mechanical causes of OA.

10.1.1 Developing a method of creating subject- and task-specific FE models

The first contribution was a method of creating and combining subject-specific geometry and load cases to create subject- and task-specific FE models. Previous FE models have used idealized shapes to model joint geometry, but using smooth, generic geometry has been shown to underestimate contact results [5]. Also, subjects experience unique loading patterns due to individual weight, muscle activation patterns, and motion patterns used to complete activities. FE models reflecting geometry and load cases specific to an individual would be beneficial in fields such as personalized medicine.

FE models with subject-specific geometry have been created previously, but no other study is known to have applied loads based on subject-specific muscle forces and joint reaction data. Generic load cases were applied to most models. One group (Yang *et al.*) did apply loads derived from motion analysis to their FE models. Load calculations required input from EMG activation timings reported in other studies for other subjects,

however, instead of being specific to the subject. Also, though this group reported model results for both extended and flexed knees, it was not clear whether flexed knee geometry was used in the FE models of the flexed knee (it appears models may have combined extended knee geometry with flexed knee loads).

This thesis sought to develop methods to create subject-specific FE models of both the extended and flexed knee. MRI scans of the knee in extension and flexion were used to create geometry of the two tibiofemoral orientations. Motion analysis and lower limb musculoskeletal models were used to calculate subject- and task-specific loads during level walking and rising from a stool. These data sets were then combined to create subject- and task-specific FE models. In addition to developing methods to create subject-specific geometry, calculate subject-specific load cases, and create subject-specific FE models, each method was then either validated or verified using intra- and inter-observer studies, comparison with values previously reported in the literature, or porcine cadaver studies.

10.1.2 Utilizing subject-specific FE models to investigate potential mechanical causes of OA

The second contribution made by this thesis was using the subject-specific FE models to investigate mechanical causes of medial OA and lateral OA. Models were first created of normal healthy knees. Various model parameters were then altered to reflect mechanical changes hypothesized to lead to OA. Contact locations in the normal and simulated mechanical change models were then compared to typical locations of cartilage lesions in OA. Models of the extended knee were compared to medial OA lesion locations; models of the flexed knee were compared to lateral OA lesion locations.

Results of the normal FE models showed widespread contact on the articulating cartilage surfaces, particularly in the models of the extended knee. Therefore, contact occurred both in regions of typical cartilage lesions as well as elsewhere on the articulating surfaces. Given this widespread contact and the relatively low stress and pressure magnitudes, the normal model results suggested these subjects would be unlikely to develop OA (in their current physiological states). This conclusion was not surprising since these models were created from data of young (less than 30 years old), normal subjects without symptoms

of OA.

The normal models were then altered to reflect three mechanical changes hypothesized to be linked to OA initiation: increased applied load, globally decreased cartilage stiffness, and locally decreased cartilage stiffness.

Two mechanisms of OA initiation were proposed based on the results of the increased load study. Increasing the applied load increased the magnitudes of the displacements, von Mises stresses, and contact pressures experienced on the articulating cartilage surfaces. These contact results may eventually be increased past damage thresholds and lead to OA initiation. Increasing the applied load also affected the contact patterns in the extended knee models; contact shifted anteriorly in the medial tibiofemoral compartment to locations of typical medial OA lesions. This shift in contact area suggested the second mechanism by which increased load may lead to OA: loading previously infrequently-loaded (and therefore less stiff [9]) regions of cartilage. On the other hand, flexed knee model contact patterns remained relatively stationary in the posterior-central region of the lateral tibiofemoral compartment (where lateral OA lesions typically occur). From these results, it can be concluded that if increased load leads to lateral OA, the mechanism likely involves increasing displacement, von Mises stress, or contact pressure magnitudes beyond the threshold value for cartilage damage instead of shifting contact regions.

Globally decreasing cartilage stiffness led to limited increases in magnitudes of displacement, limited decreases in magnitudes of von Mises stress and contact pressure, and limited effect on contact patterns. Larger (more than 20%) decreases in cartilage stiffness may be necessary to observe contact pattern changes indicative of OA initiation. Globally decreasing stiffness may also not represent the physiological conditions under which lesions form since local changes in cartilage are more likely to exist in early OA.

Local decreases in cartilage stiffness were then created in the models. Combinations of per cent decreased cartilage stiffness (20%, 45%, or 85%) and increased lesion diameter (1 mm, 2 mm, or 3 mm) were used to model different grades of OA. Locally decreasing cartilage stiffness and increasing lesion diameter increased local displacement magnitudes and decreased local stress and pressure magnitudes. Similar to the globally decreased stiffness results, minimal visual changes in contact patterns were observed in the models

of 20% locally decreased stiffness cartilage; larger changes in contact were calculated in models representing more advanced stages of OA. Contact results were most affected in the areas of locally decreased stiffness. Changes in contact were also calculated in other areas of the extended knee models, potentially indicating a shift in main contact area. As in the increased-load models, contact shifted anteriorly to locations typical of medial OA cartilage lesions. Axial and shear strains were also calculated for the locally decreased stiffness models to gain insight into how and why lesions may form. As expected, strain (calculated from displacement) increased as cartilage stiffness decreased. Axial strains were larger than shear strains in the extended knee models; conversely, shear strains were larger than axial strains in the flexed knee models. These trends might be explained by the different orientations of the mechanical axes of the femur and tibia during knee extension and knee flexion. The trends also suggested potential lesion development mechanisms in medial OA and lateral OA: medial OA lesions may be caused primarily by compressive damage (axial strain) while lateral OA may be caused mainly by tensile damage (shear strain).

In summary, contact in the normal knees was widespread and therefore did not correspond particularly well with locations of typical OA lesions. Additional models simulating mechanical changes potentially associated with OA initiation were then solved. These models showed that increasing the applied load and decreasing cartilage stiffness affected displacement, von Mises stress, and contact pressure results. Contact locations were also affected in some of the models. Anterior contact shifts were calculated in extended knee models, shifting contact to areas of typical medial OA cartilage lesions. The centre of the contact area typically did not change in models of the flexed knee; instead contact occurred in a posterior-central region and then expanded in all directions. Lateral OA lesions are frequently observed in this posterior-central region. These results suggested that increased applied load and locally decreased cartilage stiffness may lead to osteoarthritic cartilage lesions.

10.2 Future work

It is important to address limitations associated with data collection, data processing, and modelling and then suggest possible improvements to overcome these limitations.

Detailed descriptions of limitations and their effects on project results have been provided in the individual chapters. As a summary, however, the main specific limitations of this study included the resolution of the MRI scans, lack of ligaments and associated need for extra constraints in the FE models, and type of specimens used in the validation study. A general limitation of this study was the number of subjects included. Funding and time limitations only allowed for data collection of three subjects. Consequently, statistical tests could not be performed; only trends could be reported.

The remainder of this chapter proposes future work which could be used to first address some of the project limitations and then extend the methods developed in the project for use in new applications.

10.2.1 Future improvements to work

First and perhaps the biggest improvement, any future studies should incorporate better resolution medical scans. Geometry is a main feature of a subject-specific model, and it has a large effect on the FE model results. Improving the ability to accurately and systematically delineate cartilage from menisci and subchondral bone is therefore crucial to calculating representative subject-specific contact results.

A study could be conducted to investigate how scan resolution affects segmented geometry and FE model contact results. In this study, a high resolution scan could be obtained and then downsampled to create artificially lower resolution scans. Structures could then be segmented in these different resolution scans and the resulting geometries compared. FE models with these different geometries could then also be created and the results of the models compared.

The segmentation process could also be improved. This process currently requires approximately five hours per scan and a significant amount of manual input from the user. Software tools are being developed (Mimics 13.0) to help automate this process, but these tools did not function properly for the resolution of the MRI scans collected in

this study. Future studies could investigate more automatic methods of segmentation to speed model creation.

Another big improvement would be including ligaments in the FE models. After integrating ligaments, the axial-only displacement constraints could be removed from the femur, allowing all three components of the applied load and moment to be applied to and act on the model. As model results are likely to be affected by the moments and anterior-posterior and medial-lateral force components, applying these extra loads would improve model subject-specificity.

Including ligaments would also improve model stability and allow for the cartilage-menisci surfaces to separate during model solution, improving the physiological representation of the model. Without the No Separation contact constraint, stress concentrations along the cartilage-menisci interface might be avoided. Another method of avoiding these stress concentrations while creating a more physiological model of the knee would be tying the meniscal horns to the tibia (rather than to the tibial cartilage).

Future studies could also involve improving soft tissue material properties. In this project, cartilage was modelled as a homogeneous material; material properties were derived from values cited in the literature. Cartilage is a heterogeneous material [9], however, with different material properties in different zones of the cartilage as well as in different geographic locations on the cartilage surface. Material properties are also likely to vary between individuals.

An interesting future study would be to develop FE models with zone-specific cartilage material properties (such as the models created by Shirazi & Shirazi-Adl [132, 133]). Contact results calculated for models with simple and complex material properties could then be compared to investigate whether/how the specificity of the material property definitions affects the contact results. Models could also be created in which the material properties varied across the cartilage surface. Ideally, subject-specific and region-specific material properties would be used in FE models, but in the absence of *in vivo* methods of obtaining these properties, regional properties could be obtained from human cadaver studies. Similarly, zone-specific and region-specific material properties could also be determined and used to define meniscal material properties.

Finally, the validation study could be improved by repeating the procedure using human cadaver knees. Ideally, the model set-up of the validation study models would match the model set-up of the normal and simulated mechanical change models. The current validation study used porcine specimens and so assigned porcine material properties (where available) while the remaining models were of human knees and so assigned human material properties. Material properties of immature porcine specimens are relatively unknown, however, introducing uncertainty into the models. On the other hand, material properties of mature human tissues are available in the literature and were assigned to the normal and simulated mechanical change models. These same material properties could be assigned to future human validation study models.

10.2.2 Future extensions to work

Future work could also extend the described FE model creation method for use in new applications. Cartilage and menisci structures were included in these FE models, but results were only reported for the cartilage as these are the structures most closely associated with OA. Future studies could extend the mesh convergence test to include the menisci and then investigate meniscal stresses and contact pressures. This application is particularly exciting as meniscal contact results could be used to investigate potential causes of damage in the menisci, for example, meniscal tears.

Future studies could also test additional potential mechanical causes of OA. For example, the coefficient of friction could be increased to model synovitis [16]. The alignment of the femur and tibia could be adjusted to simulate varus and valgus malalignment [43]. The subchondral bone could be modelled as a separate structure and assigned increasingly stiffer Young's modulus values to mimic ossification in early OA [22]. FE models with load cases representative of additional functional activities or more demanding exercise activities could also be created as other activities (such as stair ascent, squats, or jumping activities) may be equally or more likely to lead to OA.

Future studies could also involve creating FE models based on data from patients suffering from OA. These models could then be solved and compared both to the models of normal subjects as well as to the models with simulated mechanical changes. Comparing

the results of the simulated mechanical change models and OA patient models would serve as an additional check of the simulated mechanical change trends.

The FE model creation method could also be used to create models for pre-surgery planning. Baseline models could be used to determine locations of stress concentrations prior to surgery. These models could then be altered to simulate changes made during surgery and re-solved to investigate the effects of different potential surgical procedures. In this way, the best surgical approach could be determined before surgery.

10.3 Conclusions

In summary, a method of creating and combining subject-specific geometry and load cases to create subject-specific FE models has been developed. This method was validated using a porcine validation study before being used to create FE models of normal human knees in both extension and flexion. Models were then altered to reflect mechanical changes hypothesized to lead to OA; potential mechanisms of OA initiation were proposed based on model results.

Future work could involve making the models increasingly physiological (particularly by including ligaments) or increasingly subject-specific (particularly with more specific material properties). The model creation method could also be used for a variety of new applications, such as pre-surgery planning.

Appendices

Appendix A

Instructions for Intra- and Inter-Observer Segmentation Tests

A.1 Introduction

This document gives instructions on two tasks: how to segment the femur, tibia, femoral cartilage, and tibial cartilage within an MRI scan - and how to determine the centre locations of seven registration markers. Five individuals (of which you are one) are being asked to complete the steps below so that an inter-observer test can be conducted. This test considers, for the first task, whether different individuals select the same pixels from an MRI scan when defining two of the knee's bones as well as the corresponding cartilage structures. It is important to investigate whether the segmentation is repeatable because the shapes are later used to create the geometry of finite element models. For the second task, the inter-observer test will show whether different individuals pick the same centre points of the markers. The markers will later be used to register two sets of data; therefore, it is important to have an estimate of the differences between individuals associated with selecting the marker centres used for registration.

You will be given an MRI scan of a normal human right knee. You are to segment the femur, tibia, femoral cartilage, lateral tibial cartilage, and medial tibial cartilage into separate masks which will then be made into 3D objects. The 3D objects made by the different individuals will then be compared to determine the per cent difference of the objects' volumes, surface areas, and dimensions. Locations of maximum variation

between the 3D objects created by different individuals will also be determined. You are also to select the centre points of seven markers. The per cent difference between different individuals' centre points will also be calculated.

A.2 Segmentation protocol steps

A.2.1 Screen orientation and segmentation practice

A Mimics project file will be created for you to work in. Within Mimics, most of the computer screen is occupied by three views of the knee: coronal, sagittal, and axial (Figure A.1). You will be segmenting (choosing pixels) in these three views to create the final 3D object (which is shown in the bottom right box).

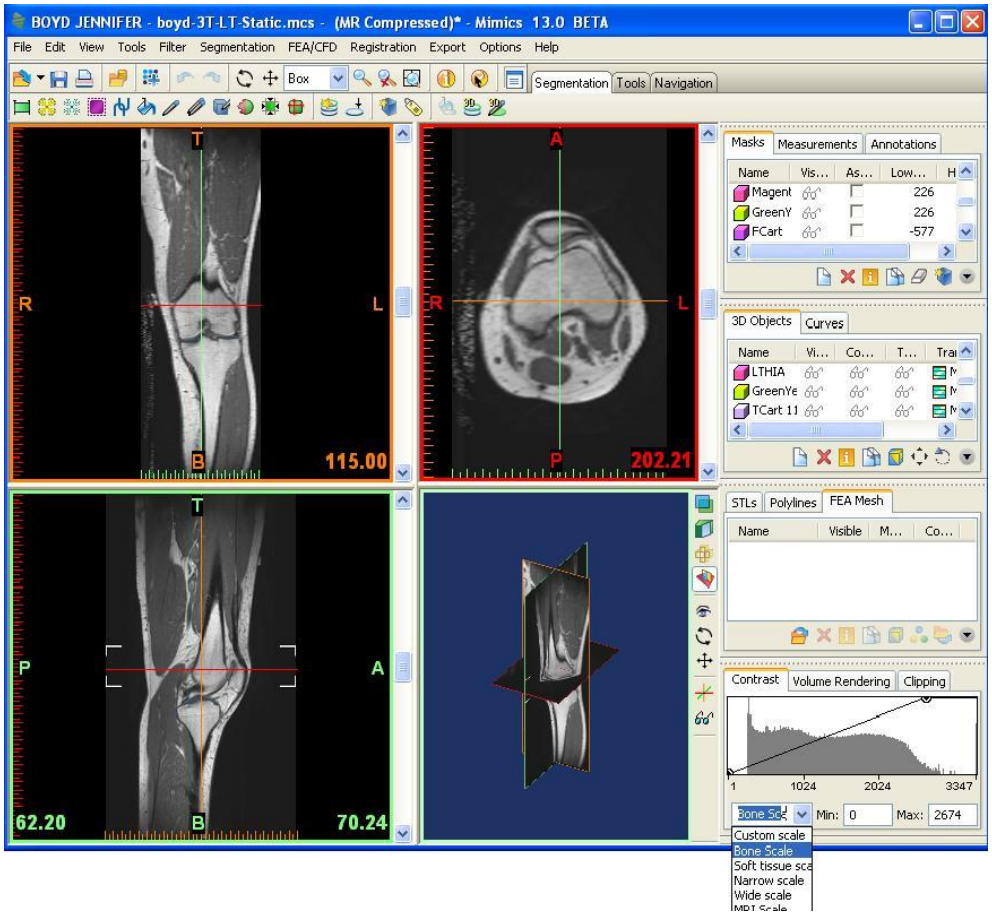


Figure A.1: Mimics work screen.

During segmentation, the vertical boxes to the far right of the screen will be important. The top box (Masks) is where you will create, rename, and select the masks you will edit.

Below that is a box (3D objects) where the 3D objects will be created and stored. Ignore the third box (STLs). The bottom box controls the contrast of the scan. This box becomes important if you accidentally right click on the figures and all of the views turn white. You can change the view back by selecting 'Bone Scale' on the dropdown box.

To segment, you will need to use the line of icons located above the three views of the knee. Below the normal File-Edit-View line are the zoom icons. To zoom into any of the three views, click the normal magnifying glass and then draw a square around the area you wish to magnify. To return to the original zoom level, click the magnifying glass with the small red cross and then click the view you want to zoom out of. Below this line, moving left to right, the icons you will use are the eighth icon (two pens indicating multiple slice edit) and the eleventh icon (a grid with arrows pointing in indicating crop mask).

You will spend most of your time using the multiple slice edit icon. When you click on this icon, a box will pop up with multiple options (Figure A.2). From left to right, you can change the radius (width or height) of the circle you use to add or remove masking pixels (theoretically you can change this circle into an oval by unselecting 'Same Width & Height'). To the right of this is a dropdown box showing the view currently being edited: coronal, sagittal, or axial. You can only edit in the currently selected view- the cursor will be a null circle in all other views. The options of remove and add are next to the right. Note: it is not necessary to click 'Apply' after editing each frame, but be careful to remember whether you have been adding to or subtracting pixels from the mask since the last time you clicked 'Apply' or you might accidentally add or delete information!

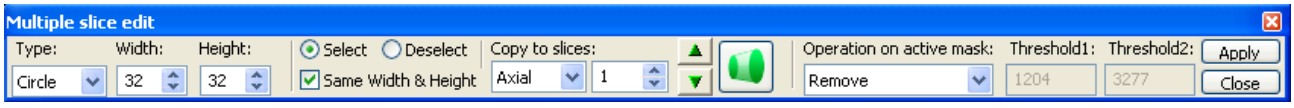


Figure A.2: Multiple slice edit toolbox.

A premade mask named 'Trial' has been created and is located in the Masks box. Please spend approximately 10 minutes familiarizing yourself with the icons, practicing adding as well as removing parts of the mask, cropping the mask, zooming in and out of

the different views, and moving through the various slices of the MRI scan in the different views. At the end of this time, feel free to ask any questions you have pertaining to the segmentation you will be completing.

A.2.2 Actual segmentation

Advance warning: This computer is known to crash - save your work often!
Now that you have practiced using Mimics, you are ready to begin segmenting. As an overview, you will first create two masks: one of the femur and femoral cartilage and a second of the tibia, lateral tibial cartilage, and medial tibial cartilage - let's call these M1 and M2, respectively. You will then subtract the cartilage structures from these masks to create two new masks - one of just the femur and one of just the tibia; we'll call these M3 and M4, respectively. Using Boolean operations, you can then subtract M3 from M1 to obtain a mask of just the femoral cartilage. Likewise, you can subtract M4 from M2 to get a mask of the lateral and medial cartilage. The tibial cartilage sections can then be separated into two separate masks as well. (Please note: reference diagrams of expected femoral and tibial cartilage locations from Human Anatomy by Gosling *et al.* [50] are provided.)

The first step in segmenting is creating a new mask. Begin by creating a mask for the femur and femoral cartilage. Click on the 'New' icon (a white empty sheet of paper located in the Masks box). A coloured thresholding hill will appear (Figure A.3). By moving the two lines back and forth, you can change which pixels are included in the mask (coloured pixels indicate pixels included in the mask). Adjust these lines so that most of the pixels representing the femur and femoral cartilage are coloured (suggested thresholding ranges are between 400 and 1800). Click 'Apply'. In the Masks box, single click the name of the mask you have just created. Rename it 'WholeF'. You have now created a mask that can be edited in the three views.

The first step of editing your mask is cropping the mask to only contain pixels in the areas of the femur and femoral cartilage. Click the 'Crop Mask' icon and move the boxes so that they include all of the pixels representing the femur and femoral cartilage but as few other pixels as possible. Note that this dimensions box can be edited in all three

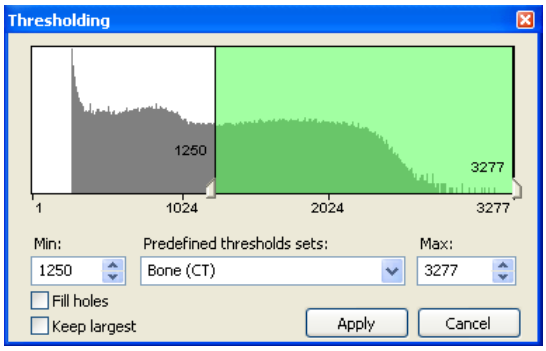


Figure A.3: Setting thresholding limits.

views. It is easiest to start in the sagittal view, then adjust in the coronal view, and finally check in the axial view. Once you are happy with the dimensions box, click 'OK'.

The remaining steps involved in segmenting include adding and removing pixels from the mask. You can do this using the multiple slice edit icon as explained previously. Begin segmenting in the sagittal view - then segment in the coronal view (which will be faster since you have already cleaned up the mask in the first view) - and then verify you are happy with your mask using the axial view. For the WholeF mask, you should include all of the femur and femoral cartilage in your mask - remove any pixels representing other soft tissues such as muscle, menisci, fat, ligaments, or tendons. To standardize the masks for later analysis, however, do not segment pixels located above the 275.04 line (include the pixels on the line). (To locate this line in the sagittal view, pan through the axial view slices; you will notice that as you move through the axial slices, the numbers at the bottom of the sagittal view change.)

When you have finished segmenting this mask, create a copy of the mask by clicking the 'Duplicate Mask' icon (two side-by-side sheets of paper) in the Masks box. Rename this new mask 'Femur'. This is the mask where you will subtract the cartilage structure. Since it is easier to see the cartilage boundaries in the original MRI colour scheme, click the eyeglass icon next to the Femur mask in the Masks box. The mask should become invisible. Now click the multiple slice edit icon towards the top of the page. Again starting in the sagittal view, highlight the femoral cartilage (being careful not to highlight any of the femur itself) and remove these pixels from the Femur mask. Femoral cartilage is located anteriorly where the femur and patella contact, along the femur's distal surfaces

where the femur and tibia contact in extension, and posteriorly where the femur and tibia contact in high flexion (Figure A.4); be sure to remove all of these areas of femoral cartilage from the Femur mask. Please note that the dark-coloured pixels beneath the cartilage are part of the subchondral bone and should NOT be removed from the Femur mask. After you have worked through the sagittal view, re-click the eyeglass icon to make the mask visible again. Check your work in the coronal view. If you are not happy with the mask you have created of the femur, edit the views until you are satisfied.

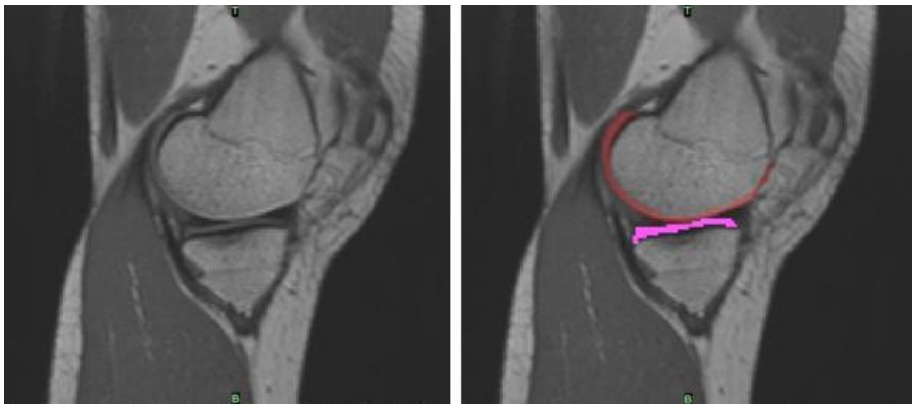


Figure A.4: Expected cartilage locations (femoral cartilage in red; tibial cartilage in pink).

Once you have completed the Femur mask, you are ready to create the mask of the femoral cartilage. To do this, click the dropdown box in the Masks box and select 'Boolean Operations'. A box will pop up. Under Mask A select 'WholeF', for the operation select 'Minus', for Mask B select 'Femur'. When you click 'Apply', a new mask will be created. Rename this mask 'FCart'. You have now segmented and created separate masks for the femur and femoral cartilage.

Next, you will segment the tibia, medial tibial cartilage, and lateral tibial cartilage. As with the femur, you will first need to create a new mask for the tibia and its associated cartilage segments. A similar thresholding range is suggested. Name this mask 'WholeT'. Crop the WholeT mask so that only pixels representing the tibia and tibial cartilage are included in the dimensions box, and then remove any pixels from the mask which do not belong to the tibia or tibial cartilage. As with the WholeF mask, standardize the WholeT mask by not selecting any pixels below the 55.58 line (as seen in the sagittal view).

When you are happy with your WholeT mask, make a copy of it. Rename this new

mask 'Tibia'. Similar to the previous steps, click on the eyeglass to make the Tibia mask disappear and then, using the multiple slice edit icon, remove both the medial and lateral tibial cartilage segments from the Tibia mask. Tibial cartilage is relatively thick in central areas where the tibia and femur contact in extension as well as posteriorly on the lateral side where tibiofemoral contact occurs in high flexion. (The reference diagrams of cartilage location will be especially helpful during this stage of segmentation.) Again, note that the dark-coloured pixels beneath the cartilage should NOT be removed from the Tibia mask. After finishing the Tibia mask, re-click the eyeglass icon so that the mask becomes visible again. Visually inspect the mask in the three views.

Next, create a mask of both cartilage segments. To do this, click the 'Boolean Operations' icon on the dropdown menu in the Masks box. Make Mask A 'WholeT', the operation 'Minus', and Mask B 'Tibia'. Click 'Apply'. Rename the new mask you have just created 'TCarts'.

The final segmentation task will be dividing the TCarts mask into separate medial and lateral tibial cartilage masks. Make a duplicate copy of the TCarts mask. Rename this copy 'MTCart'. Using the multiple slice edit icon, remove the pixels representing the lateral tibial cartilage from this mask. Then make another duplicate copy of the TCarts mask. Rename this copy 'LTCart' and remove the pixels representing the medial tibial cartilage segments. Save the Mimics project.

A.3 Registration marker centre determination steps

The second task involves finding the centre locations of seven markers in the MRI scan. The markers are located on the medial femoral epicondyle, lateral femoral epicondyle, medial tibial condyle, tibial tuberosity, fibular head, mid thigh superior to patella, and superior lateral patella.

After locating a marker (seen in the scan as approximately 15-pixel-diameter bright circles with dark centres), you will first need to determine which sagittal slice represents the middle of the marker. Scroll through the sagittal view slices to count the number of slices the marker can be seen in. Divide this number by two (rounding up if an odd number is calculated). Scroll to the sagittal slice containing the marker with the lowest

number in the bottom right corner of the sagittal view and then scroll up the number of slices you have just calculated.

Once you have determined the middle slice location of a marker, count the number of pixels that exist between the extreme top and bottom of the marker and the extreme right and left edges of the marker. Divide these numbers by two (again rounding up any odd numbers). From the marker's extreme bottom left pixel in the current slice, move up and to the right the numbers of pixels you have just calculated to reach the marker's centre location. Click this location on the screen. The x-y-z coordinates of this location (the centre of the marker) are displayed at the bottom right section of the work screen. Record this location. Also record which landmark location you believe the marker represents. Continue repeating these steps until the centre of each marker has been found.

Appendix B

Testing New Force Plate and Convertor Card

A new force plate and analog-to-digital card capable of collecting data at 4 kHz were installed in the Oxford Gait Laboratory immediately prior to data collection; therefore, the new testing equipment's resonant frequencies were determined. The resonant frequencies were then compared to the expected frequencies of heel strike to investigate the introduction of error caused by interaction of the recorded and resonant frequencies.

Testing involved sharply striking the new force plate with a pointed object while recording force data. Five trials were conducted. A periodogram was created (Matlab) for each of the trials and the resonant frequencies in the x, y, and z directions were determined (Table B.1). In both the x (medial-lateral) and y (anterior-posterior) directions, the resonant frequencies were approximately 0.7 kHz. The resonant frequency in the z (superior-inferior) direction ranged from 1.40 kHz to 1.45 kHz with a mean of 1.44 kHz. Using this data, the project's force plate collection speed was set to 1 kHz. This collection speed allowed for detailed information to be recorded while also avoiding errors introduced by recording signals close to the resonant frequency.

Table B.1: Resonant frequencies of force plate (in kHz).

	X	Y	Z
Trial 1	0.7	0.7	1.45
Trial 2	0.7	0.7	1.40
Trial 3	0.7	0.7	1.45
Trial 4	0.7	0.7	1.45
Trial 5	0.7	0.7	1.43

Bibliography

[1] Abaqus. *Theory manual, Version 6.4.* Warrington, UK: Dassault Systemes, 2003.

[2] Abaqus. *Analysis user's manual Version 6.7, Volume V: Prescribed conditions, constraints & interactions.* Warrington, UK: Dassault Systemes, 2007.

[3] Abaqus. *Getting started with Abaqus, Version 6.9.* Warrington, UK: Dassault Systemes, 2009.

[4] N.E. Akalan, M. Özkan, and Y. Temelli. Three-dimensional knee model: Constrained by isometric ligament bundles and experimentally obtained tibio-femoral contacts. *J Biomech*, 41(4):890–896, 2008.

[5] A.E. Anderson, B.J. Ellis, S.A. Maas, and J.A. Weiss. Effects of idealized joint geometry on finite element predictions of cartilage contact stresses in the hip. *J Biomech*, 43(7):1351–1357, 2010.

[6] T.P. Andriacchi, S. Koo, and S.F. Scanlan. Gait mechanics influence healthy cartilage morphology and osteoarthritis of the knee. *J Bone Joint Surg [Am]*, 91(Supplement 1):95–101, 2009.

[7] T.P. Andriacchi and A. Mündermann. The role of ambulatory mechanics in the initiation and progression of knee osteoarthritis. *Curr Op Rheum*, 18(5):514–518, 2006.

[8] T.P. Andriacchi, A. Mündermann, R.L. Smith, E.J. Alexander, C.O. Dyrby, and S. Koo. A framework for the *in vivo* pathomechanics of osteoarthritis at the knee. *Ann Biomed Eng*, 32(3):447–457, 2004.

[9] K.A. Athanasiou, A. Agarwal, and F.J. Dzida. Comparative study of the intrinsic mechanical properties of the human acetabular and femoral head cartilage. *J Orthop Res*, 12(3):340–349, 1994.

[10] J.Y. Bae, K.S. Park, J.K. Seon, D.S. Kwak, I. Jeon, and E.K. Song. Biomechanical analysis of the effects of medial meniscectomy on degenerative osteoarthritis. *Med Biol Eng Comput*, 50(1):53–60, 2012.

[11] E. Baker. *Biomechanical modelling of the foot*. University of Oxford, Department of Engineering Science, Undergraduate final-year project report, 2009.

[12] M.A. Baldwin, P.J. Laz, J.Q. Stowe, and P.J. Rullkoetter. Efficient probabilistic representation of tibiofemoral soft tissue constraint. *Comput Methods Biomech Biomed Engin*, 12(6):651–659, 2009.

[13] Y. Bei and B.J. Fregly. Multibody dynamic simulation of knee contact mechanics. *Med Eng Phys*, 26(9):777–789, 2004.

[14] P. Beillas, G. Papaioannou, S. Tashman, and K.H. Yang. A new method to investigate *in vivo* knee behavior using a finite element model of the lower limb. *J Biomech*, 37(7):1019–1030, 2004.

[15] M.Z. Bendjaballah, A. Shirazi-Adl, and D.J. Zukor. Biomechanics of the human knee joint in compression: Reconstruction, mesh generation and finite element analysis. *Knee*, 2(2):69–79, 1995.

[16] M.J. Benito, D.J. Veale, O. FitzGerald, W.B. van den Berg, and B. Bresnihan. Synovial tissue inflammation in early and late osteoarthritis. *Ann Rheum Dis*, 64(9):1263–1267, 2005.

[17] G. Bergmann, G. Deuretzbacher, M. Heller, F. Graichen, A. Rohlmann, J. Strauss, and G.N. Duda. Hip contact forces and gait patterns from routine activities. *J Biomech*, 34(7):859–871, 2001.

[18] G. Bergmann, F. Graichen, and A. Rohlmann. Hip joint loading during walking and running, measured in two patients. *J Biomech*, 26(8):969–990, 1993.

[19] J.T. Bingham, R. Papannagari, S.K. van de Velde, C. Gross, T.J. Gill, D.T. Felson, H.E. Rubash, and G. Li. *In vivo* cartilage contact deformation in the healthy human tibiofemoral joint. *Rheum*, 47(11):1622–1627, 2008.

[20] L. Blankevoort, J.H. Kuiper, R. Huiskes, and H.J. Grootenboer. Articular contact in a three-dimensional model of the knee. *J Biomech*, 24(11):1019–1031, 1991.

[21] R. Bolbos, H. Benoit-Cattin, J.B. Langlois, A. Chomel, E. Chereul, C. Odet, M. Janier, P. Pastoureau, and O. Beuf. Measurement of knee cartilage thickness using MRI: A reproducibility study in a meniscectomized guinea pig model of osteoarthritis. *NMR Biomed*, 21(4):366–375, 2008.

[22] K.D. Brandt, P. Dieppe, and E.L. Radin. Etiopathogenesis of osteoarthritis. *Rheum Dis Clin N Am*, 34(3):531–559, 2008.

[23] J.A. Buckwalter and N.E. Lane. Athletics and osteoarthritis. *Am J Sports Med*, 25(6):873–881, 1997.

[24] A.M.W. Chaudhari, P.L. Briant, S.L. Bevill, S. Koo, and T.P. Andriacchi. Knee kinematics, cartilage morphology, and osteoarthritis after ACL injury. *Med Sci Sports Exerc*, 40(2):215–222, 2008.

[25] S. Checa, M. Taylor, and A. New. Influence of an interpositional spacer on the behaviour of the tibiofemoral joint: A finite element study. *Clin Biomech*, 23(8):1044–1052, 2008.

[26] R.D. Crowninshield, R.C. Johnston, J.G. Andrews, and R.A. Brand. A biomechanical investigation of the human hip. *J Biomech*, 11(1):75–85, 1978.

[27] L.E. DeFrate, H. Sun, T.J. Gill, H.E. Rubash, and G. Li. *In vivo* tibiofemoral contact analysis using 3D MRI-based knee models. *J Biomech*, 37(10):1499–1504, 2004.

[28] S.L. Delp. *Surgery simulation: A computer graphics system to analyze and design musculoskeletal reconstructions of the lower limb*. Stanford University, Department of Mechanical Engineering, PhD thesis, 1990.

[29] S.L. Delp and J.P. Loan. A graphics-based software system to develop and analyze models of musculosketal structures. *Comput Biol Med*, 25(1):21–34, 1995.

[30] Y.Y. Dhaher, T-H. Kwon, and M. Barry. The effect of connective tissue material uncertainties on knee joint mechanics under isolated loading conditions. *J Biomech*, 43(16):3118–3125, 2010.

[31] P.A. Dieppe. Osteoarthritis and related disorders, Volume 2. In D. Weatherall, J. Ledingham, and D. Warrell, editors, *Oxford Textbook of Medicine*, pages 1676–1684. Oxford, UK: Oxford University Press, 1987.

[32] D.D. D'Lima, S. Patil, N. Steklov, S. Chien, and C.W. Colwell, Jr. *In vivo* knee moments and shear after total knee arthroplasty. *J Biomech*, 40(Supplement 1):S11–S17, 2007.

[33] D.D. D'Lima, S. Patil, N. Steklov, J.E. Slamin, and C.W. Colwell, Jr. *In vivo* knee forces after total knee arthroplasty. *Clin Orthop Relat Res*, 440:45–49, 2005.

[34] D.D. D'Lima, N. Steklov, S. Patil, and C.W. Colwell, Jr. *In vivo* knee forces during recreation and exercise after total knee arthroplasty. *Clin Orthop Relat Res*, 466:2605–2611, 2008.

[35] D.D. D'Lima, C.P. Townsend, S.W. Arms, B.A. Morris, and C.W. Colwell, Jr. An implantable telemetry device to measure intra-articular tibial forces. *J Biomech*, 38(2):299–304, 2005.

[36] Y-f. Dong, G-h. Hu, L-l. Zhang, Y. Hu, Y-h. Dong, and Q-r. Xu. Accurate 3D reconstruction of subject-specific knee finite element model to simulate the articular cartilage defects. *J Shanghai Jiaotong Univ (Sci)*, 16(5):620–627, 2011.

[37] G.A. Dumas and J.G. Reid. Laxity of knee cruciate ligaments during pregnancy. *J Orthop Sports Phys Ther*, 26(1):1–6, 1997.

[38] C.O. Dyrby, D.D. D'Lima, C.W. Colwell, Jr., A. Mündermann, and T.P. Andriacchi. *In vivo* knee loading measured by an instrumented total knee replacement during activities of daily living. In *Amer Soc Biomech (Palo Alto, California, USA)*, 2007.

[39] A. Erdemir, S. McLean, W. Herzog, and A.J. van den Bogert. Model-based estimation of muscle forces exerted during movements. *Clin Biomech*, 22(2):131–154, 2007.

[40] P. Eshuis. *Knee modelling: Internship at the AnyBody research project.* Universiteit Twente, Undergraduate final-year project report, 2004.

[41] E. Evangelou, A.M. Valdes, H.J.M. Kerkhof, U. Styrkarsdottir, Y. Zhu, I. Meulenbelt, R.J. Lories, F.B. Karassa, P. Tylzanowski, S.D. Bos, arcOGEN Consortium, T. Akune, N.K. Arden, A.J. Carr, K. Chapman, L.A. Cupples, J. Dai, P. Deloukas, M. Doherty, S. Doherty, G. Engstrom, A. Gonzalez, B.V. Halldorsson, C.L. Hammond, D.J. Hart, H. Helgadottir, A. Hofman, S. Ikegawa, T. Ingvarsson, Q. Jiang, H. Jonsson, J. Kaprio, H. Kawaguchi, K. Kisand, M. Kloppenburg, U.M. Kujala, L.S. Lohmander, J. Loughlin, F.P. Luyten, A. Mabuchi, A. McCaskie, M. Nakajima, P.M. Nilsson, N. Nishida, W.E.R. Ollier, K. Panoutsopoulou, T. van de Putte, S.H. Ralston, F. Rivadeneira, J. Saarela, S. Schulte-Merker, D. Shi, P.E. Slagboom, A. Sudo, A. Tamm, A. Tamm, G. Thorleifsson, U. Thorsteindottir, A. Tsezou, G.A. Wallis, J.M. Wilkinson, N. Yoshimura, E. Zeggini, G. Zhai, F. Zhang, I. Jonsdottir, A.G. Uitterlinden, D.T. Felson, J.B. van Meurs, K. Stefansson, J.P.A. Ioannidis, T.D. Spector, and Translation Research in Europe Applied Technologies for Osteoarthritis. Meta-analysis of genome-wide association studies confirms a susceptibility locus for knee osteoarthritis on chromosome 7q22. *Ann Rheum Dis*, 70(2):349–355, 2011.

[42] J.D. Feikes. *The mobility and stability of the human knee joint.* Department of Engineering Science, D.Phil. thesis, University of Oxford, 1999.

[43] D.T. Felson, J. Goggins, J. Niu, Y. Zhang, and D.J. Hunter. The effect of body weight on progression of knee osteoarthritis is dependent on alignment. *Arthritis Rheum*, 50(12):3904–3909, 2004.

[44] M.A.R. Freeman and V. Pinskerova. The movement of the normal tibio-femoral joint. *J Biomech*, 38(2):197–208, 2005.

[45] J.A. Friederich and R.A. Brand. Muscle fiber architecture in the human lower limb. *J Biomech*, 23(1):91–95, 1990.

[46] T. Fujisawa, T. Hattori, K. Takahashi, T. Kuboki, A. Yamashita, and M. Takigawa. Cyclic mechanical stress induces extracellular matrix degradation in cultured chondrocytes via gene expression of matrix metalloproteinases and interleukin-1. *J Biochem*, 125(5):966–975, 1999.

[47] T. Fukubayashi and H. Kurosawa. The contact area and pressure distribution pattern of the knee: A study of normal and osteoarthrotic knee joints. *Acta Orthopaed Scand*, 51:871–879, 1980.

[48] H.S. Gill. *The mechanics of heelstrike during level walking.* Department of Engineering Science, D.Phil. thesis, University of Oxford, 1996.

[49] J.W. Goodfellow and J.J. O'Connor. The mechanics of the knee and prosthesis design. *J Bone Joint Surg [Br]*, 60-B(3):358–369, 1978.

[50] J. Gosling, P.L.T. Willan, I. Whitmore, and P.F. Harris. *Human anatomy: Color atlas and text, 4th Edition.* Maryland Heights, Missouri, USA: Mosby, 2002.

[51] K.B. Gu and L.P. Li. A human knee joint model considering fluid pressure and fiber orientation in cartilages and menisci. *Med Eng Phys*, 33(4):497–503, 2011.

[52] F. Guilak, A. Ratcliffe, N. Lane, M.P. Rosenwasser, and V.C. Mow. Mechanical and biochemical changes in the superficial zone of articular cartilage in canine experimental osteoarthritis. *J Orthop Res*, 12(4):474–484, 1994.

[53] A. Gulati, R. Chau, D.J. Beard, A.J. Price, H.S. Gill, and D.W. Murray. Localization of the full-thickness cartilage lesions in medial and lateral unicompartmental knee osteoarthritis. *J Orthop Res*, 27(10):1339–1346, 2009.

[54] Y. Guo, X. Zhang, and W. Chen. Three-dimensional finite element simulation of total knee joint in gait cycle. *Acta Mechanica Solida Sinica*, 22(4):347–351, 2009.

[55] Z. Hao, D. Jin, Z. Zhang, and J. Zhang. A finite element 3D model of *in vivo* human knee joint based on MRI for the tibiofemoral joint contact analysis. In V. Duffy,

editor, *Digital human modeling*, pages 616–622. Berlin, Germany: Springer-Verlag Berlin Heidelberg, 2007.

[56] M.K. Harman, G.D. Markovich, S.A. Banks, and W.A. Hodge. Wear patterns on tibial plateaus from varus and valgus osteoarthritic knees. *Clin Orthop Relat Res*, 352:149–158, 1998.

[57] T.L. Haut Donahue, M.L. Hull, M.M. Rashid, and C.R. Jacobs. A finite element model of the human knee joint for the study of tibio-femoral contact. *J Biomech Eng*, 124(3):273–280, 2002.

[58] T.L. Haut Donahue, M.L. Hull, M.M. Rashid, and C.R. Jacobs. How the stiffness of meniscal attachments and meniscal material properties affect tibio-femoral contact pressure computed using a validated finite element model of the human knee joint. *J Biomech*, 36(1):19–34, 2003.

[59] B. Heinlein, F. Graichen, A. Bender, A. Rohlmann, and G. Bergmann. Design, calibration, and pre-clinical testing of an instrumented tibial tray. *J Biomech*, 40(Supplement 1):S4–S10, 2007.

[60] B. Heinlein, I. Kutzner, F. Graichen, A. Bender, A. Rohlmann, A.M. Halder, A. Beier, and G. Bergmann. Complete data of total knee replacement loading for level walking and stair climbing measured *in vivo* with a follow-up of 6-10 months. *Clin Biomech*, 24(4):315–326, 2009.

[61] M.O. Heller, A. Trepczynski, I. Kutzner, E.I. Kornaropoulos, W.R. Taylor, H.-C. Hege, G.N. Duda, and G. Bergmann. Validation of subject-specific musculoskeletal models. In *IUTAM Symp on Human Movement Analysis and Simulation (Leuven, Belgium)*, 2010.

[62] M.-P. Hellio Le Graverand, R.J. Buck, B.T. Wyman, E. Vignon, S.A. Mazzuca, K.D. Brandt, M. Piperno, H.C. Charles, M. Hudelmaier, D.J. Hunter, C. Jackson, V.B. Kraus, T.M. Link, S. Majumdar, P.V. Prasad, T.J. Schnitzer, A. Vaz, W. Wirth, and F. Eckstein. Subregional femorotibial cartilage morphology in women - comparison

between healthy controls and participants with different grades of radiographic knee osteoarthritis. *Osteoarthritis Cartilage*, 17(9):1177–1185, 2009.

[63] H.N. Henninger, S.P. Reese, A.E. Anderson, and J.A. Weiss. Validation of computational models in biomechanics. *Proc Inst Mech Eng [H]*, 224(7):801–812, 2010.

[64] J.K. Hofer, R. Gejo, M.H. McGarry, and T.Q. Lee. Effects on tibiofemoral biomechanics from kneeling. *Clin Biomech*, 26:605–611, 2011.

[65] A.R. Hopkins, A.M. New, F. Rodriguez-y-Baena, and M. Taylor. Finite element analysis of unicompartmental knee arthroplasty. *Med Eng Phys*, 32(1):14–21, 2010.

[66] B.K.P. Horn. Closed-form solution of absolute orientation using unit quaternions. *J Opt Soc Am A*, 4(4):629–642, 1987.

[67] S.L. Ingham, W. Zhang, S.A. Doherty, D.F. McWilliams, K.R. Muir, and M. Doherty. Incident knee pain in the Nottingham community: A 12-year retrospective cohort study. *Osteoarthritis Cartilage*, 19(7):847–852, 2011.

[68] T. Ingvarsson, S.E. Stefansson, I.B. Hallgrimsdottir, M.L. Frigge, H. Jonsson, Jr, J. Gulcher, H. Jonsson, J.I. Ragnarsson, L.S. Lohmander, and K. Stefansson. The inheritance of hip osteoarthritis in Iceland. *Arthritis Rheum*, 43(12):2785–2792, 2000.

[69] V.T. Inman, H.J. Ralston, F. Todd, and J.C. Lieberman. *Human walking*. Baltimore, Maryland, USA: Williams & Wilkins. 1981.

[70] P. Johal, A. Williams, P. Wragg, D. Hunt, and W. Gedroyc. Tibio-femoral movement in the living knee. A study of weight bearing and non-weight bearing knee kinematics using "interventional" MRI. *J Biomech*, 38(2):269–276, 2005.

[71] K.L. Johnson. *Contact mechanics*. Cambridge, UK: Cambridge University Press, 2003.

[72] M.P. Kadaba, H.K. Ramakrishnan, and M.E. Wootten. Measurement of lower extremity kinematics during level walking. *J Orthop Res*, 8(3):383–392, 1990.

[73] M. Kazemi, L.P. Li, M.D. Buschmann, and P. Savard. Partial meniscectomy changes fluid pressurization in articular cartilage in human knees. *J Biomech Eng*, 134(2):1–10, 2012.

[74] M. Kazemi, L.P. Li, P. Savard, and M.D. Buschmann. Creep behavior of the intact and meniscectomy knee joints. *J Mech Behav Biomed Mater*, 4(7):1351–1358, 2011.

[75] H.J.M. Kerkhof, R.J. Lories, I. Meulenbelt, I. Jonsdottir, A.M. Valdes, P. Arp, T. Ingvarsson, M. Jhamai, H. Jonsson, L. Stolk, G. Thorleifsson, G. Zhai, F. Zhang, Y. Zhu, R. van der Breggen, A.J. Carr, M. Doherty, S. Doherty, D.T. Felson, A. Gonzalez, B.V. Halldorsson, D.J. Hart, V.B. Hauksson, A. Hofman, J.P.A. Ioannidis, M. Kloppenburg, N.E. Lane, J. Loughlin, F.P. Luyten, M.C. Nevitt, N. Parimi, H.A.P. Pols, F. Rivadeneira, E.P. Slagboom, U. Styrkarsdottir, A. Tsezou, T. van de Putte, J. Zmuda, T.D. Spector, K. Stefansson, A.G. Uitterlinden, and J.B.J. van Meurs. A genome-wide association study identifies an osteoarthritis susceptibility locus on chromosome 7q22. *Arthritis Rheum*, 62(2):499–510, 2010.

[76] G.W. Keyes, A.J. Carr, R.K. Miller, and J.W. Goodfellow. The radiographic classification of medial gonarthrosis. *Acta Orthop Scand*, 63(5):497–501, 1992.

[77] H.J. Kim, J.W. Fernandez, M. Akbarshahi, J.P. Walter, B.J. Fregly, and M.G. Pandy. Evaluation of predicted knee-joint muscle forces during gait using instrumented knee implant. *J Orthop Res*, 27(10):1326–1331, 2009.

[78] R.U. Kleemann, D. Krocker, A. Cedraro, J. Tuischer, and G.N. Duda. Altered cartilage mechanics and histology in knee osteoarthritis: Relation to clinical assessment (ICRS Grade). *Osteoarthritis Cartilage*, 13(11):958–963, 2005.

[79] S. Knecht, B. Vanwanseele, and E. Stüssi. A review on the mechanical quality of articular cartilage - implications for the diagnosis of osteoarthritis. *Clin Biomech*, 21(10):999–1012, 2006.

[80] R.D. Komistek, D.A. Dennis, and M. Mahfouz. *In vivo* fluoroscopic analysis of the normal human knee. *Clin Orthop Relat Res*, 410:69–81, 2003.

[81] R.D. Komistek, T.R. Kane, M. Mahfouz, J.A. Ochoa, and D.A. Dennis. Knee mechanics: A review of past and present techniques to determine *in vivo* loads. *J Biomech*, 38(2):215–228, 2005.

[82] S. Koo and T.P. Andriacchi. The knee joint center of rotation is predominantly on the lateral side during normal walking. *J Biomech*, 41(6):1269–1273, 2008.

[83] S. Koo, G.E. Gold, and T.P. Andriacchi. Considerations in measuring cartilage thickness using MRI: Factors influencing reproducibility and accuracy. *Osteoarthritis Cartilage*, 13(9):782–789, 2005.

[84] G.M. Kotzar, D.T. Davy, V.M. Goldberg, K.G. Heiple, J. Berilla, K.G. Heiple, Jr., R.H. Brown, and A.H. Burstein. Telemeterized *in vivo* hip joint force data: A report on two patients after total hip surgery. *J Orthop Res*, 9(5):621–633, 1991.

[85] M. Kozanek, A. Hosseini, F. Liu, S.K. van de Velde, T.J. Gill, and H.E. Rubash. Tibiofemoral kinematics and condylar motion during the stance phase of gait. *J Biomech*, 42(12):1877–1884, 2009.

[86] M.-Y. Kuo, T.-Y. Tsai, C.-C. Lin, T.-W. Lu, H.-C. Hsu, and W.-C. Shen. Influence of soft tissue artifacts on the calculated kinematics and kinetics of total knee replacements during sit-to-stand. *Gait Posture*, 33(3):379–384, 2011.

[87] I. Kutzner, B. Heinlein, F. Graichen, A. Bender, A. Rohlmann, A. Halder, A. Beier, and G. Bergmann. Loading of the knee joint during activities of daily living measured *in vivo* in five subjects. *J Biomech*, 43(11):2164–2173, 2010.

[88] M.A. Lafortune, P.R. Cavanagh, H.J. Sommer, and A. Kalenak. Three-dimensional kinematics of the human knee during walking. *J Biomech*, 25(4):347–357, 1992.

[89] S.J. Lee, K.J. Aadalen, P. Malaviya, E.P. Lorenz, J.K. Hayden, J. Farr, R.W. Kang, and B.J. Cole. Tibiofemoral contact mechanics after serial medial meniscectomies in the human cadaveric knee. *Am J Sports Med*, 34(8):1334–1344, 2006.

[90] G. Li, L.E. DeFrate, S.E. Park, T.J. Gill, and H.E. Rubash. *In vivo* articular cartilage contact kinematics of the knee. *Am J Sports Med*, 33(1):102–107, 2005.

[91] G. Li, J. Gil, A. Kanamori, and S.L.-Y. Woo. A validated three-dimensional computational model of a human knee joint. *J Biomech Eng*, 121(6):657–662, 1999.

[92] G. Li, K. Kawamura, P. Barrance, E.Y.S. Chao, and K. Kaufman. Prediction of muscle recruitment and its effect on joint reaction forces during knee exercises. *Ann Biomed Eng*, 26(4):725–733, 1998.

[93] G. Li and O. Lopez. Reliability of a 3D finite element model constructed using magnetic resonance images of a knee for joint contact stress analysis. In *Amer Soc Biomech (Pittsburgh, PA, USA)*, 1999.

[94] G. Li, O. Lopez, and H.E. Rubash. Variability of a three-dimensional finite element model constructed using magnetic resonance images of a knee for joint contact stress analysis. *J Biomech Eng*, 123(4):341–346, 2001.

[95] L.S. Lohmander, A. Östenberg, M. Englund, and H. Roos. High prevalence of knee osteoarthritis, pain, and functional limitations in female soccer players twelve years after anterior cruciate ligament injury. *Arthritis Rheum*, 50(10):3145–3152, 2004.

[96] P. MacKinnon and J. Morris. *Oxford textbook of functional anatomy: Musculoskeletal system, Volume 1*. Oxford, UK: Oxford University Press, 2005.

[97] E.N. Marieb. *Human anatomy & physiology, 6th Edition*. Upper Saddle River, New Jersey, USA: Pearson, 2004.

[98] F.H. Martini. *Fundamentals of anatomy & physiology, 5th Edition*. Upper Saddle River, New Jersey, USA: Prentice Hall, 2001.

[99] S.D. Masouros, A.M.J. Bull, and A.A. Amis. Biomechanics of the knee joint. *Orthop Trauma*, 24(2):84–91, 2010.

[100] J.R. Meakin, N.G. Shrive, C.B. Frank, and D.A. Hart. Finite element analysis of the meniscus: The influence of geometry and material properties on its behavior. *Knee*, 10(1):33–41, 2003.

[101] E.G. Meyer, M.R. Villwock, and R.C. Haut. Osteochondral microdamage from valgus bending of the human knee. *Clin Biomech*, 24(7):577–582, 2009.

[102] K.E. Moglo and A. Shirazi-Adl. Cruciate coupling and screw-home mechanism in passive knee joint during extension-flexion. *J Biomech*, 38(5):1075–1083, 2005.

[103] M.E. Mononen, M.T. Mikkola, P. Julkunen, R. Ojala, M.T. Nieminen, J.S. Jurvelin, and R.K. Korhonen. Effect of superficial collagen patterns and fibrillation of femoral articular cartilage on knee joint mechanics - a 3D finite element analysis. *J Biomech*, 45(3):579–587, 2012.

[104] J.B. Morrison. The mechanics of the knee joint in relation to normal walking. *J Biomech*, 3(1):51–61, 1970.

[105] V.C. Mow, W.Y. Gu, and F.H. Chen. Structure and function of articular cartilage and meniscus, 3rd Edition. In V. Mow and R. Huiskes, editors, *Basic orthopaedic biomechanics and mechano-biology*, pages 182–258. London, UK: Lippincott Williams & Wilkins, 2005.

[106] A. Mündermann, C.O. Dyrby, D.D. D'Lima, C.W. Colwell, Jr., and T.P. Andriacchi. *In vivo* knee loading characteristics during activities of daily living as measured by an instrumented total knee replacement. *J Orthop Res*, 26(9):1167–1172, 2008.

[107] A.P. Newman. Articular cartilage repair. *Am J Sports Med*, 26(2):309–324, 1998.

[108] F.R. Noyes and C.L. Stabler. A system for grading articular cartilage lesions at arthroscopy. *Am J Sports Med*, 17(4):505–513, 1989.

[109] World Health Organization. *Part 3: Disease incidence, prevalence and disability.* WHO Press; France, 2004.

[110] M.G. Pandy. Determination of muscle function in human locomotion. In *IUTAM Symp on Human Movement Analysis and Simulation (Leuven, Belgium)*, 2010.

[111] M.G. Pandy, K. Sasaki, and S. Kim. A three-dimensional musculoskeletal model of the human knee joint. Part 1: Theoretical construction. *Comput Methods Biomech Biomed Engin*, 1(2):87–108, 1997.

[112] G. Papaioannou, G. Nianios, C. Mitrogiannis, D. Fyhrie, S. Tashman, and K.H. Yang. Patient-specific knee joint finite element model validation with high-accuracy

kinematics from biplane dynamic roentgen stereogrammetric analysis. *J Biomech*, 41(12):2633–2638, 2008.

[113] J.P. Paul. Force actions transmitted by joints in the human body. *Proc R Soc Lond*, 192:163–172, 1976.

[114] C.A. Peach, A.J. Carr, and J. Loughlin. Recent advances in the genetic investigation of osteoarthritis. *Trends Mol Med*, 11(4):186–191, 2005.

[115] E. Pena, B. Calvo, M.A. Martinez, and M. Doblare. A three-dimensional finite element analysis of the combined behavior of ligaments and menisci in the healthy human knee joint. *J Biomech*, 39(9):1686–1701, 2006.

[116] E. Pena, B. Calvo, M.A. Martinez, and M. Doblare. Computer simulation of damage on distal femoral articular cartilage after meniscectomies. *Comp Biol Med*, 38(1):69–81, 2008.

[117] E. Pena, B. Calvo, M.A. Martinez, D. Palanca, and M. Doblare. Why lateral meniscectomy is more dangerous than medial meniscectomy. A finite element study. *J Orthop Res*, 24(5):1001–1010, 2006.

[118] J.M.T. Penrose, G.M. Holt, M. Beaugonin, and D.R. Hose. Development of an accurate three-dimensional finite element knee model. *Comput Methods Biomech Biomed Engin*, 5(4):291–300, 2002.

[119] D. Perie and M.C. Hobatho. *In vivo* determination of contact areas and pressure of the femorotibial joint using non-linear finite element analysis. *Clin Biomech*, 13(6):394–402, 1998.

[120] B.I. Prilutsky and V.M. Zatsiorsky. Optimization-based models of muscle coordination. *Exerc Sport Sci Rev*, 30(1):32–45, 2002.

[121] C.E. Quatman, A. Kiapour, G.D. Myer, K.R. Ford, C.K. Demetropoulos, V.K. Goel, and T.E. Hewett. Cartilage pressure distributions provide a footprint to define female anterior cruciate ligament injury mechanisms. *Am J Sports Med*, 39(8):1706–1713, 2011.

[122] M. Ramachandran. *Basic orthopaedic sciences: The Stanmore guide*. London, UK: Edward Arnold Publishers Ltd., 2007.

[123] R. Riemer. *A validated, subject-specific model for predicting tibiofemoral knee force distribution from intersegmental forces*. Department of Mechanical Engineering, M.S. thesis, Michigan Technological University, 2003.

[124] H. Röhrle, R. Scholten, C. Sigolotto, W. Sollbach, and H. Kellner. Joint forces in the human pelvis-leg skeleton during walking. *J Biomech*, 17(6):409–424, 1984.

[125] D.J. Salvetti, C.J. Pino, S.G. Manuel, I. Dallmeyer, S.V. Rangarajan, T. Meyer, M. Kotov, and V.P. Shastri. Design and validation of a compressive tissue simulator with high-throughput capacity and real-time modulus measurement capability. *Tissue Eng Part C Methods*, 18(3):205–214, 2012.

[126] J.M. Scarvell, P.N. Smith, K.M. Refshauge, and H.R. Galloway. Magnetic resonance imaging analysis of kinematics in osteoarthritic knees. *J Arthroplasty*, 22(3):383–393, 2007.

[127] J.M. Scarvell, P.N. Smith, K.M. Refshauge, H.R. Galloway, and K.R. Woods. Evaluation of a method to map tibiofemoral contact points in the normal knee using MRI. *J Orthop Res*, 22(4):788–793, 2004.

[128] J.M. Scarvell, P.N. Smith, K.M. Refshauge, H.R. Galloway, and K.R. Woods. Association between abnormal kinematics and degenerative change in knees of people with chronic anterior cruciate ligament deficiency: A magnetic resonance imaging study. *Aust J Physiother*, 51:233–240, 2005.

[129] O.D. Schipplein and T.P. Andriacchi. Interaction between active and passive knee stabilizers during level walking. *J Orthop Res*, 9(1):113–119, 1991.

[130] B.B. Seedhom. Conditioning of cartilage during normal activities is an important factor in the development of osteoarthritis. *Rheum*, 45(2):146–149, 2006.

[131] K.B. Shelburne, M.R. Torry, and M.G. Pandy. Contributions of muscles, ligaments, and the ground-reaction force to tibiofemoral joint loading during normal gait. *J Orthop Res*, 24(10):1983–1990, 2006.

[132] R. Shirazi and A. Shirazi-Adl. Analysis of partial meniscectomy and ACL reconstruction in knee joint biomechanics under a combined loading. *Clin Biomech*, 24(9):755–761, 2009.

[133] R. Shirazi and A. Shirazi-Adl. Computational biomechanics of articular cartilage of human knee joint: Effect of osteochondral defects. *J Biomech*, 42(15):2458–2465, 2009.

[134] R. Shirazi, A. Shirazi-Adl, and M. Hurtig. Role of cartilage collagen fibrils networks in knee joint biomechanics under compression. *J Biomech*, 41(16):3340–3348, 2008.

[135] R.L. Smith, B.S. Donlon, M.K. Gupta, M. Mohtai, P. Das, D.R. Carter, J. Cooke, G. Gibbons, N. Hutchinson, and D.J. Schurman. Effects of fluid-induced shear on articular chondrocyte morphology and metabolism *in vitro*. *J Orthop Res*, 13(6):824–831, 1995.

[136] S.M. Smith, R.A. Cockburn, A. Hemmerich, R.M. Li, and U.P. Wyss. Tibiofemoral joint contact forces and knee kinematics during squatting. *Gait Posture*, 27(3):376–386, 2008.

[137] Y. Song, J.M. Greve, D.R. Carter, S. Koo, and N.J. Giori. Articular cartilage after MR imaging and thickness mapping of a loaded knee joint before and after meniscectomy. *Osteoarthritis Cartilage*, 14(8):728–737, 2006.

[138] J.M. Spencer, J. Loughlin, K. Clipsham, and A.J. Carr. Genetic background increases the risk of hip osteoarthritis. *Clin Orthop Relat Res*, 431:134–137, 2005.

[139] B.W. Stansfield, A.C. Nicol, J.P. Paul, I.G. Kelly, F. Graichen, and G. Bergmann. Direct comparison of calculated hip joint contact forces with those measured using instrumented implants. An evaluation of a three-dimensional mathematical model of the lower limb. *J Biomech*, 36(7):929–936, 2003.

[140] D.H. Sutherland. An electromyographic study of the plantar flexors of the ankle in normal walking on the level. *J Bone Joint Surg [Am]*, 48:61–71, 1966.

[141] D.H. Sutherland, R. Olshen, E. Biden, and M. Wyatt. *The development of mature walking*. Lavenham, Suffolk, UK: MacKeith Press. 1998.

[142] S. Tashman, D. Collon, K. Anderson, P. Kolowich, and W. Anderst. Abnormal rotational knee motion during running after anterior cruciate ligament reconstruction. *Am J Sports Med*, 32(4):975–983, 2004.

[143] S.J.G. Taylor, J. Gorjon, and P.S. Walker. An instrumented prosthesis for knee joint force measurement *in vivo*. In *Inst of Electrical Electronics Engin Colloquium: Innovative Pressure, Force and Flow Measurements (London, UK)*, 1999.

[144] S.J.G. Taylor, P.S. Walker, J.S. Perry, S.R. Cannon, and R. Woledge. The forces in the distal femur and the knee during walking and other activities measured by telemetry. *J Arthroplasty*, 13(4):428–437, 1998.

[145] W.R. Taylor, M.O. Heller, G. Bergmann, and G.N. Duda. Tibio-femoral loading during human gait and stair descent. *J Orthop Res*, 22(3):625–632, 2004.

[146] AnyBody Technology. The AnyBodyTM modeling system: Tutorials, Version 3.0.0, http://www.anybodytech.com/fileadmin/anybody.3.x.x/doc/tutorials.pdf, 2007, accessed March 2009.

[147] A. Thambyah, J.C.H. Goh, and S. Das De. Contact stresses in the knee joint in deep flexion. *Med Engin & Phys*, 27(4):329–335, 2005.

[148] K.M. Varadarajan, A.L. Moynihan, D.D. D'Lima, C.W. Colwell, Jr., and G. Li. *In vivo* contact kinematics and contact forces of the knee after total knee arthroplasty during dynamic weight-bearing activities. *J Biomech*, 41(10):2159–2168, 2008.

[149] C.L. Vaughan, B.L. Davis, and J.C. O'Connor. *Dynamics of human gait, 2nd Edition*. Cape Town, South Africa: Kiboho Publishers. 1992.

[150] M. Wawro and M. Fathi-Torbaghan. A parallel framework for the FE-based simulation of knee joint motion. *IEEE Transactions on Biomedical Engineering*, 51(8):1490–1494, 2004.

[151] J. Weidow. Lateral osteoarthritis of the knee: Etiology based on morphological, anatomical, kinematic, and kinetic observations. *Acta Orthop Scand*, 77(322):Supplement 3–44, 2006.

[152] J. Weidow, J. Pak, and J. Kärrholm. Different patterns of cartilage wear in medial and lateral gonarthrosis. *Acta Orthop Scand*, 73(3):326–329, 2002.

[153] C. Wengert and G. Bianchi. Absolute orientation, http://www.mathworks.com/matlabcentral/fileexchange/22422-absolute-orientation, 2010, accessed August 2011.

[154] S.H. White, P.F. Ludkowski, and J.W. Goodfellow. Anteromedial osteoarthritis of the knee. *J Bone Joint Surg [Br]*, 73B(4):582–586, 1991.

[155] T.L. Wickiewicz, R.R. Roy, P.L. Powell, and V.R. Edgerton. Muscle architecture of the human lower limb. *Clin Orthop Relat Res*, 179:275–283, 1983.

[156] D.R. Wilson, J.D. Feikes, A.B. Zavatsky, and J.J. O'Connor. The components of passive knee movement are coupled to flexion angle. *J Biomech*, 33(4):465–473, 2000.

[157] D.A. Winter. *Biomechanics and motor control of human movement, 3rd Edition.* Hoboken, New Jersey, USA: John Wiley & Sons, Inc. 2005.

[158] H.J. Woltring. A Fortran package for generalized, cross-validatory spline smoothing and differentiation. *Adv Eng Softw*, 8(2):104–113, 1986.

[159] N.H. Yang, P.K. Canavan, H. Nayeb-Hashemi, B. Najafi, and A. Vaziri. Protocol for constructing subject-specific biomechanical models of knee joint. *Comput Methods Biomech Biomed Engin*, 13(5):589–603, 2010.

[160] N.H. Yang, H. Nayeb-Hashemi, P.K. Canavan, and A. Vaziri. Effect of frontal plane tibiofemoral angle on the stress and strain at the knee cartilage during the stance phase of gait. *J Orthop Res*, 28(12):1539–1547, 2010.

[161] J. Yao, A.D. Salo, J. Lee, and A.L. Lerner. Sensitivity of tibio-menisco-femoral joint contact behavior to variations in knee kinematics. *J Biomech*, 41(2):390–398, 2008.

[162] D. Zhao, S.A. Banks, D.D. D'Lima, C.W. Colwell, Jr., and B.J. Fregly. *In vivo* medial and lateral tibial loads during dynamic and high flexion activities. *J Orthop Res*, 25(5):593–602, 2007.

[163] D. Zhao, S.A. Banks, K.H. Mitchell, D.D. D'Lima, C.W. Colwell, Jr., and B.J. Fregly. Correlation between the knee adduction torque and medial contact force for a variety of gait patterns. *J Orthop Res*, 25(6):789–797, 2007.